Understanding born-again planetary nebulae and their progenitors

Thesis submitted for the dregree of Doctor in Philosophy by

Borja Montoro Molina

Supervised by

Martín A. Guerrero Roncel

INSTITUTO DE
ASTROFÍSICA DE
ANDALUCÍA

EXCELENCIA
SEVERO
OCHOA

Instituto de Astrofísica de Andalucía, Consejo Superior de Investigaciones Científicias (IAA-CSIC)

UNIVERSIDAD
DE GRANADA

Programa de doctorado de Física y Ciencias del Espacio

Editor: Universidad de Granada. Tesis Doctorales
Autor: Borja Montoro Molina
ISBN: 978-84-1195-569-0
URI: https://hdl.handle.net/10481/97450

A mi familia, amigos y aquellas personas especiales
por apoyarme de manera incondicional

AGRADECIMIENTOS

En todos los agradecimientos que he visto siempre hay un tono filosófico, solemne y formal que nunca han ido conmigo porque no es algo que me salga natural, no me sale del alma. En este pequeño apartado me voy a tomar la pequeña libertad de dejarme de todas las formalidades que rodean a una tesis y expresarme como yo realmente lo haría. Hablaré de personas las cuales nunca sabrán que están apareciendo en estos agradecimientos y a las que se dirigen todas estas palabras. Muchas personas piensarán que soy malo por no decírselo, yo les diré que puede ser, pero que así soy y esas personas lo saben.

Primero me gustaría apuntar que al contrario que muchos otros compañeros científicos, por lo cuales lo siento de veras, mi etapa durante la tesis ha sido una de las mejores de mi vida. He estado cómodo, no he parado de aprender, he seguido avanzando en el campo en el que siempre he querido estudiar y nunca me he sentido solo ante la jungla que hay en el ámbito científico. En gran parte se lo debo a mi supervisor, Martín, quién ha tenido paciencia infinita, para enseñarme todo lo que podía, para corregirme mis incontables errocillos aquí y allá y por ser comprensivo en todo momento. Demasiado bien se ha portado conmigo, yo me hubiera apretado más, pero oye, no seré yo quien se queje ahora. Y parte de culpa también la tiene Jesús, por tutelarme fuera del papel a su manera, por acogerme en su propia casa y por darle chispa al asunto.

Dejando la ciencia de lado, en esta nueva etapa en Granada y en el IAA he conocido a muchas personas, muchas, pero entre ellas destaca una en especial. Es una perosna que me ha aguantado casi constantemente, con la que he discutido, me he reido (yo de esa persona y esa persona de mí) e infinidad de otras muchas cosas con las que no acabaría. A esa persona me la llevo en el corazón. Como no he dicho nombres, conozco como es y sé que esta dudando al leer estas palabras se lo aclaro, si eres tu, no dudes tanto.

Luego tenemos a un pequeño ser que la verdad no sé muy bien como condensar en un párrafo todas las cosas que hemos vivido juntos y todo lo que siento. Es alguién a quién me llevo conmigo, de forma figurada y literal. Espero seguir aguantandote y que me aguantes en los nuevos tiempos que vendrán, que sabe dios que son inciertos.

Como no podría ser de otra, agradezco a mi familia todo lo que no esta en los escritos. Son los que siempre han estado y estarán. En este caso diré nombres, a mi titas Gema e Inma, porque han sido como mis otros "padres". A mi hermano Nestor al que quiero decirle aquí por escrito que tu puedes, con todo, no mires a los lados mira hacia adelante. Y por supuesto a mi padre y a mi madre, la que por cierto me va a matar por ponerla la úlitma. A vosotros que no sé que más decir a parte de que os quiero y os llevo en el alma.

Para ir acabando para que esto no se haga eterno, quería decir que probablemente no haya hecho alusión a algunas personas que seguro se merecen estar aquí pero como soy un genio y siempre lo dejo todo para el último momento, ahora no me acuerdo de más. Aún así os doy las gracias y si teneis alguna queja, encantado de discutirla tomando un tintico de verano.

Esto sería todo, como siempre pienso en la vida hay que ser de todo menos "pesao", así que gracias por todo y nos vemos familia.

Abstrac

Born-again planetary nebulae (PNe) have unique chemical and kinematic properties. They form when the central star of the nebula, evolving to become a white dwarf, builds a He shell which at a certain point reaches critical mass and ignites, producing a very late thermal pulse. This event ejects highly processed, H-poor and C-rich material at high velocities that expand inside the previously ejected, H-rich nebula. As a result, the central stars rapidly cool and return to the asymptotic giant branch (AGB), and then follow a somehow similar evolution to that they did during the post-AGB phase. In a sense, the star is "born again."

So far, only four born-again PNe have been confirmed: V4334 Sgr (Sakurai's Object), A 30, A 58, and A 78, while others have been proposed to belong to this group, such as HuBi 1, Fg Sagittae, IRAS 15154−5258, IRAS 18333−2357, and WR 72. Despite the small number of born-again PNe, compared to the total number of PNe (∼4000), it is argued that ∼20% of of all PN central stars have gone through a born-again event. The small number is in line with the short duration of the VLTP (∼20–100 years). They are, therefore, exceptional objects whose characterization helps us understand this extraordinary phase of the stellar evolution of low- and intermediate-mass stars.

This thesis aims at contributing to the understanding of the born-again phenomenon in PNe by investigating the ionization mechanisms involved in born-again PNe, their chemical abundances, and their morphology and spatio-kinematics by means of optical integral field unit and long-slit spectroscopy. This thesis inquires into a series of issues regarding the nature of these sources and their emission mechanisms that are frequently overlooked.

We have focused our efforts on three particular born-again planetary nebulae, HuBi 1, A 58, and A 78.

In HuBi 1, the confirmation of its born-again nature was awaiting the determination of the H-poor nature of its recent ejecta. Using the capabilities of the MEGARA IFU at GTC, we have separated the emission originating from the recent ejecta, uncontaminated from the emission of the H-rich outer nebula. This has allowed the creation of extinction maps and the precise calculation of both $\mathrm{T_e}$ and $\mathrm{n_e}$ for these different structures. Using the mappings software, which accounts for the presence of shocks, the abundances in the ejecta were determined. The H deficiency of the recent ejecta is confirmed, supporting the occurrence of a born-again event in HuBi 1 about 250 ago. This has increased the number of reliably confirmed born-again cases to five.

For A 58, we conducted two studies in synergy. First, we detected variability in the emission lines of long-slit spectra of A 58 over a span of 27 years (1994-2021), approximately 80-100 years after the VLTP. The variability an lines ratios indicated the existence of shocks, rather than the previously suggested photoionization excitation of the gas, and a complex morpho-kinematic structure similar to that reported for Sakurai's Object. These results inspired us to investigate the detailed kinematics of ionized and molecular gas in A 58 using GTC MEGARA IFS and ALMA data. We proposed a model of the morphology of the ionized material in A 58, showing a complex structure indicative of an hourglass-like morphology, contrary to the disk-jet morphology seen in molecular emission. The use of ALMA data was crucial, as without it, the information provided by the optical emission could have been misinterpreted. This work, along with similar studies conducted on Sakurai's Object, highlights the significant role played by molecular gas in the evolution of born-again PNe.

Finally, for A 78 we have demonstrated by using long-slit spectra that it shows inhomogeneities in extinction, physical conditions, and chemical abundances. Treating the latter with special care, we confirm the deficiency in H in the central region and that the N/O ratio is consistent with a born-again scenario. Additionally, abundances in the structure known as the eye-like reveal a mixture between the recent H-poor ejecta and the old H-rich nebula.

These results have helped us understand in more detail the complex nature of born-again PNe and will support other studies of long-standing problems associated to these sources.

Resumen

Las nebulosas planetarias born-again (NPs) tienen propiedades químicas y cinemáticas únicas. Se forman cuando la estrella central de la nebulosa, evolucionando para convertirse en una enana blanca, desarrolla una capa de He que en cierto punto alcanza masa crítica y se enciende, produciendo un pulso térmico muy tardío. Este evento expulsa material altamente procesado, pobre en H y rico en C a altas velocidades que se expanden dentro de la nebulosa previamente expulsada, rica en H. Como resultado, las estrellas centrales se enfrían rápidamente y vuelven a la rama asintótica gigante (AGB), y luego siguen una evolución algo similar a la que tuvieron durante la fase post-AGB. En cierto sentido, la estrella "renace".

Hasta ahora, solo se han confirmado cuatro NPs born-again: V4334 Sgr (Objeto de Sakurai), A 30, A 58 y A 78, mientras que otras han sido propuestas para pertenecer a este grupo, como HuBi 1, Fg Sagittae, IRAS 15154−5258, IRAS 18333−2357 y WR 72. A pesar del pequeño número de NPs born-again, en comparación con el número total de NPs (∼4000), se argumenta que ∼20% de todas las estrellas centrales de PN han pasado por un evento renacido. El pequeño número está en línea con la corta duración del VLTP (∼20–100 años). Por lo tanto, son objetos excepcionales cuya caracterización nos ayuda a entender esta extraordinaria fase de la evolución estelar de estrellas de masa baja e intermedia.

Esta tesis tiene como objetivo contribuir al entendimiento del fenómeno renacido en las NPs investigando los mecanismos de ionización involucrados en las NPs born-again, sus abundancias químicas y su morfología y espaciotemática mediante espectroscopía de campo integral óptico y de rendija larga. Esta tesis indaga en una serie de cuestiones respecto a la naturaleza de estas fuentes y sus mecanismos de emisión que frecuentemente se pasan por alto.

Nos hemos enfocado en tres nebulosas planetarias born-again en particular, HuBi 1, A 58 y A 78.

En HuBi 1, la confirmación de su naturaleza renacida estaba pendiente de la determinación de la naturaleza pobre en H de sus eyecciones recientes. Usando las capacidades del IFU MEGARA en el GTC, hemos separado la emisión originada de las eyecciones recientes, no contaminada por la emisión de la nebulosa externa rica en H. Esto ha permitido la creación de mapas de extinción y el cálculo preciso de ambos T_e y n_e para estas diferentes estructuras. Usando el software de mapeos, que tiene en cuenta la presencia de choques, se determinaron

las abundancias en las eyecciones. La deficiencia de H de las eyecciones recientes está confirmada, apoyando la ocurrencia de un evento renacido en HuBi 1 hace unos 250 años. Esto ha aumentado el número de casos renacidos confirmados de manera fiable a cinco.

Para A 58, realizamos dos estudios en sinergia. Primero, detectamos variabilidad en las líneas de emisión de los espectros de rendija larga de A 58 durante un lapso de 27 años (1994-2021), aproximadamente 80-100 años después del VLTP. Las ratios de variabilidad y líneas indicaron la existencia de choques, en lugar de la excitación de fotoionización del gas previamente sugerida, y una estructura morfo-cinemática compleja similar a la reportada para el Objeto de Sakurai. Estos resultados nos inspiraron a investigar la cinemática detallada del gas ionizado y molecular en A 58 usando datos de GTC MEGARA IFS y ALMA. Propusimos un modelo de la morfología del material ionizado en A 58, mostrando una estructura compleja indicativa de una morfología en forma de reloj de arena, en contraste con la morfología de disco-jet vista en la emisión molecular. El uso de datos

de ALMA fue crucial, ya que sin ello, la información proporcionada por la emisión óptica podría haber sido malinterpretada. Este trabajo, junto con estudios similares realizados sobre el Objeto de Sakurai, resalta el papel significativo del gas molecular en la evolución de las NPs born-again.

Finalmente, para A 78 hemos demostrado mediante espectros de rendija larga que muestra inhomogeneidades en extinción, condiciones físicas y abundancias químicas. Tratando estas últimas con especial cuidado, confirmamos la deficiencia en H en la región central y que la relación N/O es consistente con un escenario renacido. Además, las abundancias en la estructura conocida como el ojo revelan una mezcla entre las eyecciones recientes pobres en H y la nebulosa antigua rica en H.

Estos resultados nos han ayudado a entender en más detalle la naturaleza compleja de las NPs born-again y apoyarán otros estudios de problemas de larga data asociados a estas fuentes.

Contents

List of Figures

List of Tables

Chapter 1

Introduction

The title of this thesis has three key concepts: "born-again", "planetary nebulae" and "their progenitors" in that order. However, the logical order to understand the "born-again" phenomenon and everything investigated in this research would start with the last one and then proceed with the previous two. Therefore, we will begin by discussing the evolution of the progenitors of stars that can potentially become "born-again" stars in the future.

Even before starting discussing the evolution of the "born-again" progenitors it would covenient to briefly describe the Hertzprung-Russell (HR) diagram. This is the basic used to classify stars based on their temperature and luminosity, as well as a tool to represent their evolutionary stages. The effective temperature represents the temperature of a black body with an equivalent surface area and the star's luminosity is quantified in energy units per second. On the HR diagram, the horizontal axis indicating effective temperature increases from right to left while the vertical axis depicting luminosity rises upward. This orientation is rooted in historical conventions, where the HR diagram is frequently plotted against the color index instead of temperature, transitioning from blue (short wavelength) on the left to red (long wavelength) on the right. Luminosity correlates with the bolometric magnitude M, displayed on the vertical axis in Figure 1.1, through the relationship $\mathrm{M} = 4.75 - 2.5 \log(\mathrm{L}/\mathrm{L}_{\odot})$. Note that stars appear brighter for smaller M values.

Spectral classification (or type), is assigned based on features observed in the star spectrum. The widely adopted classification system of Morgan-Keenan encompasses spectral types O, B, A, F, G, K, and M (and more recently, L type for brown dwarfs), arranged in descending order of effective temperature, as depicted in Fig. 1.1 (left panel). These spectral types are further divided into decimal subdivisions, like M0 through M9, and, in some instances, each subtype undergoes additional division. The HR diagram further organizes stars by luminosity by mean of lines labeled I through V and small letter "a" and "b" from higher to lower luminosities, as is indicated in Fig. 1.1 (left panel).

If one were to graph a random sample of stars, it would become evident that up to 90% of them, sit along a diagonal strip extending from the upper left to the lower right of the HR diagram. These stars are commonly known as main sequence (MS) stars, constituting the region where a star spends the majority of its evolutionary lifespan. Main sequence stars are engaged in H fusion at their nuclei Beyond this phase lies the giants group, encompassing

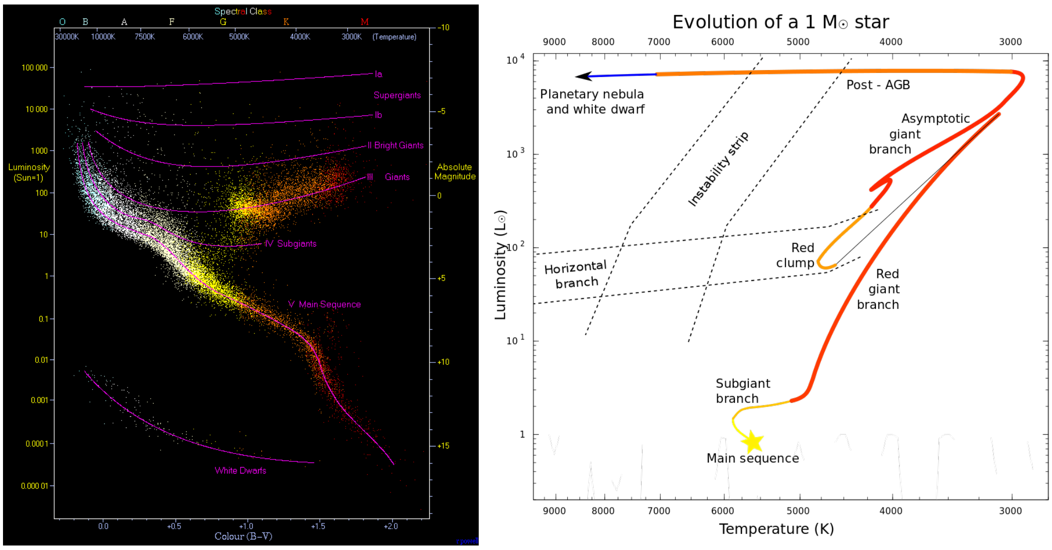

Figure 1.1: Evolutionary pathway of a sun-like star in the HR diagram (right). A plot of luminosity (absolute magnitude) against the colour of the stars ranging from the high-temperature blue-white stars on the left side of the diagram to the low temperature red stars on the right side (left).

larger stars that have left the main sequence. A star becomes a giant after it has burned all the available H in its core and departs from the main sequence. The behavior of the stars from this point onward is intimately related to its mass. The stars of interest in this work are those with low and intermediate masses, i.e. those with initial mass from 0.8-1.0 to 8-10 $M_{\odot}$, which show a common evolutionary pathway in the HR diagram, albeit with some variations. In Fig. 1.1 (left panel) is shown the evolutionary pathway of a sun-like star in the HR diagram. This includes the red giant branch (RGB), the asymptotic giant branch (AGB) phase, post-AGB or planetary nebula (PN) phase and, ultimately, the white dwarf (WD) phase.

1.1 Evolution of low- and intermediated-mass stars

Stars are classified as low, intermediate and high mass based on the nuclear reactions they are able to undergo behind the MS and most notably during the AGB phase. Figure 1.2 shows this in a schematic representation. Massive stars are defined as those that develop a non-degenerate carbon core and, therefore, can fuse carbon in a non-violent manner. These are capable of undergoing a series of progressing nuclear reactions (C to O, O to Ne, etc.) that lead them to the building an iron core. They will eventually suffer a core collapse and a supernova explosion, leaving behind a neutron star or a black hole. As for low and intermediate-mass stars, which are the star of interest here, both their evolution after leaving the main sequence and their final products, as WD, are reasonably similar to each other and completely different from those of massive stars.

In the following subsections, we briefly summarize the stellar evolution of low- and intermediate-mass stars from the main sequence to the white dwarf phase.

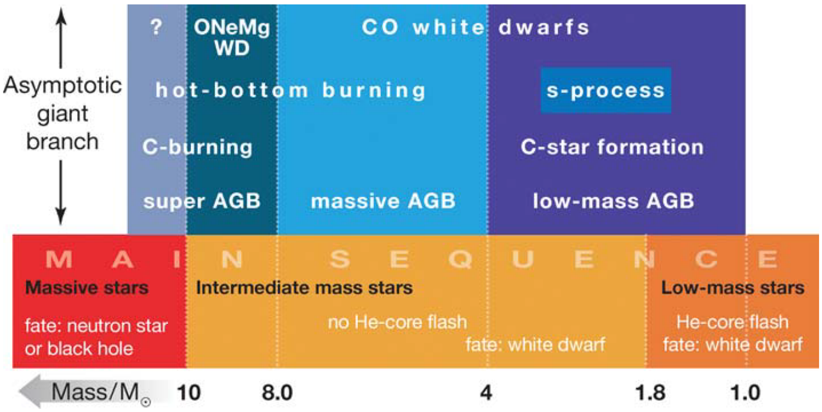

Figure 1.2: Classification of stars by mass on the main sequence (lower part) and on the AGB (upper part). The lower part shows mass designation according to initial mass. The upper part indicates the mass classification appropriate for AGB stars. Approximate limiting masses between different regimes are given at the bottom. Figure adopted from Herwig (2005).

1.1.1 From the main sequence to the red giant branch

Stars are primarily composed of H (about 75%) and He (about 25%), with minor amounts of other light elements such as carbon, nitrogen, and oxygen, alongside traces of heavier elements. During the MS, which constitutes the majority of a star's nuclear-burning lifespan, the star consumes H in its core. The duration of this phase varies with the star's initial mass; lower mass stars have a longer life and vice versa. Throughout this stage, the depletion of H produces He in the core of low- to intermediate mass stars.

After the depletes its core H in the MS, it transitions to the RGB phase where it fuses H in a shell around a core composed mostly He. The He core, which maintains thermal equilibrium, is below the Schönberg–Chandrasekhar limit and will evolve depending on the star's mass and the metallicity.

At the bottom of the RGB phase, stars exhibit a similar effective temperature, around 5,000 K, with luminosities varying according to their mass. As stars ascend the RGB, the fusion of H layers produces more He, causing an increase in both the core mass and temperature. This accelerates the H fusion, making the stars brighter, larger and somewhat cooler. The ascent involves internal events such as the first dredge-up (FDU)[1] and the RGB bump[2], giving rise to observable features (see Figure 1.3).

For stars with a degenerate He core, there is a limit to this growth in size and luminosity, known as the tip of the RGB (TRGB), where the core reaches sufficient temperature to begin fusion. This fusion begins explosively in an event known as the He flash. The star overall becomes less luminous and hotter and migrates to the horizontal branch (HB). During this brief phase the star progresses into a new equilibrium phase by fusing He in their cores and H

---

[1] The FDU occurs as the convective layer deepens progressively until it reaches the previously convective core. Consequently, fusion products from lower layers (He, C, N, and O) ascend, leading to a noticeable change in the outer layer chemical abundances.

[2] It occurs when the H-burning shell around the He core moves outward and encounters a discontinuity in the H profile of the star. This results in a temporary slowdown in the ascent of the star along the RGB, causing a slight pile-up of stars at this point in the HR diagram.

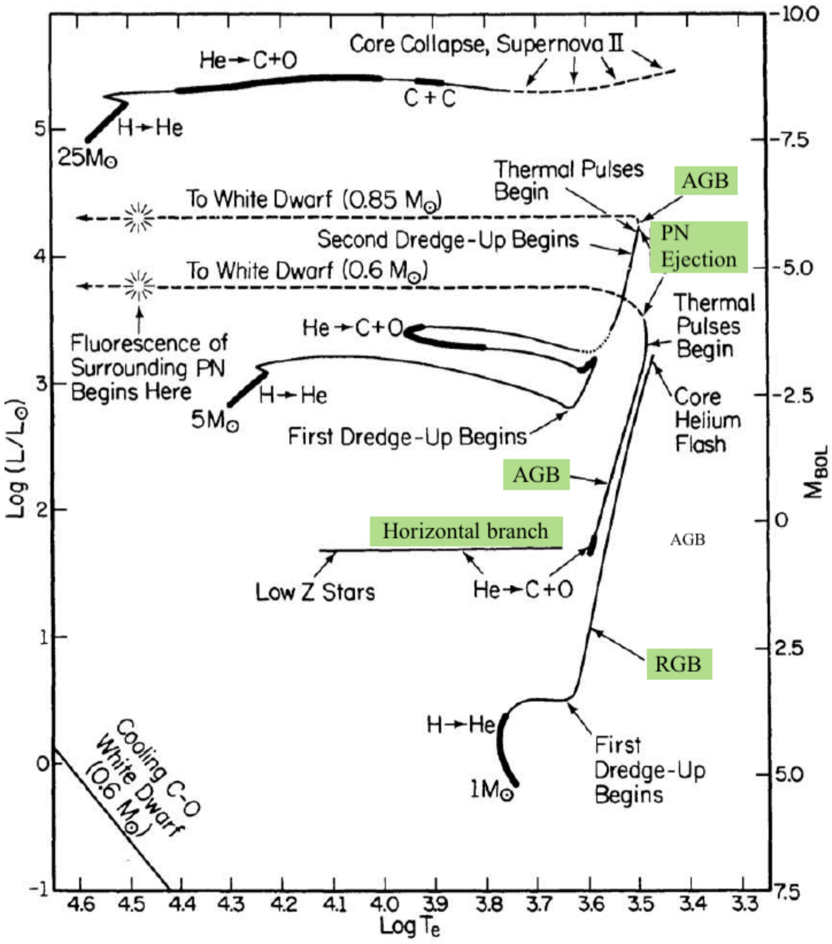

Figure 1.3: Stellar evolutionary tracks for stars with initial masses of 1, 5 and 25 M$_\odot$. The different nuclear burning phases are labeled. Figure adopted from Iben (1995).

in the surrounding layer through the CNO cycle. The cores of all stars in the HB phase have very similar masses ($\sim$0.5 M$_\odot$, Lee et al. 1993), implying similar luminosities. Stars initially more massive than 2 M$_\odot$ have non-degenerate He cores on the RGB. These star become hot enough to start triple-alpha fusion before reaching the TRGB and before the core becomes degenerate. They then leave the RGB and perform a blue loop before returning to join the AGB.

1.1.2 Asymptotic giant branch

The onset of the AGB phase occurs when stars with initial masses between 0.8-8 M$_\odot$ develop a degenerate C-O core after having depleted He during the HB (Iben & Renzini 1983; Herwig 2005, and references therein). The term "asymptotic" is employed because the Temperature-Luminosity relationship of low-mass AGB stars ($T^\star$-$L^\star$) overlaps with that of stars on the RGB (see the case of 1 M$_\odot$ in Fig 1.3). The AGB can be categorized into two phases: (i) the early-AGB (E-AGB) and (ii) the thermal-pulsing AGB (TP-AGB).

As helium becomes exhausted in the core, helium burning begins in shells around the core and the star evolves towards the E-AGB. The carbon and oxygen contract in the inner regions, so the core becomes the electron degenerate, while the outer layer starts a new expansion

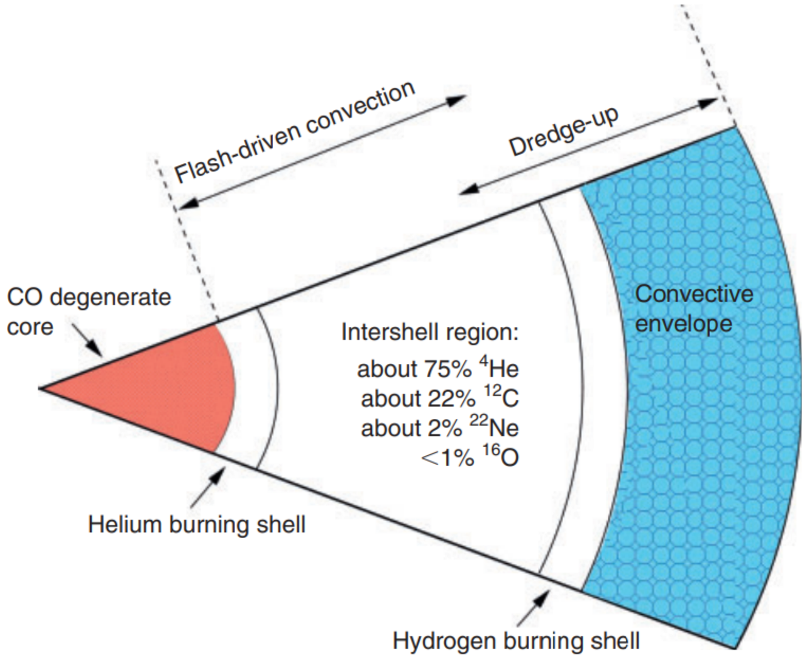

Figure 1.4: Schematic view of the layers of an AGB star, showing the degenerate CO core surrounded by a He-burning shell, a H-burning shell, and a convective envelope. Figure adopted from Karakas & Lugaro (2010).

phase. The He-burning shell is also surrounded by a deep convective envelope of H. Figure 1.4 shows a sketch of the structure of a AGB star. In the intermediate-mass stars (> 4 M$_{\odot}$), as He-burning stopped in the core, the strong expansion extinguishes the H-burning shell, and a similar enrichment to the FDU episode that takes place in the RGB (Becker & Iben 1979) ocurrs now. This event, known as the second dredge-up (SDU), alters the surface composition, increasing ^{4}He and ^{14}N while reducing ^{12}C, 13C and ^{16}O. For stars with masses below 4 M$_{\odot}$, this dredge-up process does not occur as the H shell burning continues. Depending on the core mass, the E-AGB phase has a lifetime of approximately 10^{7} yrs (Iben & Renzini 1983). Accurate evolutionary timescales and properties of the AGB-phase are presented in Table 1.1.

The mass of the He layer just below the H-burning shell increases over a period between 10,000 and 100,000 years, based on recent calculation (Miller Bertolami 2016). This leads to an increase in the triple-alpha reaction rate. The He shell will eventually ignite in a violent process known as He-shell flash or thermal pulse (TP) (Schwarzschild & Härm 1965; Iben 1975), the star then enters the aforementioned TP-AGB phase.

For TP-AGB stars, the luminosity averaged over the He-flash cycle can be aproximated by the core-mass luminosity relationsship $L_{\star} = 59250\ (M_c/M_{\odot} - 0.52)L_{\odot}$ (Paczyński 1970), reaching intensity peaks thousands of times greater than the luminosity of the star. After this peak the observed luminosity rapidly decreases exponentially within just a few years. The flash induces the expansion and cooling of the star, causing the cessation of H shell burning and initiating strong convection in the region between the two shells. As the He shell burning nears the base of the H shell, elevated temperatures rekindle H fusion, restarting the cycle.

Table 1.1: Main properties of the sequences from the ZAMS to TP-AGB. Table adopted from Miller Bertolami (2016).

M_i [$M_\odot$]	τ_{MS} [Myr]	τ_{RGB} [Myr]	HeCF	τ_{HeCB} [Myr]	τ_{eAGB} [Myr]	M_c^{1TP} [$M_\odot$]	$\tau_{TP-AGB(M)}$ [$M_\odot$]	$\tau_{TP-AGB(C)}$ [Myr]	#TP (AGB)	M_f [$M_\odot$]	N_C/N_O
Z_0=0.02											
1.00	9626.5	2043.9	yes	131.60	11.161	0.5119	0.65512	0.0000	4	0.5281	0.400
1.25	3857.6	1262.8	yes	124.96	10.302	0.5268	0.89729	0.0000	6	0.5615	.368
1.50	2212.4	480.67	yes	114.64	11.508	0.5267	1.2959	0.16583E-01	11	0.5760	2.20
2.00	1055.0	33.928	no	307.42	19.420	0.4873	2.9196	0.97759E-01	18	0.5804	1.12
3.00	347.06	4.6762	no	83.942	6.2381	0.6103	0.79992	0.10622	18	0.6573	1.66
4.00	163.85	1.5595	no	28.196	1.9150	0.8086	0.32029	0.0000	34	0.8328	.812
Z_0=0.01											
1.00	7908.5	1697.2	yes	113.53	11.965	0.5128	0.73881	0.0000	4	0.5319	.372
1.25	3259.5	988.43	yes	110.20	11.177	0.5276	1.0972	0.14698E-01	8	0.5660	3.93
1.50	1889.2	400.18	yes	101.54	11.439	0.5289	1.2904	0.75163E-01	10	0.5832	1.13
2.00	921.34	27.072	no	282.61	12.747	0.5170	1.6179	0.37651	13	0.5826	1.98
2.50	509.27	8.6930	no	148.01	7.6400	0.5728	0.71424	0.41896	12	0.6160	2.48
3.00	318.67	4.0683	no	73.307	4.1321	0.6755	0.31492	0.14332	13	0.7061	1.97
Z_0=0.001											
0.800	12430.	1313.5	yes	116.80	13.089	0.4918	0.35321	0.0000	0	0.4971	.271
0.900	8020.9	1024.7	yes	102.38	10.345	0.5167	0.77626	0.0000	3	0.5340	.316
1.00	5413.9	808.66	yes	95.343	10.531	0.5282	0.85648	0.75481E-01	4	0.5517	6.61
1.25	2368.4	533.69	yes	103.72	8.2357	0.5439	1.0575	0.15402	7	0.5849	5.89
1.50	1300.9	288.15	yes	99.209	7.7074	0.5573	0.74257	0.46337	8	0.5995	5.79
1.75	951.65	46.973	no†	210.27	8.2381	0.5298	1.1446	1.1904	15	0.5867	6.41
2.00	671.98	17.363	no	151.06	7.5069	0.5717	0.60336	1.0910	15	0.6182	6.59
2.50	389.98	5.9308	no	70.605	3.6796	0.6976	0.11696	0.49306	16	0.7101	6.98
3.00	255.51	2.9146	no	41.077	2.0364	0.8244	0.22804	0.82625E-01	24	0.8314	2.38
Z_0=0.0001											
0.800	11752.	891.50	yes	98.484	10.089	0.5049	0.77058	0.0000	3	0.5183	.194
0.850	9425.1	768.48	yes	93.850	9.5246	0.5128	1.1515	0.28265E-01	4	0.5328	6.45
1.00	5255.3	525.95	yes	94.476	8.3594	0.5280	1.3575	0.92408E-01	5	0.5631	7.00
1.50	1261.4	241.51	yes	112.01	8.1327	0.5526	0.76920	0.89965	12	0.6024	6.50
2.20	470.74	10.813	no	98.665	3.2623	0.7022	0.12220	0.48387	16	0.7130	4.86
2.50	349.85	5.8835	no	66.012	2.6371	0.7568	0.20994	0.20654	17	0.7543	5.70

Notes. M_i: initial mass of the model (at Zero-Age Main Sequence, ZAMS). τ_{MS}: duration of the main sequence until $X_H^{center} = 10^{-6}$. τ_{RGB}: lifetime from the end of the main sequence to He-ignition, set at $\log L_{He}/L_\odot = 1$. HeCF: full He-core flash (and subflashes) at the beginning of the core He-burning phase. τ_{HeCB}: lifetime of core He-burning until $X_{He}^{center} = 10^{-6}$. τ_{eAGB}: lifetime of the early AGB phase from the end of core He burning to the first thermal pulse. M_c^{1TP}: mass of the H-free core at the first thermal pulse (defined as those regions with $X_H < 10^{-4}$). $\tau_{TP-AGB(M)}$: lifetime of the star in the TP-AGB as an M-type star $N_C/N_O < 1$). $\tau_{TP-AGB(C)}$: lifetime of the star in the TP-AGB as a carbon star ($N_C/N_O > 1$). #TP: number of thermal pulses on the AGB. M_f: final mass of the star. N_C/N_O: C/O ratio in number fraction at the end of the TP-AGB phase. "no†" indicates that a mild He-burning runaway appeared but no full He-core flash and subflashes finally developed.

The number of thermal pulses throughout the TP-AGB depends on the star mass (more pulses for more massive stars) and also to some degree on the mass loss rate (higher mass loss will result in fewer He pulses). During each of these episodes, several interesting events occur: (i) at the He flash, the temperature inside a flash-driven convective shell is high enough for N to be converted into Ne; (ii) after the flash, the base of the convective envelope reaches down past the H/He discontinuity and a dredge up of heavy elements, know as third dredge-up, occurs whose efficiency determines how much of this nucleo-enriched material will reach the surface; (iii) for higher masses (4 $M_\odot$), nuclear burning can occur at the bottom of the convective envelope where C is converted to N, the so-called hot-bottom burning, and the stellar luminosity can reach very high values (Iben 1991, see also Fig. 1.2).

The low $T_{\rm eff}$($\sim$3000 K) and high luminosities reached during the AGB phase in conjunction with the current masses (below 8 $M_\odot$) result in surface gravities 4-5 orders of magnitude below of Sun-like star. This makes AGB star prone to mass loss from its outer layers in the form of a stellar wind. Adding the even higher discrete mass loss episodes associated with thermal pulses led the star to lose 50 to 70% of its mass during the TP-AGB phase (Wood et al. 2004). Mass-loss rates of AGB stars, determined with various observational methods, are typically in the range of 10^{-8} to 10^{-5} $M_\odot$ yr^{-1}, but values as high as 10^{-4} $M_\odot$ yr^{-1} have been reported (Höfner & Olofsson 2018). The mass-loss rate could be as high that it even governs the evolutionary timescales instead of nuclear burning.

1.1.2.1 Circumstellar envelopes of AGB stars

The gas and dust particles that escape the stellar gravitational attraction form a stellar wind that is observable as an expanding circumstellar envelope (CSE) around the AGB star. The winds of AGB stars are relatively slow, with typical values ranging between 5-15 km s^{-1}, but the range can be extended to 3-30 km s^{-1}. The characteristics of the CSEs could vary considerably depending also on varying mass-loss rates and acceleration efficiencies.

The chemical compositions of the gas and dust in the CSE reflect the composition of the stellar atmosphere at the time when the material was ejected, although not necessarily in a straightforward way. In particular, the relative abundances of C and O are important, both for the atmosphere and CSE, due to the high binding energy of the CO molecule. CO forms deep inside the atmosphere, effectively exhausting up the less abundant of the two species (which therefore also determines the abundance of CO) and leaving the rest of the more abundant species to form other molecules and solids. Consequently, the stellar spectra and wind acceleration by radiation pressure on dust are both strongly affected by the C/O ratio.

1.1.3 From Post-AGB phase to the white dwarf

In the latest AGB stage, the star suffers several mass loss episodes with a typical rate up to $\sim 10^{-3}$ $M_\odot$ yr^{-1}, the so-called superwind phase. The departure from the AGB occurs as a consequence of winds reducing the mass of the H-rich envelope (Schoenberner 1979). Consequently, this transition occurs gradually and the definition of the beginning of the post-AGB

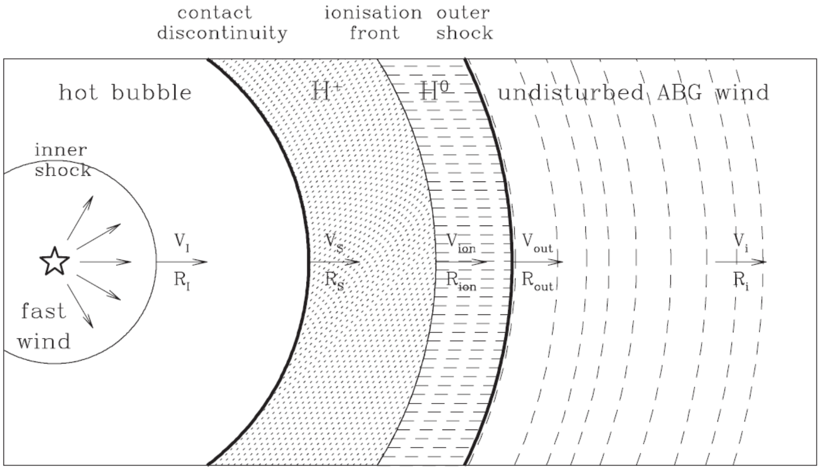

Figure 1.5: Sketch of the system composed by the central star, shocked PN shell, and undisturbed AGB wind. Figure adopted from Marigo et al. (2001).

phase (i.e., the end of the AGB) is somewhat arbitrary (Miller Bertolami 2016). Eventually when the total mass of the envelop ($\mathrm{M_{env}}$) drops below a certain mass ($\mathrm{M_{env}}/M_{\mathrm{star}}{\sim}0.01$) and only the inner parts remain, the star contracts for the last time and leaves its CSE behind. The star, now as a post-AGB star, and the CSE form the protoplanetary nebula (pPN).

As the star increases its temperature, the stellar wind driven by radiation pressure intensifies. Effective temperatures above 30,000 K produce a considerably faster mass loss due to higher radiation pressures. Stellar winds can reach terminal velocities up to $\sim$ 2000 km $\mathrm{s^{-1}}$. As a result, the new fast stellar wind sweeps up the material previously ejected during the AGB phase, creating a high-density, shell-like structure (Kwok et al. 1978). The interaction between the two winds (the slow one produced during the AGB phase and the newly mentioned fast one) creates a high-temperature bubble that exerts pressure on the shell (Shklovsky 1957; Abell & Goldreich 1966; Paczyński 1970), causing it to expand. The increasing output of UV photons will gradually ionize the shell, which at the same time is growing in mass as more material from the AGB wind is swept up. This set of ionized envelopes by the central star is what is known as a planetary nebula (PN), and the post-AGB star becomes the central star of a planetary nebula (CSPN). A sketch of this scenario is showed in Figure 1.5.

During the post-AGB phase, the temperature increases at a constant luminosity, so the path of a post-AGB star on the HR diagram is a horizontal line. The timescales of the post-AGB phase are extremely dependent on the initial mass but do not depend strongly on the surface metallicity of the population at the end of the AGB (Miller Bertolami 2016). While CSPN higher mass models ($\geq$0.7 $\mathrm{M_\odot}$) require only a few hundreds of years to cross the HR diagram and only thousands of years to fade by a factor of 100, CSPN lower mass models ($\leq$0.55 $\mathrm{M_\odot}$) require more than 10 kyr to cross the HR diagram and more than 100 kyr to decrease their luminosity only by an order of magnitude. Table 1.2 shows the main post-AGB properties. The timescales in this table are represented by the customary used parameters τ_{tr} and τ_{cross} (Renzini 1989; Schoenberner 1990; Vassiliadis & Wood 1994; Marigo et al. 2004; Weiss & Ferguson 2009). The first one correspond to the duration of the early post-AGB phase, i.e. the transition time from the end of AGB (taken at $\mathrm{M_{env}}$=0.01 for these models) to

Table 1.2: Main properties of post-AGB H-burning sequences. Table adopted from Miller Bertolami (2016)

M_i [$M_\odot$]	M_i [$M_\odot$]	τ_{tr} [kyr]	τ_{cross} [kyr]	X_H	X_{He}	X_C	X_N	X_O	$\Delta M_{env}^{winds}/\Delta M_{env}^{total}$
Z_0=0.02									
1.00	0.5281	9.14	24.9	0.671	0.309	.287E-02	.181E-02	.952E-02	0.167
1.25	0.5615	4.09	5.97	0.673	0.307	.265E-02	.203E-02	.956E-02	0.208
1.50	0.5760	3.39	4.49	0.637	0.308	.281E-01	.218E-02	.170E-01	0.223
2.00	0.5804	2.27	1.99	0.661	0.309	.985E-02	.271E-02	.117E-01	0.244
3.00	0.6573	1.21	0.378	.645	0.321	.133E-01	.322E-02	.107E-01	0.327
4.00	0.8328	.587	.499E-01	.627	.333	.622E-02	.159E-01	.102E-01	0.569
Z_0=0.01									
1.00	0.5319	36.1	63.0	0.701	0.289	.133E-02	.105E-02	.474E-02	0.201
1.25	0.5660	4.61	9.30	0.586	0.310	.733E-01	.990E-03	.248E-01	0.154
1.50	0.5832	3.10	4.22	0.700	0.285	.503E-02	.117E-02	.592E-02	0.173
2.00	0.5826	2.43	2.40	0.685	0.292	.109E-01	.144E-02	.734E-02	0.188
2.50	0.6160	1.67	1.22	0.675	0.300	.129E-01	.163E-02	.691E-02	0.216
3.00	0.7061	1.08	0.339	0.684	0.297	.850E-02	.171E-02	.576E-02	0.293
Z_0=0.001									
0.900	0.5340	9.89	67.3	0.731	0.268	.111E-03	.136E-03	.468E-03	0.052
1.00	0.5517	4.49	10.4	0.684	0.284	.262E-01	.115E-03	.528E-02	0.060
1.25	0.5849	2.46	3.44	0.649	0.296	.444E-01	.166E-03	.101E-01	0.074
1.75	0.5867	1.82	2.14	0.549	0.332	.872E-01	.371E-03	.181E-01	0.078
2.00	0.6182	1.57	1.28	0.661	0.294	.345E-01	.185E-03	.698E-02	0.097
2.50	0.7101	0.937	0.318	0.642	0.297	.463E-01	.532E-03	.882E-02	0.195
3.00	0.8314	0.763	0.117	0.691	0.278	.767E-02	.168E-01	.428E-02	0.275
Z_0=0.0001									
0.850	0.5328	4.63	42.5	.459	.346	.161	.142E-04	.333E-01	0.038
1.00	0.5631	3.02	5.44	.677	.286	.310E-01	.147E-04	.590E-02	0.038
1.50	0.6024	1.76	1.98	.619	.308	.557E-01	.191E-03	.114E-01	0.049
2.20	0.7130	.951	.377	.641	.297	.310E-01	.172E-01	.847E-02	0.116
2.50	0.7543	.715	.184	.566	.326	.603E-01	.205E-01	.141E-01	0.189

Notes. M_i: initial mass of the model (at ZAMS). M_f: final mass of the star. τ_{tr}: timescale from the end of the AGB (taken at $M_{env} = 0.01\ M_\star$) to the moment in which log $T_{eff} = 3.85$. τ_{cross}: timescale from the moment in which log $T_{eff} = 3.85$ to the point of maximum effective temperature. X_H, X_{He}, X_C, X_N, and X_O: H, He, C, N, and O surface abundances of the post-AGB models.ΔM_{env}^{winds} and ΔM_{env}^{total}: reduction of the H-rich envelope (M_{env}) from log T_{eff} = 3.85 to the point of maximum T_{eff} owing to winds and the combined effect of winds and H-burning, respectively.

Table 1.3: White dwarf spectral classification by McCook & Sion (1999)

Type	Characteristics
DA	Only Balmer lines; no He I or metal present
DB	He I lines; no H or metals
DC	Continuous spectrum, no lines deeper than 5% in any part of the spectrum
DO	He II strong; He I or H present
DZ	Metal lines only; no H or He lines
DQ	Carbon features, either atomic or molecular in any part of the spectrum

the moment in which log T_{eff}=3.85 (∼7000 K, this value could vary for others models). This correspond to the time until the radiation-drive hot wind sets in (technically the point when it is larger than the Reimers wind, see Weiss & Ferguson 2009). The second τ_{cross}, in turn, gives the timescale of the later post-AGB evolution from T_{eff}=3.85 to the point of maximum effective temperature, i.e. the turn-around point at the “knee” of the track followed by a post-AGB star in the HR diagram.

After the CSPN has reached a maximum effective temperature (∼10^5 to 2×10^5 K), it starts to cool down, resulting in a decrease in its luminosity. The PN continues to expand to larger sizes until it has completely faded away. The central star continues to cool as a WD. The nebular material dissolves into the interstellar medium, mixing with other existing material, from where new stars may be born.

The WD phase is the final stage of low to intermediate mass single stars. WDs are divided into two groups, namely those with a H-dominated atmosphere (DA), and those with a H-deficient atmosphere (DB). Table 1.3 lists spectral classification codes for white dwarfs by McCook & Sion (1999). This general classification has been updates accounting for SDSS data releases, Gaia contribution, magnetic WDs among others (Kleinman et al. 2013; Ferrario et al. 2015; Gentile Fusillo et al. 2019). Section 1.2.2 presents possible evolutionary paths followed by a post-AGB star, some of them resulting in the different types of WDs described in Tab. 1.3. It worth to mention that the H-deficient atmosphere WDs constitute ∼25 of the population (Bédard 2024). As will be detailed later, these are presumably the result of a thermal pulse after the post-AGB phase, the so-called born-again event (Iben et al. 1983; Herwig et al. 1999; Blöcker 2001; Lawlor & MacDonald 2003; Althaus et al. 2005; Miller Bertolami et al. 2006).

The pertinent portion of stellar evolution relevant for this body of work is post-AGB evolution. While it is largely true that most low and intermediate mass stars enter the WD cooling track in a way similar to what is described here, there are some that defy this standard evolutionary path. One small subgroup enters the WD cooling track in this way, but leaves it one last time, returning to the AGB. It is this small subgroup that comprises those that experience the born-again phenomenon.

1.2 The born-again phenomenon

In previous seccions, an explanation of the evolutionary path of a star with low and intermediate mass to potentially undergo a Very Late Thermal pulse (VLTP) was given. Those star phase burns H and He alternatively in the AGB as they undergo He-shell flashes or cyclic thermal pulses, ejecting large amounts of matter and leaving an inert core of carbon and oxygen. These pulsating cycles last until the H envelope mass falls below a critical value, and energy generation ceases, causing the star's envelope to contract. A radiatively driven wind from the contracting star can then compress the surrounding material, and when the effective temperature becomes high enough (30,000 K), UV photons ionize the ejecta, now forming a PN. The post-AGB star evolves, increasing its surface temperature at roughly constant luminosity, burning the rest of its envelope until H is exhausted. The CSPN then enters the WD cooling track, irradiating thermal energy and cooling down. However, in certain cases, CSPNe are capable of building a He shell eventually reaching the critical mass to ignite, before depleting all surrounding H (Schoenberner 1979; Iben et al. 1983). For this pulse to be considered VLTP, it must occur when H-burning has practically ceased in the early WD cooling branch (Miller Bertolami et al. 2006, , see also section 1.2.2). Indeed, this is crucial as the observed abundances afterward depend on the time when this thermal pulse occurs (Todt & Hamann 2015).

During a VLTP, He turns into C and O, and highly processed, H-deficient material is ejected, expanding into the old H-rich nebula. As the stellar envelope expands, it cools dramatically, pushing the CSPN back to lower effective temperatures ($T_{\rm eff}$), first as an H-deficient giant, later as a late C-rich Wolf–Rayet ([WC]) type star[3] (e.g., Crowther et al. 1998; Górny & Tylenda 2000; García-Rojas et al. 2013, and references therein). It is also believed that oxygen-rich, H-deficient PG 1159 stars may result from this event (Dreizler & Heber 1998; Werner 2001). The star then embarks on an extended phase of quiescent He burning, during which it retraces very closely (and on approximately the same timescale) the same path in the H-R diagram which it traversed during the H burning phase. Figure 1.6 (left pannel) shows the pathway followed by the CSPN in the HR-diagram after it underwent a VLTP. The planetary nebula shell brightens again, but now at a much larger radius than during the first phase of excitation. In this sense, the central star and its PN are **born-again**.

1.2.1 The born-again event

The onset of the born-again event is clearly marked by the occurrence of the He flash followed by subsequent violent proton burning. Its end however, is ill defined. It is typically defined as the moment when the star returns to the giant branch regime (τ_{BA}, e.g. Iben & MacDonald 1995; Herwig et al. 1999; Miller Bertolami et al. 2006), but there are no unique prescriptions for the values of temperature and luminosity when this occurred. values indicating that the star is in the giant branch regime, but rather a region in the HR diagram considered as the giant branch regime. In fact, some authors do not specify this exact moment in their models,

---

[3] The [WC] are stars with carbon-rich surfaces that exhibit spectra reminiscent of massive Wolf-Rayet stars and are differentiated by adding [].

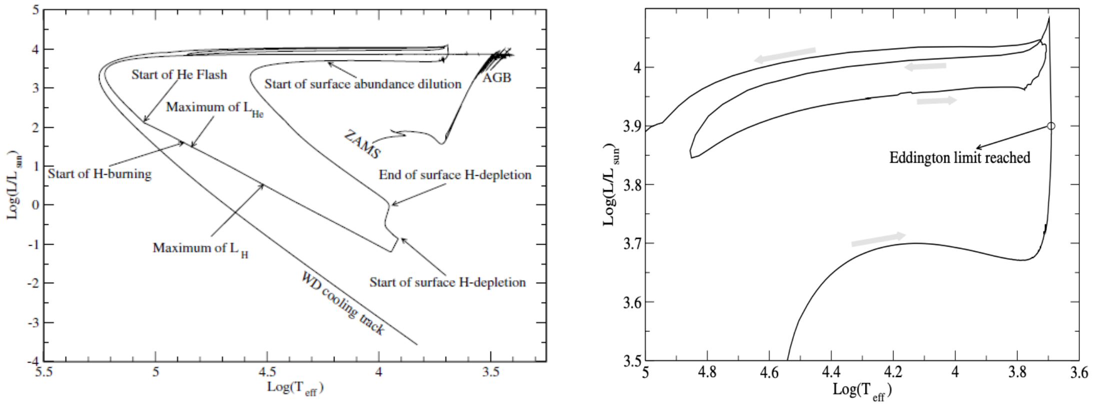

Figure 1.6: In the left panel it is shown the pathaway followed by a CPSN in the HR-diagram after undergone a VLTP. In the right panel a zoom of part of ht previous evolution in the HR diagram. Here we see the typical double loop pattern due to successive H and He driven expansions. The location where our model reaches the Eddington limit is shown. Both panels were presented by Miller Bertolami et al. (2006).

so it is recommended to review those in detail to make fair comparisons between models and observations.

Next, we will examine both the timescales calculated in different theoretical models and the changes in the star's composition after undergoing a VLTP.

1.2.1.1 Born-again timescales

Initially, Iben & MacDonald (1995) conducted evolutionary calculations incorporating appropriate time-dependent mixing procedures, yielding timescales around 17 yr. In contrast, Herwig et al. (1999) and Lawlor & MacDonald (2003) obtained times of 350 yr, which do not match well with observations, which have shown an evolution of less than two decades for Sakurai's object (see section 1.3.1. In order to reconcile observations with theory, Herwig (2001a) suggested the convective mixing velocity in the He-burning layer to be much lower than that given by the standard Mixing-Length Theory (MLT), approximately a factor of 100. Althaus et al. (2005), without extreme care of the time-step during the violent proton burning, reported longer born-again times (20–40 yr). This temporal variation is non-trivial and depends, among other factors, on the adopted theory of the physical processes during VLTP (MLT, GNA convection[4] ,...), and specific parameters in each (temporal resolution, diffusion coefficient, ...). In particular, Miller Bertolami et al. (2006) found that when the minimum allowed time step is below $5{\times}10^{-5}$ yr with the MLT theory, they obtain born-again times of 5-10 yr. In the case of adding chemical gradients in the mixing velocity calculation, the times tend to increase by a factor of 2 (10-20 yr). The results from these simulations are in good agreement with the observed born-again times of Sakurai's object. On the other hand, Miller Bertolami & Althaus (2007) investigated the temporal dependence of born-again in terms of the remnant mass star.

---

[4] The "GNA theory" refers to a double-diffusive convection theory for fluids with composition gradients. This theory incorporates the effects of a chemical gradient ($\nabla\mu$) in the mixing processes and energy transport within stars.

Within the standard MLT not considering any reduction in mixing efficiency, the H-driven[5] expansion that leads to shorter born-again times is expected to occur only in VLTP of low-mass remnants. The transition mass value dictating whether the expansion is H-driven or He-driven (the later leading to longer timescales) is around 0.6 $M_\odot$. Times vary from 5-15 yr to over 100 yr for the first and second cases, respectively.

The evolution timescales beyond the born-again event is not clear but exist some theoretical estimations. In the most recent models (Miller Bertolami et al. 2006), the star remains in the giant phase for the next 26 years (low $T_{\rm eff}$). This estimate that contradicts the rapid reheating observed in the Sakurai's object (Hajduk et al. 2005), probably due to the hydrostatic approximation adopted in the model. Subsequently, the star increases its temperature until reaching $T_{\rm eff}$ ∼60000 K about 100 yr after the He flash, and begins an expansion driven by He that lasts about 250 yr, bringing it back to the giant regime for the second time. After describing these loops in the HR diagram (see right panel in Fig. 1.6), the star contracts again and gradually increases its temperature, similar to when it departs from the AGB phase. Finally, the time until the star reaches again the point where it experienced the VLTP within the cooling track is estimated to be around 43,000 years (Iben et al. 1983). Unfortunately, any trace of the born-again event will have likely vanished by that time, as the H-poor ejecta would have mixed with the H-rich old nebula and that are dispersed into the interstellar medium (ISM). An example of evolved PNe after its CSPNe have underwent a VLTP are A 30 or A 78, estimated to have experienced the VLTP approximately 1000 yr ago (Reay et al. 1983; Guerrero et al. 2012; Fang et al. 2014). The ejecta in expansion are being mixed with the surrounding nebulae revealing H-rich abundances enhanced in some element originating from the VLTP. Further details will be provided in chapter 6.

1.2.1.2 Chemical changes after VLTP

Throughout the born-again event, physical properties and chemical abundances undergo drastic changes. Table 1.4 provides a comparison of mass fraction surface abundances for elements before and after the VLTP. The chemical abundance distribution pre-VLTP is essentially that of its AGB predecessor. Such a contrast indicate that the mixing of the surface abundances during the VLTP is much more pronounced than the mixing occurring in thermal pulses during the AGB phase. These variations arise because the convection zone powered by the burning He shell grows in mass until its outer edge reaches the H-rich layer during the VLTP, allowing convection to mix He and other heavier elements into the envelope. In contrast, the presence of a high entropy barrier prevents this from happening[6] in the AGB phase.

As the outer edge of the convection zone reach layers with a greater abundances of H, the proton burning increases at the same time as the luminosity. At the moment the energy generation in the H-burning shell becomes comparable to that in the He-burning shell the original convective region splits into two distinct convective zones. The upper one is proton-

---

[5] By H-driven or He-driven, we refer to the primary energy source coming from the fusion of H or He, respectively.

[6] We refer to the entropy barrier as a physical thermodynamic condition that prevents convective mixing between H and He layers. The sharp gradient in entropy between each shell creates a stabilizing effect. However, TP can temporarily disrupt the entropy gradient, causing brief episodes of mixing (drege-ups).

Table 1.4: Surface stellar abundances (in mass fraction) from VLTP theoretical models at different moments during the stellar evolution. In the last column the values of the total amount of H in the star after the VLTP are presented (if available).

		H	He	C	N	O	$M_H^{total}/M_\odot$
BEFORE FLASH	z=0.001	0.699	0.287	0.0094	0.0004	0.0028	...
	z=0.004	0.709	0.281	0.0043	0.0005	0.0028	...
	z=0.01	0.702	0.286	0.0020	0.0010	0.0049	...
	z=0.02	0.675	0.304	0.0030	0.0018	0.0101	...
AFTER FLASH	MLT (early VLTP)	3.7×10^{-4}	0.324	0.371	0.0145	0.217	3.19×10^{-6}
	MLT ($f = 0.03$)	5×10^{-6}	0.307	0.378	0.0129	0.229	7.24×10^{-9}
	GNA ($\nabla\mu = 0$)	3.2×10^{-5}	0.316	0.378	0.0129	0.221	2.19×10^{-7}
	GNA	3.3×10^{-5}	0.316	0.378	0.0127	0.221	6.76×10^{-9}
	LM2003 D/10^{-4}†	0.06	0.57	0.26	...	0.07	2×10^{-6}
	LM2003 D/10^{-3}†	0.02	0.55	0.28	...	0.08	3×10^{-7}
	LM2003 D/10^{-2}‡	0.04	0.54	0.28	...	0.08	...
	Herwig et al. (1999)	...	0.388	0.362	...	0.219	4×10^{-11}

The abundances before undergoing the He flash are taken from models of Lawlor & MacDonald (2003). The abundances calculated by Miller Bertolami et al. (2006) after flash once the star has reached for the first time the giant region are presented in the four middle rows. The next 3 rows correspond with the abundances obtained by Lawlor & MacDonald (2003) (LM2003) at the moment the star has reach the first time the giant region (†) and once it has reached the white dwarf cooling track after the VLTP (‡). Abundances derived by Herwig et al. (1999) are also included (being "D" the diffusion coefficient).

burning convection zone (PBCZ) while the lower one is powered by He. Within a period of few days the PBCZ suddenly moves outwards promoting the transport of material from H-rich layers to hotter deeper layer, increasing vigorously the fusion and the luminosity. It is at that point when the luminosity attains its maximum. The VLTP, therefore, is divided into two brief phases, one where the He layer pushes the outer edge of the convective zone and another where proton ingestion occurs. The depletion of H occurs primarily through the chain ^{12}C + p → ^{13}N + γ → ^{13}C + e$^+$ + ν, given the high abundance of ^{12}C in the He-shell and via ^{13}C + p → ^{14}N + γ as the ^{12}C turn into ^{13}C and the abundance of the later increases (Herwig et al. 1999; Lawlor & MacDonald 2003; Miller Bertolami et al. 2006, for further details). This mixing enriches the star's surface in He, carbon, nitrogen, oxygen, neon, and other metals.

The differences between the abundances calculated by Lawlor & MacDonald (2003) and by Miller Bertolami et al. (2006) shown in Table 1.4 are likely due to the more detailed treatment by the latter, as described above. Specifically, the relatively high H abundances obtained by Lawlor & MacDonald (2003) taken once the star returns to the WD cooling track contrast sharply with those by Miller Bertolami et al. (2006). The empirical-theoretical results on hot WDs obtained by Bédard et al. (2023) rather agree with the range of H abundance found by the latter author.

The precise amount of H that remains on the surface of the CSPN time after undergoing a VLTP is still uncertain. Most theoretical studies of the VLTP scenario assert that convective

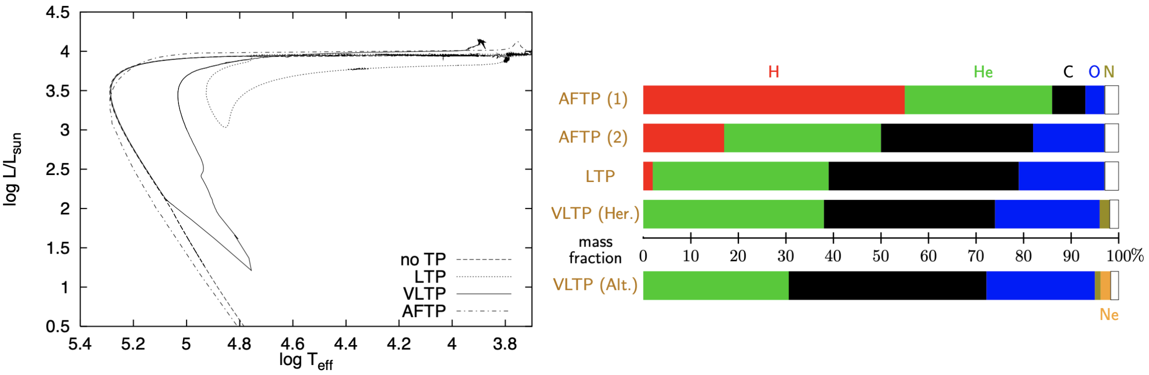

Figure 1.7: In the left panel, from Herwig (2001a), is represented the evolutionary tracks in the H-R diagram for a progenitor star with an initial mass of 2 M$_\odot$, which have undergone a LTP (dot line), VLTP (solid line), AFTP (dot-dashed line) and any of the previuos pulses (dashed line), respectively. The right panel shows the expected abundance patterns for [WC] stars from stellar evolutionary models presented by (Todt & Hamann 2015). (Her.) denoted abundnaces obtained by Herwig (2001a) while (Alt.) those derived by Althaus et al. (2005).

dilution, along with modest mass loss rates in the giant stage, will erode the last vestiges of H remaining in the star before it returns to the cooling sequence (Iben et al. 1983; Althaus et al. 2005; Werner & Herwig 2006; Miller Bertolami et al. 2006). However, the spectral evolution of hot WDs firmly challenges this assertion (Bédard et al. 2023; Bédard 2024). Indeed, a few objects known as hybrid PG 1159 stars[7] also show traces of H, indicating that they did not get rid of their entire H content (Bédard 2024). Leaving the uncertainties about precise amount of H aside, the abundances expected to be observed in the material ejected during the VLTP are clearly extremely poor in H (this is the key aspect), and rich in highly-processed materials.

1.2.2 Other late thermal pulse scenarios

In addition to the VLTP, another two thermal pulse scenarios have been proposed to describe the formation of [WC] CSPN, an asymptotic giant branch final thermal pulse (AFTP) and a late thermal pulse (LTP) (see for instance, Blöcker 2001; Herwig 2001a; Werner 2001; Werner & Herwig 2006). Figure 1.7 (left panel) depicts different evolutionary tracks for a star with an initial mass of 2 M$_\odot$. The surface abundances of a H-deficient star (including the amount of H retained) strongly depend on the occurrence time of a thermal pulse beyond the AGB phase (Todt & Hamann 2015). Figure 1.7 (right panel) shows the resulting surface abundances in mass fraction for different evolutionary scenarios.

- The **AFTP** occurs at the end of the AGB, when the envelope has a very low mass of $\sim$10^{-2} M$_\odot$ and the CS has not yet gone through a CSPN phase, i.e. the CS have not yet reached the T$_{\rm eff}$ to ionized the circumstellar envelope. This process dilutes the surface abundance of H, while it enriches C and O. The AFTP makes H-deficient surface abundances, but the remaining H fraction is very high ($>$ 15% by mass). Therefore, it cannot explain the typical surface abundances of [WC] stars. However, it may naturally

---

[7] These are a subcategory of the broader PG 1159 class of stars, which are extremely hot. Unlike their counterparts, these present traces of H, indicating that the star has retained some H on its surface.

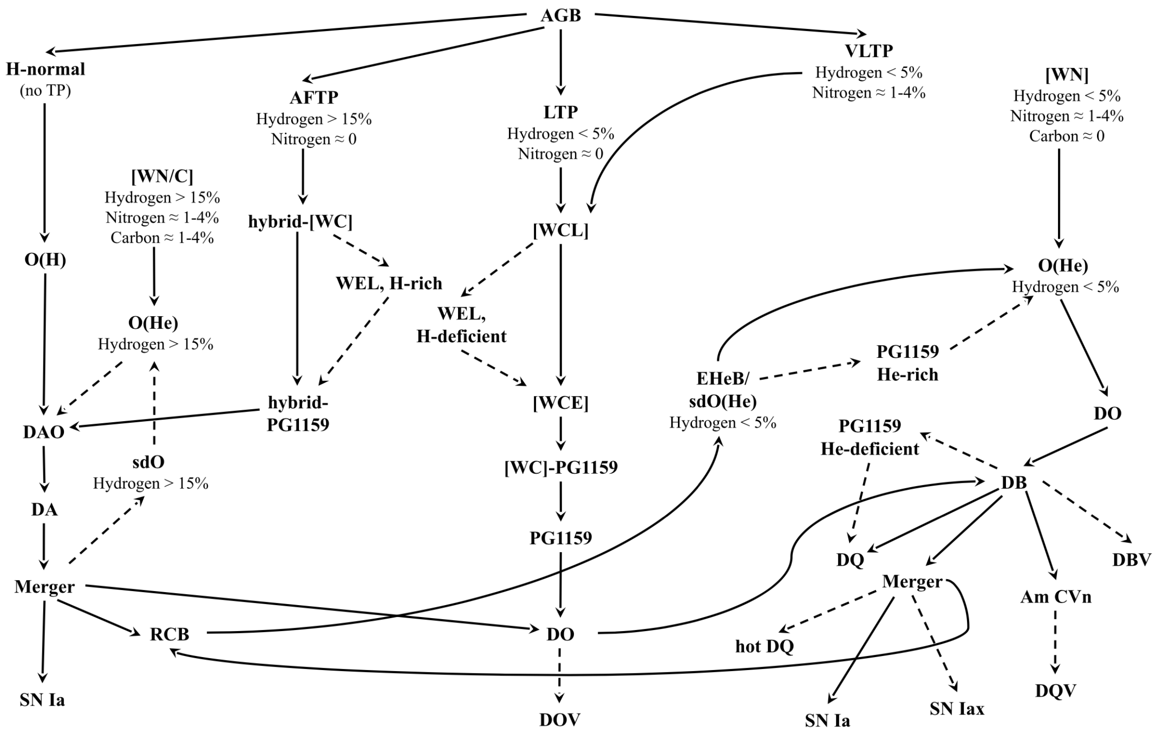

Figure 1.8: Post-AGB evolutionary paths of CSPNe summarized from the literature. Figure adopted from Danehkar (2014).

explain the relatively high H abundances in the hybrid-PG1159 stars and some [WR] stars.

- The **LTP** occurs while the star moves from the AGB phase towards the WD with constant luminosity, and the CS has recently evolved into the CSPN phase. The H surface abundance remains unchanged through the thermal pulse. A H-deficient surface is produced only when the star returns to the AGB phase, and a dredge-up mixing process decreases H at the surface to a few percent ($\leq 5\%$ by mass). This type of evolution has been proposed, for example, in Hen 3-1357, the Stingray Nebula (Reindl et al. 2014, 2017; Lawlor 2021) or in Fg Sagittae (Herwig 2001a; Jeffery & Schönberner 2006).

In addition to the three previous possibilities, some more exotic scenarios could result in H-deficient stars. These have not been described or considered since they usually require the presence of a companion and are not outcomes of the evolution of single stars. Such scenarios involve accretion in binary systems (Abell 48, LMC N66?), common envelope ejections, or stellar mergers (R CrB, KPD 0005+5106?) (Frew et al. 2014). Figure 1.8 summarizes different scenarios in which some type of thermal pulse occurs and their possible paths. This scheme is general and may not include all the cases or specific situations reported in the literature.

It is convenient to establish a criterion to discern whether a CSPN (and obviously the PN) is a born-again or not. In this thesis, the requirement considered for this purpose is that the CSPN has undergone the thermal pulse once the WD phase has started and not during the post-AGB phase (on the horizontal path toward higher temperatures in the HR diagram). In other words, the thermal pulse must be VLTP and not simply late LTP or AFTP. Note that this criterion has not been universally accepted within the scientific community but rather has been a selection based on experience during the period of work of this thesis. Therefore, it is possible that other works may include other sources which have undergone a LTP within the born-again category (see, for instance, Ohnaka & Jara Bravo 2022).

Under this criteria, currently only 5 PNe are considered bona fide members of the born-again planetary nebulae group, namely, Sakurai's Object, A 30, A 58, A 78, and HuBi 1. Particularly, at the beginning of this doctoral thesis, HuBi 1 was not yet fully confirmed; the calculation of abundances in the recent inner ejecta, still pending, are presented here in Chapter 3. Additionally, certain sources have been proposed to potentially belong to this reduce group. These are: PM 1-89, WR-72, IRAS 18333-235, Fg Sagittae and NGC 40. One can reasonably think that given the low percentage of born-again stars (5 out of ∼4000 PNe), this event is rather anecdotal; however, predictions say otherwise. CSPNe can be expected to go through a born-again event with an ocurrence rate ranging between 15 and 25% (Lawlor & MacDonald 2003; Iben 1984; Weidmann et al. 2020). This estimate agrees with observational evidence from hot WDs that show a high deficiency in H, which is estimated to be around ∼25% (Iben 1984; Bédard et al. 2023; Bédard 2024). The discrepancy between confirmed born-again cases and the estimates is still unclear. It is likely due to a set of various factors, such as the short duration of this phase, the difficulty in confirming that a VLTP has occurred or the relative lack of knowledge about stellar evolution in phases beyond the AGB among others.

1.2.3 Planetary nebulae around born-again central stars

The results of this thesis primarily focus on the ejecta recently expelled after the born-again event, describing both its chemistry and its morpho-kinematics. As a starting point and for comparison, we use the corresponding external nebulae. These provide us with useful information about the abundances prior to the VLTP, the ionization structure, and the nature of the CSPN, among others. It is advisable to briefly describe some aspects relevant: timescales, interactions with the ISM, or the typical chemistry expected in a PN.

1.2.3.1 Timescales of PNe

The lifespan of a PN is the time during which it can be observed, in other words, the period of detectability. This largely depends on the relationship between two different timescales: the evolutionary timescales of the CSPN, which provide ionizing photons (see 1.1.3), and the dynamical timescales of the circumstellar material expelled at the end of the AGB phase (Marigo et al. 2001). If the CSPN evolves too quickly, the brightness of the ionized PN would correspond to a short-lived event with a low detection probability. Conversely, if the CSPN evolves too slowly, it would reach the capacity to ionize the nebula only when it has already dispersed to radii too large to be detected. These timescales in turn depend on various factors, making them far from simple to predict.

To estimate the stellar evolutionary timescales, we must rely on post-AGB stellar evolution models (see previous section). Among all available, those presented by Miller Bertolami (2016) are the most precise, as they include an updated treatment of microphysics and a current description of mixing processes and winds that play a key role during the thermal pulses in the AGB phase. Their results are in good agreement with the empirical determinations carried out by Gesicki et al. (2014) in the Galactic Bulge. In general, it can be said that models that depart from the AGB with less massive envelopes or with higher luminosities (i.e., faster burning) show shorter timescales, although metallicity adds variations to the scales in a way not directly proportional to the mass. The stellar evolution timescales can be seen in Table 1.2 for different masses and metallicities. Adding the periods $\tau_{\rm r}$ and $\tau_{\rm cross}$, the evolutionary timescales can range from 0.6 to 100 kyr.

As for the nebular dynamical timescales, these depend on several factors including: i) the properties (mass loss rates and terminal velocities) of both the AGB wind (super and/or slow) and the fast post-AGB wind, ii) their dynamic interaction that produces gas shocks with related heating/cooling processes, and iii) the effects of ionization, which tends to expand and accelerate the nebula as a result of increased thermal pressure. Marigo et al. (2001) presented a series of models (see their Table 2) taking into account all the aforementioned factors, with greater or lesser extent simplifications, also assuming spherical symmetry and a triple wind model in the formation of the nebula (Schmidt-Voigt & Koeppen 1987; Marten & Schoenberner 1991). The evolutionary models for the CSPNe adopted were those obtained by Vassiliadis & Wood (1994). Figure 1.9 shows the evolution of the main parameters up to 30 and 55 kyr for H-(left) and He-burning (right) models with CSPNe of masses ~0.6 M, representative to some extent of the rest of the models. The interpretation of the evolution of the parameters is far from simple, for which we strongly recommend comparing the detailed analysis carried out by the authors for each one. However, it is worth highlighting a particularly relevant result. The evolutionary times of He-burning CSPNe are greater than those of H-burning, so the peak of ionization is reached later when the nebula has expanded to larger radii.

In our case this is especially interesting, since PNe whose CSPNe potentially undergo a VLTP (see Section 1.2) will have a higher probability of detection when the dynamic ages of the PNe, usually defined as $\mathrm{t_{dyn}} = {}_{\mathrm{ion}}/\mathrm{v_{exp}}$, are large. McCarthy et al. (1990) suggested that in cases where old PNe with young CSPNe are observed, it could be because they are born-again sources and that the PN is already expanded while the star is still near the AGB region. The short evolution timescale of a star after a VLTP event needs to be yet considered .

1.2.4 Interactions between ISM and PNe

The interaction between PNe and the ISM is an important process whose effects allow us to gain a better understanding of the two components involved. On one hand, it enables us to understand the structure and physical properties of the ISM such as density, filling factor of coronal gas, and magnetic field effect. On the other hand, it is helpful for studying the evolution of old PNe and PN haloe. This process can also be used to predict the direction of movement of the CSPN and to better understand the "missing mass phenomenon" (i.e., the mass difference between the WD and its parent star).

The criteria for determining whether a PN is interacting with the ISM have been defined with slight differences over the years (Tweedy & Kwitter 1996; Rauch et al. 2000; Wareing

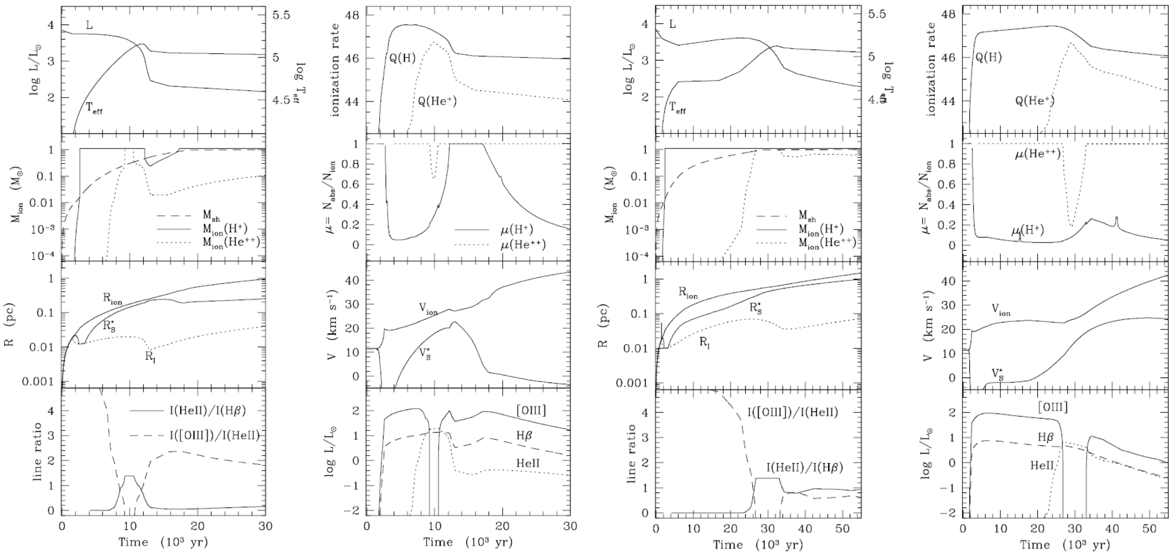

Figure 1.9: Predicted evolution of basic parameters corresponding to PNe models ionised by a H-burner (left) and He-burner (right) CS with a mass of ∼0.6. Figure adopted from Marigo et al. (2001).

et al. 2007). The most basic and functional would be: i) displacement of the central star relative to the center of the nebula, ii) flux enhancement located at a distinct edge in the outer regions of the nebula, iii) and drop in the ionization level in the regions just mentioned. Each of these criteria alone is not sufficient to confirm interaction, and it is generally necessary to observe all of them to confirm that an interaction exists. On other occasions, we can rely on more "complex" clues such as the presence of stripes in a nebula, which are speculated to be caused by interactions with the interstellar magnetic field (Soker & Zucker 1997). Ali et al. (2012) presents a statistical analysis of 117 interacting PNe (IPNe) confirmed based on their physical parameters, their preferential galactic orientation, and their morphological classifications. Moreover, it is well known that the material expelled during the AGB phase tends to become more spherical as it progresses (Plait & Soker 1990; Soker 1994; Mellema 1993). Therefore, if the outer nebulae present a completely rounded profile, there is little room for doubt in saying that this nebula does not interact with the ISM.

By the time a CSPN undergoes a VLTP, the outer PN (hereinafter simply called born-again PNe) around it should be old and reasonably expanded. A natural question would then be whether this PN has expanded to such an extent that interaction with the ISM has begin. This possibility will be discussed on section 1.3.5.

1.2.4.1 Chemical abundances and physical properties

The outermost layers of the born-again PNe provide a reference point to compare the chemical abundances and physical properties seen in the internal ejecta expelled during the VLTP, which is the focus of this work. Both their abundances and physical properties are expected to be typical of usual PNe.

Classic PNe can be classified according to their chemical abundances into four types following the scheme proposed by Peimbert (1978). According to this classification, type I contains

Table 1.5: chemical abundances in galactic PNs.

	Type I		Type II-III		Sun
Elements	Simple Values	Log notation	Simple Values	Log notation	Log notation
He/H	0.137 ± 0.029 (85)	11.14	0.103 ± 0.015	11.01	11.0
C/H	$(5.27\pm2.93)\times10^{-4}$(15)	8.72	$(6.56\pm3.67)\times10^{-4}$(105)	8.82	8.67
C/H	$(3.94\pm2.60)\times10^{-4}$(64)	8.60	$(1.17\pm1.14)\times10^{-4}$(99)	8.07	7.99
C/H	$(4.64\pm2.24)\times10^{-4}$(75)	8.66	$(4.57\pm2.45)\times10^{-4}$(103)	8.66	8.92
C/H	$(1.11\pm0.56)\times10^{-4}$(55)	8.05	$(9.71\pm5.78)\times10^{-4}$(80)	7.99	7.92

Chemical abundances in Galactic PNe for the most abundant elements. The number of PNe averaged is showed in parentheses. The Table adopted from Perinotto (1991). have been omitted

PNe with either He/H $>$ 0.125 or log N/O > -0.3. These PNe have been recognized to be morphologically filamentary and not central symmetric, but instead bipolar or biaxial; to have very strong forbidden lines of quite different excitation, from [O I] to [Ne V] and with kinematics and Galactic distribution resembling those of Population I stars. Type II contains (no He-N rich) PNe in the solar neighborhood with an average height over the Galactic plane of $|Z| = 150$ pc. These PNe have been later subdivided into IIa [log (N/H) +12 $>$ 8.0] and IIb [log (N/H)+12 $<$ 8.0] by Faundez-Abans & Maciel (1986). They are considered to resemble stars of intermediate Population I. Type III contains the PNe, not belonging to the halo, with a high velocity Type IV refers to halo PNe, i.e., to those that are at high distance from the Galactic plane or belong to a globular cluster. The averages abundances of the most abundant elements separately for type I and type II-III PNs are provided in Table 1.5.

The electronic temperatures in PNe are generally found in the range between 10000-20000 K (Osterbrock & Ferland 2006). These can be derived from the ratios of the emission line triplets of [O III] or [N II], which will systematically always be lower if derived from the nitrogen doublet. As for the electronic densities, the range is broader, starting from around 100 to 10000 cm^{-3}, measured using doublet line ratios like [S II] and [Ar IV] (Osterbrock & Ferland 2006). High densities might be found in younger nebulae or nebulae with compact structures.

1.3 Bona-fide born-again PNe sample

In this section, detailed historical descriptions are provided for the confirmed born-again PNe in the order in which, a priori, they have experienced the VLTP.

1.3.1 Sakurai's object

On February 20 1996, an 11.4 "nova-like object" was discovered in Sagittarius by the amateur astronomer Y.Sakurai and reported by Nakano et al. (1996). Figure 1.10 shows four images of the ejecta and the surrounding nebula. Sakurai's object (hereafter SO), which would later be given the variable star name V4334 Sgr, is the prototype of VLTP and the flagship of

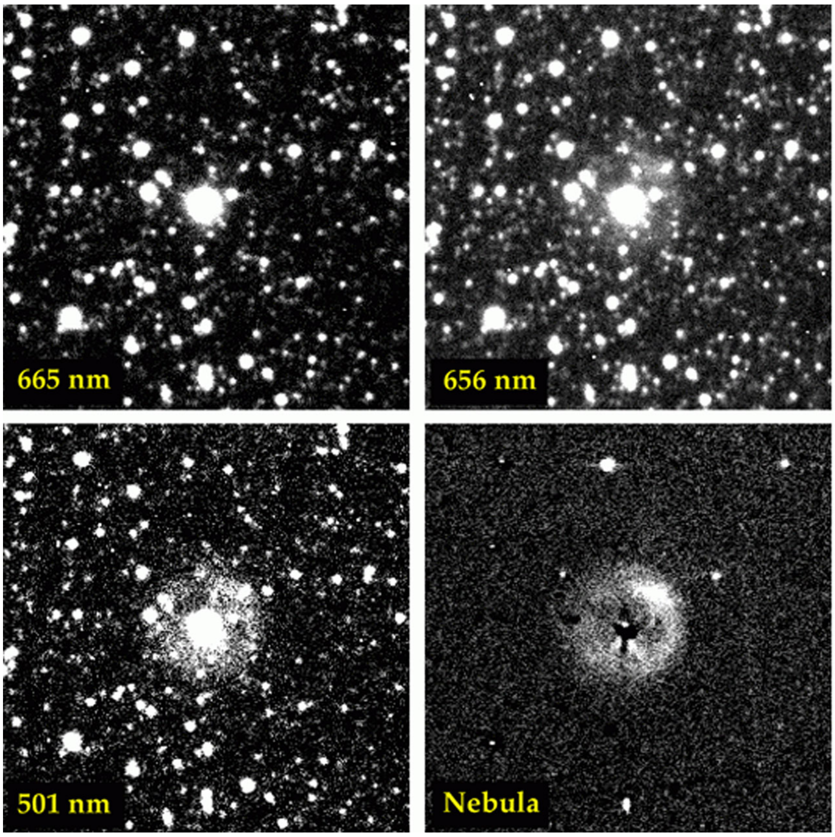

Figure 1.10: Images of SO obtained with the CCD Camera at the Dutch 0.9-metre telescope at the European Southern Observatory (ESO) La Silla Observatory by Hilmar Duerbeck. The field of view is 1.4 x 1.4 arcmin. North is up East to the left

born-again PNe. As such, it has been exhaustively monitored to date by numerous groups across a broad spectrum, predominantly in the optical and infrared ranges. Its evolution can be divided into four different stages: pre-collapse, VLTP and AGB return, dust formation and ejecta reionization. In Figure 1.11 a diagram of the main events order in time is presented.

1.3.1.1 Pre-collapse

Before its final flash, the progenitor of SO was identified in 1976 as a faint ($m_j \sim 21$) object by Duerbeck & Benetti (1996) in an image from the ESO sky survey. These authors and Duerbeck et al. (1997) reported possible previous detections in observations by K. Takamizawa on June 3 and September 25, 1994, at a magnitude of 15.5, and on February 10, 1995, at a magnitude of 12.4. If these observations were true, the VLTP would have occurred a year before its discovery at least. Within a week, the variable star V4334 Sgr was independently associated by Duerbeck (1996) and Pollacco (1996) with an old planetary nebula based on radial velocities of 115 and 113 km s^{-1} obtained from stellar and nebular lines, respectively. Duerbeck & Benetti (1996) also estimated the expansion velocity of the nebula to be 25 km s^{-1} using [O III] lines. Assuming a constant expansion and a distance of 5.5 kpc, the estimated kinematic age of the nebula was 17,000 years. Although the true age may differ from kinematic ages (Jacob et al. 2013), it aligned with the times estimated by Iben (1984) for a central star to undergo a VLTP after entering the PN phase (∼20,000 years). This is also in agreement with a

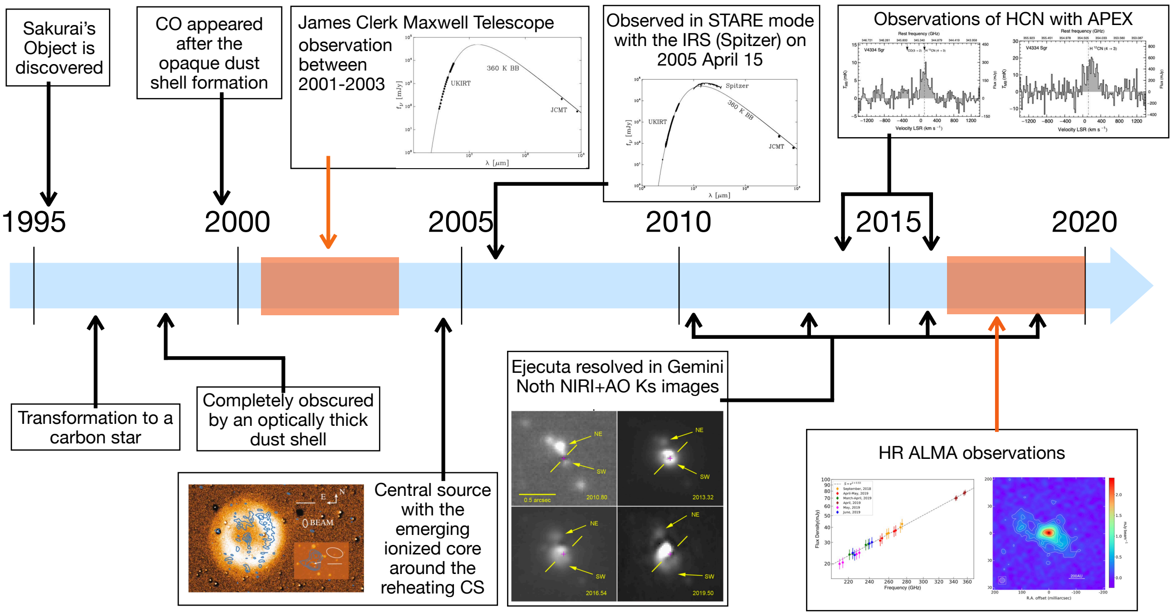

Figure 1.11: Timeline diagram of SO evolution showing the main events from its discovery to the present

star temperature of 98000±7000 inferred by Kerber et al. (1999) from the surrounding nebula properties, which indicated that the star had reached the top of the WD's cooling track.

1.3.1.2 VLTP and return to the AGB regime

In the period following the VLPT, V4334 Sgr evolved very quickly. The temperature steadily decreased from May 1996 (JD 24150144) to ∼400 days later, dropping from 8000 K to about 6000 K, while the luminosity gradually increased from just under 7000 to 10000 $L_\odot$ (Duerbeck et al. 1997). Both magnitudes were calculated assuming that the source was at a distance of 8 kpc. The UBVRzi light curves exhibited a gradual increase along with low-amplitude, short-period oscillations superimposed, associated with pulsational instabilities occurring in stars with a high mass-luminosity ratio.

On the other hand, the chemical evolution of the star between May and October 1996 revealed a surface H abundance decrease of 0.7 dex and an increase in the abundances of Li, Sr, Y and Zr (Asplund et al. 1997). The H-poor, C-rich chemical composition, enriched with light s-process elements, along with the observed changes in T and L, supported the notion that the star underwent rapid evolution after a VLTP. The presence of Li indicated that a WD merger had not taken place, as the expected temperature would have destroyed it (Clayton et al. 2011), although the possibility that these elements could have formed during the AGB phase and mixed in the VLTP was not ruled out (Asplund et al. 1999). Given the low $^{12}C/^{13}C$ ratio, $1.5 \leq {}^{12}C/^{13}C \leq 5$, later corroborated by Pavlenko et al. (2004) $^{12}C/^{13}C = 4 \pm 1$ using high-resolution infrared spectra from 1998, Asplund et al. (1997) suggested that the atmosphere could not be a simple mix of initial gas and must have undergone additional processing, likely triggered by H ingestion.

The central star was classified as a cool carbon star by Duerbeck et al. (1997) just two years after the VLTP. This fact was later confirmed by Eyres et al. (1998a), reporting features corresponding to CN, C_2, and CO. In the same year, Asplund et al. (1997) suggested that the chemical composition resembled that seen in R Coronae Borealis (RCrB) stars[8].

During 1998, Eyres et al. (1999) reported the appearance of a broad absorption line, associated with the He 10830 Å triplet, whose depth increased in each of the three observations conducted. Assuming the absorption was due to a wind and interpreting it as a P Cygni profile, it indicated a wind velocity of $\sim$670±50 km s^{-1}. The C I 10690 Å line seen prior to the appearance of this He line disappeared. Additionally, UBVRI photometry found at least two episodes of optical fading and recovery, accompanied by changes in color indices (Liller et al. 1998b,a; Jacoby et al. 1998), consistent with dust formation throughout 1998. Altogether led Eyres et al. (1999) to suggest that the source had entered a new phase, making it a member of RCrB stars. However, the absorptions were deeper than in the fading episodes of any known RCrB star, implying that a complete dust shell had formed (Duerbeck et al. 2000) and the source entered the phase of dust formation.

1.3.1.3 Dust Formation

The rapid cooling experienced by V4334 Sgr, surrounded by carbon-rich material, provided conditions for dust condensation. Duerbeck et al. (1997) did not detect any dust emission in the photometry taken in February 1996. In early 1997, an excess in the infrared became apparent, coinciding with a visual brightening of the star that was less than expected, attributed to the onset of condensation of surrounding dust (Arkhipova et al. 1998). This excess could be due to free-free emission in the material that had passed the pseudo-photosphere and formed an extended atmosphere (Duerbeck et al. 2000).

Excesses in the infrared were reported due to the presence of dust at temperatures of 1500, 1800, 1800, and 680 K surrounding the star in February, March, May, and April 1997, respectively (Kerber et al. 1999; Kimeswenger et al. 1997; Kamath & Ashok 1999; Eyres et al. 1998b). Eyres et al. (1998a) revealed the presence of C_2, CN, CO, while Asplund et al. (1997) reported the presence of Ballik-Ramsay bands[9] reflecting the appearance of C_2 Swan bands in the optical indicative of carbon-rich dust. The higher temperatures reported by Kimeswenger et al. (1997) and Kamath & Ashok (1999) (1800 K) implied dust condensation at a distance of $\sim$7 R_* from the star, with an estimated radius of 70 $R_\odot$. These temperatures were later questioned, as part of the infrared excess could be attributed to carbon nucleation products and part to free-free continuum emission (Duerbeck et al. 2000). By early 1998, the temperature of the extended atmosphere had dropped below 2000 K (Lynch et al. 2002), allowing for the formation of carbon dust. By early 1999, the optical emission from V4334 Sgr had significantly dropped, becoming practically undetectable in this range (Duerbeck et al. 2000; Tyne et al. 2000; Tatarnikov et al. 2000). Tyne et al. (2000) reported that the emission from the newly formed dust shell in the 1-4.75 μm range was dominated by amorphous carbon at a temperature

---

[8] Rare type of variable stars known for their peculiar and dramatic declines and rapid recovery to original brightness likely due to erratic dust cloud formation.

[9] Molecular absorption bands associated with the molecule C2 detailed by Ballik & Ramsay (1963).

Table 1.6: Dust luminosity, mass and V4334 Sgr Blackbody Temperatures collected by Hinkle & Joyce (2014) from the literature.

Date	$\lambda_{\rm max}$ (μm)	$(\lambda F_\lambda)_{\rm max}$ (W cm^{-2} $\times$ 10^{-15})	θ (mas)	L_d^c (L$_\odot$)	Q_e	M_d^c (M$_\odot$)	T^a (K)	T$_{\rm BB}$^{b} (K)	Reference
1999 Sep	4.6	1.71	21.0	6500	0.15	1.4×10^{-7}	…	630	Tyne et al. (2002)
1999 Sep	…	…	…	…	…	…	740	…	Hinkle & Joyce (2002)
2000 Apr	5.4	4.25	45.6	15750	0.1	9.6×10^{-7}	…	537	Tyne et al. (2002)
2000 Apr	…	…	…	…	…	…	670	…	Hinkle & Joyce (2002)
2000 Jun	4.3	1.43	16.5	5300	0.2	6.2×10^{-8}	680	…	Hinkle & Joyce (2002)
2000 Jun	…	…	…	…	…	…	620	…	Hinkle & Joyce (2002)
2000 Jul	…	…	…	…	…	…	<500	…	Lynch et al. (2002)
2000 Oct	…	…	…	…	…	…	950	…	Kauffmann et al. (2003)
2001 Feb	…	…	…	…	…	…	600	…	Lederle et al. (2001)
2001 May	5.0	2.81	31.8	10100	0.13	3.6×10^{-7}	…	580	Tyne et al. (2002)
2001 Jun	…	…	…	…	…	…	600	…	Kauffmann et al. (2003)
2001 Sep	5.5	3.07	40.3	11250	0.1	7.3×10^{-7}	520	527	Tyne et al. (2002)
2003 Sep	8.0	1.26	55.3	4800	0.04	3.5×10^{-6}	360	360	Eyres et al. (2004)
2005 Apr	11.3	1.46	117.0	5600	0.02	3.2×10^{-5}	180-210	210-256	Evans et al. (2006)^d
2007 Jun	…	…	…	…	…	…	<200	…	Worters et al. (2009)

Notes: ^{a} Published value. ^{b} BB fit to published data. ^{c} Computed assuming D=3 kpc ^{d} $T_{\rm dust}$ from fit.

of T$_d$∼600 K, later confirmed by Tyne et al. (2002) and Eyres et al. (2004). In the subsequent years, the dust temperature decreased to minimum values of 180-210 K in April 2005 (Evans et al. 2006). Table 1.6, taken from Hinkle & Joyce (2014), summarizes all the estimated temperatures from blackbody fits to infrared photometry.

The variations in dust temperature have also been linked to changes in both luminosity and mass loss rate. Assuming a distance of 3 kpc, all the changes in luminosity reported from May 1999 to Sep 2005 are presented in Tab. 1.6. Simultaneously, there were also reports of an increase in the mass loss rate, ranging from $\sim10^{-8}$ to 10^{-7} M$_\odot$ yr^{-1} from February 1997 to February 1998 (Kerber et al. 1999) to 5×10^{-6} in May 1999, and further to 1 $\times10^{-5}$ M$_\odot$ yr^{-1} in September 2001 (Tyne et al. 2002). These authors concluded that from February 1997 to September 2001, the mass loss increased by a factor of $\sim10^3$, independent of distance. Evans et al. (2004) found a mass loss rate in 2003 of 3×10^{-5} M$_\odot$yr^{-1}, suggesting that the mass loss rate had stabilized. van Hoof et al. (2007) also computed from photoionization modeling the total ejected mass as 10^{-4} M$_\odot$. Dust models estimated that dust formation have ended sometime in 2001 (Evans et al. 2006).

1.3.1.4 Ejecta reionization

Once the dust formation phase ceased, the dust continued to cool and expand at an angular expansion rate of 0.02 arcsec yr^{-1}, causing the dust shell to become optically thin. In June 2001, Kerber et al. (2002) reported the detection of spatially extended H-deficient gas (∼ 2 arcsec) and freshly ionized in the vicinity of the star. Additionally, in FORS2 spectra were also detected the emission lines of [N II], [O I], [O II], and weakly [S II]. Two components were reported in the [N II] line at velocities of -350 ± 50 and 200 ± 50 km s^{-1} relative to V3443 Sgr. The data quality did not allow for discerning whether ionization was caused by shocks or photoionization. This raises questions about the detection of the Hα line (see for instance chapter 3), since this line is strongly contaminated by He II Pickering lines, even dominating over Hα. Nevertheless, the deficiency of H in the inner ejecta was significant.

Following these results, Hajduk et al. (2005) obtained VLA data at 8.6 GHz in October 2002, apparently supporting the onset of photoionization. They detected a marginally resolved bipolar source identified as the emerging ionized ejecta around the CS. Given that previous radio observations showed no emission in that region (Eyres 2002), it indicated that V4334 Sgr was rapidly reheating, in contrast to theoretical predictions (Herwig 2001b). The Spitzer mid infrared spectra obtained by Evans et al. (2006) contains features from organic molecules with an excitation temperature of ∼450 K. The dust temperature derived from the same spectrum was 180-210 K. They concluded that to produce this excitation temperature the dust distribution must be strongly asymmetric.

The evolution and monitoring between February 2004 and June 2006 were presented by van Hoof et al. (2007). They found that radio emission between 2004 and 2005 was either constant or slowly decreasing, while in 2006, there was a sudden rise from 80 to 320 μJy. Simultaneously, optical emission showed an exponential decrease in both excitation and ionization. The optical line emission and early radio flux were attributed to a fast shock (and not photoionization as was suggested earlier) which occurred around 1998. van Hoof et al. (2008) reported that the decreasing trend in optical line flux observed since 2002 continued in 2007. The declining trend in emission lines, however, would change from 2008 onwards, and they would begin to increase their emission until 2015 (van Hoof et al. 2015). Contrary to the previously suggested photoionization, they interpret this emission as coming from a region near the star and excited by a second shock. In this case, the shock could have been induced by an increase in stellar mass loss and wind velocity associated with an increase in stellar temperature. Hinkle & Joyce (2014) also detected He lines in near-infrared spectra, which were atributted to a wind shock. This was later corroborated by van Hoof et al. (2018), until them, no evidence for photoionization was found, with all previous observed features caused by dust or shocks.

1.3.1.5 Morphology of the recent ejecta

Chesneau et al. (2009) identified a compact dust disk 30×40 mas in size that is highly inclined. They estimated the inclination of the disk to be $75\pm3°$ with a large-scale height of 47 ± 7 AU (assuming a distance of 3.5 kpc). The position angle (PA) of the major axis of the disk ($132\pm3°$) was found to be aligned with an observed asymmetry in the old PN. Based on adaptive optics observations in the Ks band, Hinkle & Joyce (2014) identified two sources near V4334 Sgr. Between September 2010 and April 2013, both sources transitioned from being partially resolved and connected by a faint continuum to separating by a distance of 0.3 arcsec along PA∼13° direction. The sources were consistent with debris clouds expanding at a rate of 0.058 mas d^{-1} since 1997. On the other hand, the emission lines of He associated with a

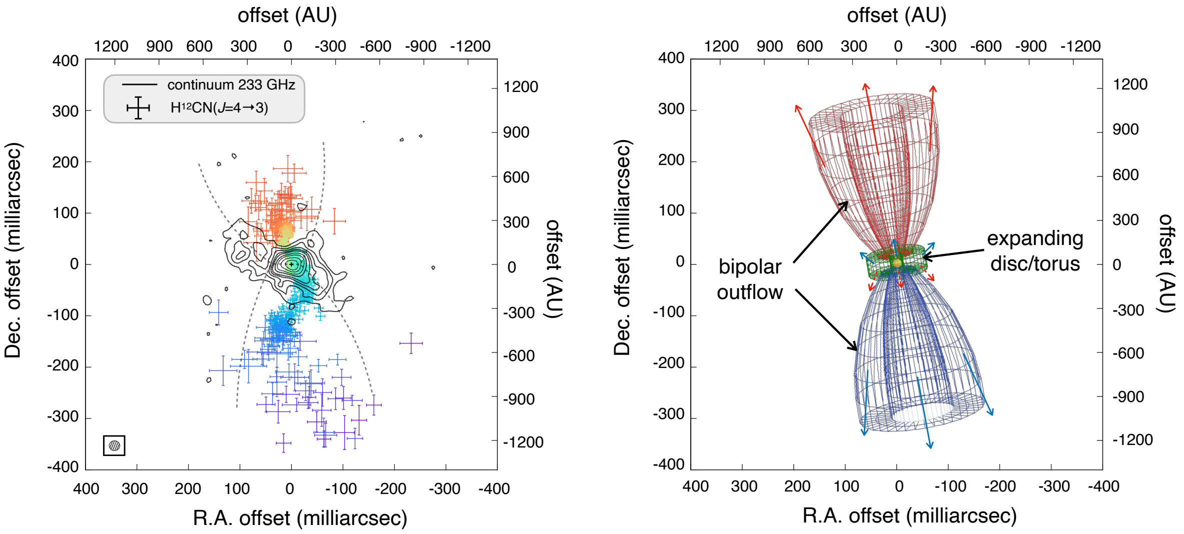

Figure 1.12: Bipolar outflow and expanding disc around SO. Left: $H^{12}CN(J=4 \rightarrow 3)$ line emission and 233 GHz continuum emission. The dashed lines delineate the hourglass morphology suggested by the continuum emission. Right: hourglass model for the spatial-kinematical distribution of the bipolar outflow in SO. The right and top axes indicate the linear scale assuming a distance of 3.5 kpc to the source. Figure presented by Tafoya et al. (2023).

shock exhibited a fragmented and spatially asymmetric distribution.

Hinkle et al. (2020) conducted a similar monitoring between 2015 and 2019. A model for the dust was presented, consisting of a disk/torus along with two bipolar clouds expanding with a certain offset from the perpendicular of the disk, at PA 13° and 190° (see their Figure 2). Most of the dust mass in the disk was at a temperature of 200 K, but a small fraction was at 780 K. Simultaneously, tomography of the He I 10830 Å line emission, excited by shocks, revealed a bipolar structure. The bipolar flow had a PA of 21±5° in the direction perpendicular to the disk plane at a velocity several magnitudes higher than the debris clouds.

Tafoya et al. (2023) presented the first direct detection of the disk without the obstruction of the dust disk. Atacama Large Milimeter/submillimeter Array (ALMA) observations of molecular gas revealed the presence of a molecular disk, inclined at 72° in the line of sight, along with a bipolar flow. Figure 1.12 shows the model of the molecular gas. The expansion velocity in the disk was 53 km s^{-1}, while the projected velocity of the bipolar flow was approximately 1000 km s^{-1}. Finally, it was proposed that the structure of the bipolar flow had an hourglass shape with an open angle of 60°. This disk-jets or disk-outflows structure is not exclusive to V4334 Sgr but it will next be seen it is also present in V605 Aql, A30, and A78 (Tafoya et al. 2017, 2022; Fang et al. 2014).

1.3.2 A 58

1.3.2.1 V605 Aql on 1919

V605 Aql, the central star of A 58, experienced an outburst on July 4, 1919, initially classified as a nova event (Nova Aql No. 4, Wolf 1920). V605 Aql brightened over a period of two years from $m_{pg} \sim 15$ to a peak of 10.2 in 1919 August(Lundmark 1921). Lundmark classified

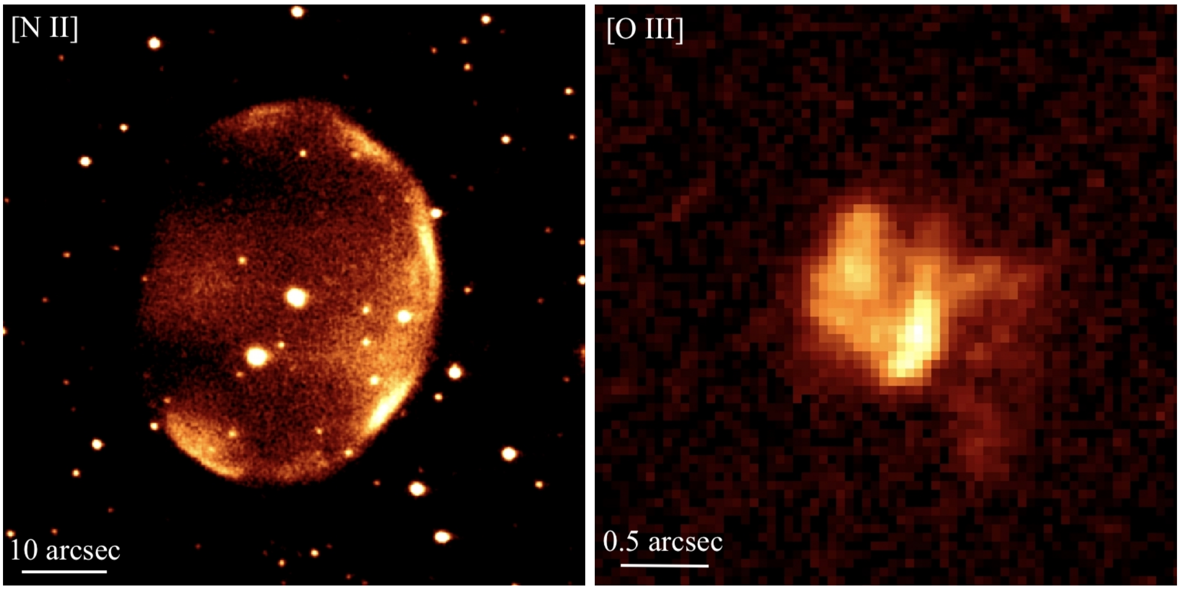

Figure 1.13: HST WFPC2 WF3 F658N image of A 58 (left) and HST WFPC2 PC F502N image of its H-deficient central knot (right).

the spectrum of V605 Aql as R0 and suggested its similarity to HD 182040, a well-known H-deficient carbon star (HdC). Between 1919 and 1923, V605 Aql underwent three episodes of fading and brightening (Seitter 1985; Harrison 1996). Ludendorff (1922) was the first to propose a potential connection between V605 Aql and RCrB stars, characterized by fading episodes caused by surrounding dust clouds. Indeed, in the qualitative comparison made by Clayton & De Marco (1997), a spectrum recovered from observations with the Crossley Telescope in September 1921 and a spectrum of an RCrB star from the Large Magellanic Cloud showed significant similarities. Both spectra were typical of a cold RCrB star (5000 K), with deep Swan bands of C2 and the absence of Balmer lines and ^{12}C ^{13}C bands, indicative of H deficiency. After 1923, V605 Aql completely disappeared from the sky, obscured by the dust envelope that had formed. the brihtening and fading timescales of A 58 are thus very similar to these of SO. It was not until 1971 when it was discovered that the position of V605 Aql coincided with the center of an old nebula (Bidelman 1971; Ford 1971; van den Bergh 1971), although there were previous hints of this spatial coincidence (Herbig 1958).

1.3.2.2 The outer nebula

The ancient nebula A 58, identified by Abell (1966), was initially observed with a spatial extension of 44x36 arcsec^2. The ground-based images in Hα and [N II] obtained by Guerrero & Manchado (1996) revealed a well-defined nebula elongated along the N-S direction with a kidney-like morphology. Both Hα and [N II] emissions showed brightening on the eastern edge, likely due to the interaction of the nebula as it moves through the ISM. Pollacco et al. (1992) using optical high-resolution spectroscopy estimated a nebula expansion of 31±4 km s^{-1} from the double-peaked emission profile of the Hα line.

Spectra of A 58 revealed emission lines typical of a PN, but with Hα emission weaker than [N II] (Ford 1971; Seitter 1985). Pottasch et al. (1986) demonstrated the presence of at least one knot in the central region of A 58 and obtained rough abundances showing it to be H-deficient. The physical properties of the outer nebula were found to be a T_e=12000 K and n_e 300 cm^{-3} (Seitter 1987), where the densities were derived from the radius/mass relation for PNe given by Pottasch (1980). These result were consistent with the 200 cm^{-3} from the [S II]λλ6716,6730 lines assuming a T_e of 10000 K (no diagnostic lines available) estimated by Guerrero & Manchado (1996). Later on, Wesson et al. (2008) could estimate an extinction from the Hα/Hβ ratio of c(Hβ)∼1.04, but no diagnostic line was available to calculate T_e and n_e. Assuming the density of 200 cm^{-3} estimated previously, these authors derived chemical abundances for three T_e, 7.5, 10, 15 kK estimating N/O and Ne/O ratios ranged between 0.38-1.2 and 0.49-0.74, respectively. Following Peimbert (1978)'s criteria, A 58 would be classified as a type I PN if its temperature is higher than about 8500 K.

1.3.2.3 Spectroscopy of V605 Aql through the year

The first spectrum of the central knot of A 58 was presented by Seitter (1987). Using low-resolution spectra obtained at the 3.6m ESO Telescope between 1986 and 1987, they successfully subtracted the contribution of A 58 from the central knot (assuming spherical symmetry). As for the outer nebula, T_e= 14000 and n_e 5×10^4 were derived. The spectra also exhibited strong C IV emission at λ5801/11 Å in the knot, from which Seitter inferred a stellar origin. The FWHM of the line, at 2300 km s^{-1}, suggested a Wolf-Rayet WC-type star, but no further classification could be made as no other broad features were detected. This represented the first detection of V605 Aql since 1923.

Pollacco et al. (1992) presented optical high-resolution spectroscopy of the central knot covering the [O III] λ5007 [N II] λλ6548,6584 and Hα emission lines. The spectrum clearly resolved the emission from the central knot and the outer nebula in the [N II] lines. A later review hinted at a marginal detection of the Hα line in the knot, possibly due to the emission of He II lines from Pickering (see chapter 4). They also demonstrated that the expansion velocity of the knot was 100 km s^{-1}. The asymmetric profile led Pollaco to suggest that the central knot might exhibit a bipolar morphology, with the blueshifted part detected in the spectra and the redshifted obscured by dust lying close to the CS. Indeed Clayton et al. (2013) modeled the emission as a symmetric shell, with the redshifted part obscured by dust. From intermediate dispersion spectra obtained with the 3.5m telescope at CAHA, Guerrero & Manchado (1996) determined the physical properties and abundances of the central knot. Consistent with earlier suggestions, they found that the central knot was H-poor with T_e and n_e of 12450±350 K (derived from the ratio of [N II]λλ6548,6584 lines and the auroral λ5755) and 2600±350 cm^{-3}, respectively. It was clear the discrepancy between this value and those obtained by Seitter (1987) that could not be attributed to the expansion over the 10 yr interval. The inferred chemical abundances in the central knot revealed that H was almost converted into He. Surprisingly, an unreliable high abundance of oxygen was found, which was attributed to the presence of a shock in the central knot. It is worth mentioning that the broad emission line of stellar C IV λ5801/11 was clearly visible in the spectrum in the absence of other features. This indicated that the star was extremely faint. Clayton & De Marco (1997) estimated that if the C IV emission dominated the stellar spectrum, then V605 Aql currently has an effective temperature exceeding 50000 K.

Through high-resolution optical spectra, Clayton et al. (2006) indirectly measured the emission from the CS and estimated $T_{\rm eff}$=95000±10000 K and R^{*}=0.37±0.07 $R_{\odot}$, based on the C IV λ5801,11/He II ratio and the absence of O IV $\lambda\lambda$3811,3834. Clayton also estimated a stellar wind of 2500 km s^{-1} with a mass loss rate ratio of 1.3×10^{-7} and an abundance ratio of He:C:O = 54:40:5 with a mass uncertainty of 10%-15%. They suggested that around the central star there is a thick toroid of dust, which we observe edge-on. The emission measured from the central star is the sum of scattered light and light escaping in polar directions, so actual temperature measurements could be even higher. In fact, radio observations indicate a significant increase in the ionization of V605 Aql since 1987, suggesting that $T_{\rm eff}$ may have continued to rise until now (van Hoof et al. 2006, 2008).

Wesson et al. (2008) also obtained high-resolution optical spectra of the central clump around V605 Aql. They estimated a c(Hβ) of 2.38 and 2 from Balmer lines (considering pickering line contamination) and He I recombination lines, respectively. The abundances were possible to be derived from both collisionally excited lines (CELs) and optical recombination lines (ORLs) (although these are questionable, see chapter 4). These can be consulted in Table 7 of Wesson et al. (2008), but we will highlight two results here. First, the C/O ratio is below unity, which, according to current VLTP models, conflicts with the born-again scenario predicting a C/O > 1 (Miller Bertolami et al. 2006). Second, the high abundance discrepancy factor derived on oxygen is $\simeq$ 90. According to Wesson et al. (2003) and Liu et al. (2006), there is a link between PNe showing high ADFs and classical novae, see 1.5 for more details. Possible alternative origins were discussed by Lau et al. (2011), who proposed two scenarios involving different chemical composition of novae in order to explain the previously calculated abundances and ADFs.

Simultaneously to the previous work Hinkle et al. (2008) obtained a medium-resolution optical spectrum with the KPNO telescope. The spectrum revealed the broad He I λ10830 line with FWHM similar to those seen in SO, indicative of the presence of a shock.

1.3.2.4 Imaging of A 58 through the year

In August 1991 the first images of the central knot were obtained with the *Hubble Space Telescope* (HST) Faint Object Camera (FOC) using four bandpasses, of which only the image obtained with the F501N filter showed the knot's emission. Subsequently, Bond et al. (1993) presented a deconvolved FOC image where a knot with a diameter ∼0.5 arcsec was resolved, showing no emission from the central star. An alternative deconvolution of this filter was presented by Clayton & De Marco (1997). Later on, Guerrero & Manchado (1996) presented ground-based images in Hα and [N II] of the central knot in which the central knot was only visible in the [N II] image. Once the contribution from the CS was subtracted it was revealed that the knot had an irregular shape, with a larger and brighter patch of emission 0.75 arcsec to the southwest (PA 220) and a fainter, smaller emission patch almost diametrically opposite. The diameter of the knot is approximately 2.5 arcsec. This structure were clearly seen in optical HST images of V605 Aql obtained by Hinkle et al. (2008). The authors reported a double emission of the clump separated by a dark band and diffuse emission in the SW region. In addition, the H and J bands showed a bright central point with a region of diffuse emission in the optical range.

A noteworthy result is the presentation of the first direct detection of the central star since 1923 by Clayton et al. (2013). The deep HST image obtained with the F547M filter, dominated by Wolf-Rayet C IV emission, showed a hot spot, which the authors interpreted as emission from the central star. The magnitude of the star was V = 20.2±1 mag in 2009, although they estimated V ∼16.2 in 2013. They also obtained images of [N II] and [O III] in 2009 with the best spatial resolution to date. These images, along with those available from 2001 (Hinkle et al. 2008), allowed them to determine expansion factors of 8±2% and 5±3% for [O III] and [N II] emissions, respectively.

1.3.2.5 Dust around V605 Aql

Many other works have derived the properties of the dust and CSPN from observations of V605 Aql in the infrared range. However, there was considerable confusion regarding the identification of the star. In summary, Herbig (1958) identified a faint star in the correct position but failed to notice the presence of the (faint) nebula. van der Veen et al. (1989) and later Harrison (1996) incorrectly identified V605 Aql as a star 35 arcsec away from the center of the PN. As a result, magnitudes reported in the near-infrared were much brighter than the correct values, and errors propagated in the literature. Kimeswenger et al. (2000) correctly identified V605 Aql and the aforementioned star using DENIS NIR images. Hinkle et al. (2001), through JHK photometry, confirmed the identification of Kimeswenger and reported no variability in the star over a period of 3 months. V605 Aql was also observed as a bright and very red source by ISO, with flux ranging from 0.5 Jy at 4.5 μm to 6.4 Jy at 14.5 μm (Kimeswenger et al. 1998).

Once the confusion was clarified, Koller & Kimeswenger (2001) noted that a single temperature, single grain size model did not fit the IRAS/ISO photometry for V605 Aql. Instead, a good fit over the 3.5 to 100 μm wavelength range was achieved by using a distribution of grain sizes heated by the central star, modeled as a blackbody at 100,000 K. However, they had to adopt a different distance and luminosity (5 kpc, 5800 $L_\odot$) than reported before. Hinkle et al. (2008) also modeled the dust thorugh JHK infrared images obtained with Hokupa'a/QUIRC. Using two temperatures of ∼1500 K and ∼350 K, suggesting the possible structure of the dust disk according to the authors (see Figure 5 in Hinkle et al. (2008)). The authors suggested that the dust disk had hot dust in the shock region (where the He I line appears), marking the inner radius (3 AU) and the cold region marking the outer edge (60 AU). There were dust clouds in the polar regions and an optical emission zone surrounding all of this structure.

A few years later Clayton et al. (2013) compiled photometric data from the literature (see their Table 2) and also presented a new infrared spectrum obtained with the VLTI. In this case dust emission were adjusted with three different components of carbon dust at temperatures of 75, 235, and 810 K, unlike the two components reported by Hinkle et al. (2008). They estimated the dust mass to be around 10^{-5} solar masses and a geometric distance of ∼4.6 kpc.

1.3.2.6 Current Status of A58

Clayton et al. (2013) provided an update on V605 Aql, compiling all known information to date, adding results from their own observations. Additionally, they presented a detailed model of the central knot of A 58 consisting of an inclined central disk/torus and material expanding in the polar regions similar to SO. The material in the NE direction would be approaching us, while that in the SW would be receding and more extincted. The authors also digitally reconstructed the high-optical spectra of Pollacco et al. (1992), since it was impossible to recover the original one. The systemic velocity was then recalculated as ∼96 km s^{-1} in the local standard of rest (LSR) system and the expansion velocity was ∼215 km s^{-1}.

After the previous work, A 58, like the rest of the born-again PNe, was somewhat forgotten. It was not until 2017 when Tafoya et al. (2017) rekindled interest in this source by reporting molecular emission of CO with the APEX telescope in V605 Aql. This led the authors to obtain high-resolution submillimeter observations with ALMA (Tafoya et al. 2022). In this work, the spatio-kinematic distribution of molecular material around a born-again was presented for the first time. The emission from the detected molecules, CO, HCN, HCO, and $H^{13}CN$, all exhibited a clumpy ring structure with an extension of ∼1 arcsec in diameter. This emission was attributed to an expanding disk (v∼80 km s^{-1}) inclined at i∼60º with respect to the line of sight. Additionally, in the CO emission, compact high-velocity components (v∼280 km s^{-1}) appear in directions perpendicular to the disk (see their Figure 5). The surprising aspect of this emission is that the authors estimated a kinematic age of 20 yr, suggesting either that it is currently being ejected by V605 Aql or being dragged from the disk by the stellar wind. Finally, they derived $^{12}C/^{13}C$ ratio of 5.6±0.6, supporting the single-star scenario rather than the previously suggested nova-like event.

1.3.3 HuBi 1

At the time this thesis is being written, HuBi 1 has already been confirmed as a born-again PN, which is one of the main outcomes of this work as detailed in chapter 3. However, at the beginning of the thesis, the nature of this object was still debated.

HuBi 1 (also known as PM 1-188) was first investigated by Hu & Bibo (1990) who described it as a low-excitation nebula with a CSPN, the bright IR source IRAS 17514-1555, having a late-type [WC] spectral type, see Figure 1.14. According to Pollacco & Hill (1994), this PN consisted of a faintly extended outer shell of low density (n_e cm^{-3}) with typical PN abundances and an unresolved inner shell with apparent bipolar structure. The density derived from the [S II] λλ6716,6730 doublet for the inner region was 2×10^4 cm^{-3}. This high density was actually an artefact caused by contamination from C II lines to the sulfur doublet. Pollacco also estimated extinction values and temperatures of E(B-V) ∼0.83±0.10 and 0.25 and 5000 K and 8000 K for the outer and inner shells, respectively. However, the values for the inner nebula should be taken with caution as they were derived from lines likely contaminated by carbon lines. Although the derived abundances were typical for a PN, the He I emission line was extremely bright, suggesting a large He/H ratio, typical in born-again ejecta.

Peña et al. (2001) conducted a study of a sample of PNe with [WR] central stars, including

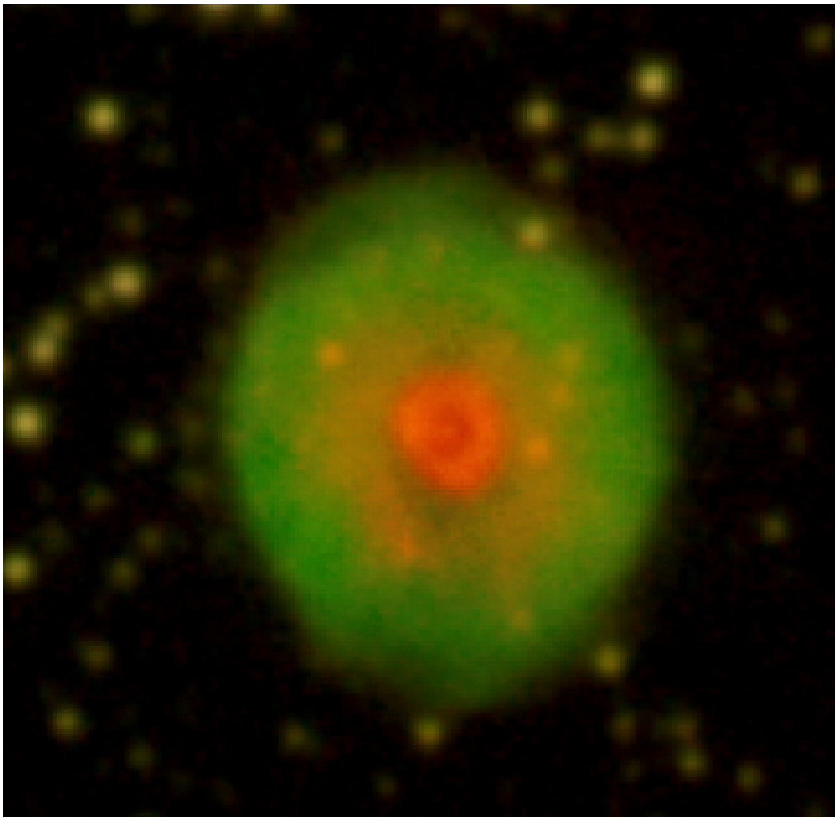

Figure 1.14: Colour-composite optical image of HuBi 1 obtained with the [N II] (red) and Hα (green) narrow-band filters at the Nordic Optical Telescope (NOT).

PM 1-188, estimating their physical conditions. Discrepancies in the observed density (n_e<1000 cm^{-3}) and the much higher expected density for the nebula around a [WR]-late star led her to propose two possible scenarios. The first assumed that the central star had undergone a VLTP and become a born-again star, while the second favored a very slow evolution off the AGB due to its low mass (Górny & Tylenda 2000). Comparing the observed low ionization (no He II lines detected) in the nebula with other known born-again sources up to that date (V605 Aql, V4334 Sgr), the authors suggested that the slow evolution scenario was more likely. Indeed, the $T_{\rm eff}$ of 35000 K for the CSPN calculated by Leuenhagen & Hamann (1998) was too low compared to what was expected for an evolved CSPN after undergoing a VLTP. Subsequently, Peña (2005) presented low-resolution spectroscopic data for HuBi 1. The observed extinction for the nebula was around 1.22 with T_e and n_e of 9400 K and 800±300 cm^{-3}, respectively. The abundances remained typical for a PN but with an unusually high He$^+$ abundance, especially considering the temperature of the CSPN. The author noted that the magnitude of the central star had been decreasing over the years, from 11.85 in 1996 (Crowther et al. 1998) to 13.50 in 2002 (Peña 2005), suggesting a variable star. Finally, the authors concluded that HuBi 1 was not a born-again star but rather a low-mass star with slow evolution.

It was not until recently that the possibility of the born-again scenario gained strength again. Guerrero et al. (2018) noticed certain unique peculiarities in HuBi 1, even if it were a born-again star. They reported a fading of the CSPN brightness by approximately 10 magnitudes in the last 46 years, attributed to the formation of a circumstellar veil of carbon-rich dust. This was suggested by the abundance of carbon lines in the spectra of Pollacco & Hill (1994) and Hu & Bibo (1990) and the infrared emission reported by Hu & Bibo (1990). Such a quantity of carbon would be consistent with the characteristics of material ejected after a VLTP (Miller Bertolami et al. 2006). The carbon-rich material at high-velocity had been expanding while cooling, reaching optimal conditions for dust condensation. The decrease in ionizing flux would cause recombination of the outer shell, which was already beginning to be observed by that time. On the other hand, the detection of the He II λ4686 emission line in the inner shell, combined with the atypical inverted ionization structure with He emission encompassing [N II] and [O III] emission, indicated shock ionization. Indeed, the detection of material expanding up to ≈300 km s^{-1} in the innermost region of HuBi 1 (Rechy-García et al. 2020) lends strong support to the shock excitation of this region by recent ejecta. They also estimate a kinematical age of 250 yr for the inner ejecta.

The results pointed again to the born-again scenario, but Peña et al. (2021) reported normal abundances for the outer and inner shells based on high-resolution spectra. The results were to some extent questionable. For instance, to derive abundances, the CLOUDY software was used, which only considers photoionization, despite clear indications of the existence of shocks in the inner region revealed in the diagnostic diagrams presented by the authors, the ionization mechanism for both shells seemed to be different. It was also assumed for abundance calculations that the emission from the inner shell is much brighter than the outer, as it is typically the case but not for the Balmer lines in HuBi 1 (Peña 2005; Guerrero et al. 2018). Since contamination from the outer shell was not subtracted from any of the Balmer lines, the subsequent abundances of the inner extremely overestimated the H content.

1.3.4 The twins nebulae A 30 and A 78

A30 and A78 were initially discovered by Abell (1966) as two extended, low surface brightness PNe containing a CSPN belonging to the O VI sequence (Greenstein & Minkowski 1964; Smith & Aller 1969). Both sources gained significance when exceptional dust enrichments were observed in comparison to other PNe during the analysis of infrared (IR) photometric observations of 113 PNe in the wavelength range from 2.2 to 22 μm (Cohen & Barlow 1974). The infrared emissions were spatially extended at 10 and 18 μm around the core of A 30, but on a much smaller scale (∼25 arcsec) than the optical diameter (130 arcsec). They also found strong emission near the core of A 78, but lacked information on its spatial extent. In both cases, the emission was attributed to thermal radiation from cold dust at a temperature of approximately 140 K, while the estimated effective temperature of their CSPNe exceeded 100000 K. Difficulties to reconciling the presence of dust against thermal ion sputtering and the sweeping action of the winds of the CSPNe led Cohen & Barlow (1974) to propose that dust grains were continuously forming in the high-velocity mass outflow from the CSPNe (see also Moseley 1980). Later, Cohen et al. (1977) obtained variable aperture photometry of A 30 and A 78 in the 1.6-3.5 μm region, revealing the existence of a second population of dust in both nebulae at a much higher temperature of 1000 K. This dust extended spatially over the same regions as the colder dust in A30 (≥10-30 arcsec).

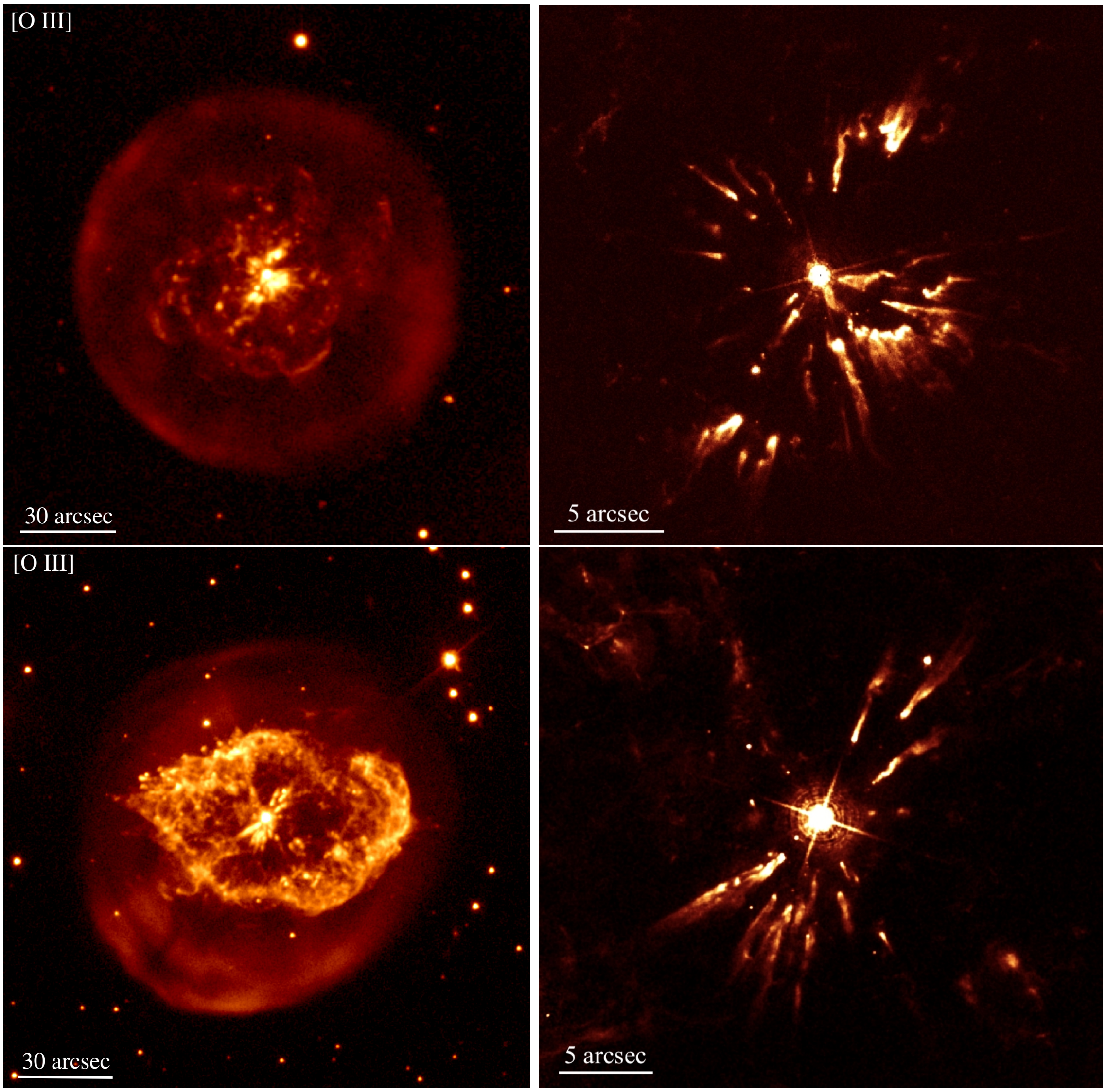

Figure 1.15: Images of the born-again PNe A 30 (top panels) and A 78 (bottom panels). The left-hand panels show optical [O III] images obtained at the Kitt Peak National Observatory Mayall telescope for A 30 and the NOT for A 78. Right-hand panels show a close-up HST WFC3 F502N images of the central region of both nebulae.

1.3.4.1 Early optical observations

The structures of A 30 and A 78 were first imaged by Jacoby (1979). A 78 consisted of a series of central clumps arranged around the star, along with other more distant clumps forming an eye-like structure, all surrounded by an old elliptical nebula with low surface brightness. In A 30, the central core was composed of 4 clumps (J1-J4) near the CSPN (see also Hazard et al. 1980), surrounded by a somewhat diffuse structure with no apparent shape and a faint external circular nebula. The central clumps in A 30 expanded at a velocity of 25 km s^{-1}, while the external nebula did so at a velocity of 40 km s^{-1} (Reay et al. 1983), implying kinematic ages of 1500 and 18000 yrs, respectively, for a distance of 1.3 kpc.

Spectroscopic observations obtained by Jacoby & Ford (1983) revealed that the clumps in the inner regions were extremely deficient in H and rich in He (see also Kaler 1981). Despite the lack of H, the composition of A 78 and clump J4 of A30 appeared somewhat "normal," while in clump J3, the abundances of N and O were a factor of 3 lower than expected, and C exceeded expectations by a factor of 8. The authors speculated that the central clumps had resulted from a second, "recent" ejection within the old nebula, as previously proposed by Jacoby (1979).

Iben et al. (1983) described the born-again event in which such ejections may occur in some PNe during the post-AGB phase of their CSPNe (see also Schoenberner 1979). The high temperatures of the CSPNe, ranging between 60000-150000 K, and the monstrous winds ($>$3400 km s^{-1}) derived from P Cygni profiles in UV observations (Heap 1979; Kaler & Feibelman 1984; Harrington & Feibelman 1984; Kaler et al. 1988), indicated that both had evolved into a second phase of WD, suggesting that the VLTP had occurred quite some time ago.

1.3.4.2 UV observations

During the 1980s, A 78 and A 30 underwent extensive studies in the ultraviolet (UV) range. Harrington & Feibelman (1984) determined the abundance ratios of N/C and C/He in the central knots of A 30 and proposed that these knots might have an inhomogeneous chemical composition with cold cores rich in carbon. Additionally, the observed strength of CELs relative to the He II λ1640 recombination line implied an energy exceeding the photoionization produced by the CSPN. This suggested that mass-loss due to strong stellar winds might be causing a shock with the external nebula. Similarly, Kaler et al. (1988) obtained a N/C ratio close to unity in the wind, which appeared to be decelerated, halted against the inner edge of the internal nebula, resulting in a compressed structure expanding only between -25 and -80 km s^{-1}. The mass loss rate was estimated to be around 4×10^{-9} M$_{\odot}$ yr^{-1} (see also Koesterke & Werner 1998).

On the other hand, Kaler & Feibelman (1984) noted that the UV emission, heavily affected by dust, was less reddened in the central region of A 78 than in A 30, even though infrared observations indicated similar amounts of dust in both regions. The authors thus suggested that the dust formed a toroidal structure, with A 78 being edge-on and A 30 being face-on. The first direct IR image of any born-again planetary nebula was presented by Dinerstein & Lester (1984), confirming the earlier suggestion that the dust distribution was clumpy. Furthermore, their near-infrared images of the central region of A 30 suggested that the dust was primarily distributed along a broken disk, although the spatial resolution of the observations was not optimal.

1.3.4.3 Morphology and spatio-kinematic

Clegg et al. (1993) were the first to resolve the inner structures of A 30 and A 78, but the unprecedented capabilities of the HST revealed them in great detail (Borkowski et al. 1993). The internal emission was resolved into a series of clumps with bright heads (0.15-0.5 arcsec) and long comet-like tails distributed around a broken disk with a pair of jet-like ejections in the polar regions, somewhat more diffuse in A 78. In the case of A 30, new near-infrared K-band images revealed the presence of hot dust (0.0007 μm in size) in an expanding equatorial ring (35 km s^{-1} derived by Clegg et al. (1993), as previously suggested by Dinerstein & Lester (1984), consistent with the optical disk (Borkowski et al. 1994). No emission was detected at the poles, suggesting a dust deficiency there. Their dust model estimated that only 2% of the dust mass was in the disk, while the rest resided at significantly greater distances, dominating the far-infrared. The same model would apply to A78 with a correction factor of 0.75 (Kimeswenger et al. 1998). The multiple C IV absorption components observed in the UV spectra of A 78 were interpreted within the context of a wind-blown bubble, where H-poor material is stripped from dense clumps near the stellar wind termination shock, accelerated to high velocities, and partially mixed with the stellar wind, creating a mass-loaded flow (Harrington et al. 1995). Borkowski et al. (1995), based on HST WFPC2 observations, described a similar situation in A 30. These authors also suggested that, since the polar knots in A 78 appeared as diffuse emission at very high velocity, while in A 30 they still appeared as compact clumps, the former represented a more advanced stage of acceleration.

From high-resolution Echelle spectra, Meaburn & Lopez (1996) and Meaburn et al. (1998) refined the calculations of the previously estimated velocities in the different components of A 30 and A 78, respectively. The knots in the broken disks were expanding at velocities of ≈25 and ≈39 km s^{-1} for A 78 and A 30, respectively. In the eye-like H-deficient structure of A 78, features with velocities as high as ∼400 km s^{-1} were found, while in the petal-like structure of A 30, these features reached velocities of 200 km s^{-1}, (see also Pismis 1989; Clegg et al. 1993). In both works, expansion velocities of the H-rich outer nebulae were also reported to be in the range of 40 km s^{-1} for both A 30 and A 78.

Years later, Fang et al. (2014) was able to calculate the tangential expansion velocity of all resolved clumps in the inner regions of A 30 and A 78, as well as several regions of the eye-like structure of A 78, through multi-epoch images from the HST. The expansion velocities of the knots tended to increase with distance, resulting in kinematic ages between 610-950 and 600-1140 yrs for A 30 and A 78, respectively. Fractional expansion, on the other hand, decreased with distance, meaning that the innermost knots exhibited higher acceleration. Additionally, the angular expansion of the outer filaments showed a dependence on the position angle, indicating that the interaction of the stellar wind with the inner knots channels the wind along preferential directions. The authors presented radiation-hydrodynamical simulations illustrating how the ejection of a single star, followed by the onset of a fast stellar wind and photoionization of the star, reproduced the clumps and filaments seen in both nebulae.

1.3.4.4 Chemical abundances in A 30 and A 78

The abundances in both the outer nebulae and the inner regions of A 30 and A 78 have been extensively studied by various groups (Jacoby & Ford 1983; Manchado et al. 1988; Kingsburgh & Barlow 1994; Guerrero & Manchado 1996; Medina & Peña 2000; Wesson et al. 2003; Phillips et al. 2005), among others.

Manchado et al. (1988) conducted the first optically resolved spectroscopic study of A 78, providing information on the eye-like and internal disk structures. The inner disk showed significantly enhanced chemical abundances not only of He but also of N, O and Ne, confirming the H-poor nature and chemical enrichment of the ejections. The eye-like structure also exhibited enhanced abundances of O and Ne, but He and N abundances typical of PNe. It is worth noting that the authors adopted an average temperature and density of 18,000 K and 100 cm^{-3}. Medina & Peña (2000), in regions near those studied by Manchado et al. (1988) and adopteding T_e and n_e of 20000 K and 100-700 cm^{-3}, respectively, obtained very similar results, except for the O/H ratio in the outer nebula, which was six times lower than expected. The authors attributed this result to strong temperature fluctuations affecting the abundances in A 78 caused by different ionization mechanisms. Phillips et al. (2005) presented spectroscopic information on the eye-like structure of A 78 but did not conduct an extensive analysis. A subsequent review of all previous spectra suggests that the reported abundances were a mixture of the internal ejecta with the surrounding nebula.

Regarding A 30, abundances in the outer nebula have not been firminly derived but have been contaminated by the emission from the inner region, leading to falsely enhanced values for processed elements (see for instance Kingsburgh & Barlow 1994). For the case of the knots (J1-J4) of A 30, being in the innermost parts, abundance calculations are not heavily contaminated by the H-rich nebula, making them reliable.

As mentioned earlier, Jacoby & Ford (1983) was the first to obtain abundances for these, revealing the scarcity of H and the overabundance of He, hinting at a possible chemical segregation among the knots. Guerrero & Manchado (1996) demonstrated that previous abundance estimates had overestimated H abundances by not accounting for contamination from He II series lines to the Balmer series. They also confirmed the segregation between the equatorial clumps J1 and J3 and J2 and J4, with the former having higher He abundances (see also Simpson et al. (2022)). Wesson et al. (2003) obtained high-resolution spectra that allowed them to characterize the physical and chemical conditions of clumps J3 and J4 with unprecedented precision. The [O III] nebular-to-auroral transition provided an electron temperature (T_e) of 17000 K. They used He line ratios to derive temperatures of 8850 and 4600 K for clumps J1 and J3, respectively. Finally, they used O II recombination lines to directly measure temperatures of the colder regions of the clumps, 2500 and 500 K for J3 and J1, respectively. Abundances calculated from CELs and ORLs, which were extremely high in heavy elements, indicated that the hypothesis that the knots had cold cores enriched with highly processed material (Harrington et al. 1995) was correct. In fact, Ercolano et al. (2003) presented models reproducing the photoionization of A 30 containing a cold ionized core surrounded by a warmer shell, successfully reproducing most of the observed spectrum, although the required abundances did not closely match those determined empirically.

Two other relevant results from the work of Wesson et al. (2003) are emphasized. The abundances derived from CELs and ORLs allowed for the calculation of the ADF in clump J3, resulting in a value of ∼700, the highest ever reported. In the case of clump J4, the estimated ADF had a much lower value of approximately 35 (Simpson et al. 2022), once again supporting the chemical segregation between the clumps. Second and no less important, Wesson et al. (2003) estimated a carbon-to-oxygen (C/O) abundance ratio well below unity, in sharp contrast with the evolutionary prediction of single-star models after undergoing a VLTP (Miller Bertolami et al. 2006). This led him to suggest that perhaps the origin of the clumps is more closely related to a nova event. However, it was later found that when accounting for the amount of carbon trapped in dust in A 30, the resulting ratio is well above unity (Toalá et al. 2021a), reconciling theory with observations once again.

1.3.4.5 High-energy spectra

The only two born-again PNe in which X-ray emissions have been reported are A 30 and A 78. Borkowski et al. (1995), who extensively described the mass-loading process caused by the stellar wind impacting the knots, stripping mass and subsequent accelerating in A 30, was the first to suggest that, under these conditions, one could expect soft X-ray emission. This emission was later confirmed in A 30 by serendipitous *ROSAT* PSPC observations, revealing a source of soft X-ray emission at a plasma temperature of $\sim 4.5\times10^5$ (Chu & Ho 1995). A follow-up *ROSAT* HRI observation showed a central point source and indications of diffuse emission associated with the innermost H-poor knots (Chu et al. 1997), although the detection of diffuse emission is uncertain due to the low signal-to-noise ratio (S/N). Observations conducted by Guerrero et al. (2012) for A 30 and Toalá et al. (2015) for A 78 allowed for the resolution of X-ray emission in point sources associated with their central stars, while the diffuse emission is linked to the innermost H-poor knots and petal-like and eye-like structures in A 30 and A 78, respectively. This diffuse X-ray emission originates, as previously suggested by Borkowski et al. (1995), from shock heating processes and mass loading of stellar winds, as well as ablation of H-poor knots. However, some of the diffuse X-ray emission may result from charge transfer reactions between stellar winds and H-poor ejecta in the form of knots and dust (Guerrero et al. 2012). On the other hand, despite certain proposed origins for the point source of X-ray emission at the central stars of A 30 and A 78, its origin remains unclear.

1.3.5 Interactions between ISM and born-again PNe

Figures 1.10, 1.13, 1.14 and 1.15 show images of the 5 confirmed born-again PNe, describe in the previous sections, and their outermost layers. Both the Sakurai's object and A 30 show completely round outer nebulae, so there is no doubt that neither has interacted with the ISM. HuBi 1 shows a slightly elongated structure in the polar directions with a slight decrease in surface brightness but none of the previously mentioned features.

The case of A78 is particularly interesting as it does show a brightening at the edge located in the SE while the opposite edge is barely visible. The proper motion of the CSPN is -3.0203 ± 0.0232 (pmra) 0.4275 ± 0.0232 (pmdec) mas yr^{-1} may hint a possible interaction. Nevertheless, as will be explained in detail in chapter 6, this increase in flux may be caused by the material ejected during the VLTP that has "pierced" the eye-like structure at those points and escapes to the outer nebula. The interaction is still not rejected. Lastly, A58 is the only nebula that might potentially be interacting with the ISM. It shows a well-marked brightening on its western edge while on the opposite edge the nebula gradually decreases in brightness, similar to a bow-shock. This effect may be caused by the ISM slowing down the nebula as it advances, however, this has not been confirmed to be true.

It can be said that by the time the CSPNe undergoes a VLTP and at least 1000 years

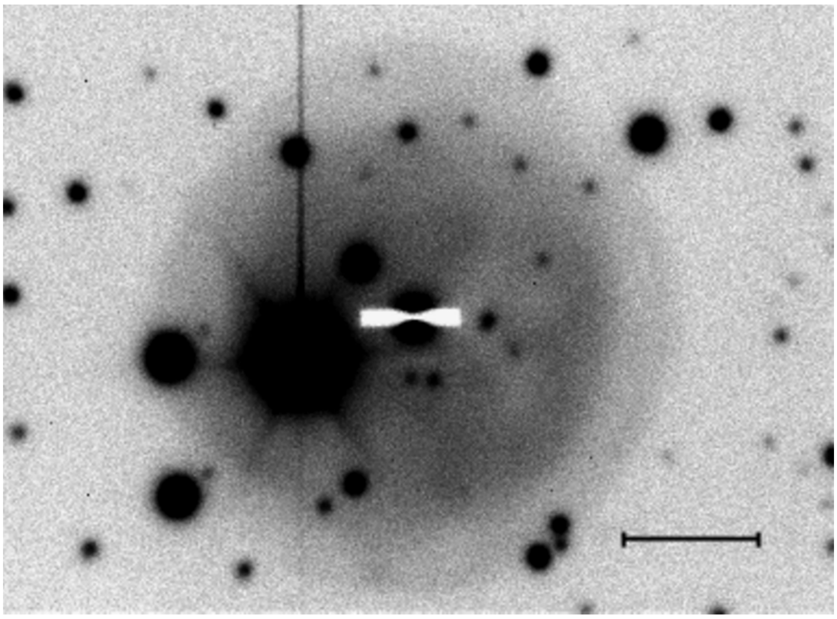

Figure 1.16: TV guider image of FG Sge obtained on 1996 June 10 with the Keck 10 m telescope during the spectroscopic observation. The slit is visible as a white horizontal bar in the center of the frame. The visual magnitude of FG Sge at that time was about 15.3. The scale bar on the lower right is equal to 10 arcsec. North is at the top, and east to the left. Image presented by Gonzalez et al. (1998).

thereafter (since A 30 and A 78 do not reveal interaction features Fang et al. 2014), the born-again PN has still not begun to interact with the ISM.

1.4 Born-again candidates

Over the years, several sources have been proposed to belong to the small group of born-again stars. As of today, and under the criteria of this thesis, they can not be considered as such yet. These include PM 1-89, WR-72, IRAS 18333-2357, Fg Sagittae and NGC 40. Below follows a brief historical summary of each source and the reasons why they do not belong to this group.

1.4.1 Fg Sagittae

Fg Sagittae (hereafter Fg Sge) is undoubtedly the most studied source among those mentioned above, with over 200 publications in the ADS database. It is at the same time the most controversial, since it continues to be considered as born-again for some authors (see, for instance, Ohnaka & Jara Bravo 2022).

The nature of Fg Sge, the central star of the PN He 1-5, has been puzzling given the variability recorded over the past approximately 140 years. In Figure 1.16 is shown the best image of Fg Sge available in the literature, whose quality is apparently poor. The evolution of Fg Sge in terms of effective temperature and luminosity has been established from long-term photometric studies (van Genderen & Gautschy 1995; Jeffery & Schönberner 2006, see also Figure 1 from Jeffery & Schönberner (2006)). Since 1880, Fg Sge evolved from a hot CSPN to become an F-type supergiant around 1970. In the 1970s, the visual brightness rate decreased and the star began to experience periodic fluctuations in its visual brightness with an initial period of 80 days that increased to 130 days (Jurcsik 1992; Guinan et al. 1992). The accepted interpretation for such changes is that Fg Sge had undergone a final flash of He in an early stage of white dwarf (Paczyński 1971; Langer et al. 1974; Christy-Sackmann & Despain 1974; Schoenberner 1979; Iben 1984; Bloecker & Schoenberner 1997; Gonzalez et al. 1998).

In the fall of 1992, the periodic pulsations ceased (Hinkle et al. 1995) and the optical brightness decreased by 5 mag in less than two months (Arkhipova 1994). At the same time, the SED from 1 to 18 μm evolved quite abruptly towards a 1000 K blackbody spectrum, very different from the stellar photospheric blackbody SED of 5600 K observed 10 years earlier (Woodward et al. 1993). This behavior of the SED is known to occur in classical novae (Gehrz 1999) and WR stars (Hackwell et al. 1979), which eject discrete gas layers that condense dust grains blocking the light from the star. Woodward et al. (1993) attributed the first abrupt visual light decrease of Fg Sge to the formation of a visually thick dust layer with a mass of 3.3×10^{-9} $M_\odot$ condensed from an ejected gas layer from the CS. The visual light curve revealed that Fg Sge has been experiencing irregular large-amplitude oscillations varying between 200 and 400 days in duration since the first dust formation episode. Since the initial decrease in visual brightness and the slow recovery of 1992-1993, several episodes of decline and recovery of visual brightness have occurred, which have been attributed by Gonzalez et al. (1998) to ejecta of discrete dust shells similar to those implicated in the R CrB phenomenon. These fading episodes were also extensively reported in V4333 Sgr (Liller et al. 1998a; Jacoby et al. 1998; Eyres et al. 1999).

Alongside the aforementioned changes, there was also an evolution in the chemical abundances in the stellar photosphere, which are only traceable between approximately 1960 (the first spectra with sufficient quality to derive abundances) and 1996, when Fg Sge was obscured due to the newly formed circumstellar dust layer. The spectra presented by Herbig & Boyarchuk (1968) between 1960 and 1965 revealed relatively normal abundances of He, C, and O, although it is not ruled out that the C/O ratio could be above unity. A slight enhancement in certain s-processed elements (Sr, Ba, Eu) was also detected, but Y and Zr remained normal (these elements provide key clues about the processes involved). At some point between 1965 and 1972, there was a dramatic increase in the abundances of s-process elements (Y and Zr appeared 1 dex overabundant, which remains a mystery), while light elements and iron-peak elements remained normal (Langer et al. 1974). According to spectra obtained by Cohen & Phillips (1980) in 1975, 1976, and 1978, the increase in s-processed elements continued gradually. Finally, the last available spectra were published by Gonzalez et al. (1998) between 1992 and 1996. Somehow, Fg Sge then exhibited poor abundances in H, and there was little evidence of an unusual abundance of carbon before the appearance of the C2 bands (which require C/O $>$ 1).

The behavior and composition similar to SO and V605 Aql seen in Fg Sge led to the consideration for some years that this source had the same origin as the former. To some extent, this was correct as the models available until the 1990s described the behavior of a CSPN after undergoing a final flash of He (Schoenberner 1979; Iben et al. 1983), but did not distinguish between LTP and VLTP. The introduction of LTP and VLTP models as such was introduced by Herwig et al. (1999), with the thermal pulse occurring on the horizontal and descending part of the post-AGB evolutionary path, respectively (see section 1.2.2). Estimates of Fg Sge's $T_{\rm eff}$ of 50000 K and $<$ 55000K prior to its expansion obtained from the associated nebula (Hawley & Miller 1978; Harrington & Marionni 1976) place the He flash along the horizontal part of the post-AGB phase, indicating that LTP was the most plausible scenario.

The disappearance of H previously observed presents a conflict because LTP models predict that surface H should not be depleted until a deep convection zone is established, and then only $\sim10^4$ years after the pulse occurs (Blöcker 2001). In the case of Fg Sge, this H depletion occurred before the star reached its minimum temperature, but substantially after the time it is predicted to occur after a VLTP (Herwig 2001a). Alternative models of the post-AGB star evolution followed by a VLTP were presented by Lawlor & MacDonald (2003); Miller Bertolami et al. (2006); Miller Bertolami & Althaus (2007), in which the star describes a double loop before advancing to evolve into a WD again. These models satisfactorily explained the rapid evolution of SO (Duerbeck 2002) and the appearance and subsequent contraction of V605 Aql (Clayton & De Marco 1997). In the case of Fg Sge, the models would place it in its second redward loop; however, several weaknesses appear. First, it is predicted that surface abundances should be highly processed, i.e., H-deficient and carbon-rich, a fact that was not observed. And second, models also assert that the star would have been a WD, with $T_{\rm eff} >$ 100000 K, in a comparatively recent past; too hot to meet the nebula's diagnosis, and possibly too old for the nebula to have survived (which has happened).

The inconsistencies seen lean the balance more towards the scenario that Fg Sge underwent an LTP instead of a VLTP. In fact, most authors support this view more and consider Fg Sge and V4334 Sgr as examples of LTP and VLTP sources, respectively (Herwig 2001b; Jeffery & Schönberner 2006, for instance).

1.4.2 IRAS18333-2357

IRAS 18333-2357 is a nebula in the galactic halo belonging to the globular cluster M22 (NGC 6656), discovered as a strong infrared source by Gillett et al. (1989). PNe are very rare objects to see in globular clusters, as their low-mass stars do not evolve rapidly enough to ionize the expelled envelopes before dissipation into the star crowded ISM. In fact, only 5 PNe have been detected in clusters of our galaxy (Jacoby et al. 1997; Fragkou et al. 2022). The M 22 cluster has an angular diameter of ∼32 arcmin and a central diameter of 2.66 arcmin (Hartwick et al. 1982), and its turnoff mass is 0.83 M, implying an age of 12 Gyr (Sippel & Hurley 2013). IRAS 18333–2357 is located in the core of M 22, ∼1 arcmin from the cluster center, which has a well-determined distance of 3.1 kpc (Frogel et al. 1983). Moving at a velocity of 158 km s^{-1} relative to the galactic center, the ram pressure of the Galactic halo gas is causing a strong asymmetry in the morphology of the PN associated with IRAS 18333-2357 (Borkowski et al. 1990; Borkowski & Harrington 1991), stripping the nebular gas from the star. What was truly striking about this source was that in the IUE UV spectra presented by Cohen & Gillett (1989), both the central star and the associated PN showed a total absence of Balmer lines, whether in absorption or emission. According to the authors, the detected stellar absorptions could be associated with

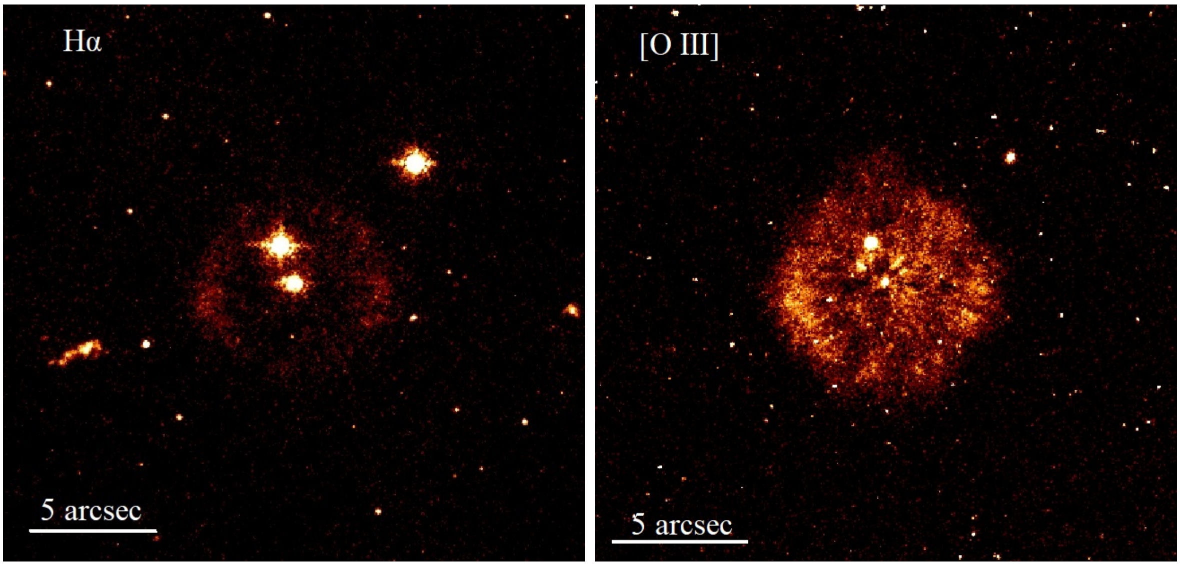

Figure 1.17: .

He II, and the absence of the He I λ4471 lines implied $T_{\rm eff} \geq 50000$ K. Given the relatively high temperature and oxygen deficiency, IRAS 18333-2357 was packaged alongside A 30, A 58, A 78, now well-known born-again PNe, for some years. Later, Harrington & Paltoglou (1993) presented optical spectra, which closely resembled those of SdO star KS 292, with enhanced abundances in H shell burning and He burning products. The authors suggested that the star was H-rich with a temperature of 75000K.

Given that there are no further studies confirming the photospheric temperature or H deficiency of the central star, we can not confirm IRAS18333-2357 as a bona-fide born-again PN.

1.4.3 PM 1-89 and WR 72

PM 1-89 (a.k.a IRAS 15154-5258) and WR 72 (also known as Sand 3) are two poorly studied nebulae, similar to IRAS 18333-2357. Unlike it, they show potential signs that they might be born-again PNe.

PM 1-89 was classified as H-poor PN with an infrared excess hosting a CSPN [WC4] Manchado et al. (1989). The nebular diameter is reported as 35 arcsec and the electron density $n_e = 10^2$ cm^{-3}, while the presumably H-poor region where the Hα line is not detected has a diameter of 9 arcsec (Harrington 1996). The previous diameters have been measured from unpublished HST images obtained with the Planetary Camera, Figure 1.17. The HST Hα image in the left-hand panel of Fig. 1.17 shows a rounded shell of 4 arcsec radius illuminated along the EW direction and two jet-like features (not yet reported) roughly ≈8 arcsec from the CSPN. The HST [O III] image (Fig. 1.17, right) shows unexpectedly larger shell (O^+ ionization potential is greater than that of H) and strong fragmentation of the emission, with a series of radial features near the CSPN. These resemble the comet-like knots of A 30 and A 78 resulting from the born-again event. The spectroscopic data supporting this nature, however, have limited spectral resolution and do not spatially resolve the emission from the old nebula

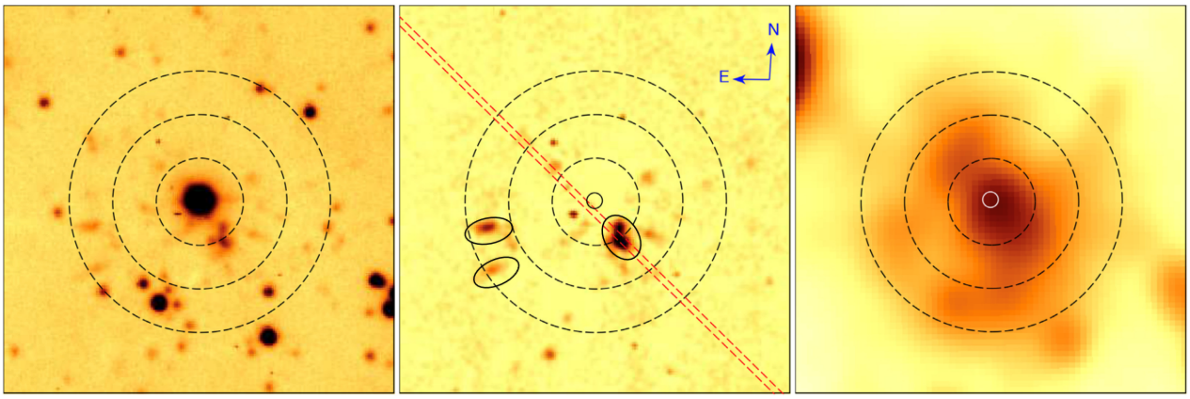

Figure 1.18: From left to right: SALT [O III] λ5007 Å and continuum-subtracted images of (H-poor) knots around WR72 , and WISE 4.6 μm, image of the central shell (with position of WR 72 indicated by a circle). The orientation and the scale of the images are the same. Concentric, dashed circles of angular radius of 10, 20, and 30 arcsec are overplotted on the images to make their comparison with each other and Fig. 4 more convenient. The location of the 1.5 arcsec wide RSS slit is shown by a (red) dashed rectangle. At the distance to WR 72 of 1.42 kpc, 30 arcsec corresponds to $\approx$0.2 pc. Figure adopted from Gvaramadze et al. (2020).

and possible recent H-poor knots (Suárez et al. 2006). Stellar contamination of these spectra by broad C lines also makes the conclusions about the H-poor nature of this PN questionable.

WR 72 is a CSPN [WO1] according to the classification scheme of Crowther et al. (1998). Since no PN associated with WR 72 was found at that time, Barlow & Hummer (1982) suggested that it had already dispersed into the ISM and was no longer detectable. Subsequent searches for a nebula around this star did not yield positive results (van der Hucht et al. 1985; Marston et al. 1994; Feibelman 1996; Keller et al. 2014). Finally, Gvaramadze et al. (2020) found the nebula around WR 72 by detecting infrared emission in the WISE 22, 12, 4.6 (see right panel in Figure 1.18), and 3.4 μm bands (see also Griffith et al. 2015). The image in the 24 μm band (see their Figure 1) revealed a bright unresolved source of 2 arcmin in diameter surrounded by a diffuse halo of $\sim$5 arcminutes, while in the 12 μm band, a bright source of $\sim$1 arcmin appeared slightly elongated in the N direction with a diffuse halo of the same size as the bright emission at 22 μm. As a result of this discovery, these same authors obtained new [O III] images and optical spectra with the SALT telescope, showed in the left panel in Fig. 1.18. The images revealed a series of scattered knots around the star that appear to extend radially from it as in A 30 and A 78, although the spatial resolution of 1.6 arcsec of the image does not provide an accurate description of their morphology and spatial distribution. As for the spectra, due to their low dispersion and being taken under adverse conditions (seeing 2.1 arcsec), the chemical abundances in the newly detected knots could not be determined, although it was suggested that they were H-poor.

Since there are indications that both sources have the potential to be born-again, we present an observation proposal to ESO in program P113 requesting VLT MUSE IFS spectroscopic data for PM 1-89 and WR-72. At the time this thesis is being written, the proposal has been accepted and we are awaiting observations to clarify the nature of these objects. A priori, these objects will not be considered born-again for the remainder of the work.

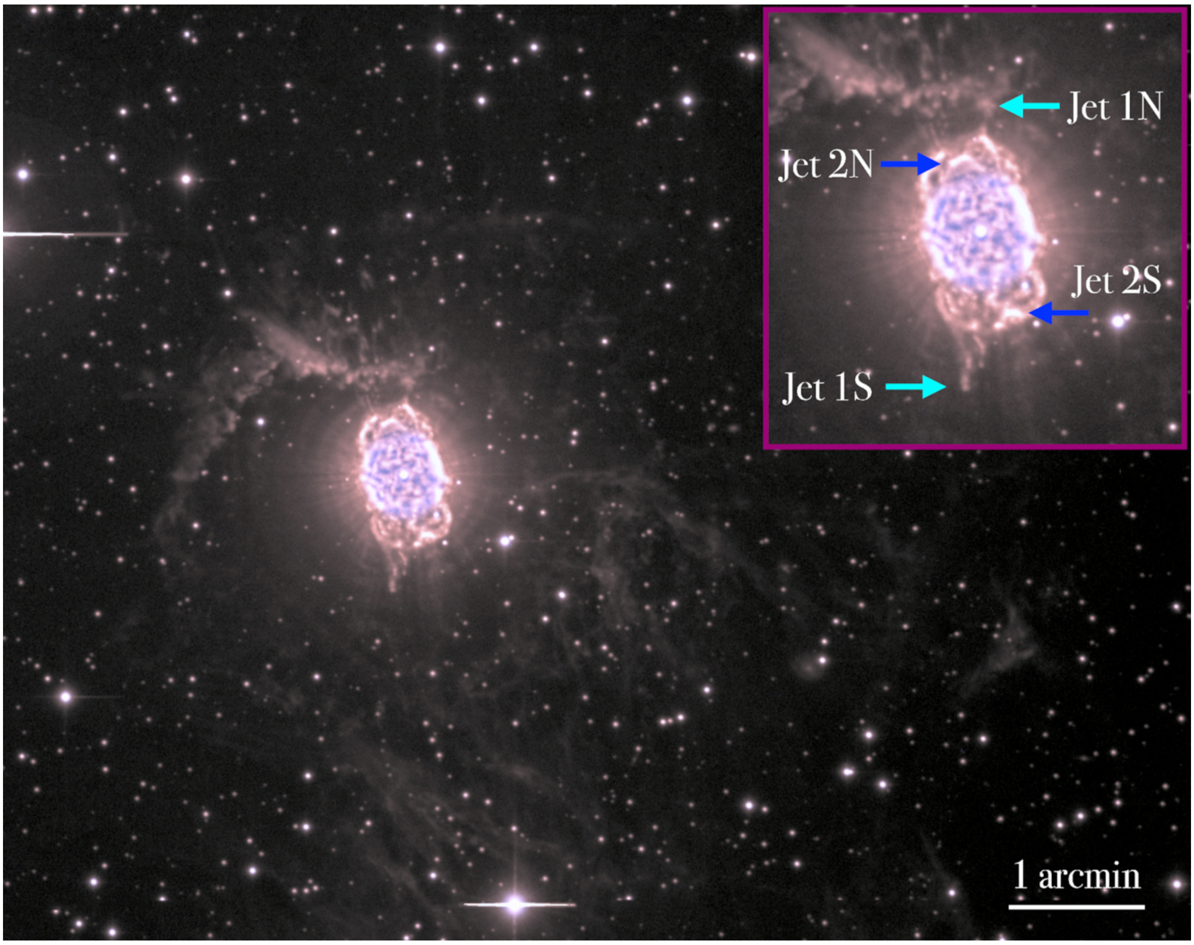

Figure 1.19: Isaac Newton Telescope (INT) Wide-Field Camera (WFC) colour-composite picture of NGC 40. Red and green correspond to the Hα+[N II] emission and blue is [O III]. The inset shows a close-up of the main nebula around HD 826, the central star of NGC 40, in which we have labelled the main jet-like features identified by Meaburn & Lopez (1996). North is up, east to the left. Figure directly taken from Toalá et al. (2019).

1.4.4 NGC 40

The planetary nebula NGC 40, commonly known as the 'bow-tie' PN, is located around the central star HD 826, see Figure 1.19. The nebula displays a rich morphology consisting of a barrel-like main cavity whose northern and southern caps open into a set of lobes or blisters, and a set of optical and IR concentric rings surround the previous structure (Corradi et al. 2004; Ramos-Larios et al. 2011). The abundances calculated by Pottasch et al. (2003) from CELs show a large C/O ratio, consistent with the carbon-rich [WC8]-type of its central star (Crowther et al. 1998) and with simple stellar evolution models after a VLTP (Miller Bertolami et al. 2006). Additionally, the ISO IR nebular spectrum exhibits features associated with a carbon-rich chemistry (Ramos-Larios et al. 2011).

On the other hand, the $T_{\rm eff}$ of HD 826 has been estimated to be ~90 kK, by fitting NLTE models to the optical and UV spectra (Bianchi & Grewing 1987; Leuenhagen et al. 1996; Marcolino et al. 2007), and approximately 40 kK, based on photoionization models or rough estimates using the Zanstra and Stoy methods (Harman & Seaton 1966; Pottasch et al. 2003;

Monteiro & Falceta-Gonçalves 2011). A carbon-rich curtain around HD 826 was proposed to explain this discrepancy (Bianchi & Grewing 1987), similar to what has occurred in HuBi 1.

Toalá et al. (2019) presented an infrared study with Spitzer data and modeled the spectra of the central star using PoWR software. After reviewing the abundances obtained, he concluded that these favored an LTP instead of a VLTP and suggested it as born-again. However, as we have mentioned here, we will only consider those PNe that undergo a VLTP as born-again, so this source will not be considered as such.

1.5 Discrepancies and outstanding questions in born-again planetary nebula

As data from the 5 born-again planetary nebulae have been obtained with higher quality and precision, and studies across much of the spectral range have been conducted, observations have increasingly aligned with the latest updates of theoretical models (Lawlor & MacDonald 2003; Miller Bertolami et al. 2006). However, some observed facts directly conflict with the predictions of the models of a single star scenario after undergoing a VLTP.

1.5.1 Abundance C/O ratios below unity

Based on optical spectroscopic observations, Wesson et al. (2003) and Wesson et al. (2008) derived a C/O abundance ratios of 0.19, 0.21 and 0.06 for knots J1 and J3 of A 30 and for the central ejecta of A 58, respectively. This is in stark contrast to with the predicted abundances summarized in Tab. 1.4, from which the C/O ratios are estimated to be above unity (Lawlor & MacDonald 2003; Althaus et al. 2005; Miller Bertolami et al. 2006). Indeed, the low C/O reported were difficult to reproduce even in more general stellar models. Karakas et al. (2009) demonstrate that the C/O ratio in a PN can be less than unity but not less than 0.38 in number ($\sim$0.29 in mass). The ratio being less than unity was more favorable in the case of a nova (Lau et al. 2011), questioning the born-again nature (i.e., having undergone a VLTP) of the sources.

It must be considered that the aforementioned ratios were obtained from abundances derived from ionized gas. Since both C and O are prone to depletion into dust (carbon more than oxygen), one should take into account how much C and O is trapped in it. Toalá et al. (2021a) precisely realized this fact and modeled the dust measured in the infrared observations of A 30 using the CLOUDY software. The results showed that 40% of the mass ejected during the VLTP could have coagulated into carbon-rich dust, which was not accounted for in previous nebular estimates of the C/O ratio. Taking into account the mass of C in both gas and dust (which in their models was entirely formed by C), the revised C/O ratio resulted in a value $\geq$ 1.27. This ratio was consistent with those predicted by born-again single star models. Despite this, it should be noted that in A 30, the presence of a binary has been confirmed (Jacoby et al. 2020), although it is not clear what role it plays in terms of abundances. A similar result could be expected for A 78, the twin nebula of A 30 with similar conditions.

In A 58, SO, and HuBi 1, something similar might be occurring, but the situation becomes more complicated because there is likely a shock in the central ejecta (see Chapters 4 and 5).

In fact, for HuBi 1, the shock is actually confirmed, see Chapter 3. Modeling the dust in these sources could not be carried out using CLOUDY; it requires the use of more complex tools that takes into account the interaction of shocks, such as MAPPINGS. Even then, it is not an easy task as it requires precise knowledge of the shock to accurately determine the formation of dust due to it (see for instance Dopita et al. 2018). In any case, and pending future work on the subject, in these three sources the C/O ratio is not as expected for a born-again PNe.

1.5.2 Anomalous high Ne abundance

Another conflict arises from the extremely high Neon abundances observed, which are not possible to obtain through a VLTP and can only be reached if there is dredging of Ne from a Neon core. These Neon abundances not only appear in A 58 as reported by previous authors but also in A 78 obtained by ourselves, being discussed in detail in chapter 6.

Lau et al. (2011) explored in detail the case of A 58, describing two possible scenarios resulting in a primary nebula rich in H, followed by an ejecta poor in H and rich in Ne and O. The first scenario invoked a merger between an ONeMg WD and a main-sequence star, while in the second scenario, the ejecta are formed in part by a nova explosion closely following a classic final flash. In the merger scenario, a series of assumptions were made for the observed result to be plausible, resulting in the inability to test the frequency at which this process could occur. On the other hand, in the nova scenario, its frequency was tested via a population synthesis analysis, but it turned out to be unlikely; such a system would occur once every 5000-10000 years. Assuming that A 58, Sakurai object, A 78, and A 30 originate from a common origin (even considering only A 58 and Sakurai object), these objects are more common than those arising from a nova event followed by a VLTP.

Recently, a alternative scenario based on VLTP followed by common envelope has been proposed to explain the morphology of some born-again nebulae (Rodríguez-González et al. 2022, see the following section). This might suggest that the reasoning of Lau et al. (2011) was partly correct and that the existence of a companion, albeit with less specific characteristics than those proposed by these authors, could alleviate the discrepancy in Ne. However, currently, there is a clear lack of such theoretical studies.

1.5.3 Extreme abundance discrepancy factor

One of the biggest unresolved problems in nebular astrophysics is the discrepancies between the abundances of heavy elements derived from collisionally excited lines (CEL) and those derived from optical recombination lines (ORL). These discrepancies are commonly quantified using the so-called abundance discrepancy factor (ADF), which is defined as:

$$ADF(X^{i+}) = (X^{i+}/H^{+})_{\mathrm{ORLs}}/(X^{i}+/H^{+})_{\mathrm{CELs}}. \tag{1.5.1}$$

Typical ADF values in planetary nebulae (PNe) range between 1.6 and 3, but much higher values have been reported for some PNe, for example, an ADF of 10 for NGC 6153, 70 for Hf 2-2 (see Liu et al. 2006, and references therein) and 120 for the exceptional case of A 46

(Corradi et al. 2015)[10]. It has been proposed that their origin may be due to the presence of two gases (e.g. Liu et al. 2000, 2001; Tsamis & Péquignot 2005; Liu et al. 2006; Yuan et al. 2011): one hot where the CELs can be efficiently excited and another much colder (∼1000 K) deficient in H, but with a significantly enhanced content of heavy elements mostly derived from the ORLs. In HII regions, this is indeed caused by temperature inhomogeneties quantified by T^2 (Méndez-Delgado et al. 2023)

This problem is even more pronounced in the case of born-again PNe, where values of ∼90, 600, and 770 have been reported for the central knot of A 58 and for the J3 and J1 knots of A 30. It is true that in A 58, a subsequent review of the same spectra casts doubt on the measurement of abundances from the ORLs and the same could be happening for A 30 (see Chapter 4). In any case, we will take these results as true for the moment. Liu et al. (2006) was the first to speculate that the high ADFs might be the result of the existence of a binary star and a common envelope process after studying the case of Hf2-2 (with a binary CSPN). Later, Corradi et al. (2015) and Jones et al. (2016) also suggested that many (if not all) PNe where high ADFs have been measured are post-common envelope (CE) binaries. Moreover, Corradi et al. (2015) emphasized that the opposite hypothesis may not be true, i.e., not all post-CE PNe have high ADFs (for example, the case of NGC 5189 as noted by Manick et al. (2015). It was finally Wesson et al. (2018) who, from a sample of known PNe with close binary central stars, revealed a clear link between binarity and ADF and an anticorrelation between this and nebular electron densities. All nebulae with close binary central stars with a period less than 1.15 days had an ADF exceeding 10 and an electron density less than 1000 cm^{-3}.

Currently, it is known that A 30 contains a binary central star (Jacoby et al. 2020), and in the case of A 58, it is speculated that it does too, although it has not yet been confirmed. However, the explanation for why the measured ADFs in A 30 (and to a lessier extent in A 58) are so extremely high is not clear. For the rest of the born-again PNe, ADFs have not yet been measured, and it has not been confirmed whether they possess binary stars or not, so speculation about whether undergoing a VLTP has any influence on subsequent ADFs cannot be reached. As argued by Wesson et al. (2018), it seems to indicate that it does not.

1.5.4 Single star evolution against the disk-jets morphology

The morphologies seen in born-again PNe and their kinematics contrast markedly with those expected in the scenario of a single-star event through VLTP. Mass ejection from a single star cannot produce a bipolar morphology (e.g., García-Segura et al. 2014). In A 30, the morphology is more consistent with a fast bipolar outflow (Meaburn & Lopez 1996) and an expanding broken disk (Borkowski et al. 1993; Harrington 1996). A similar case is seen in A 78 with a disk similar to that of A30 and bipolar outflows (Borkowski et al. 1993; Meaburn et al. 1998), although for this nebula the outflows appear more as diffuse emission rather than concentrated knots, probably due to erosion by strong stellar winds (e.g, Borkowski et al. 1995). Therefore, the bipolar structure of H-deficient knots in A 30 and A 78 (broken disk + jet) must

---

[10] For a complete compilation of ADFs measured in planetary nebulae, the reader can visit https://nebulousresearch.org/adfs/

be attributed to the action of a companion, either stellar or, as suggested decades ago by Soker (1997), substellar.

Rodríguez-González et al. (2022) presented a morpho-kinematic model for A 30 based on echelle data using the SHAPE software. They proposed that the physical structure and discrepancies in abundances observed in the H-deficient knots could be explained through a common envelope phase with a companion after the VLTP. The kinematic properties of jet-like features are currently similar to those of the CE phase, while clumps in the disk have experienced strong acceleration caused by the rapid stellar wind (Fang et al. 2014). This scenario would also provide a plausible explanation for the clumps in the disk having higher velocities than those observed in the jets (see Figure 6 in Rodríguez-González et al. 2022).

In the cases of the younger born-again PNe, such as SO and A 58, the morphologies are more consistent with the presence of a binary companion. For Sakurai object, optical observations obtained in 2001 detected a rapid bipolar flow in [N II] emission with systemic velocities of −350±50 and +200±50 km s^{-1}, respectively (Kerber et al. 1999). Subsequently, modeling of the infrared emission carried out by Chesneau et al. (2009) suggested the presence of a structure similar to a disk obscuring the central star. Additionally, Tafoya et al. (2023) reported ALMA observations of molecular emission revealing an hourglass structure incompatible with mass ejection from a single star. For A 58, the situation is similar; the optical emission of the ejecta presents a bipolar morphology (Clayton et al. 2013), while the molecular emission reveals a disk-jet structure (Tafoya et al. 2022). In fact, optical observations with integral field spectroscopy data indicate a structure similar to that reported in Sakurai object (see Chapter 5). It is worth noting that despite all indications, the binarity of A 58, A 78, or the Sakurai object has not yet been confirmed.

Finally, HuBi 1 is perhaps the only born-again PN in agreement with the models regarding morphology. The rounded structure of the inner layer (Pollacco & Hill 1994; Rechy-García et al. 2020) could have plausibly originated after a VLTP of a single star. Three-dimensional hydrodynamic simulations predict that, as a consequence of the dramatic reduction in the stellar wind speed and ionizing photon flux during the VLTP, the velocity and pressure structure of the outer H-rich nebula are affected, creating turbulent ionized structures surrounding the inner layer (Toalá et al. 2021b). These structures have been detected from optical observations obtained with GTC-MEGARA in the emissions of [N II] and [S II] lines, detailed in chapter 3. Subsequent analysis is undergoing.

1.6 Motivation of the thesis

This thesis aims at contributing to the understanding of the born-again phenomenon in PNe by investigating the mechanisms of ionization involved in born-again PNe, their chemical abundances and their morphology and spatio-kinematics by means of optical integral field unit (IFU) and long-slit spectroscopy. This thesis inquires on a series of issues on the nature of these sources and their emission mechanisms that are frequently overlooked.

The results presented are expected to provide the basis for other studies in addressing some of the unresolved questions mentioned in previous sections. One example is the dilemma caused by the observed C/O ratio, which seems to contradict the theoretical expectations of VLTP events. To account for the amount of C trapped in dust, which may reconcile observations and theoretical predictions, the group led by Jesús A. Toalá at the Institute of Radio Astronomy and Astrophysics in Mexico is modeling dust in born-again nebulae. These models require precise abundances determinations as those that will be provided here. To this respect, we note that the investigation of the high ADF values reported in these sources is not addressed here, as the group led by Jorge García Rojas at the Institute of Astrophysics of the Canary Islands has made notorious advances for more than a decade (see for instance, García-Rojas et al. 2012, 2022; Méndez-Delgado et al. 2023). Furthermore the determination of the dust content of born-again PNe demands a characterization of the ionization mechanisms, either photoionization or shocks (or both, most likely), which will serve as input for CLOUDY models of photoionization or MAPPINGS models of shocks to be used to obtain synthetic observations to be compared with the real ones.

The thesis also aims at providing a comprehensive view of some born-again PNe, complementing previous studies on these sources. A 58 and HuBi 1 have been specifically investigated here. As for A 58, Tafoya et al. (2022) recently presented a morpho-kinematic model of the molecular gas in the disk and outflows of its recent ejecta. This study suggests the existence of material currently being expelled directly from the CSPN, which is rather unexpected. The observations and spatio-kinematic model of the optical gas presented by Clayton et al. (2013) has ample room for improvement, particularly with the advent of IFU observations and the availability of multi-epoch long-slit spectra. As for HuBi 1, it has been suggested to be a new addition to the exclusive group of born-again PNe (Guerrero et al. 2018), which seems to be confirmed by the high expansion velocity of its internal shell (Rechy-García et al. 2020). However, a confirmation of its true nature as born-again PN requires the determination of its chemical abundances, with the scarcity of H in the central ejecta being the key to prove it.

This thesis is structured as follows. Chapter 2 includes a detailed description of the data reduction, both long-slit spectra and IFS. Chapter 3 focuses on HuBi 1, first presenting emission maps of the emission lines available in optical IFS observations both for the inner and the outer shell, then computing extinction maps for both shells. The study is completed with the identification of the ionization mechanism and calculation of chemical abundances through MAPPINGS. Chapters 4 and 5 present two different works on A 58, discussing first changes in the ionization structure over recent years and then investigating the central ejecta morpho-kinematics using optical IFS data to obtain a precise model using SHAPE of the ionized material to be compared with that of the molecular gas. Chapter 6 investigates the extinction and chemical abundances in the different structural components of A 78. Finally, Chapter 7 presents a summary of all results, additional conclusions, and possible future lines of work.

Chapter 2

Methods

The studies carried out during this doctoral thesis have been based almost entirely on the analysis of data obtained from either integral field or long-slit spectroscopic observations, but also photometric observations. The data files obtained directly from the observations require preprocessing to be used in the analysis, commonly known as data reduction. This process aims 1) to clean the data from any contamination that arises during the observations, such as cosmic rays, atmospheric emission lines, moonlight, CCD thermal emission, etc.; 2) to account for sensitivity variantions, and 3) to calibrate in wavelength and flux. Note that each telescope and instrument has its own requirements or peculiarities that require additional corrections to be taken into consideration throughout the reduction process. Moreover some instruments have their own data reduction pipeline, which although follows the same steps as a usual reduction process, may present extra challenges. A clear example of this is the Multi-Espectrógrafo en GTC de Alta Resolución para Astronomía (MEGARA) instrument on the Gran Telescopio Canarias (GTC), which requires a specific data tree architecture and a series of specific libraries previously installed in the computer for its reduction.

2.1 Long-slit spectroscopy reduction

Long-slit spectra produce two-dimensional data that provide spatial information along the direction in which the slit has been placed in the sky, and spectral information, which is constrained within a specific spectral range by the diffraction grating or grism. A sketch of how a spectrograph works is shown in left-hand panel of Figure 2.1. This research has used the spectrograph Optical System for Imaging and low-Intermediate-Resolution Integrated Spectroscopy (OSIRIS) and ALhambra Faint Object Spectrograph and Camera (ALFOSC) located at GTC and the 2.5m Nordic Optical Telescope (NOT), respectively[1]. Below are the steps for reducing long-slit spectra carried out using the Image Reduction and Analysis Facility (IRAF) software, which is almost exclusively dedicated to the processing of astronomical images. Since this software is becoming obsolete, its Python version Pyraf has been used on some occasions, which practically includes all the routines developed in IRAF.

---

[1] Also archival data from Twin Spectrograph at the Cassegrain of the 3.5m telescope of the (TSC) Centro Astronómico Hispano en Andalucía (CAHA) and Intermediate-dispersion Spectrograph and Imaging System (ISIS) at the 4.2m William-Herschel Telescope (WHT) were used.

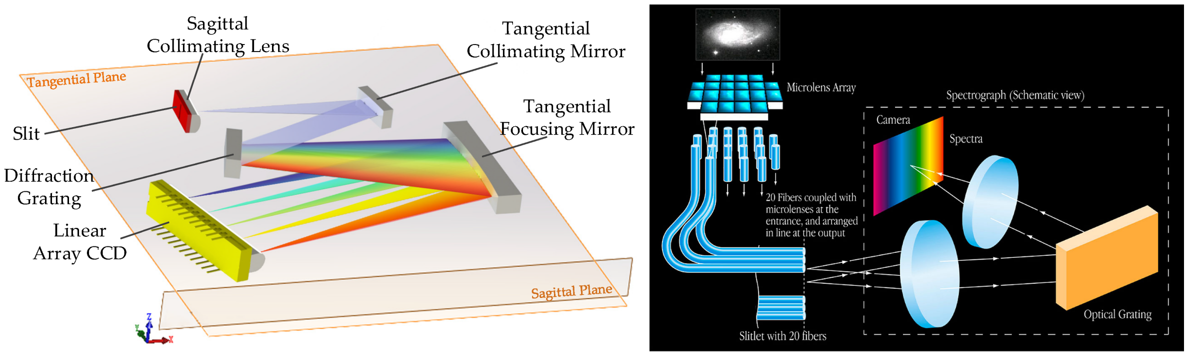

Figure 2.1: Schematic diagrams of how an spectrograph (left-hand panel) and IFU (right-hand panels) work.

2.1.1 Preliminary Steps

The raw files, except for limited exceptions, are usually in FITS format[2] to contain both technical and observational information. Sometimes certain layers do not provide any useful information, so it is advisable to discard them and keep only a single layer exclusive to data. Additionally, both observation and calibration files may have what is known as over-scan[3] regions at the edges of the files. This region could be used to subtract the bias if no other bias files are available, otherwise it is convenient to trim it. A copy of the desired layer could be made from the original files and cropped to remove the over-scan region using the *imcopy* task.

Once the files are cropped, the next step would be to combine the corresponding files, i.e., the observed object, flats, bias, etc., into a single file of each type for reduction. This is done to clean them of cosmic rays hitting the CCD during the observation period and saturating certain pixels. To achieve this, we use the *imcombine* task which applies a median, mean or clipping algorithm among other, across all images. This step usually works well if we have three or more different observations of the object. In cases where only two or even a single observation is available, a sigma clipping filter is applied instead to remove such hot pixels. IRAF also provides specific task such *zerocombine* or *flatcombine* focused to combine bias and flat files. In this work when is possible, a hand-made work is always chosen.

2.1.2 Corrections to the CCD

Biases, or zero-second exposures, are calibration files that contain electrical signal present even when no light is reaching the detector, caused by internal factors of the detector, such as applied voltages or electronic characteristics. This bias can be generated by different components of the detection system, such as detector pixels or readout electronics. Bias is an additive term, stored in the masterbias (combination of all biases), that needs to be subtracted from the

---

[2] The acronym FITS stands for "Flexible Image Transport System". FITS is a widely used file format in astronomy for the storage, processing, and transmission of data, including images, spectra, and data tables. It was developed specifically to meet the needs of the astronomical community due to its ability to store multidimensional data and descriptive metadata, as well as its flexibility to be used in a variety of applications and platforms.

[3] The over-scan region refers to the area of the image sensor (typically a CCD or CMOS detector) that extends beyond the active imaging area. It includes pixels typically located at the edges of the sensor that are not exposed to light during the observation.

signal of the image to eliminate its effect on the actual source signal. It is also convenient to subtract this same signal from all calibration files. This step could be easily carried out using the *imarith* task.

It should be mention that the potential wells in CCD detectors spontaneously generate electron-ion pairs at a rate that is a function of temperature. For very long exposures this translates into a current that is associated with no light source and that is commonly referred to as dark current. Modern CCD detectors have negligible dark current. In this thesis it was not necessary to applied this correction.

The next step is applying the flat field to the spectra. These are used to correct for variations in pixel-to-pixel sensitivity across an imaging sensor, as well as to compensate for vignetting[4] and other optical artifacts that might be present in the imaging system. Flats are typically acquired using a uniform and diffuse light source, such as a flat light screen or an internal lamp of contamination light, typically filament of tungsten (usual for long-slit spectra) or the sky at sunset or sunrise when sunlight is evenly scattered in the atmosphere (for imaging). The idea is the illumination to be as uniform as possible across the entire flat. Furthermore, if a lamp is used, which is the case for the reductions in this work, the flats are in turn affected by its spectral response, which produces unwanted gradients that need to be removed.

Before applying the flat to our spectrum, we must correct both the spectral response and the vignetting caused by the optics of the system. We can do this through various means, for example, IRAF has some tasks such as *ccdproc* or *response* that are specific for correcting such artifacts. However, in this work, we have opted for a more artisanal approach. First, each pixel is averaged with a certain number of adjacent pixels along the spectral direction. In this way, we achieve profiles from which the spectral response has been erased. Then we perform the same process but in the spatial direction, correcting for possible vignetting in the flats. Next, we normalize our original flat by this smoothed flat. This ideally normalized flat only contains the information of the pixel-to-pixel variations that we will finally apply to our spectrum.

2.1.3 IRAF parameters

The core fitting engine within the IRAF software is consistently used across various tasks involving function adjustments, such as *fitcoords, background, etc...* Consequently, the parameters controlling these adjustments are generally the same, although some tasks may have additional specific parameters. The subsequent steps of the reduction process required to used some of these task. We thus show the relevant parameters involved in the fitting process:

- `high_rej`: Indicates the number of sigmas above the fit above which data points are not considered.
- `low_rej`: Indicates the number of sigmas below the fit below which data points are not considered.

---

[4] Vignetting refers to a reduction in image brightness or saturation at the periphery compared to the image center. This phenomenon typically occurs due to optical limitations of the telescope or camera system, where light passing through the edges of the lens or telescope aperture is obstructed or not focused as effectively as light passing through the optical axis.

- `niterat`: Indicates the number of iterations for rejecting points.
- `function`: Indicates the type of function for fitting: legendre, spline, Chebyshev...
- `order`: Indicates the order of the function.

2.1.4 Wavelength calibration

Wavelength calibration is carried out using arcs. The "arcs" are images containing the emission line spectrum of a discharge arc lamp, where spectral lines of very accurately know wavelength are very sharp and well-defined. These lines serve as known markers of wavelengths, allowing for precise calibration of the spectrum. The most commonly used arcs are He, ThAr, HgAr, ThNe.

Firstly, we need to access the line maps (or spectra) of the specific arc lamps of each instrument and diffraction grating containing the wavelength of each of the arc accurately measured lines in the laboratory. Next, in IRAF, through the *identify* task, we select a column/row (depending on the spectral direction on the CCD) of the spatial axis to visualize the spectrum of the selected arc. A relevant parameter is `nsum`, which indicates the number of adjacent columns/rows to sum along the spatial axis to smooth irregularities in the arcs and increase the SNR of the lines. This number should not be excessively high given the shape of the arcs. Then, we must identify each emission line in the spectrum one by one, which have positions ranging from 0 to R (with R being the maximum number of pixels along the spectral axis), comparing them with the maps and assigning them the corresponding wavelengths. A preliminary fit $\lambda = f(x)$ or $\lambda = f(y)$ i smade to assess the line identification and help with the assignment of of additional lines. When we have identified a sufficient number of lines in a column/row of the spatial axis, we use the *reidentify* task to extend the identification done with identify throughout the spatial axis. This is done because each of the emission lines from the arcs is not at the same position (pixel) along this axis but presents a curved emission similar to an arc, hence the name of these calibration files. In other words, the wavelenght depends both on x and y, λ=$f(x, y)$.

The number of lines to be initially identified with the 'identify' task depends on each observation; ideally, the greater the number of identified lines (N), the better the subsequent adjustment would be, although this is not always true in practice. Once the lines are identified across the spatial axis, we use the 'fitcoords' task to create functions, f(x, λ), that fit the positions of the emission lines with the assigned wavelengths in each row/column of the spatial axis. In the IRAF viewer, we can see the residuals of the fit between the function and the wavelengths of each emission line, and interactively modify both the type, splines, splines3, Lorentzian,..., and the order, n=1,2,3,..., inf, of the functions until reasonable fits are obtained. A fit could be considered reasonably good when the order of the function is not excessively high (i.e., the order is not equal to or similar to the number of identified lines N) and the resulting residuals have low rms. A practical way to test the required order is to visually check if the residuals are "disordered" (which is ideal) or, conversely, if they show any kind of trend, in which case the function needs a higher order to fit all the points. Another alternative to the manual line identification mentioned earlier is to download the corresponding file for each instrument containing all the wavelengths of the emission lines present in each spectral lamp. However, in practice, not all emission lines appearing in the files are always visible in the spectra of the arcs, either because they are very weak, because they are blended with other lines, etc., resulting in unavoidable errors in the function fit. Ideally, if multiple data reductions are performed, selecting the most reliable lines in a separate file would allow for automating the process without the risk of error. Finally, with the 'transform' task, the functions are applied to the object observation files to effectively apply the wavelength calibration to the source images.

2.1.5 Background subtraction

This step aims to remove all sky lines originating from the Earth's atmosphere from the spectra. The process is quite simple. Using the IRAF *background* task, we select a row/column of the spectral axis of the already calibrated 2D spectrum and adjust the parameters shown in section 2.1.3. By modifying these parameters, the background continuum and the sky lines should be adjusted. It is also necessary to review the fit for several rows/columns, not just those where there are sky lines, since the previous parameters are unique for the entire spectral axis, and the resulting function may not be optimal for all points. Sometimes, a compromise must be made between fitting and subsequently subtracting the sky lines to avoid subtracting relevant emission.

2.1.6 Flux calibration

The last step of the reduction process involves calibrating our 2D spectra, whose emission was previously indicated in counts, into flux. In this step, observations of known calibration stars or spectro-photometric standards are required, ideally taken during the same night or even better just before or after the observation of the source and at similar airmass. These are stars of whose spectra and flux values for the desired spectral range are precisely known. In the cases of observations of PNe, white dwarfs, hot subdwarfs or O and B stars are used. The idea is, knowing the observing conditions, to adjust a function to the star's spectrum in counts so that when passed to flux, we obtain the previously known spectrum and then apply this function to the source observed under the same sky conditions.

Prior to flux calibration, all previously explained calibrations must be applied to the calibration star files as well. Once calibrated to this point, a one-dimensional spectrum of the standard star must be extracted to capture **all** the emission of the 2D spectrum (which typically appears as a thick, continuous line in the spectral axis). For this, we can use the IRAF task *apsum*, which selects an aperture of the desired width from the 2D spectrum. Once the one-dimensional spectrum is extracted, a series of tasks must be applied to obtain the final calibration function. It is worth noting that these tasks are available in IRAF and are optimized for this purpose, but there are other software or even scripts from individuals that carry out the same process.

The first task is *standard*, which searches for the file with flux values of the calibration star spectrum within the integrated library in IRAF and displays the values of the points along the spectral range, that are included for each wavelength in the file, to save the relationship between the value in counts of the one-dimensional spectrum and the corresponding flux value. Ideally, the points at the ends of the one-dimensional spectrum and any absorptions that appear should be removed, as they introduce errors in the function fit. The next task is *sensfunction*, which takes the output file from the 'standard' task with the relationships of the selected points and creates a function that fits them. Like in previous tasks, this function is adjustable, and it should be modified so that the rms is optimal. Finally, the *calibrate* task applies the obtained function to the desired source, taking into account even the extinction in the direction of observation according to the observatory where the observation was made. These files are available in the observatories' archives.

2.2 Integral field spectroscopy reduction

Integral Field Spectroscopy (IFS) is an advanced technique that simultaneously captures spatial and spectral information from a source or field within a single observation. This approach allows to obtain a spectrum for every spatial element in the observed area, effectively producing a three-dimensional dataset that combines two spatial dimensions with one spectral dimension. The products is commonly know as data cube. IFS is conducted using an IFU, which can employ various technologies such as fiber bundles, lenslet arrays, or image slicers to dissect the incoming light into spectra while preserving spatial information. A schematic representation of how a IFU works is shown in the right-hand panel of Fig. 2.1 Although data cubes are not a new concept in the field of radio astronomy, where they have been in use for over 60 years, they are relatively new in the optical and more recently in the infrared domains. Therefore, there is not as much information available on handling this type of data (reduction and analysis) or the tools developed for it, leaving much room for improvement.

2.2.1 GTC-MEGARA instrument

The data cubes used in these thesis were obtained using MEGARA at GTC. The instrument is a fiber-fed spectrograph with both Integral-Field (IFU) and Multi-Object (MOS) capabilities. The IFU, called the large compact bundle (LCB), covers a field of view (FoV) of 12.5×11.3 arcsec^2, plus eight additional minibundles, located at the edge of the FoV, to provide simultaneous sky subtraction. The MOS assembly (which is not used in this thesis) can place up to 92 minibundles covering a target area per minibundle of 1.6 arcsec and a total coverage area on the sky of 3.5×3.5 arcmin^2. The spatial sampling in both modes is 0.62 arcsec per fibre[5].

Both the LCB and the MOS are located at the folded Cassegrain F (FC-F) focus of GTC. The 623 (567+56) fibers of the LCB and the 644 fibers of the 92 robotic positioners of the MOS are routed from the FC-F rotator to the Nasmyth A platform following a 44.5m-long path until they reach the MEGARA spectrograph. The spectrograph is an all-refractive system (with f/3 and f/1.5 focal ratios for collimator and camera, respectively) and includes a set of 18 volume

---

[5] This size corresponds to the diameter of the circle on which the hexagonal spaxel is inscribed.

phase holographic (VPH) gratings placed at the pupil in the collimated beam. These gratings offer three spectral modes with different resolving power, R, labelled as low resolution (LR), R(FWHM) = 6000; medium resolution (MR), R(FWHM) = 12000; and high resolution (HR), R(FWHM) = 20000.

2.2.2 Data reduction process

The basic data reduction process for MEGARA shares certain similarities with long slit data reduction, however, the methodology to follow is notably different. Such are the differences and complexity of the "operations" that it have been necessary to develope its own pipeline, `megaradrp`, based on the Python programming language. The data reduction process and steps to follow are extensively explained in the already published MEGARA cookbook. Here, a summary explaining the steps (or, if I may take the liberty, translating into mortal language) and the mode of work to follow the information present in the cookbook is presented, as well as pointing out some of the most common errors I have faced and for which there is no further information beyond pure experience.

2.2.2.1 Preliminary considerations and data organization

It is essential to have the `megaradrp` pipeline installed on the device where data reduction is to be carried out. The pipeline consists of 9 steps, although one step (the one performing lighting corrections) is not really necessary, in which similar correction effects are applied as in the reduction of long-slit spectra (albeit with technical and specific differences). During the execution of steps 1 to 5, the output files are strictly necessary for continuing the reduction process and do not allow room for error. The output files or products obtained after each step can be divided into three types. These are:

- Full-frame FITS image products:
    - **master_bias.fits**: Final image of the MasterBiasImage recipe.
    - **reduced_image.fits**: Final image after all individual exposures have been processed and combined.
- Raw-Stacked Spectra (RSS) FITS image products:
    - **master_fiberflat.fits**: Image to be applied to correct for variations in sensitivity between fibers and from blue-to-red within each fiber.
    - **reduced_rss.fits**: Processed image prior to the subtraction of the sky spectrum.
    - **sky_rss.fits: RSS** image showing signal only in the valid sky fibers. All other pixels are set to zero.
    - **final_rss.fits**: Processed image after the subtraction of the sky spectrum is performed.
- Structure products:

  - **master_wlcalib.json** (MegaraArcCalibration): File with the information on the wavelength calibration solution for every fiber.
  - **master_traces.json** (MasterTraceMap): File with the tracing information.
  - **master_model.json** (MasterModelMap): File with the information on how to account for the cross-talk[6] between adjacent fibers in the detector.

In addition to the above, it should be noted that the pipeline is designed to work under a specific data organization and with specific directory names. The directory where the reduction is to be carried out must contain a folder named `MEGARA` along with a control file named *control.yaml*, necessary to run the pipeline and in which the path to the directory containing `MEGARA` must be included.

```
Reduction_directory
├── MEGARA
│   └── ca3558e3-e50d-4bbc-86bd-da50a0998a48
├── control.yaml
├── Target1
└── Target2
```

As shown in the tree structure above, under the `MEGARA` directory, the directory `ca3558e3-e50d-4bbc-86bd-da50a0998a48` must be included, in which the calibration products to be used for each recipe (step) must be included in the corresponding directory. This refers to what was mentioned earlier that it is necessary to obtain these calibration products in order to continue the reduction; otherwise, the pipeline will fail. The organization of this directory for an observation carried out, for instance with a VPH-HR-R, must be: would be:

```
│   LinesCatalog
│   ├── ThAr
│   │   └── HR-R
│   │       └── HR-R_ThAr.lis
│   └── ThNe
│       └── HR-R
│           └── HR-R_ThNe.lis
├── MasterBPM
│   └── masterbpm.fits
├── MasterBias
│   └── masterbias.fits
├── MasterFiberFlat
│   └── LCB
│       ├── HR-R
│       │   ├── master_fiberflat.fits
│       │   └── MOS
│       └── HR-R
│           └── master_fiberflat.fits
└── MasterSensitivity
    └── LCB
        └── HR-R
            └── master_sensitivity.fits
```

---

[6] "Cross-talk" refers to the unwanted transfer of electronic signals between adjacent fibers in the spectrograph.

```
    MOS
        HR-R
            master_sensitivity.fits
MasterSlitFlat
MasterTwilightFlat
ModelMap
    LCB
        HR-R
            master_model.json
    MOS
        HR-R
            master_model.json
TraceMap
    LCB
        HR-R
            master_traces.json
    MOS
HR-R
    master_traces.json
WavelenghtCalibration
    LCB
        HR-R
            master_wlcalib.json
    MOS
        HR-R
            master_wlcalib.json
```

It is only necessary to fill one of the directories corresponding to the selected mode of observation, LCB or MOS.

The directories corresponding to the targets must contain the files of the recipes for each step of the reduction. In addition, a folder necessarily named `data` which contains all the calibrations and target observation files must be included in the same directory as the recipes. An example would be:

```
Reduction_directory
├── ...
├── Target1
│   ├── 0_bias.yaml
│   ├── 2_modelmap.yaml
│   ├── 3_wavecalib.yaml
│   ├── 4_fiberflat.yaml
│   ├── 5_twilight.yaml
│   ├── 6_Lcbadquisition.yaml
│   ├── 7_Standardstar.yaml
│   ├── 8_reduce_LCB.yaml
│   └── data
│       ├── 0001251794-20170626-MEGARA-MegaraLCBImage.fits
│       ├── 0001251795-20170626-MEGARA-MegaraLCBImage.fits
│       ├── 0001251796-20170626-MEGARA-MegaraLCBImage.fits
│       └── ...
└── Target2
    ├── 0_bias.yaml
    ├── 1_tracemap.yaml
    ├── 2_modelmap.yaml
    ├── 3_wavecalib.yaml
    ├── 4_fiberflat.yaml
    ├── 5_twilight.yaml
    ├── 6_Lcbadquisition.yaml
    ├── 7_Standardstar.yaml
    ├── 8_reduce_LCB.yaml
    └── data
        ├── 0001287845-20170730-MEGARA-MegaraLcbImage.fits
        ├── 0001287846-20170730-MEGARA-MegaraLcbImage.fits
        ├── 0001287847-20170730-MEGARA-MegaraLcbImage.fits
        └── ...
```

The recipe files must contain the ID of the VPH used and the names of the corresponding observed calibration files. Additionally, each recipe also has a series of commands that allow for some flexibility during its execution. Both the workflow structure and the execution recipes for the pipeline can be downloaded from the links available in the MEGARA cookbook.

It should be mention that execution of the pipeline is carried out using the `numina` package, which is installed alongside `megaradrp`, and is performed directly from the terminal. For instance, the pipeline recipe for the bias subtraction is executed as follows:

```
(megara) bash-3.2$ numina run 0_bias.yaml -r ../control.yaml
```

The final products are stored in the directory `obsid0_bias_result/` while the files used are stored in `obsid0_bias_work/`.

```
│ obsid0_bias_work/
│  ├─ 0001310880-20170827-MEGARA-MegaraBiasImage.fits
│  ├─ 0001310881-20170827-MEGARA-MegaraBiasImage.fits
│  ├─ 0001310882-20170827-MEGARA-MegaraBiasImage.fits
│  ├─ 0001310883-20170827-MEGARA-MegaraBiasImage.fits
│  ├─ 0001310884-20170827-MEGARA-MegaraBiasImage.fits
│  ├─ 0001310885-20170827-MEGARA-MegaraBiasImage.fits
│  ├─ 0001310886-20170827-MEGARA-MegaraBiasImage.fits
│  ├─ 0001310887-20170827-MEGARA-MegaraBiasImage.fits
│  ├─ 0001310888-20170827-MEGARA-MegaraBiasImage.fits
│  ├─ index.pkl
│  └─ master_bpm.fits
└─ obsid0_bias_results/
   ├─ master_bias.fits
   ├─ processing.log
   ├─ result.yaml
   └─ task.yaml
```

After each step the final product file must be placed in their respective folders within the `ca3558e3-e50d-4bbc-86bd-da50a0998a48` directory previously mentioned.

2.2.2.2 Bias subtraction

An average bias image named *master_bias.fits* is obtained, considering the file *masterbpm.fits* included in the downloadable workflow structure, which contains a map of bad spaxels. In the case of the MEGARA CCD (a 4k x 4k pixels CCD231-84 E2V chip), since the detector is always read using two diagonally-opposed amplifiers (to speed up the reading process while minimizing electronic cross-talk), the bias is slightly different in the upper and bottom halves of the image.

The dark current in MEGARA have proved to be negligible even for very long-exposure times. Therefore in the reduction proccess dark images are neither needed nor used. This is also the case for slit flat correction (pixel-to-pixel response). Though have been tested to have no impact this correction is implemented in the `megara drp`.

2.2.2.3 Tracing fibers

Tracing fibers (Trace Map): The subsequent processing step combines a sequence of fiber-flats to create a master "trace map". These fiber-flats are acquired by illuminating the instrument focal plane with a continuum (halogen) lamp. This step generates the necessary tracing information for extracting the flux of the fibers. The output is saved in a file named *master_traces.json* within the result directory.

The position of the fibers traces at the detector are shifted depending on the ambient temperature so if a continuum halogen near in time to the target observation was acquired, the traces will likely appear shifted. To verify this one can visualize the *reduce_image.fits* alongside the fiber traces in the file ds9_raw.reg (in the *work*) and ensure that each trace passes through the center of the fiber. If the traces deviate from the fiber, appear only partially, or exhibit similar anomalies, it may indicate that the VPHs for the halogen lamps is not the same as for the target. These calibration files are automatically obtained in observations, and it is possible that the astronomer includes those corresponding to another observation from the same night. Requesting the correct calibration files resolves this issue easily. In the work case that the halogen lamps have been observed far in time to the target observations, it is recommended to repeat the observation requesting extreme care in this step. Although it is not advisable, a halogen of adjacent nights with similar ambient temperature could be used. Another more challenging problem arises with VPHs towards the blue end of the spectrum since MEGARA does not perform well in these spectral ranges, resulting in curved traces that completely deviate from the fibers. Currently, efforts are underway to address this issue.

Tracing fibers (Model Map): This process involves analyzing a series of continuum flat images acquired in either Trace Map or Fiber Flat modes to generate essential fiber profile data necessary for advanced fiber extraction in subsequent steps. It is important to note that this processing step may take several minutes (ranging from 10 to 40 minutes) depending on the hardware specifications. The images undergo similar processing as in the Trace Map recipe. In this case, the approximate central positions of the fibers are derived from the previously computed *master_traces.json* file. Subsequently, for every 100 columns of the reduced image, a vertical cut is made, and the image is fitted to a sum of fiber profiles. Each profile consists of a Gaussian function convolved with a square function. Once the fitting process is completed for all columns, the profiles' central positions and standard deviations (sigma) are interpolated to cover all columns using splines. The resulting spline coefficients are then stored in the final *master_model.json* file. Checks and potential errors during this step are similar to those encountered in the preceding process.

2.2.2.4 Wavelength Calibration

In this step, wavelength calibration solutions for each fiber are obtained from the arc-lamp spectra. Before executing the recipe, it's crucial to ensure that the traces (regions in *ds9_raw.reg*) align with the center of the arc emission in each fiber. If the traces deviate by a certain number of pixels, it's necessary to include this shift in the recipe file under the parameter *extraction_offset*. If the traces appear above the fiber in the raw image, the offset is represented as a negative number measured in pixels. Conversely, if the traces are below the fiber, the offset is represented as a positive number.

2.2.2.5 Flat-field and ilumination correction

As mentioned earlier, obtaining a flat-field to correct the pixel-to-pixel response is not strictly necessary, although it is always recommended. This process generates the *master_fiberflat.fits* file.

The ilumination corrections step is optional and in most cases does not need to be applied. In fact, it has not been applied in any of the data used for this thesis, so we will not delve into any explanation regarding it.

2.2.2.6 Flux calibration

Flux calibration (Acquisition): The flux calibration is conducted by observing one or several spectrophotometric stars using the same instrument configuration as for the scientific observations. Depending on the number of stars observed and atmospheric conditions, we can perform either an absolute or relative flux calibration (see cookbook for more details). To ensure the recovery of the entire flux of the spectrophotometric standard star, the LCB IFU bundle must be utilized. The recipe employed here aims to process and extract the spectra in the standard star observation while determining the centroid position of the target in the LCB field of view. This centroid serves as a reference around which the total flux of the star will later be recovered. Similar to the wavelength calibration, we must calculate the shift between the fiber emissions and the traces following the same procedure and include the result in the parameter *extraction_ offset* in the recipe file. Upon executing this recipe, an intermediate file named *reduce_ rss.fits* is generated, containing 2D images of the observation with all preceding calibrations applied. Subsequently, sky subtraction is performed by combining the signals from 56 fibers dedicated to this purpose in LCB mode, resulting in the final file *final_ rss.fits*. Next, centroids around the field center and the brightest spaxel are calculated using the signal from the 3 rings of fibers (totaling 37 fibers) surrounding these two spaxels. The displacements necessary to center the object in the LCB field center are returned in both millimeters and arcseconds.

Flux calibration (Standard): These centroid offsets (typically used in mm) are crucial for recovering all the flux from the standard star and deriving the instrument sensitivity curve for a specific setup using the recipe designed for this step (via the *position* parameter). Once again, the *extraction_ offset* needs to be incorporated, as in the previous step. The final product of this stage is the file *master_ sensitivity.fits*.

It should be noted that using this file to calibrate our target is optional, and if desired, flux calibration could be performed manually. In such a case, both steps must still be executed in the same manner, but one would simply proceed with the *final_ rss.fits* file. This "_rss.fits" file needs to be converted into a cube format (3D), as will be indicated in a section below, and subjected to a calibration analogous to that described for long-slit spectra. The one-dimensional spectrum in this case would be obtained by selecting and summing all pixels within a region capturing the entire star emission, while the rest of the calibration process remains identical.

2.2.2.7 Scientific calibraction

The final step of the pipeline simply involves applying all the previous calibrations to the observation files of our target object. The resulting data is saved in the file *final_ rss.fits*.

It's important to note that this file is still in 2D format, and it still needs to be converted into a cube. There are several methods available for this conversion.

2.2.3 From 2D rss file to 3D data cube

The final product of the MEGARA pipeline is either a final_rss.fits or reduce_rss.fits file, with or without sky subtraction, respectively. Each file is a 2D image where each row represents a single fiber and the columns represent the spectral axis. This still needs to be converted into a 3D data cube.

The process is conceptually simple. Each fiber has spatial information (its position in the sky) and spectral information. Remember, each fiber is placed in a hexagonal spaxel of about 0.6 arcsec. First, each of the fibers is placed in its corresponding position on a 2D grid while transforming the hexagonal spaxel into square pixels. The flux within the spaxel is distributed among the corresponding pixels, whose size is a free parameter for the person performing the reduction. It is recommended that the pixel size not be less than 0.2 arcsec^2 and obviously never greater than 0.6 arcsec$^{\mathbf{2}}$. The size of the 2D grid is in principle a free parameter, but this is often already set by the transformation tools that we will mention next. Once the spaxles are placed, all that remains is to fill the gaps between fibers within the FoV. This is done through simple interpolation. The final product would be a 3D data cube with spatial information on the (x,y) axes and spectral information on the (z) axis.

One can carry out this process oneself, but it is useful to know that there are already several tools or routines focused on transforming the _rss.fits files from the MEGARA pipeline. The megaradrp package itself already has a tool for this, megaradrp-cube. There are also other options external to the pipeline. The most widely used is the one developed by Javier Zaragoza Cardiel from INAOE, which can be obtained through GitHub at this link.

Both approaches are straightforward and easy to use, producing nearly identical cubes if the same parameters are selected. The main difference lies in the size of the cubes: the pipeline produces cubes of size 4300×62×68, whereas Zaragoza's routine generates cubes of size 4300×52×58. This discrepancy arises from data processing, but the flux and emission values for each pixel are equivalent.

Chapter 3

Chemistry and physical properties of the born-again planetary nebula HuBi 1

Chapter based on the article published in Monthly Notices of the Royal Astronomical Society Astrophysics by Montoro-Molina B., Guerrero M. A., Pérez-Díaz B., Toalá J. A., Cazzoli S., Miller Bertolami M. M., Morisset C. in 2022 volume 512, 4003. doi:10.1093/mnras/stac336

Abstract

The central star of the PN HuBi 1 has been recently proposed to have experienced a VLTP, but the dilution of the emission of the recent ejecta by that of the surrounding H-rich old outer shell has so far hindered confirming its suspected H-poor nature. We present here an analysis of the optical properties of the ejecta in the innermost regions of HuBi 1 using MEGARA high-dispersion integral field and OSIRIS intermediate-dispersion long-slit spectroscopic observations obtained with the 10.4m Gran Telescopio de Canarias. The unprecedented tomographic capability of MEGARA to resolve structures in velocity space allowed us to disentangle for the first time the Hα and Hβ emission of the recent ejecta from that of the outer shell. The recent ejecta is found to have much higher extinction than the outer shell, implying the presence of large amounts of dust. The spatial distribution of the emission from the ejecta and the locus of key line ratios in diagnostic diagrams probe the shock excitation of the inner ejecta in HuBi 1, in stark contrast with the photoionization nature of the H-rich outer shell. The abundances of the recent ejecta have been computed using the MAPPINGS V code under a shock scenario. They are found to be consistent with a born-again ejection scenario experienced by the progenitor star, which is thus firmly confirmed as a new “born-again” star.

3.1 Introduction

HuBi 1 has been one of the latest PN to be proposed to belong to the class of born-again PNe (Guerrero et al. 2018). This object has been gaining attention over the years, demonstrating to have a unique late evolutionary behaviour. Hu & Bibo (1990) noticed it to be a low-excitation PN whose CSPN, the bright IR source IRAS 17514−1555, has a late [WC] spectral type. According to Pollacco & Hill (1994), this PN consists of a faint extended low-density outer shell with typical PN abundances and an unresolved inner shell with apparent bipolar structure[1]. Discrepancies between the observed electron density (n_e $\lesssim$1000 cm^{-3}) and that much higher expected for a nebula around a late [WC] CSPN led Peña et al. (2001) to propose either a born-again scenario for HuBi 1 or the slow evolution of a low-mass AGB star. The chemical abundances derived at that time (Pollacco & Hill 1994; Peña 2005) were somehow similar to that of typical Galactic PNe, although the bright He I λ5876 emission line suggested a large He/H abundance ratio. On the other hand, the low effective temperature T_eff $\simeq$35,000 K of the CSPN (Leuenhagen & Hamann 1998) rather supported the latter scenario (Peña 2005).

It has not been until recently that the born-again scenario in HuBi 1 has gained momentum. Guerrero et al. (2018) noticed a decrease in the CSPN brightness $\simeq$10 mag in the last 46 yr that was attributed to a circumstellar veil of C-rich dust suggested by the presence of numerous carbon lines in the optical spectrum of the CSPN (Pollacco & Hill 1994) and by the strong IR emission (Hu & Bibo 1990). Such C-rich material would have been ejected through a VLTP event and, as it expands and cools down, reaches optimal conditions for its condensation on dust grains (e.g., Perea-Calderón et al. 2009).

Guerrero et al. (2018) proposed that the decreasing ionizing flux of the CSPN causes the recombination of the outer shell, whereas the detection of He II emission from the inner shell and its atypical inverted ionisation structure, with He II emission embracing the emission of [O III] and [N II], rather suggest it is shock-heated. Indeed, the detection of material expanding up to $\simeq$300 km s^{-1} in the innermost region of HuBi 1 (Rechy-García et al. 2020) lend strong support to the shock excitation of this region by a recent ejecta.

The most convincing evidence to fully declare HuBi 1 to be part of the class of born-again PNe would come from the chemical abundances of the recent ejecta, since noticeable abundances discrepancies are expected in a born-again event. H-poor material and enhanced C, N and O abundances would be present in the most recent ejecta produced by the VLTP (Miller Bertolami et al. 2006) with the outer nebula exhibiting “normal” PNe abundances. However, Peña et al. (2021) have recently reported no abundances differences between the inner and outer shells of HuBi 1, in accordance with previous studies. These results ought to be questioned as they are based on the assumption of the photoionisation of the inner shell, which does not seem to be the case given the evidence for shock excitation. Most importantly, since these authors did not remove the contamination of the bright H Balmer emission lines from the outer shell to the inner shell, their analysis of its spectrum can be expected to artificially enhance its H content.

---

[1] Pollacco & Hill (1994) also reported an extremely high density for this inner shell, but it resulted from the contamination of the density sensitive [S II] $\lambda\lambda$6716,6731 doublet by stellar C II emission lines.

In this chapter we combine optical high-dispersion integral field spectroscopy (IFS) and intermediate-dispersion long-slit spectroscopic observations of HuBi 1 to isolate the emissions of its inner and outer shells in order to determine the H, He, N, and O abundances of the inner shell. The observations and data reduction are presented in Section 3.2. The data analysis is discussed in Section 3.3, where two appendices are presented in order (i) to assess the contribution of the emission from the outer shell to the emission of the inner shell, and (ii) to correct the effects of the atmospheric differential chromatic refraction that affects the long-slit spectroscopic observations[2]. The results are presented in Section 3.4, including maps of extinction and electron density of the inner shell, the assessment of the importance of shocks and ultimately the calculation of the chemical abundances. Finally, the discussion and summary are provided in Sections 3.5 and 3.6, respectively.

3.2 Observations and data reduction

3.2.1 GTC MEGARA IFS observations

IFS observations of HuBi 1 were obtained on 2020 August 6 (Program ID GTC96-20A, PI Guerrero) using MEGARA (Pascual et al. 2019) at the 10.4 m GTC. The HR-VPH grism VPH665 and the medium-resolution MR-VPH grism VPH481 were used.

The observations consisted of three 900 s HR-VPH and six 1000 s MR-VPH exposures obtained under optimal transparency conditions and excellent seeing 0.8 arcsec as measured at the DIMM station. The VPH665 grism provides a spectral dispersion of 0.093 Å pix^{-1} and a full-width at half-maximum (FWHM) spectral resolution $\approx$ 15 km s^{-1}, that is, $R \approx$ 20050, while the VPH481 grism provides a spectral dispersion of 0.105 Å pix^{-1} and FWHM spectral resolution $\approx$ 23 km s^{-1}, i. e., $R \approx$ 13200. The spectral ranges 4585.7–5025.1 Å and 6405.6–6797.1 Å covered by these two VPHs contain the key emission lines of He II λ4686 Å, Hβ, [O III] $\lambda\lambda$4959, 5007 Å, [N II] $\lambda\lambda$6548, 6584 Å, Hα, He I λ6678 Å, and [S II] $\lambda\lambda$6716, 6730 Å. The IFU mode was used. It has 567 hexagonal spaxels with a diameter of 0.62 and a FoV of 12.5×11.3 arcsec^2, as shown in Figure 3.1.

The raw MEGARA data were reduced following the Data Reduction Cookbook (Pascual et al. 2019) using the *megaradrp* v0.10.1 pipeline released on 2019 June 29. This pipeline applies sky and bias subtraction, flat-field correction using halogen internal lamps, wavelength calibration, and spectra tracing and extraction. We note that there is an appreciable illumination pattern making brighter the East and West edges of the FoV, which reduced the cube useful FoV to a region 11.3×11.3 arcsec^2 in size. The result is a row-stacked spectrum, which is converted into a 52×58 map of 0.2 arcsec square spaxel on spatial dimension and 4300 spaxel on spectral axis using the regularization grid task *megararss2cube*. The flux calibrations were performed using observations of the spectro-photometric standard HR 7596 obtained immediately after those of HuBi 1.

---

[2] Peña et al. (2021) used the same long-slit spectroscopic data set presented here, but did not apply any correction for atmospheric differential chromatic refraction. The correction of these effects will be shown to be essential for an appropriate determination of the physical properties and chemical abundances of the inner shell of HuBi 1.

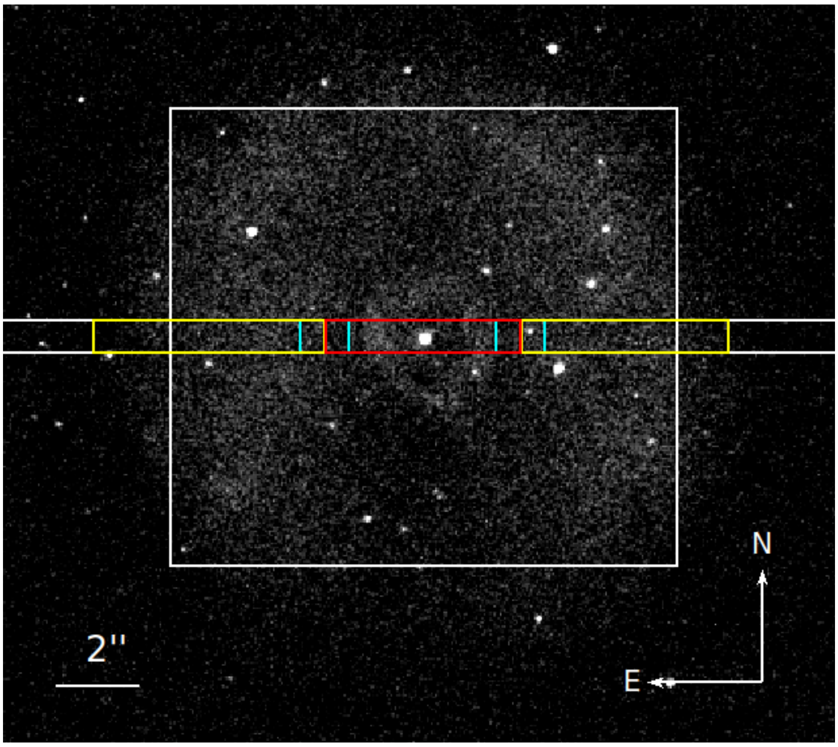

Figure 3.1: *HST* WFPC2 F656N image of HuBi 1. The positions of the 12.5×11.3 arcsec^2 FoV of MEGARA's IFU and the 0.8 arcsec-width OSIRIS long-slit are overlaid using white lines lines. This *HST* image reveals clearly the position of background stars included in the apertures of these instruments. The apertures used for extraction of 1D spectra in the OSIRIS data for the inner and outer regions, and from an additional intermediate region are overlaid in red, yellow, and cyan lines, respectively.

3.2.2 GTC OSIRIS long-slit spectroscopic observations

Intermediate resolution long-slit spectroscopy was acquired on 2018 May 14 (Program ID GTC112-18A, PI Guerrero) with OSIRIS[3] at the GTC. The observation consisted of 4 exposure of 1575 s on long-slit spectroscopy mode. The R1000B grism was used, providing a spectral dispersion of 2.12 Å pix^{-1} in the spectral range 3630–7500 Å at a spectral resolution $R \approx 1120$. The slit position was placed at a position angle (PA) 90° across the central star (see Fig. 3.1).

The raw data were bias and sky subtracted and flat-field corrected following standard routines in IRAF (Tody 1993). The wavelength calibration was carried out using Ne and HgAr lamps, whereas the flux calibration was obtained using observations of the spectro-photometric standard star GD 140 obtained in the same night.

The relative flux calibration of the GTC MEGARA and OSIRIS data was checked by comparing the flux of a number of bright emission lines measured from identical spatial apertures in both data sets. These fluxes were found to agree within a few percent.

---

[3] http://www.gtc.iac.es/instruments/osiris/media/OSIRIS-USER-MANUAL_v3_1.pdf

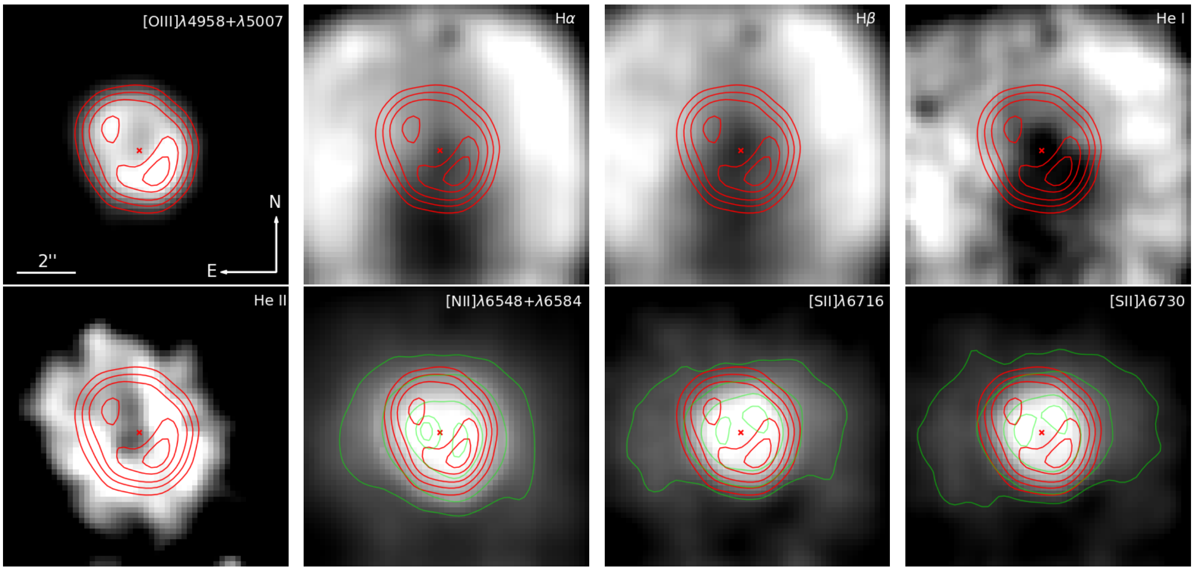

Figure 3.2: GTC MEGARA maps of HuBi 1 in different emission lines. From left to right, the panels represent the maps of [O III] λλ4959,5007 Å, Hα, Hβ, and He I λ6678 Å (top), and He II λ4686 Å, [N II] λλ6548,6584 Å, [S II] λ6716 Å, and [S II] λ6730 Å (bottom). To facilitate the comparison among the different images, red contours extracted from the [O III] image tracing the inner shell are overlaid on all images. Green contours are also overlaid in the [N II] and [S II] images to emphasise the emission from these lines from an intermediate region external to the inner shell. The red contours have been selected at 66%, 55%, 44%, 33%, and 22% of the [O III] brightness peak, whereas the green contours have been selected at 75%, 70%, 55%, 25%, and 15% of the [N II] brightness peak, and 95%, 80%, 55%, and 40%, of the [S II] brightness peak.

3.3 Data Analysis

The OSIRIS long-slit spectra and MEGARA IFS observations provide a wealth of information on the spatially-resolved spectral properties of HuBi 1 that has allowed us to investigate the ionisation structure and extract clean spectra of its inner shell. These are described in the next sections.

3.3.1 The inverted ionisation structure of HuBi 1

The final MEGARA data cube allows the extraction of background-subtracted narrow-band images in emission lines of interest, thus providing great versatility to investigate the complex structure of HuBi 1. The data analysis method is as simple as selecting appropriate ranges of spectral channels encompassing an emission line to build a background-subtracted narrow-band image of that emission line.

The images of the total integrated flux of key emission lines extracted from the MEGARA data presented in Figure 3.2 confirm the remarkable inverted ionisation structure of HuBi 1.

The leftmost-top panel of Figure 3.2 presents the [O III] emission, which was obtained by adding the [O III] 4959 Å and [O III] 5007 Å emission lines to improve the signal-to-noise ratio (SNR). This emission has a ring-like appearance with an averaged extension of ∼2.5 arcsec in radius. The emission is elongated along the NE direction, with brighter emission at the tips, as shown by the [O III] contours overplotted. The [O III] emission lines uniquely trace the inner region of HuBi 1 and thus [O III] contours will be overplotted on the other key emission line maps of Figure 3.2 for comparison.

The images in the Hα, Hβ and He I 6678 Å emission lines in Figure 3.2, on the other hand, trace the outer nebular shell of HuBi 1. Unfortunately, the MEGARA FoV does not cover the full extent of this shell, which has an averaged diameter of ∼15 arcsec. The inner shell of HuBi 1 shown by the red [O III] contours is encompassed by the emission in the Hα, Hβ and He I lines. It is not possible, however, to assess whether the inner shell emits in these emission lines or whether the emission detected inside the [O III] contours of the inner shell in these images is rather due to projection effects.

Maps of the low-ionisation [N II] and [S II] emission lines are also presented in Figure 3.2, where green contours have been used to highlight the distribution and extent of their emission. The bulk of the emission in these low-ionisation lines is confined within the red [O III] contours that define the inner shell, with two peaks separated by ∼1.5 arcsec aligned mostly along the East-West direction, i.e. they are clearly misaligned with the peaks in the [O III] image. These images also reveal the presence of an intermediate region[4] spreading out ∼4 arcsec the emission of the inner shell into the outer shell along the East-West direction.

Finally, the leftmost-bottom panel of Figure 3.2 shows the spatial distribution of the emission in the line of He II λ4686 Å, the one with the highest ionisation potential in the nebular spectrum of HuBi 1. The emission from the inner shell in this emission line is the most extended, with an angular radius of ∼4×3 arcsec oriented along a PA similar to that of the emission in the [O III] lines. The He II emission encircles that of the [O III], which surrounds that of the [N II] and [S II] emission lines. The inverted ionisation structure of the inner shell of HuBi 1, suggested originally by Guerrero et al. (2018) using 1D line emission spatial profiles, is therefore firmly confirmed in the MEGARA 2D emission maps shown in Figure 3.2.

3.3.2 Dissecting the inner shell of HuBi 1 with MEGARA

The emission of the inner shell of HuBi 1 in the images presented in Figure 3.2 would generally include a contribution from the outer shell, as the former is seen through the latter. The emission from the different shells of HuBi 1 can be kinematically separated given their distinct expansion velocities (Guerrero et al. 2018; Rechy-García et al. 2020; Peña et al. 2021) taking advantage of the MEGARA IFS high spectral resolution, although the quality (and reliability) of the kinematic separation of the emission from the two shells in a given emission line would depend certainly on the spatio-kinematic distribution of that line. A detailed description of the different types of lines according to the varying relative contributions of the different structures of HuBi 1 in each emission line is given in Appendix A.1. These are briefly discussed in the following.

---

[4] Here the emission from the [N II] λ6548 Å and [N II] λ6584 Å emission lines has been added to enhance the weak emission from the intermediate region, whereas the [S II] lines are presented separately because the smaller intensity contrast of the emission from the inner shell and intermediate region allows an easier view of the latter.

First, the images of the [O III] and He II emission lines can be attributed purely to emission from the inner nebula. We will refer to them as purely internal (PI; see Appendix A.1) emission lines. On the other hand, the emission of He I arises uniquely from the outer shell and this will accordingly be referred as a purely external (PE; see Appendix A.1) emission line.

There are then a number of emission lines whose images definitely include emission from both the inner and outer shells. The images of the emission from the [N II] and [S II] lines is mostly dominated by the emission from the inner shell, but there is a non-negligible contribution of emission arising from regions outside the inner shell. These lines are thus referred as internal lines with emission from the external shell (IwE; see Appendix A.1). We note that the spatial distribution of the outer emission in these lines do not follow the shell-like morphology of the emission in the Hβ, Hα and He I emission lines, but it is rather spread between the inner and outer shells in a sort of intermediate region. The spatio-kinematic distribution of the emission in these lines from this intermediate region does not allow a clear separation from the emission of the inner shell (see discussion section in Toalá et al. 2021b).

Finally, the emission of the Hβ and Hα Balmer lines in the spectral range covered by the MEGARA observations are dominated by the outer shell emission, but the emission from the inner shell can be still kinematically resolved. These lines are referred in Appendix A.1 as external lines with inner emission (EwI). Assessing the specific Hα and Hβ fluxes of the inner and external shells will help us accurately unveil the extinction contribution and abundances for each shell. The emission from the inner shell in these two emission lines will be extracted applying two different methods in the next two subsections.

3.3.2.1 High-velocity component isolation in the Hβ and Hα emission

The inner shell of HuBi 1 can be described as a fast expanding shell-like structure or outflow with expansion velocities up to $\simeq$300 km s^{-1}, well exceeding that of the outer shell $\lesssim$50 km s^{-1} (Rechy-García et al. 2020). The high-velocity emission from the inner shell is indeed revealed as red and blue wings in the Hβ and Hα line profiles in the velocity ranges from -14 to $+20$ km s^{-1} and $+108$ to $+122$ km s^{-1} for Hβ, and from -96 to $+11$ km s^{-1} and $+109$ to $+171$ km s^{-1} for Hα. The differences in the velocity ranges of the wings of Hα and Hβ can be attributed to the larger SNR of the former emission line.

The spectral channels of the MEGARA data cube corresponding to the velocity intervals described above have been added to obtain the images of the inner shell in these emission lines shown in the top panels of Figure 3.3. The Hα map (top-left panel of Fig. 3.3) is notably less noisy than the Hβ one (top-right panel of Fig. 3.3) due to the better spectral resolution of the HR-VPH and higher SNR of the Hα line. The emission in this Hα map is closely inscribed within the emission of the inner shell represented by the red contours extracted from the [O III] image (leftmost-top panel of Fig. 3.2). Both the Hα and Hβ maps peak at the Southwest tip of the inner shell, as it does the [O III] emission from the inner shell. Total integrated fluxes of 8.1×10^{-15} erg cm^{-2} s^{-1} in Hα and 4.8×10^{-16} erg cm^{-2} s^{-1} in Hβ were derived adding the flux in all pixels within a circular area 2.5 arcsec in radius.

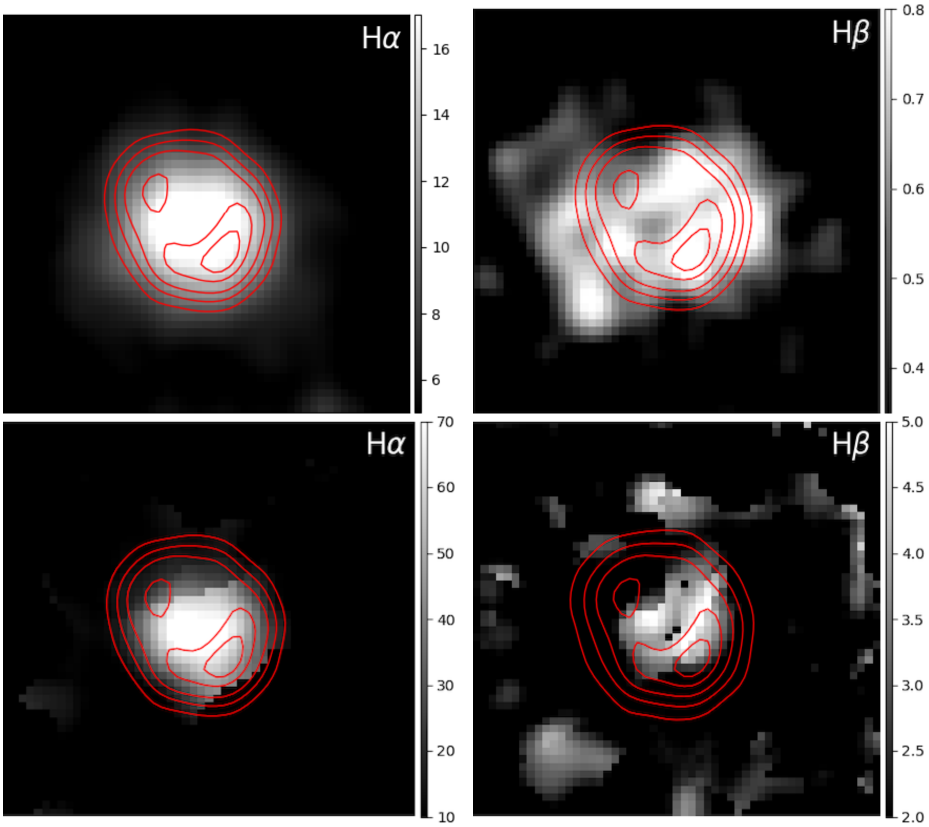

Figure 3.3: GTC MEGARA Hα and Hβ images of the inner region of HuBi 1 corresponding to the high-velocity components in these emission lines as derived from the isolation of the MEGARA channels within a velocity interval (top panels, see Sec. 3.3.2.1) and from the best multi-Gaussian fits (bottom panels, see Sec. 3.3.2.2). The extent of the inner shell is shown for comparison using the red contours derived from the [O III] image in Figure 3.2. The side scale shows the surface brightness in units of 10^{-17} erg cm^{-2} s^{-1} arcsec^{-2}.

3.3.2.2 Multi-Gaussian fit to the Hα and Hβ emission lines

Although the method described in Sec. 3.3.2.1 has proven effective to isolate the emissions of the Hα and Hβ lines from the inner shell and to estimate their fluxes, it has some shortcomings. In particular, the selection of the spectral channels (or velocity intervals) mapping the emission of the inner shell is affected by the differing spectral resolution and SNR of the Hβ and Hα lines. As a result, the Hβ map is derived from a velocity interval shorter than that of the Hα map, which may have effects on the Hα/Hβ ratio and on the estimate of the logarithmic extinction coefficient c(Hβ) of the inner shell based on that ratio. Moreover, the channels corresponding to the low-velocity tail of the emission from the inner shell had to be discarded because they were actually dominated by emission from the much brighter outer shell, which may lead to an underestimation of the flux from the inner shell. We remind the reader that one of the main objectives of this work is the determination of the Hα (or Hβ) flux to assess whether the chemical abundances of the inner shell of HuBi 1 are consistent with those of a born-again nebula. It is thus critical to obtain reliable values of the Hβ and Hα fluxes for the inner shell.

Therefore we have explored the determination of these fluxes using multi-Gaussian fits at

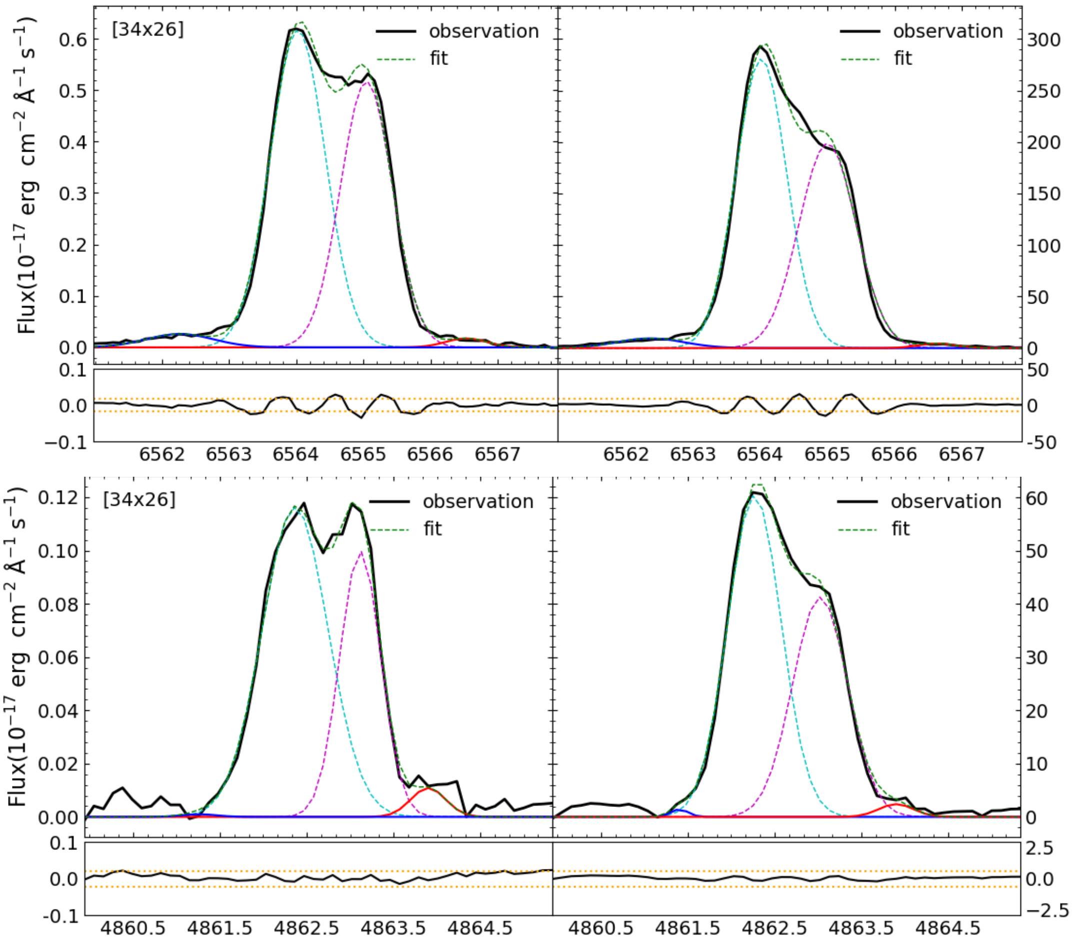

Figure 3.4: Examples of Hα (top) and Hβ (bottom) multi-Gaussian fits (*left*) for the spectrum of the pixel (34,26), which is offset 1.3 arcsec along PA 285° from the centre at pixel (28,25), and (*right*) for the integrated spectrum of the inner shell, extracted from a circular aperture 2.6 arcsec in radius. The solid black line corresponds to the observed line profile, whereas the green dotted lines represents the multi-Gaussian fit to this profile. The blue, cyan, magenta, and red solid lines correspond to the individual Gaussian components for the fast approaching component of the inner shell, the approaching and receding sides of the outer shell, and the fast receding component of the inner shell, respectively. The bottom panels show the residuals of the fit in solid black lines, whereas the dotted horizontal orange lines correspond to 3σ of the continuum noise derived from representative spectral ranges at both sides of the Hα and Hβ lines, respectively.

each pixel onto the inner shell of HuBi 1 to excise the emission of the dominant outer shell from that of the inner shell (see a similar approach in the case of M 2-31, Rechy-García et al. 2021). As described above, this is possible because the inner shell of HuBi 1 has a much larger expansion velocity than the outer shell (Rechy-García et al. 2020). The distinct kinematic behavior of the inner and outer shells reflects in the spectral profiles of the Hα and Hβ emission lines at the location of the inner shell (approximately the innermost 2.5 arcsec in radius central region), where up to four velocity components can be found; two from the main nebula with slow velocity (one approaching and one moving away) and another two from the inner shell that are detected as high-velocity red and blue wings.

An example of multi-Gaussian fits to the Hα and Hβ emission lines for a pair of pixels projected onto the inner shell[5] is shown in Figure 3.4. These are overplotted with the best multi-Gaussian fits revealing the presence of weak red and blue wings corresponding to the inner shell. The small flux contribution from these components might have escaped the previous determination of the Hα and Hβ fluxes. After applying this method to all pixels, the resulting total flux is 1.6×10^{-14} erg cm^{-2} s^{-1} in Hα and 1.1×10^{-15} erg cm^{-2} s^{-1} in Hβ, i.e., about two times the flux derived by the previous method. Maps with the the best multi-Gaussian fits for each pixel are presented in the bottom panels of Figure 3.3 for comparison with those obtained in the previous subsection.

3.3.3 OSIRIS spectra of HuBi 1

The GTC OSIRIS long-slit spectrum, with a broader spectral coverage than the MEGARA data, has been used to extract one-dimensional spectra of the inner and outer shells of HuBi 1. The emission of the inner shell was extracted from a 5 arcsec in length central aperture of the OSIRIS two-dimensional spectrum covering the extent of the [O III] λ5007 emission in the MEGARA maps (the red rectangular aperture in Fig. 3.1). The emission of the outer region was extracted from two apertures of ∼5 arcsec in length at both sides of the central region (the yellow rectangular apertures in Fig. 3.1) and then added together. The emission of a transition region between the inner and outer shells was also extracted from two small apertures 1 arcsec in length (the cyan rectangular apertures in Fig. 3.1) to assess the variation of key emission lines from one region to the other.

The resulting spectra are shown in Figure 3.5, with insets to zoom in two spectral regions of interest. These spectra reveal notable spectral variations among the different regions. The [O III] λ5007 emission line is almost as intense as the Hβ line in the inner region (bottom panel of Fig. 3.5) but, as we moved to more external regions, it fades and mostly disappears (top panel in Fig. 3.5). On the other hand, the [N II] λ6584 emission line prevails over the Hα line in the inner shell, while in the outer shell their relative importance is reversed (see figure 8 in Guerrero & Manchado 1996, for a similar case for the born-again PN A 58). These variations in line ratios imply an anomalous ionisation structure.

A standard analysis of these spectra involves the measurement of the relative line intensities

---

[5] The outer shell was also fitted with one, two or up to three components, depending on the spatial location, for continuity with the fit to the inner shell.

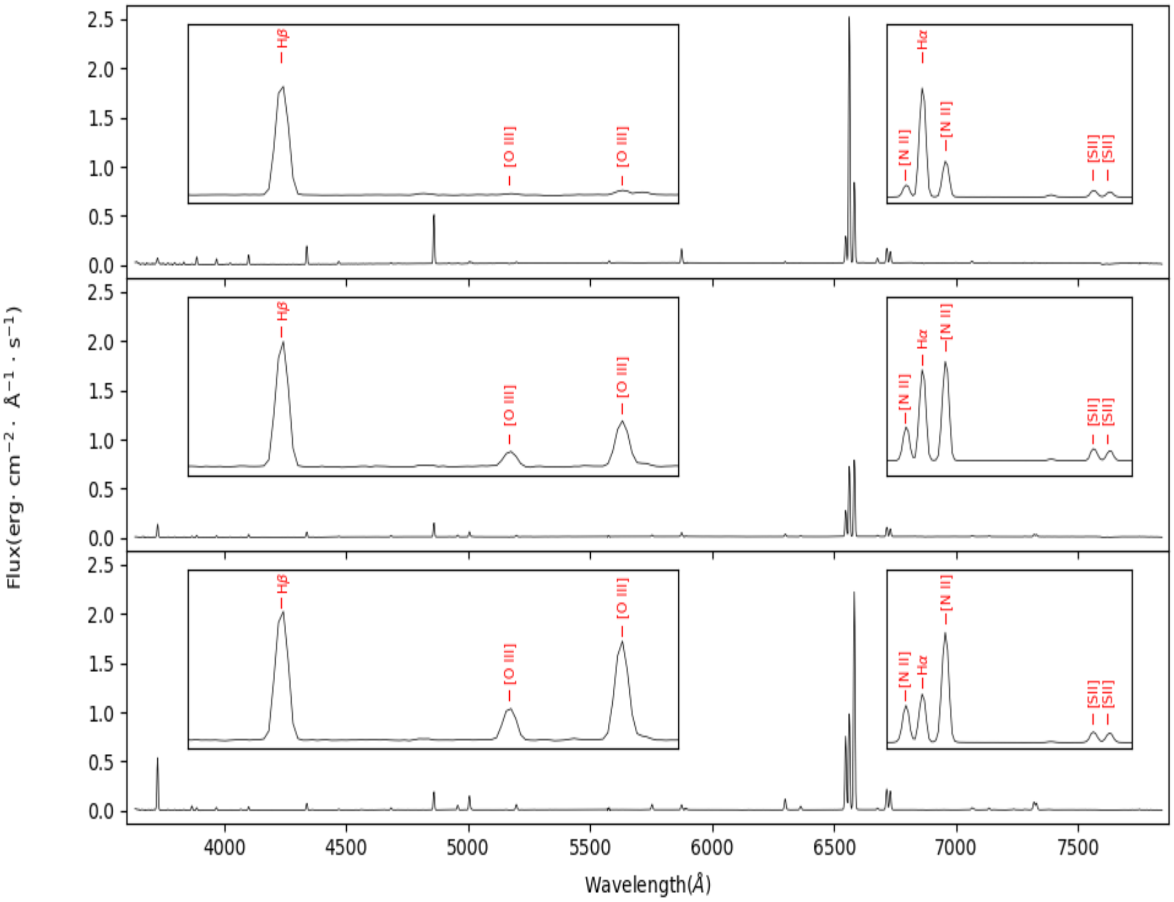

Figure 3.5: OSIRIS intermediate-dispersion spectra of the outer shell (top), intermediate region (middle), and inner shell (bottom) of HuBi 1 extracted from the yellow, cyan, and red apertures shown in Figure 3.1, respectively. Two spectral regions of interest are zoomed to reveal the notable variations in the key emission lines among the different shells.

(e.g., Peña et al. 2021), but it must be noted that the GTC OSIRIS spectrum of HuBi 1 was acquired at a low elevation, when the effects of differential chromatic refraction (DCR) along the parallactic angle cannot be neglected for data obtained over such a broad spectral range (Filippenko 1982). This is a problem particularly serious for these observations, whose slit is almost orthogonal to the parallactic angle. As a result, the apparent position of the slit on the sky for emission lines at different wavelengths will shift noticeably. The details and extent of these effects and a solution using the OSIRIS data in conjunction with the MEGARA data to measure the relative line intensities of the emission lines in the OSIRIS spectra are described in detail in Appendix A.2.

The observed line flux ratios F with respect to an arbitrary intensity of 100 for the Hβ line together with the Hβ flux for the inner and outer shells of HuBi 1 are presented in Table 3.1. The features at $\simeq$4566 Å, $\simeq$7236 Å, $\simeq$7289 Å, and $\simeq$7379 Å seem stellar, but none of them except the C II λ7236 line can be unambiguously identified. It shall be noted that the emission arising from the inner shell for a number of emission lines is strongly contaminated by their emission arising from the outer shell. This issue is aggravated for the OSIRIS data, whose low spectral resolution does not allow the spectral split of the emissions from the inner and outer

Table 3.1: Relative fluxes and line intensities with respect to Hβ (=100) of the emission lines of HuBi 1 measured from OSIRIS and MEGARA data. Emission lines from OSIRIS for which MEGARA data are available have been replaced by the later. Due to the DCR effects affecting the OSIRIS data, each line of this set is normalized by the Hβ flux computed for the equivalent aperture derived from the MEGARA data (see Appendix A).

Line	Inner shell		Outer shell	
	F	I	F	I
[O II] 3727	2330	8360	27.7	38.3
[Ne III] 3869	197	622	...	...
Hζ + He I 3889	...	...	17.1	28.2
Hϵ + [Ne III] 3969	...	...	14.8	37.8
He I 4026	...	...	4.1	5.0
[S II] 4069	43.4	111	...	...
Hδ 4101	...	...	22.5	34.2
Hγ 4340	...	...	46.7	62.8
[O III] 4363	16.1	30.6	...	...
He I 4471	...	...	8.3	9.9
C I:O II:N II:4562+4570	27.6	39.6	...	...
He II 4686	108	134	...	...
Hβ 4861	100	100	100	100
[O III] 4959	113	101	...	...
[O III] 5007	386	324	...	...
He I 5016	...	...	3.5	2.8
[N I] 5199	114	75.6	4.7	3.2
[N II] 5755	159	60.2	...	...
He I 5876	34.1	20.5	39.7	19.3
[O I] 6300	339	95.5	...	...
[S III] 6312	18.5	4.5	...	...
[O I] 6363	121	28.3	...	...
[N II] 6548	1590	330	50.0	21.1
Hα 6563	1460	274	666	301
[N II] 6584	6820	1390	214	90
He I 6678	...	...	10.0	4.0
[S II] 6717	727	135	42.0	16.7
[S II] 6731	611	112	32.4	12.8
He I 7065	...	...	6.6	2.1
C II 7064 + C I 7066	8.4	1.2	...	...
[Ar III] 7135	80.2	11.1	...	...
C II 7236	33.1	4.3	...	...
C I:O II 7289	25.5	3.2	...	...
[O II] 7320	254	31.6	...	...
[O II] 7330	212	26.2	...	...
N I:O II:7379	22.6	2.7	...	...
$\log F(\mathrm{H}\beta)$ (erg cm^{-2} s^{-1})	-14.9		-13.3	
$c(\mathrm{H}\beta)$	2.16±0.21		1.09±0.11	

shells. Following the PI, PE, IwE and EwI classification of the different emission lines according to the relative contribution of the emission of the outer shell to that of the inner shell provided in Section 3.2, the flux of each line has been determined as described in Appendix A.1.

The intensities of the Hα and Hβ lines have been used to derive the value of the logarithmic extinction coefficient, c(Hβ), for the inner and outer shells of HuBi 1. A recombination Case B was adopted with values for the theoretical I(Hα)/I(Hβ) lines flux ratio (Osterbrock & Ferland 2006) according to the physical conditions of each shell following Ueta & Otsuka (2021)'s prescriptions. Thus a theoretical I(Hα)/I(Hβ) value of 2.74 was adopted for the inner shell, suitable for a value of T_e of 20000 K (close to that reported in Section 3.4.3), and 3.04 for the outer shell, suitable for a value of T_e of 5,000 K (Guerrero et al. 2018; Peña et al. 2021). The values of c(Hβ) derived for the inner and outer shells are 2.16±0.32 and 1.09±0.16, respectively. These have been used in conjunction with the extinction curve of Howarth (1983) to deredden the relative line intensity ratios I also presented in Table 3.1.

3.4 Results

The GTC MEGARA and OSIRIS data presented above allow a detailed spatially resolved spectroscopic investigation of HuBi 1. The results of these analyses are provided in the next sections.

3.4.1 Extinction maps

The determination of c(Hβ) in the previous section reveals notable higher extinction values for the inner shell. This result is in sharp contrast with the results presented by Pollacco & Hill (1994) and Peña et al. (2021) that did not find spatial variations of the extinction across HuBi 1, with similar values of c(Hβ) for the inner and outer shells. These studies did not accounted for the contamination of the emission of the inner shell by the foreground emission of the outer shell, which is particularly severe for the Hα and Hβ Balmer lines used for the determination of c(Hβ).

The tomographic capability of the GTC MEGARA observations highlighted in Sections 3.3.2.1 and 3.3.2.2 to isolate the Hα and Hβ emissions of the inner shell from those of the outer shell can be used to investigate the details of the spatial variations of c(Hβ) in HuBi 1. As described in Section 3.3.2.2, the maps derived using multi-Gaussian fits on a spaxel-by-spaxel basis (lower panels of Fig. 3.3) are affected by small variations of the fit parameters and are noisier than the maps derived isolating the wings of the high-velocity components (upper panels of Fig. 3.3). The maps derived using the latter method will be used to produce cleaner c(Hβ) maps, although the velocity range of the Hα and Hβ emission profiles will be restricted to be the same for both lines, as allowed by the SNR of the fainter Hβ line: from -14 km s^{-1} to $+13$ km s^{-1} for the approaching component and from $+115$ km s^{-1} to $+122$ km s^{-1} for the receding component. In this way, it is warrantied that the Hα to Hβ ratio are derived from similar velocity ranges, although the velocity range for Hα is narrower than that used for the images presented in Figure 3.3.

The final extinction maps of the inner and outer shells of HuBi 1 derived from the Hα and Hβ flux map ratios are presented in Figure 3.6. These maps indeed confirm that the extinction in the inner shell is larger than that of the outer shell. In order to compare the values in these $c(\mathrm{H}\beta)$ maps with the values of $c(\mathrm{H}\beta)$ derived in the previous section, average values of $c(\mathrm{H}\beta)$ have been derived for the inner and outer shells. For this calculation, pixels with SNR $\leq$3 have been ignored. In addition, pixels of the inner shell beyond the second contour in Figure 3.6-*left* were excised because the low Hβ flux, as well as pixels of the outer shell at the corners of the MEGARA IFU FoV where vignetting effects are appreciable. The averaged values of $c(\mathrm{H}\beta)$ derived for the inner and outer shells are 2.09±0.21 and 1.14±0.11, respectively, which are consistent with the values derived in the previous section.

The extinction maps presented in Figure 3.6 and the averaged values derived above confirm that the extinction in the inner shell is noticeable higher than that of the outer shell. The spatial distribution of the extinction in the inner shell revealed in the left panel of Figure 3.6 seems to peak in the innermost regions of the inner shell, at a location between the two peaks of the [O III] map where the CSPN IRAS 17154−1555 is located. The extinction in the outer shell is basically flat, but a small increase is found in the regions of the outer shell projected onto the inner shell. This can be attributed to the absorption of the emission from the receding outer shell as it goes through the inner regions of HuBi 1.

Guerrero et al. (2018) attributed the brightness decrease of the CSPN of HuBi 1 of $\simeq$10 mags in the last 50 years to the ejection of C-rich material that condensed into dust grains and veiled the light from the star rather than to surface temperature of the CSPN. The larger extinction of the inner shell of HuBi 1 found here, in conjunction with the wealth of carbon emission lines detected in its 1991 spectrum (Pollacco & Hill 1994), lends further support to the hypothesis that it contains C-rich material from a recent ejecta, while the outer shell is formed by pristine nebular material.

3.4.2 Diagnostic diagrams

The peculiar ionisation structure of HuBi 1, with emission from forbidden lines of [O III] and [N II] dominating the inner shell, but emission from recombination lines of H I and He I in the outer shell, and the presence of He II emission in the inner shell, which cannot be photoionized by its CSPN as its effective temperature is T_{eff} $\approx$38,000 K, led Guerrero et al. (2018) to propose that the inner shell is mostly shock-excited. The association of the inner shell of HuBi 1 with a fast expanding ($\simeq$300 km s^{-1}) shell-like structure ejected around 200 yrs ago (Rechy-García et al. 2020) provided the means for shock-excitation. More recently, Peña et al. (2021) attributed temporal variations in different line intensity ratios of the inner shell and the increase of the electron temperature in this shell to shock-excitation, but the limitations of their analysis of the spectrum of the inner shell pose questions on their reliability. In particular, the line ratios presented by these authors based on the same GTC OSIRIS data set have not been corrected from DCR effects, which questions the reported line intensity ratio variations (see Appendix A.2).

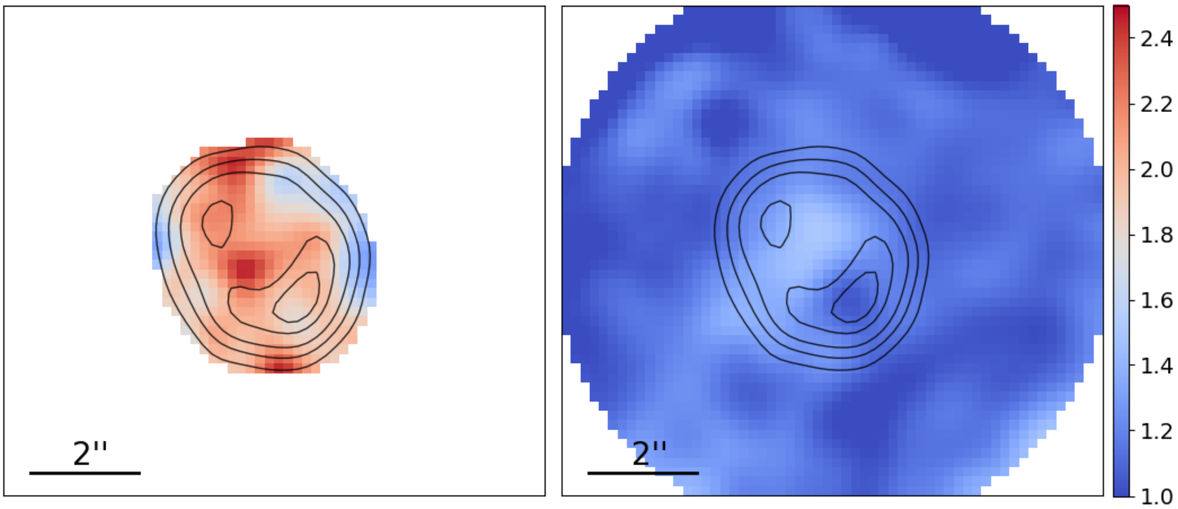

Figure 3.6: GTC MEGARA maps of the logarithmic extinction coefficient $c(\mathrm{H}\beta)$ of the inner (left) and outer (right) shells of HuBi 1 derived from the Hα to Hβ line flux ratios. Contours of the inner shell derived from the [O III] map are overlaid on the maps. Pixels at the corner regions in the map of the outer shell have been ignored due to vignetting effects.

Line intensity ratios diagrams have long been used to distinguish between different ionisation mechanisms (for instance, the ones defined by Baldwin et al. 1981). These diagrams, often used to classify galaxies among AGNs, starburst galaxies or LINERs (Veilleux & Osterbrock 1987; Kewley et al. 2001), can also be applied to PNe. The usual line intensity ratios used for line ratio diagrams are [O III]/Hβ vs [N II]/Hα, [S II]/Hα or [O I]/Hα, but other ratios such as [O III]/Hα vs [S II]/Hα or [N II]/Hα have been used in proto-planetary nebula (pPNe) and PNe and their FLIERs as well (e.g., Raga et al. 2008).

The GTC MEGARA Hβ, Hα, [O III], [N II], and [S II] maps of the inner and outer shells of HuBi 1 have been used to obtain the pixel-by-pixel distributions of the $\log_{10}$([O III]/Hβ) vs $\log_{10}$([N II]/Hα) and $\log_{10}$([S II]/Hα) in the line ratio diagrams presented in Figure 3.7. Integrated ratios for the inner and outer shell have been also computed using the GTC OSIRIS long-slit data. The extinction effects in these line ratios is expected to be negligible, given the small wavelength difference, yet the intensity ratios of all points have been corrected using the extinction maps in Figure 3.6.

The line ratio diagrams in Figure 3.7 clearly reveal that two different mechanism of ionisation are present in HuBi 1, being the inner shell dominated by shocks while the outer shell is undoubtedly photoionized. We note that the interpretation of diagnostic diagrams using spatially-resolved IFU data can be misleading due to ionization stratification mimicking the behaviour of shock-excited nebulae (Morisset 2018), but this is not the case here as the integrated values of the line ratios obtained from GTC OSIRIS long-slit data share similar loci in these diagrams (Fig. 3.7). The spread of the data points in these diagrams is notably larger than that in the line ratio diagrams presented by Peña et al. (2021), with values of $\log_{10}$([O III]/Hβ), $\log_{10}$([N II]/Hα) and $\log_{10}$([S II]/Hα) close to unity for the inner shell. These points are located in the region of these line ratio diagrams that can be interpreted as the result of shock-excitation. The spectral coverage of our MEGARA data does not cover the

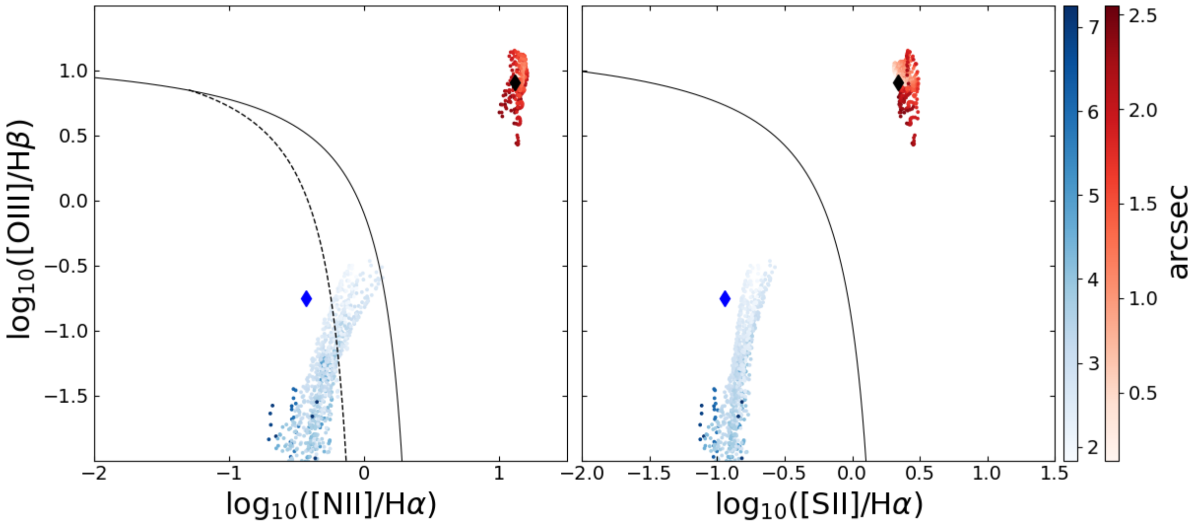

Figure 3.7: Pixel by pixel distributions of the [O III]λ5007/Hβ, [N II] λ6584/Hα, and [S II]$\lambda(6716 + 6730)$/Hα line intensity ratios in the corresponding BPT diagrams for the inner (red points) and outer (blue points) shells of HuBi 1. The blue scale represents the distance of the points of the outer shell to the centre of the nebula from 2.5 to 7.5 arcsec, whereas the red scale shows the distance of the points of the inner shell to the centre of the nebula from 0 to 2.5 arcsec. Data points representative of the inner and outer shells of HuBi 1 derived from the GTC OSIRIS long-slit spectra are shown as cyan and magenta diamonds for the outer and inner shell respectively. The solid and dashed curves correspond to the theoretical models of Kewley et al. (2006) and Kauffmann et al. (2003), respectively.

shock-sensitive [O I] λ6300 emission line, but we note that the value of the [O I] λ6300/Hα line intensity ratio derived from the OSIRIS data for the inner shell, $\simeq$0.95, locates it in the region of shock excitation of the $\log_{10}$([O III]λ5007/Hβ) vs $\log_{10}$([O I] λ6300/Hα) line ratio diagram.

The distributions of the points of the outer shell in these line ratio diagrams show a notable spread, with the innermost points closer to the shock ionisation region in the line ratio diagrams and the more external points well located in the photoionisation region of these diagrams. Such correlation between ionisation and radial distance could originate from the regions of diffuse [S II] and [N II] in the so-called intermediate shell, whose ionisation may include the effects of shocks. The born-again 3D radiation-hydrodynamic model of HuBi 1 presented by Toalá et al. (2021b) suggests that these structures can appear as the result of the diffusion of turbulence from the ejecta onto the outer shell, which would explain the mixed excitation.

3.4.3 Physical conditions of the inner shell

We used PyNeb (Luridiana et al. 2015) to investigate the physical conditions of the inner shell[6] of HuBi 1. The corresponding diagnostic diagrams are shown in Figure 3.8, where the shaded areas have been computed assuming a 10% uncertainty for the measured line intensities.

As for the electron density, n_e, the [S II] λ6716 to λ6731 line ratio (the label 'nn' stands for nebular-nebular) draws an area for n_e ranging from a few tens to 1000 cm^{-3}. This value is

---

[6] An investigation of the physical conditions of the outer shell cannot be performed because no temperature-sensitive auroral lines are detected in its spectrum.

constrained to 200-600 cm^{-3} in regions where the density diagnostic curve for the [S II] λ6716 to λ6731 line ratio crosses the temperature diagnostic curves.

As for the electron temperature, T_{e}, the situation is a bit more complex: the [O III] λ4363 to λ5007 line ratio points to T_{e} between 45,000 K and 70,000 K, while the [N II] λ5755 to $\lambda\lambda$6548,6584 line ratio points to much lower values, in the range from 16,000 K to 26,000 K. This result can be interpreted as lower ionization N^{+} species prevails over higher ionization O^{++} species in regions where the gas have had more time to recombine since the shock passed, and then to cool down. The situation is even more extreme for the [O II] λ3727 to $\lambda\lambda$7320,7330 ratio, which implies a very cold T$_{\mathrm{e}}$, in the range between 6,000 K and 9,000 K, and for [S II] $\lambda\lambda$6716,6731 to λ4069 line ratio (labeled 'an' for auroral-nebular), which points to a very high Te, not even shown in the diagram. These results would be hard to reconcile in a photoionized gas, since the O^{+}, N^{+}, and S^{+} regions are expected to be co-spatial, thus sharing similar physical properties. In the case of shocked regions, however, the steep T_{e} gradient may cause the emission of a given species to arise from regions at very different temperatures.

The extreme values of T_{e} derived from the [O II] and [S II] temperature-sensitive line ratios may have an alternative explanation. Both line ratios involve red and blue lines, but in the opposite way, with the nebular [O II] λ3727 line and the auroral [S II] λ4069 line in the blue range. In the next sections, we will see that the blue [O II] λ3727 and [S II] λ4069 lines, but also the [Ne III] λ3869 line and in a less extent the [O III] λ4363 line are systematically underpredicted by shock models. If the intensity of the [O II] λ3727 line and [S II] λ4069 lines was, indeed, overestimated, it would result in the predicted low T_{e} for the [O II] line ratio and high T_{e} for the [S II] line ratio in Figure 3.8. Indeed, the value of T_{e} derived from the [N II] line ratio is the most insensitive to extinction, as it involves lines in the red spectral range.

3.4.4 Electron density map

The spatial distribution of the nebular density can be derived from the density-sensitive [S II] λ6716, 6731 doublet intensity ratio independently of the excitation mechanism (shocks or photoionisation). As described in Section 3.2 and Appendix A.1, the [S II] emission lines are classified in Table A.1.1 as IwE, i.e., the emission is mostly attributed to the inner shell with some contribution at systemic velocities arising from the intermediate shell. Their flux maps have thus been computed using a method similar to that applied to the Hα and Hβ lines in Section 3.3.2.1 with the small differences detailed in Appendix A.1.

The resulting [S II] $\lambda\lambda$6716,6730 maps are then used to obtain the electron density map using the usual relation between the [S II]λ6716/[S II]λ6730 ratio and n_{e} (Osterbrock & Ferland 2006) assuming for T_{e} a value of 30,000 K for the inner shell, within of range of values derived from the [N II] and [O III] temperature-sensitive ratios in the previous section, and 5,000 K for the outer shell. Figure 3.9 shows the electron density map for all pixels with SNR$>$ 3. We obtained averaged densities of n_{e} $\approx$500 cm^{-3} for the inner shell and n_{e} $\approx$100 cm^{-3} for the outer shell, the latter in the low-density limit of the density diagnostic provided by the [S II] doublet. The electron density of the outer shell is quite flat, but the inner shell shows two peaks more or less coincident with the [O III] emission peaks.

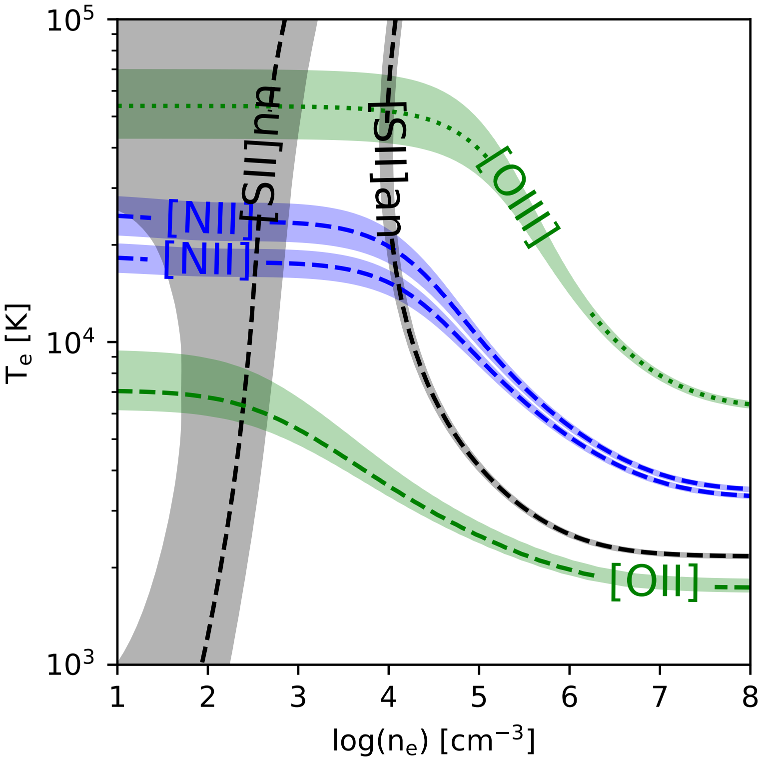

Figure 3.8: Diagnostic diagrams for the different temperature- and density-sensitive line ratios available in the spectrum of the inner shell of HuBi 1. The shaded areas have been computed assuming a 10% uncertainty for the measured line intensities. The 'an' and 'nn' labels for the [S II] line ratios stand for the auroral λ4069 to nebular λλ6716,6731 and nebular λ6716 to nebular λ6731 line ratios, respectively.

The electron density of the inner shell agrees with that reported by Guerrero et al. (2018), whereas the extreme high electron density $n_e \simeq$20,000 cm^{-3} reported by Pollacco & Hill (1994) can be discarded as those authors did not account for the contamination of the [S II] emission lines by stellar C II lines. Peña et al. (2021) reports values for the electron density of the inner and outer shells of HuBi 1 for different epochs between 2000 and 2018 that are suggestive of higher n_e for the inner shell than the outer shell, although the large spread of n_e values makes such result only qualitatively consistent with those obtained here.

3.4.5 Chemical abundances

Using diagnostic diagrams and the scheme laid out by BPT, we have demonstrated in Section 3.4.2 that shocks is the main excitation mechanism of the inner shell of HuBi 1. Indeed, the high values of the auroral-to-nebular line ratios [O III] λ4363 Å/[O III] λ5007 Å ∼0.09 and [N II] λ5755 Å/[N II] λ6584 Å ∼0.33 are also clear indicators of shocks (Dopita 1977). Since shock excitation has to be taken into account for abundances determination in the inner shell of HuBi 1, we computed those making use of the MAPPINGS V code (Sutherland et al. 2018). Details of the code can be found in Appendix A.3.

For our modelling, we consider shocks as the only source of ionisation in the inner shell as

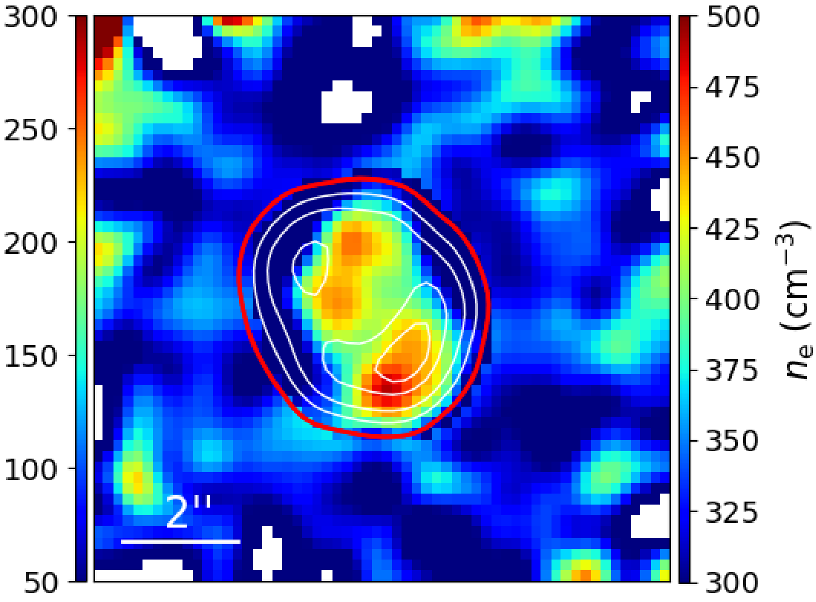

Figure 3.9: Electron density n_e map of HuBi 1 derived from the [S II] λ6716 to [S II] λ6730 line intensity ratio. The contours of the emission in the [O III] λ5007 line showing the extent of the inner shell are overlaid. The most extended red contour separates the inner and outer shells of HuBi 1. Their densities n_e were computed assuming an electron temperature of 30,000 K for the former (right colorbar) and 5,000 K for the latter (left colorbar).

the large extinction towards the CSPN basically absorbs all its UV emission. We ran a number of models taking into account the emission from both the shock and its precursor (Allen et al. 2008; Sutherland & Dopita 2017). According to analyses of spectroscopic observations of the outer shell of HuBi 1 (e.g., Guerrero et al. 2018), shocks in these simulations are assumed to propagate into a fully ionised medium (i.e., H/H$^+$ = He/He$^+$ = 1) with a preshock temperature of 10^4 K.

We start by fixing the values of the shock velocity v_s at 80 km s^{-1} as smaller velocities can be precluded (Rechy-García et al. 2020), the pre-shock density n at 1 cm^{-3} (similar to that found for non-fully radiative young shocks by Dopita et al. 2018), and the strength of the magnetic field B at 1 μG. The later is low for a PN (Rodríguez et al. 2017), but plausible if we assume that magnetic field scales with density $B \propto n^{1/2}$ as proposed by Cox (2005) for average ISM properties.

We then ran a number of MAPPINGS V models varying the O and N abundances, keeping the He abundance at 12+log$_{10}$(He/H)=13.0 and scaling the abundances of the other heavy elements with those of O according to the Solar abundances (Asplund et al. 2009). The MAPPINGS V models studying the variations of the O and N abundances are presented in Table A.3.1 of Appendix A.3, where the model line emission strengths are compared with those observed reported in Table 3.1 to determine the best values for the O and N abundances. The emission line ratio [O III] λ4363 Å/[O III] λ5007 Å, which is particularly sensitive to the shock conditions (Dopita 1977), is used as a main indicator, but the intensities of the [O III], [O II] and [N II] emission lines are also considered

The N/H abundances were first fixed to their Solar values and the O/H abundances allowed to vary (columns 3 to 7 of Tab. A.3.1). It can be seen there that, although O abundances below $12+\log_{10}(\mathrm{O/H})<9.8$ reproduce best the auroral-to-nebular [O III] ratio, they clearly underestimate the flux of all O emission lines. Higher O abundances tend to overestimate the [O III] emission lines and predict auroral-to-nebular [O III] ratios much smaller than observed. The model with $12+\log_{10}(\mathrm{O/H})=9.8\pm0.1$, which best reproduces most of the [O III] emission lines, is adopted as best fit model. The O/H abundances were then fixed to this value and the N/H abundances allowed to vary (columns 8 to 12 of Tab. A.3.1). As for the O abundances, the intensity of the N lines require abundances two orders of magnitudes higher than Solar values, with the best fit achieved at $12+\log_{10}(\mathrm{N/H})=9.9\pm0.10$.

We tried then to assess the He abundance that best reproduces the intensity of the He recombination lines. Table A.3.2 shows that predicted intensity of the He recombination lines scales with the He abundance, although it also has noticeable effects in important collisional lines, such as [N II] λ6584, implying variations at factors of about one half in the N abundances anti-correlated with those of He. On the other hand, the intensity of the O lines and thus their abundances are quite insensitive to variations in the He abundances. We varied the He abundance around a value of $12+\log_{10}(\mathrm{He/H})=13$, but the He II λ4686 line was always underestimated, whereas the He I λ5876 line was clearly overestimated. A value of $12+\log_{10}(\mathrm{He/H})=13.00\pm0.15$ was selected as a best compromise.

Finally, we investigated whether the adopted pre-shock density and shock velocity may explain the discrepancies found in some emission line ratios for our fixed set of chemical abundances. In Table A.3.3 we show that increasing the shock velocity v_s from 100 to 200 km s^{-1} tend to decrease all emission line ratios with respect to the [O III] emission lines. Therefore, we conclude that a shock velocity v_s of 80 km s^{-1} is the best choice in agreement with Guerrero et al. (2018). Similarly, we show in Table A.3.4 that increasing the pre-shock density makes closer the estimation of the [O III] ratio to the observed one, but other important emission lines as the [S II] doublet, [O II] and [N II] lines are not well reproduced. Lower densities lead to lower [O III] λ4363/[O III] λ5007 ratios, making them differ more notably from the observed one. Therefore, the best models are adopted to have a pre-density n_pre of 1 cm^{-3}.

We list in Table 3.2 the parameters of our preferred model to reproduce the shock-excited spectrum of the inner shell of HuBi 1. We note that the C abundances in this table are scaled from the O abundances assuming a Solar C/O ratio of ∼0.55 (Asplund et al. 2009), as the available line ratios do not provide a suitable constraint to the C abundances. The [O III] and [N II] lines are fairly well described by this model, with the most notable discrepancies for the He I λ5876 and [O II] λ3727 emission lines. These discrepancies will be discussed in further details in the next section.

3.5 Discussion

HuBi 1, the inside-out PN, has proven to be a remarkable object, with extreme changes recorded in the past decades (e.g., Guerrero et al. 2018; Peña et al. 2021). Similar variations in human-time scales have also been reported for the two youngest born-again PNe identified thus far, namely the SO and A 58, a.k.a. Nova Aql 1919 (see Clayton et al. 2013; Evans et al. 2020, and

Table 3.2: mappings v model considered to reproduce the emission from the inner shell in HuBi 1. The emission lines are referred to $I(\mathrm{H}\beta)$=100.

Parameter	Preshock	Postshock
Density $(n)[\mathrm{cm}^{-3}]$	1	3.7
Electronic Density $(n_{\mathrm{e}})[\mathrm{cm}^{-3}]$	5.8	21.4
Temperature (T)[K]	30000	380000
Magnetic field $(B)[\mu\mathrm{G}]$	1	3.7

Chemical abundances		$12+\log_{10}(\mathrm{X/H})$
H		12.00
He		13.00±0.15
C		9.53
N		9.90±0.10
O		9.80±0.10
Ne		9.03

Line	Observation	Model
[O ii] 3727	8360	571.2
[Ne iii] 3869	622	54.9
[S ii] 4069	111	14.2
[O ii]i 4363	30.6	25.0
He ii 4686	134	66.8
[O ii] 4959	101	129.2
[O ii]i 5007	324	373.4
[N ii] 5199	75.6	119.3
[N ii] 5755	60.2	66.3
He i 5876	$<$20.5	336.7
[O i] 6300	95.5	30.4
[S iii] 6312	4.5	5.3
[O ii]i 6363	28.3	9.7
[N ii] 6548	330	552.2
Hα	274	407.4
[N ii] 6584	1390	1624
[S ii] 6717	135	104.0
[S ii] 6731	112	115.0
[Ar iii]	11.1	7.8
[O ii] 7320	31.6	43.1
[O ii] 7330	26.2	34.8

references therein), as well as for the LTP star SAO 244567 and the nebula around it (Reindl et al. 2017; Balick et al. 2021). Indeed, the dramatic decline in brightness of the CSPN of HuBi 1 by ≃10 mag in ∼50 years and the strong IR emission and the profusion of C emission lines from the innermost regions detected in the oldest available spectra (Pollacco & Hill 1994) are suggestive of the ejection of highly-enriched material that had resulted in the sudden formation of large amounts of dust, well in agreement with a born-again scenario. If this were the case, there are a number of predictions that can be uniquely tested using the unequalled capabilities of MEGARA at the GTC to disentangle the inner shell emission from that corresponding to the outer H-rich PN.

Since VLTP events result in the production of large amounts of dust, one basic expectation would be that the inner shell of HuBi 1 should be more extincted than the outer shell. We have for the first time obtained clean extinction maps of the inner and outer shells by dissecting the different contributions of their emission to the H Balmer lines. These unpolluted extinction maps confirm that the inner shell exhibits larger $c(\mathrm{H}\beta)$ values than the outer nebula, in contrast with the similar values for both shells reported in previous works (e.g., Peña 2005; Peña et al. 2021). Incidentally, these extinction maps allow us the proper reddening correction of the spectra extracted for the inner and outer shells using the appropriate value of $c(\mathrm{H}\beta)$ for each of them.

After experiencing a VLTP event, the CSPN is expected to go back for a short period of time to the locus of the H-R diagram occupied by AGB stars, reducing considerably its effective temperature and thus its ionisation photon flux. As a result, photoionisation cannot be the main excitation mechanism of the emission arising from the innermost regions of young born-again PNe. Combining MEGARA and OSIRIS data sets, we have obtained reddening-corrected [O III]/Hβ, [N II]/Hα and [S II]/Hα line ratios that have been used to produce standard diagnostic diagrams. The position in these diagrams of data points from the inner shell undoubtedly demonstrate that the main emission mechanism in the inner shell of HuBi 1 is shocks, confirming the original proposition explored by Guerrero et al. (2018).

The most critical test of the born-again nature for the inner shell of HuBi 1 would be a H-poor abundance. We have computed those from the line ratios measured in the MEGARA and OSIRIS data sets using the MAPPINGS V code to conform to the shock-excitation of this region. The best-fit model (Tab. 3.2) is capable to reproduce most of the emission lines detected in our spectra, although the strength of the [O II] λ3727 doublet is notoriously underestimated, whereas those of the He II λ4686 and He I λ5876 emission lines cannot be simultaneously matched. The significant differences between the observed and predicted intensities of the [O II] λ3727 and [O II] $\lambda\lambda$7320,7330 emission lines may reveal the complexity of the physical conditions and possibly varying optical depth of the O^{+}-emitting region. Alternatively, these discrepancies can be partially attributed to the effects of the relatively small photoionization produced by the cool CSPN of HuBi 1 (T_{eff} ≈35–38 kK; Leuenhagen & Hamann 1998; Guerrero et al. 2018), which would raise the emissivity of the [O II] λ3727 doublet and He I λ5876 emission line. More likely there is an over-correction of the extinction of the intensity of the emission lines in the blue end of the spectrum due either to spatially varying absorption or to the use of a generic extinction curve of the interstellar medium, but probably not suitable for the peculiar chemical abundances of the ejecta. Section 3.4.3 already noted the discrepancies between the electron temperature derived from line ratios involving [O II] and [S II] "blue" and "red" lines. Indeed, the shock models here presented does not only underestimate the "blue" [O II] λ3727 and [S II] λ4069 lines, but also the [Ne III] λ3869 emission line.

The best-fit model in Table 3.2 implies the notable hydrogen deficiency in the innermost ejecta of HuBi 1, with He/H $\simeq$10, O/H $\simeq$0.006, and N/H $\simeq$0.008, well above those typical for PNe. These results are in sharp contrast with those recently presented by Peña et al. (2021), who claimed that the chemical composition of the inner and outer shells of HuBi 1 were similar among them and typical of PNe. We note, however, a number of flaws in the analysis presented by Peña et al. (2021): (1) the extinction-correction of the outer shell was applied to the inner shell of HuBi 1, which is inadequate and result in the incorrect determination of the physical conditions of the inner shell, (2) the notable DCR effects in the same OSIRIS long-slit spectra presented here (see Appendix A.1) were not corrected, (3) photoionisation was assumed as the excitation mechanism for the calculation of the inner shell chemical abundances, although they had proven the prevalence of shocks as the main excitation mechanism, and (4) more importantly, the dominant contamination of the outer shell to the Hβ and Hα emission from the inner shell was not subtracted, artificially enhancing the hydrogen content of the inner shell.

The abundances by number obtained in our analysis considering shocks are in excellent agreement with the abundances determined from CELs from the H-poor knots of born-again PNe (Jacoby & Ford 1983; Manchado et al. 1989; Guerrero & Manchado 1996; Wesson et al. 2003, 2008). Our He/H abundance of 10 is as well in the same range from 3.2 to 11.7 to that obtained for A 30 and A 58 (see table 7 in Wesson et al. 2008). It can thus be concluded that the chemical abundances of the inner shell of HuBi 1 are consistent with the H-poor nature of a born-again scenario.

The chemical abundances of HuBi 1, as those derived for other born-again PNe using CELs, are far from the theoretical expectations from born-again scenarios (e.g., Miller Bertolami et al. 2006). It is well-known that observed chemical abundances in born-again PNe only become consistent with those theoretically predicted when they are computed using ORLs, as the ADF, i.e., the ratio between the chemical abundances derived from ORLs and CELs, is extremely high among born-again PNe, with values up to 700 for A 30 (Wesson et al. 2003) and $\simeq$90 for A 58 (Wesson et al. 2008). For comparison, the average ADF[7] Unfortunately, the ORLs needed for the determination of the ADF in HuBi 1 are not available in its spectrum. If an ADF of 100 were adopted, which seems reasonable for born-again PNe, total "ADF-corrected" abundances by mass of 0.01, 0.58, 0.06, 0.16, 0.15 and 0.04 for H, He, C, N, O and Ne, respectively, would be obtained.

These "ADF-corrected" chemical abundances are in the range of the theoretical expectations from born-again scenarios considered above (Miller Bertolami et al. 2006), but for the N/O ratio close to unity, which seems otherwise typical of nova events (see Lau et al. 2011). This scenario, however, is unlikely, since the slowest novae have velocities $\sim 300 - 700$ km s^{-1}

---

[7] See `https://www.nebulousresearch.org/adfs` for the most up to date list of ADFs in PNe. of hydrogen-rich PNe is $\simeq$2 (Wesson et al. 2018).

(see,e.g., Santamaría et al. 2020, and references therein), whereas the bulk of material of the hydrogen-poor ejecta of HuBi 1 expands at 80–100 km s^{-1}.

The details of these "ADF-corrected" abundances do not completely agree with those estimated for the CSPN of HuBi 1 using non-LTE atmosphere models (Leuenhagen & Hamann 1998; Guerrero et al. 2018): the nebular abundances by mass of 0.58 for He and 0.15 for O differ from the stellar values of 0.33 and 0.10, respectively, the nebular N/O ratio is about 10 times larger than the stellar N/O ratio (0.1), and the nebular C abundances are about 8 times smaller than the stellar ones (0.5). On the other hand, the stellar abundances are perfectly matched by the theoretical predictions (Guerrero et al. 2018). We suspect that the differences between the "ADF-corrected" abundances of HuBi 1 and the stellar abundances and theoretical predictions arise from a notable underestimation of the C abundances and in a minor degree of the O abundances. The C and Ne abundances obtained with our shock model have been estimated using their Solar ratios with respect to the O abundances, but the wealth of C II and C III lines detected by Pollacco & Hill (1994) point to a significant overabundance of C. Moreover, large amounts of C are to be trapped into C-rich dust such as amorphous carbon species as shown in the born-again PNe A 30 and A 78 (Toalá et al. 2021b). In addition, C and O atoms might be trapped into CO molecules, which in the case of the born-again PN A 58 amount to a mass $\simeq 10^{-5} M_{\odot}$ (Tafoya et al. 2022). If those effects were to be taken into account, the C fraction by mass would increase notably, reducing that of the other elements, and the N/O ratio would be reduced. The total abundances by mass of He, C, N, and O would then become consistent with those of 0.33, 0.5, 0.01, and 0.10, respectively, estimated for the CSPN (Guerrero et al. 2018). The case of the C abundances of the born-again ejecta of HuBi 1 will be addressed in a subsequent paper (Rodríguez-González et al., in prep.) using IR observations to obtain a coherent set of chemical abundances of H, He, C, N, and O (see Toalá et al. 2021b). Future studies that simultaneously model the gas, dust and molecules of born-again PNe will help strengthen our understanding of the evolutionary sequences of the progenitors of such unique objects.

3.6 Conclusions

We have analysed integral field MEGARA and long-slit OSIRIS optical spectroscopic data of HuBi 1, the inside-out PN. The combined capabilities of these two GTC instruments have allowed us to study the ionisation structure of HuBi 1 in unprecedented detail and to determine the true chemical abundances of the recent ejecta in its innermost regions. Our main findings can be summarised as follows:

- The multiple shell structure of HuBi 1 is clearly dissected, with an inner shell associated with the recent ejecta, an outer shell, and additional emission mainly in the low-ionization [N II] and [S II] lines from an intermediate region. The inverted ionization structure of the inner shell of HuBi 1 is dramatically confirmed, with the emission in the He II λ4686 line encompassing that in the [O III] lines, which in addition surrounds that of the low-ionization [N II] and [S II] emission lines. The morphology of the intermediate region and its excitation are indicative of the interaction between the expanding ejecta of the inner shell and the old nebula. This intermediate region can be envisaged as the precursor of the petal-like structure clearly developed in the evolved born-again PNe A 30 and A 78.

- The high-dispersion integral field spectroscopic data obtained with MEGARA have proven to be conclusive to separate for the first time the faint emission of the H Balmer lines from the inner shell from the bright emission of the outer shell. The emission in the Hβ and Hα lines from the inner shell of HuBi 1 have been accurately obtained, allowing us to compute reliable relative line intensity ratios to determine the spatially varying extinction and excitation, and to compute the true chemical abundances of the inner shell.

- The extinction coefficient c(Hβ) of the inner shell ($\simeq$2.2) is on average twice that of the outer shell ($\simeq$1.1). The increased absorption towards the central regions of HuBi 1 is consistent with the idea that large amounts of dust have been recently produced there as suggested by the remarkable brightness reduction of its CSPN, IRAS 17514−1555, by $\sim$10 magnitudes in the last 50 years.

- The improved relative line intensity ratios have allowed us to undoubtedly confirm that the inner shell is ionised by shocks using BPT diagrams. On the other hand, the outer shell is located on the photoionisation zone of these diagram. Interestingly, the distributions of data points of the outer shell in the line ratio diagrams show a gradient, with points from the outermost regions clearly in the photoionisation zone, but points from the innermost regions of the outer shell spatially consistent with the intermediate region described above being closer to the locus for shocks. This supports the idea that the intermediate region is partially shock-excited by the interaction of the recent ejecta with the old nebula.

- The total abundances by number considering shocks are in agreement with the chemical abundances obtained from CELs in the hydrogen-poor knots of other born-again PNe such as A 30, A 58, and A 78. This is also the case for the total abundances by mass computed assuming an ADF of 100 similar to other born-again PNe. In particular, the large amount of He complies the hydrogen-poor nature of the ejecta predicted in born-again scenarios. Our observation did not detect any carbon lines and we could not measure its abundances, but it can be expected that large amounts of carbon are to be trapped into C-rich dust. Moreover some carbon and oxygen can be found forming CO molecules. It is suggested that the depletion of carbon and oxygen into dust grains and CO molecules can bring the chemical abundances of the recent ejecta in HuBi 1 close to those of its [WC] CSPN.

Chapter 4

Spectral variability of the H-poor ejecta in A 58

Chapter based on the article published in The Astrophysical Journal by Montoro-Molina B., Guerrero M. A., Toalá J. A., Rodríguez-González J. B. in 2022, volume 934, 18. doi:10.3847/1538-4357/ac771b.

Abstrac

Born-again PNe allow investigating stellar evolution, dust production, and nebular shocks in human timescales. Here we present an analysis of multi-epoch optical spectroscopic observations of the born-again PN A 58 around V605 Aql, which experienced a VLTP about a century ago. The H-deficient ejecta has experienced a considerable brightening in the time period considered, from 1996 to 2021, with notable changes also in many emission line ratios. Neither the reduction of the extinction caused by the dilution of the ejecta nor the increase of the ionizing photon flux from the central star seem capable to produce these spectral changes, which are instead attributed to shocks in the bipolar H-poor outflow dissociating molecular material and propagating through the outer nebula.

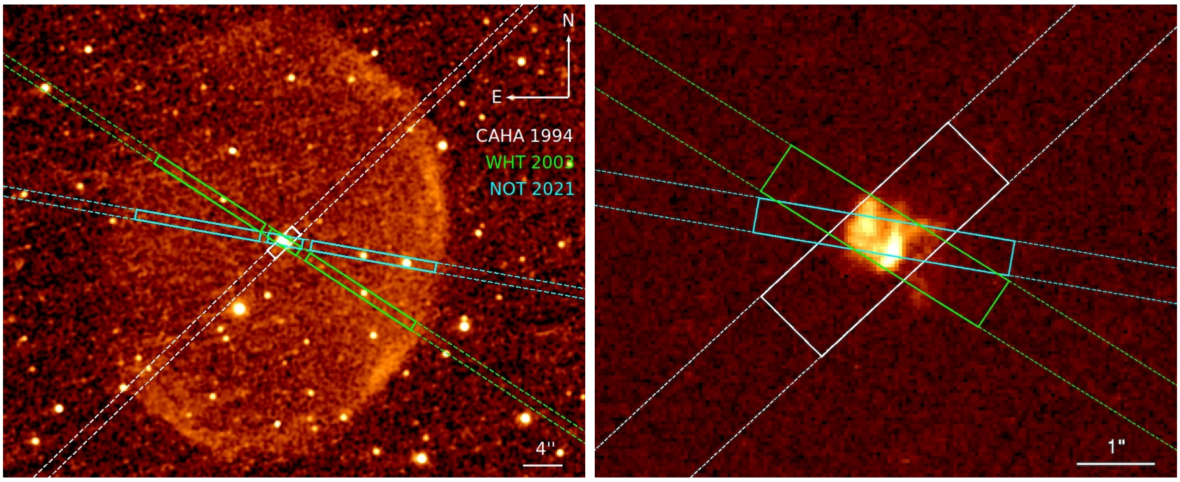

Figure 4.1: HST WFPC2 WF3 F658N image of A 58 (left) and HST WFPC2 PC F502N image of its H-deficient central knot (right). The dashed lines show the CAHA (white), WHT (green), and NOT (cyan) slits. The apertures used for extraction of 1D spectra are overlaid in solid-lines.

4.1 Introduction

Born-again PNe have been reported to exhibit great variability. Optical and IR studies have demonstrated that their ionization structure and dust properties change in human **timescales** (Clayton et al. 2013; Guerrero et al. 2018). For instance, the physical properties of the dust in the youngest born-again PN, the Sakurai's Object, have changed dramatically in only 20 years (Evans et al. 2020). Meanwhile the ionized H-poor ejecta of the ∼1000 yr old born-again PNe A 30 and A 78 reveals complex processes of photoevaporation, ablation, and mixing as it interacts with the current fast wind and ionizing photon flux from their CSPNe (Fang et al. 2014).

V605 Aql, the CSPN of A 58, experienced an outburst in 1919 July 4 (Wolf 1920) that was initially classified as a nova event (Nova Aql No. 4). Subsequent spectroscopic analyses demonstrated that the progenitor star was instead a H-deficient cool carbon star (Lundmark 1921; Bidelman 1973). By the mid-90s different authors reported the presence of broad emission of C IV 5806 Å in V605 Aql, a feature typically found in C-rich [Wolf-Rayet]-type stars with effective temperatures $T_{\rm eff} \gtrsim$50,000 K (see, e.g., Guerrero & Manchado 1996; Clayton & De Marco 1997; Harrison 1996, and references therein). The H-poor nature of the knot at the center of A 58 confirmed its born-again nature (Seitter 1987; Guerrero & Manchado 1996; Wesson et al. 2008). For a detailed review of the history of A 58 see section 1.3.2.

Time variations of the properties of the H-deficient ejecta around V605 Aql have been reported. Its first detection in radio in 2005 (van Hoof et al. 2006) implied a steep emission rise when compared to the previous upper limit reported by Kameswara Rao et al. (1987). It was attributed either to the optical depth decrease of the ejecta as a consequence of its expansion or to emission increase as V605 Aql is becoming hotter. Both possibilities can be true, as multi-epoch narrow-band HST images of A 58 have shown the expansion of its H-deficient ejecta at a rate of 10 mas yr^{-1} (Clayton et al. 2013), while detailed non-LTE stellar atmosphere modeling of V605 Aql have reported an effective temperature of 95,000 K (Clayton et al. 2006).

The H-deficient ejecta of A 58 has a bipolar morphology, with a disk-like (or torus) structure and a pair of ∼1 arcsec in size expanding lobes, more or less with an hourglass shape, oriented along a position angle of $\approx 60°$ (Clayton et al. 2013). Tafoya et al. (2022) recently presented ALMA observations of A 58 that provide the first image of the molecular content in the ejecta around a born-again star. This molecular emission was used to trace the kinematics of the toroidal region and the bipolar outflow in A 58. The former expands radially with a velocity of 100 km s^{-1}, while the bipolar ejection has an expansion velocity of $\approx$280 km s^{-1} and a dynamical age $\lesssim$20 yr. The molecular component is thus younger than the VLTP outburst, suggesting that the bipolar outflow is still been launched.

In this chapter we use multi-epoch optical spectroscopic observations of the old H-rich nebula A 58 and its recent H-deficient ejecta to investigate spectral time variations. The observations are described in Section 4.2, the results on the spectral evolution and its possible origins are presented in Sections 4.3 and 4.4, respectively, and a final remark is presented in Section 4.5.

4.2 Observations and data preparation

We have gathered optical long-slit intermediate-dispersion spectroscopic observations of A 58 from three different epochs spanning from 1994 to 2021. These include two data sets of previously published observations obtained with the Twin Cassegrain Spectrograph (TCS) at the 3.5 m telescope of the CAHA on 1994 July 26–28 (1994.57) and with ISIS at the 4.2 m WHT of the Observatorio de El Roque de los Muchachos (ORM) on 2003 August 1 (2003.58). Details of these observations were presented by Guerrero & Manchado (1996) and Wesson et al. (2008), respectively[1]. The slit PAs, widths and spectral resolutions of the CAHA observations were 134°, 1.2 arcsec, and 4 Å and 3.5 Å for the TCS blue and red arms, respectively, and those of the WHT observations were 57°, 0.78 arcsec, and 2.3 Å and 3.5 Å for the ISIS blue and red arms, respectively.

We observed A 58 on 2021 June 11 (2021.44) with ALFOSC mounted on the 2.5 m NOT of the ORM. The E2V CCD detector was used, providing a spatial scale of 0.21 arcsec pix^{-1}. Three 1800 s exposures were obtained with Grism #7, which has a dispersion of 1.7 Å pix^{-1} and a spectral range 3650–7110 Å. The slit was placed at a PA of 80° and its width was set at 0.5 arcsec, providing a spectral resolution of 4.2 Å. The average seeing of the night was ∼1 arcsec. All observations were processed following IRAF standard routines (Tody 1986, 1993).

The slit positions of the observations are presented in Figure 4.1, where the left panel presents an HST [N II] narrow-band image of A 58 obtained on 2001 May 27 (2001.40, Prop. ID.: 90920; PI: K. Hinkle), whereas the right panel presents a zoom-in view of the central knot from an HST [O III] narrow-band image obtained on 2009 March 19 (2009.21, Prop. ID.: 11985; PI: G. Clayton).

---

[1] We note that the CAHA observations are proprietary, whereas the WHT observations are public and were downloaded from the Isaac Newton Group Archive at http://casu.ast.cam.ac.uk/casuadc/ingarch.

4.3 Spectral time evolution of A 58

The comparison of multi-epoch spectroscopic observations requires a careful cross-calibration and assessment of the observation conditions (sky transparency, seeing, ...) and instrumental configurations (slit width, slit position angle, spectral resolution, spatial scale, signal-to-noise ratio, ...) To gauge all these effects in the analysis of the spectral time evolution of A 58, we will investigate first the outer nebula, where the intensity of emission lines is expected to vary only on long timescales (Guerrero et al. 2018), and then proceed to the analysis of its central knot.

These analyses will make use of Hβ, Hα, [O III] λ5007 and [N II] λ6584 surface brightness (SB) profiles extracted from the spectroscopic observations. SB profiles along the slits of the spectroscopic observations have also been extracted from the HST WFPC2 WF3 [O III] and [N II] narrow-band images for comparison. The SB profiles are shown in Figure 4.2, where we note the low S/N ratio of the HST [O III] SB profile.

4.3.1 The outer nebula

The comparison of the HST, WHT and NOT [N II] and [O III] SB profiles in Figure 4.2 reveals an excellent match, confirming that there are no drastic SB variations of the outer shell of A 58 in the 2001.40 to 2021.44 period covered by these observations. This is also the case for the HST and CAHA [O III] SB profiles, but not for the [N II] ones, with a larger SB for the CAHA data. A similar SB mismatch is found for other emission lines derived from the CAHA TCS red arm spectrum with respect to the WHT and NOT spectra in nebular regions around the central knot where the SB levels were expected to be similar. We therefore decided to scale down the flux of the CAHA TCS red arm data, which will be not used to investigate SB variations.

The comparison of the CAHA, WHT and NOT Hβ, Hα, [O III] and [N II] SB profiles in Figure 4.2 indicates that the WHT and NOT slits register regions of the outer nebula of similar SB and excitation, but not the CAHA one, with notably different spatial extent and SB variations. The latter would then be excluded for the investigation of the possible time evolution of emission line ratios in the outer nebula.

Spectra of the outer nebula were extracted from the WHT and NOT apertures shown in Figure 4.1 and in the bottom panels of Figure 4.2, which have similar SB profiles in different emission lines. The line fluxes were then measured using the IRAF routine *splot* and their errors computed following the scheme described by Tresse et al. (1999).

The Hβ and Hα fluxes were corrected from the contribution of the He II $\lambda\lambda$4860,6560 Pickering lines scaling their intensities to that of He II λ4686 by 0.052 and 0.136, respectively (Hummer & Storey 1987). These were then used to derive the value of the logarithmic extinction coefficient, c(Hβ), adopting a recombination Case B (Osterbrock & Ferland 2006). The theoretical value of the Hα/Hβ ratio depends on the $T_{\rm e}$, but the $T_{\rm e}$ sensitive [O III] λ4363 and [N II] λ5755 auroral lines are not detected and only upper limits can be set. Using an iterative method for $T_{\rm e}$ and c(Hβ), we estimated upper limits for $T_{\rm e}$ [N II] <3,900 K and $T_{\rm e}$ [O III]

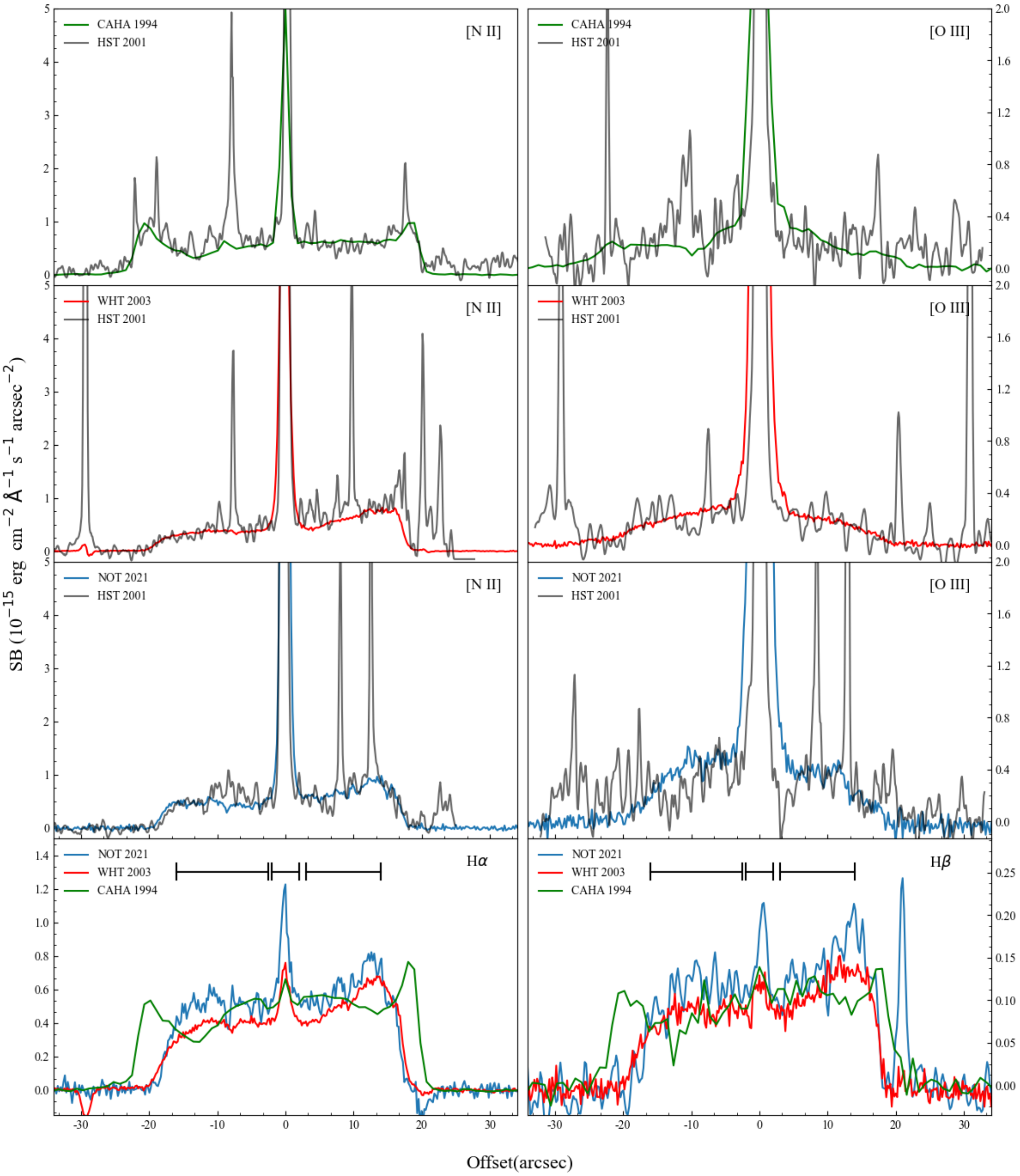

Figure 4.2: Comparison of SB profiles of the HST WFPC2 F502N and F658N (2001.44), and CAHA (1994.57), WHT (2003.58), and NOT (2021.44) Hβ, Hα, [O III] λ5007 and [N II] λ6584. The CAHA Hα and [N II] SB profiles (green in the top-left and bottom-left panels) extracted from the red arm have been scaled by 0.65 to match the HST WFPC2 F658N SB profile. The apertures used to extract the spectra are shown in solid black lines.

Table 4.1: De-reddened line fluxes relative to $F(\mathrm{H}\alpha)$=1 and physical parameters obtained for the three spectroscopic observations of A 58.

	Central knot					Outer nebula	
	CAHA TCS (July 1994)	WHT ISIS (August 2003)		NOT ALFOSC (June 2021)		WHT ISIS (August 2003)	NOT ALFOSC (June 2021)
c(Hβ)	1.15	1.21±0.20	1.15	1.07±0.19	1.15	0.57±0.07	0.64±0.06
[O II] 3727	...	38±7	34±7	104±20	115±23	77±2	...
[Ne III] 3869	...	29±5	27±5	155±27	170±32	12.5±0.8	...
Hζ + He I 3889	...	...	...	2.0±0.5	2.2±0.6	4.6±0.7	...
Hϵ + [Ne III] 3969	...	12±2	11±2	50±9	54±10	7.3±0.7	...
[S II] 4069	...	0.8±0.2	0.7±0.2	1.1±0.3	1.2±0.3	...	...
Hδ 4101	...	...	...	...	...	7.3±0.5	...
Hγ 4340	...	...	...	...	...	16.1±0.6	15.6±0.4
[O III] 4363	...	7.3±1.2	6.9±1.1	16±2	17±3	<0.3	<0.09
He I 4471	...	0.5±0.1	0.5±0.1	0.9±0.2	0.9±0.2	...	...
He II 4686	...	0.4±0.1	0.3±0.1	1.3±0.2	1.4±0.2	9.3±0.4	6.4±0.2
[Ar IV] 4711	...	0.4±0.1	0.4±0.1	1.1±0.2	1.3±0.2	...	...
[Ar IV] 4740	...	0.7±0.1	0.70±0.1	1.0±0.2	1.1±0.2	...	...
Hβ 4861	...	0.4±0.1	0.4±0.1	0.4±0.1	0.4±0.1	32.9±0.8	32.9±0.5
[O III] 4959	27±5	67±10	64±10	172±25	181±26	31.4±0.7	31.7±0.4
[O III] 5007	85±15	205±31	196±30	512±74	537±78	98±2	108±2
[N I] 5199	...	1.7±0.3	1.6±0.3	1.2±0.2	1.2±0.2	...	...
[N II] 5755	0.6±0.1	0.8±0.2	0.8±0.2	0.9±0.2	0.9±0.2	<0.07	<0.03
C IV 5806	8.1±1.6	11±2	11±2	10±2	10±2	...	...
He I 5876	0.8±0.2	2.0±0.4	1.9±0.4	2.7±0.5	2.8±0.5	6.2±0.2	...
[O I] 6300	8.9±2.0	11±2	11±2	13±3	13±3	...	...
[O I] 6363	2.9±0.7	4.0±0.8	4.0±0.8	4.8±0.9	4.8±1.0	1.2±0.1	...
[N II] 6548	6.0±1.4	8.6±1.8	8.7±1.9	10±2	10±2	34±1	28.6±0.5
Hα 6563	1.0±0.2	1.0±0.2	1.0±0.2	1.0±0.2	1.0±0.2	100±3	100±2
[N II] 6584	19±5	25±5	25±6	31±6	31±7	100±3	90±2
He I 6678	0.4±0.1	0.6±0.1	0.6±0.1	0.7±0.1	0.7±0.1	1.3±0.1	...
[S II] 6717	0.5±0.1	1.0±0.2	1.0±0.2	1.0±0.2	1.0±0.2	18.2±0.9	14.4±0.3
[S II] 6731	0.9±0.2	1.4±0.3	1.4±0.3	1.4±0.3	1.4±0.3	12.9±0.4	10.4±0.2
He I 7065	1.1±0.3	1.0±0.2	1.0±0.3	1.0±0.2	1.0±0.2	...	...
C II 7064 +C I 7066	1.0±0.3	1.0±0.2	1.0±0.2	1.0±0.2	1.0±0.2	...	...
[Ar III] 7135	2.2±0.6	1.7±0.4	1.7±0.4	...	...	3.7±0.1	...
[O II] 7320	10±3	6.3±1.6	6.4±1.6	...	...	...	...
[O II] 7330	8.6±2.3	5.3±1.3	5.4±1.4	...	...	...	...
C IV 7724	...	1.1±0.3	1.1±0.3	...	...	...	...
$\log_{10}(F(\mathrm{H}\alpha))$	−15.3	−15.0		−14.80		−13.97	−13.88
SB (10^{-16} erg cm^{-2} s^{-1} arcsec^{-1})	0.6	...	3.9	...	8.0	6.7	8.9
T_e([N II])	14200±100	14700±900	14400±900	13700±600	13800±600	<4400	<3900
T_e([O III])	...	21200±300	20800±300	19200±200	19200±200	<8100	<6100
n_e([S II])	2200±2000	2500±200	2500±200	2700±100	2800±100	<100	<100
n_e([Ar IV])	...	...	...	2600±200	2400±200	...	...

<6,100 K. An intermediate value of 5,000 K was thus assumed for a theoretical value of 3.04 for Hα/Hβ. We note that the values of T_e are notably low, but this seems to be the trend for the outer nebulae of born-again PNe as a consequence of the reduction in the stellar UV flux after the VLTP event (Guerrero et al. 2018).

The values of c(Hβ) are then estimated to be 0.57±0.07 and 0.64±0.06 for the WHT and NOT data, respectively, which can be considered to be consistent among then. Assuming that the extinction is purely interstellar, it can be used to assess the distance to A 58. According to Bayestar19[2] (Green et al. 2018), the extinction along the direction of A 58 varies from $E(g-r)$=0.31±0.02 mag at 0.88 kpc to 0.39±0.03 mag at 3.89 kpc, and then increases to 0.47±0.02 mag for distances above 6.20 kpc. The conversion from $E(g-r)$ to $E(B-V)$ (Schlafly et al. 2018) implies c(Hβ) in the range 0.45 to 0.57 for distances in the range 0.88 to 3.89 kpc, and 0.69 for distances above 6.20 kpc, which bracket the values reported here, but dismiss the lower value of 0.29 and higher value of 1.04 reported previously by Guerrero & Manchado (1996) and Wesson et al. (2008), respectively. The reddening-distance diagram derived from Bayestar19 and the extinction derived from the WHT and NOT data imply a distance of $4.3^{+1.7}_{-0.6}$ kpc towards A 58.

The dereddened line intensities of the outer nebula of A 58 derived from the WHT ISIS and NOT ALFOSC spectra are listed in the rightmost columns of Table 4.1.

4.3.2 The central knot

Spectra of the central knot of A 58 were extracted from the CAHA, WHT, and NOT data using the apertures shown in Figure 4.1 and in the bottom panels of Figure 4.2. Note that the faint emission of the H I Balmer and He I and He II lines from the VLTP ejecta is diluted by the bright emission from the H-rich old nebula (see, for instance, the sophisticated analysis required by the emission of the born-again ejecta of HuBi 1 presented by Montoro-Molina et al. 2022a). This contamination affects specially the CAHA spectrum that used a wider long-slit. To remove the contribution of the emission from the outer H-rich nebula, an average spectrum of the outer nebula was extracted from apertures adjacent to that of the central knot and subtracted from the central knot spectrum after scaling it according to their relative aperture sizes.

The central knot line fluxes were measured from its background-subtracted spectrum as described above for the outer nebula. The fluxes of the Hα and Hβ emission lines were also computed from the SB profiles presented in Figure 4.2 and found consistent with those measured from the central knot spectra. As described in the previous section, the Hβ and Hα line fluxes were corrected from the contribution of the He II $\lambda\lambda$4860,6560 Pickering lines.

The intensities of the Hα and Hβ emission lines were then used to derive the value of c(Hβ) adopting also a recombination Case B and following the iterative method with T_e described above. In this case, a theoretical I(Hα)/I(Hβ) flux ratio of 2.76 was adopted, as appropriate for a T_e value of 20,000 K (see Table 4.1). Values of c(Hβ) for the knot of A 58 are found to be 1.21±0.20 and 1.07±0.19 for the WHT and NOT observations, respectively. The decrease of

---

[2] `http://argonaut.skymaps.info`

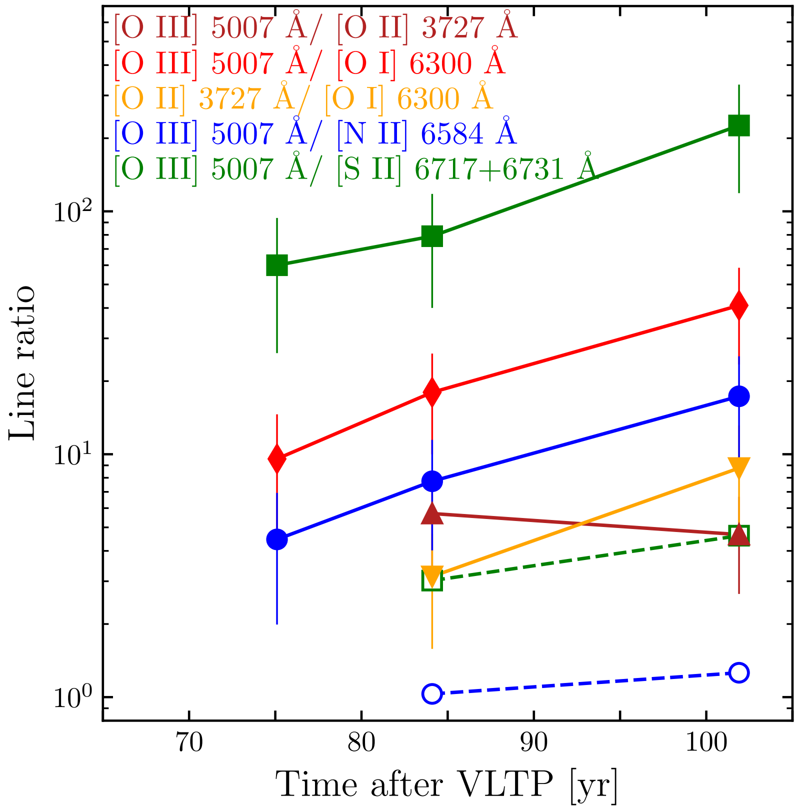

Figure 4.3: Variation with time of selected line ratios of A 58 for its H-deficient knot (filled symbols, solid lines) and H-rich outer nebula (open symbols, dashed lines). Symbol shapes and colors represent different ratios. Time is measured from the VLTP event of V605 Aql in July 1919.

the value of $c(\mathrm{H}\beta)$ in the time period from 2003.58 to 2021.44 is not considered to be significant given the uncertainties of each individual value. The intrinsic line intensities of the central knot of A 58 referred to a value of unity for Hα are presented in Table 4.1. The line intensities of the WHT and NOT spectra were dereddened using the value of $c(\mathrm{H}\beta)$ derived for each one, but also using an average value of 1.15. The latter is used for the CAHA TCS spectrum due to its red arm calibration uncertainty.

4.3.3 Spectroscopic evolution

The emission line intensities and Hα fluxes and SBs of the outer H-rich nebula and the H-deficient knot of A 58 derived from multi-epoch optical spectroscopic observations spanning from 1994 and 2021, including CAHA 1994.57, WHT 2003.58, and NOT 2021.44 data, are presented in Table 4.1. These correspond to 75.1, 84.1, and 101.9 yrs after the VLTP event, respectively. Information on the [O III] λ5007 and [N II] λ6584 emission lines is also provided by the 2001.40 (81.9 yrs) and 2009.21 (89.7 yrs) HST WFPC2 data. Different line intensity ratios derived from these data sets are presented in Figure 4.3, that will be used in conjunction with the SB profiles shown in Figure 4.2 to investigate the spectral variability of the outer H-rich nebula of A 58 and the H-deficient ejecta near its central star V605 Aql.

The ≈30% increase of the Hα SB of the outer shell of A 58 in the time period between

2003.58 and 2021.44 shown in Table 4.1 and Figure 4.2 is suggestive of an apparent overall nebular brightening. We note, however, that it might be within the cross-calibration uncertainty and certainly affected by the different nebular regions probed in these two epochs. On the other hand, the line intensities in Table 4.1 indicate moderate ≈10% increase of [O III] and decline of [N II] in the same time period, with larger ≈25% reductions of the He II and [S II] emission lines. These trends are illustrated for the [O III]/[N II] and [O III]/[S II] line ratios in Figure 4.3.

On the other hand, the emission line intensities, the Hα SB, and the SB profiles of the H-deficient knot reveal unquestionable changes with time. Its Hα emission has brightened by a ≈13 factor, whereas the line intensity ratios imply also significant variations, with a general increase of all line intensity ratios with respect to Hα. This emission enhancement affects notably the high-excitation emission lines of [Ne III], He II, and [O III]. As for the low-excitation emission lines, the [O II] emission lines increases its intensity notably from 2003 to 2021, whereas those of [N I] and [S II] $\lambda\lambda$6716,6731 present marginal 5%–10% decrements. These large variations reflect in the obvious trends shown in Figure 4.3.

4.3.4 Comparison with previous spectroscopic information

As noted in Section 3.1, the values of $c(\mathrm{H}\beta)$ derived for the outer shell here and those reported by Guerrero & Manchado (1996) and Wesson et al. (2008) differ notably. This is also the case for the central knot, for which our value of $c(\mathrm{H}\beta)$ of 1.15 is notable smaller than that of 2.0 reported by Wesson et al. (2008).

A detailed comparison with the line ratios presented by these authors confirms the issue with the flux calibration of the CAHA TCS red arm of the data set used by Guerrero & Manchado (1996) reported in Section 3.1. The line ratios of the outer shell among the different works may differ up to 25%, which can be considered otherwise generally consistent given the different apertures used to extract the spectra here and in these works. The latter included the low-excitation nebular edge that was purposely excluded here to allow a multi-epoch comparison. As for the central knot, the dependence with the definition of the spectral aperture, which is not provided by these authors, is even more critical, given its small angular size. Moreover the determination of the Hβ and Hα line fluxes relies strongly on the capability to remove the contribution of their bright emission from the outer shell to that of the central knot.

A careful double-check of the flux calibration used here for the WHT ISIS and NOT ALFOSC data against the spectro-photometric standard stars has been successfully passed. Therefore, it can be concluded that, besides the issue in the CAHA TCS red arm calibration discovered here, the difference in the line intensity ratios fluxes presented in this chapter with respect to those presented by Guerrero & Manchado (1996) and Wesson et al. (2008) can be interpreted in terms of the different spectral apertures defined by each author and the method used to subtract the nebular emission of the outer shell from the central knot.

4.4 Origins of the variations

The analysis presented in the previous section implies that the emission from the outer shell of A 58 presents only subtle variations if any in the time period investigated, whereas its central H-deficient knot has brightened dramatically and experienced notable spectral variations. Its emission has indeed brightened in the period 1994.57 to 2021.44 by factors ≈13 for Hα and $\gtrsim$80 for [O III], in line with the radio brightening observed since 2005 (van Hoof et al. 2006).

Three different non-exclusive mechanisms can be argued to produce these variations: *i*) the expansion of the H-deficient ejecta can be expected to reduce its optical thickness and, as it becomes more transparent with time, the extinction will also reduce, *ii*) the effective temperature increase of the CSPN of A 58 results in a much larger ionizing photon flux that changes the ionization balance, and *iii*) the shocks associated with the expansion of the H-deficient ejecta reach a larger volume of gas with time.

4.4.1 Dilution of the Ejecta

The values of the logarithmic extinction $c(\mathrm{H}\beta)$ obtained for the WHT (2003.58) and NOT (2021.44) observations are consistent within their error values. It seems that a reduction of the extinction can not be invoked to fully explain the observed SB variations. Furthermore, the variations in ionization stage would be difficult to explain by changes in the transparency of the ejecta, neither the radio brightening.

4.4.2 Stellar Evolution

To assess the effects of the possible evolution of the ionizing flux from the CSPN of A 58, the photoionization code Cloudy (Ferland et al. 2017) was used to compute a number of synthetic spectra that were accordingly compared to those observed at different epochs. The emitting region was assumed to be a shell with density of 2,000 cm^{-3} and outer radius of 0.02 pc (1 arcsec at our distance estimate of 4.3 kpc, see Sec. 4.3.1). The gas abundances were then adopted to be those reported by Wesson et al. (2008), whereas the stellar parameters of V605 Aql at a time close to those of the WHT observations were adopted to be T_{eff}=95,000 K and L = 600 L$_{\odot}$, similar to those reported in Clayton et al. (2006), i.e., scaling the luminosity to 4.3 kpc. The NLTE PoWR code[3] (see Hamann & Gräfener 2004; Todt & Hamann 2015, and references therein) was then used to produce an input ionizing flux. The inner radius of the emitting region was then varied until the Hα and Hβ fluxes, and the [N II] $\lambda\lambda$6548,6584 and [O III] $\lambda\lambda$4959,5007 line intensity ratios were reproduced. This model, however, could not reproduce the intensities of the auroral [N II] λ5755 and [O III] λ4363 emission lines, neither those of the [S II] $\lambda\lambda$6717,6730, [O I], and [O II] emission lines. A large number of Cloudy models were then attempted varying both the inner radius of the shell and the effective temperature of a black-body model between 70,000 and 115,000 K to probe both the evolution of the size of the ionized region and effective stellar temperature. Whereas these models were able to reproduce the intensity enhancement of the [O III] and [N II] emission lines, they under-predicted largely

---

[3] `https://www.astro.physik.uni-potsdam.de/~wrh/PoWR/powrgrid1.php`

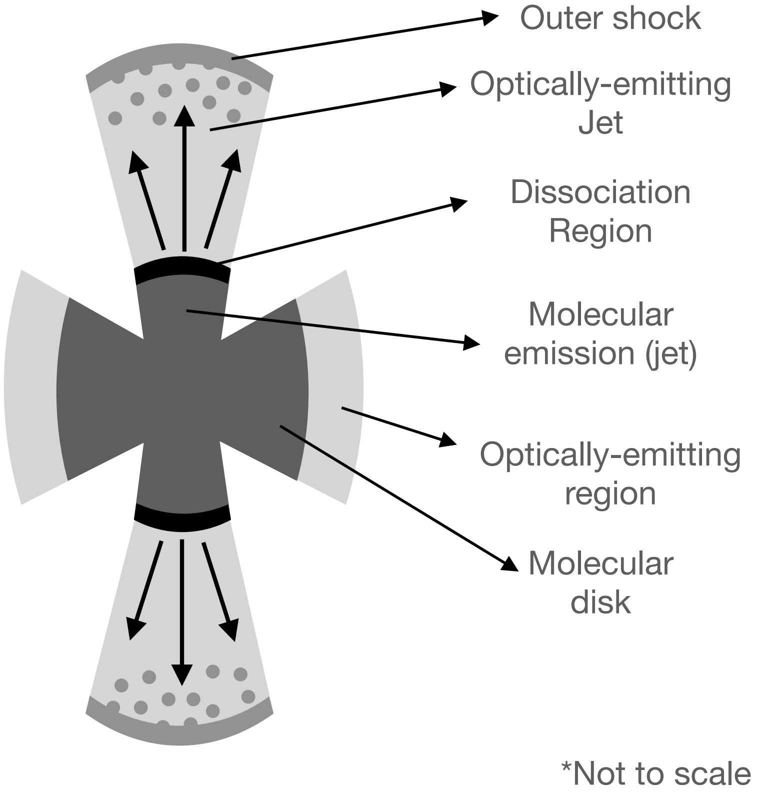

Figure 4.4: Sketch illustrating the molecular and ionized components of the H-deficient ejecta of A 58. The propagation of the molecular jet component produces a shock that dissociates the molecules (dissociation region), whereas the propagation of the ionized jet component shocks the old H-rich nebula (outer shock).

the intensity of the [S II] lines and failed notably to reproduce the time evolution of the [O II] doublet. In this simplistic model for the physical structure of the ejecta and input ionizing flux, the time evolution of the size of the ionized region and effective stellar temperature can not fully explain the observed line intensity ratio variations.

4.4.3 Shocks

It shall be noticed that the most problematic emission lines for the photoionization models, i.e., the [O II] and [S II] emission lines, are very prone to the effects of shocks. As a matter of fact, the [O III]/Hβ, [N II]/Hα, and [S II]/Hα line ratios observed at different epochs in the central knot of A 58 occupy loci associated with shocks in BPT ionization diagrams (Baldwin et al. 1981). This is also the case if these ratios were to be corrected by the low H content implied by the abundances measured by Wesson et al. (2008). These authors actually discarded the relevance of shocks arguing that the mechanical luminosity of the stellar wind was a tiny fraction of the stellar luminosity. This is certainly the case, as it is also that the fast stellar wind ($v_{\infty} = 2,500$ km s^{-1}) is not responsible of the shocks resulting in the line ratios observed in the central knot of A 58. These are otherwise indicative of much smaller velocity shocks that would be associated with the 180–270 km s^{-1} expansion of the H-poor ejecta (Pollacco et al. 1992; Tafoya et al. 2022).

We therefore propose that shocks contribute significantly to the total emission observed in the central knot of A 58, being responsible for the time evolution of its emissivity and ionizing stage. The recent detection of a fast ($\sim$280 km s^{-1}) bipolar molecular outflow at the heart of A 58 (Tafoya et al. 2022) with an apparent kinematic age ($\lesssim$20 yr) much smaller than that of the VLTP event ($\approx$100 yr) suggests the concurrent presence of molecular and ionized components in this outflow. This is illustrated in the scheme of the collimated outflow of A 58 shown in Figure 4.4, which is reminiscent of the early evolution of a common envelope with a companion just after the main star experienced a VLTP (Rodríguez-González et al. 2022) inspired by the recent suggestion of a cooler companion of the CSPN of the born-again PN A 30 (Jacoby et al. 2020).

The molecular outflow is still been launched and, as it shocks material previously ejected, molecules would be dissociated and incorporated to the ionized component. Meanwhile the ionized component itself would be propagating an outer shock through the old nebula. As these two shocks proceed, the mass of the ionized gas increases, and thus its emissivity, whereas the emission from species sensitive to the velocity regime of the shock, such as O^{++}, O^{+}, and N^{+}, is enhanced.

4.5 Final Remarks

The analysis of multi-epoch spectroscopic observations of the outer shell and central knot of the born-again PN A 58 spanning over two decades has revealed a clear brightening and spectral evolution of the latter. We note that the multi-epoch spectroscopic observations do not probe exactly the same spatial regions, but the apertures used to extract spectra at each epoch have been carefully selected to register regions with similar properties. At any rate, the observed spectral changes are too large to be explained by this alone.

Finally we note that the chemical abundances derived for the central knot of A 58 would vary notably depending on whether the emission originates from shocked or photoionized plasmas (see, for instance, Montoro-Molina et al. 2022a). If shocks were indeed the prevalent excitation mechanism, the current abundances estimates (Guerrero & Manchado 1996; Wesson et al. 2008) would need to be revisited accordingly. This would require a major model effort (physical structure and velocity field of the ejecta, shock models, ...) that is besides the scope of this work (Rodríguez-González et al., in preparation) and that should account for the different spatial coverage of the available multi-epoch spectroscopic observations.

Chapter 5

Optical tomography of the born-again ejecta of A 58

Chapter based on the article published in Astronomy & Astrophysics by Montoro-Molina B., Tafoya D., Guerrero M. A., Toalá J. A., Santamaría E. in 2024, volume 684, A107. doi:10.1051/0004-6361/202348528

Abstrac

In a born-again PN, processed H-deficient material has been injected inside the old, H-rich nebula as a result of a VLTP event. Long-slit spectra have been used to unveil the chemical and physical differences between these two structures, but the ejection and shaping processes remain still unclear. In order to peer into the morpho-kinematics of the H-deficient ejecta in the born-again PN A 58, we present the first integral field spectroscopic observations of a born-again PN as obtained with GTC MEGARA. We detect emission from the Hα, He I, [O III], [N II] and [S II] emission lines, which help us unveil the expansion patterns of the different structures. In combination with ALMA and *HST* data we are able to produce a complete view of the H-deficient ionized and molecular ejecta in A 58. We propose an hourglass structure for the ionized material that embraces molecular high-velocity polar components, while bisected by an expanding toroidal molecular and dusty structure. Our results leverage the role of a companion in shaping the VLTP ejecta in this born-again PN.

5.1 Introduction

Models predict that the duration of the VLTP is short (10–200 yr; Miller Bertolami et al. 2006), which makes it difficult to identify born-again PNe. This would explain that only a handful of objects have been identified as born-again PNe, being A 30, A 58, A78 and the SO the most studied cases (see, e.g., Jacoby 1979; Nakano et al. 1996; Clayton et al. 2006). Spectroscopic studies have helped unveil the extreme abundances differences between the born-again ejecta and those of the outer H-rich nebula (Jacoby & Ford 1983; Hazard et al. 1980; Manchado et al. 1988; Montoro-Molina et al. 2022a, 2023; Wesson et al. 2008; Simpson et al. 2022).

The kinematics of the H-deficient ejecta is far from simple. High-dispersion optical spectroscopy works of the most evolved objects of this class, A 30 and A 78, found that the H-deficient material in these born-again PNe has velocities ranging from 40 km s^{-1} up to 500 km s^{-1} (Meaburn & Lopez 1996; Meaburn et al. 1998). In addition, *HST* observations show that the inner structures of the H-deficient ejecta in A 30, A 58 and A 78 have bipolar morphology consisting of a disk-like (or toroidal) structure and a pair of bipolar ejections (Borkowski et al. 1993, 1995; Clayton et al. 2013). The H-deficient clumps have a tadpole (clump-head and tail) morphology, which is indicative of the complex interactions of this material with the photoionization flux and the current fast wind from the CSPN (Fang et al. 2014; Rodríguez-González et al. 2022).

The disk-jet morphology of the H-poor ejecta in born-again PNe is suggestive of the action of binary systems. Moreover born-again PNe are listed among the PNe with the highest abundance discrepancy factor, which is interpreted as caused by the evolution through a binary system (Wesson et al. 2018). The C/O abundances ratio of born-again ejecta seems also consistent with those of novae (Lau et al. 2011), although, once that the C trapped in dust is accounted for, the C/O ratio is actually more consistent with the predictions of a VLTP event of single stellar evolution models (see Toalá et al. 2021a, for the case of A 30). Although VLTP events and binary systems would seem unrelated, a common envelope phase with a binary companion after the VLTP event has been recenlty invoked to explain the bipolar structures and their specific kinematic signatures (Rodríguez-González et al. 2022).

It is thus clear that an appropriate determination of the kinematics of the H-deficient ejecta is most needed to peer into the single versus binary scenarios. Thus far, the best determination for the youngest born-again PNe have been achieved studying the molecular emission. ALMA observations of the SO and A 58 have shown that in both cases the molecular CO emission exhibit bipolar outflows protruding from an expanding toroidal structure; in the SO the deprojected disk velocity is 53 km s^{-1} and that of the bipolar outflow ∼1000 km s^{-1} (Tafoya et al. 2023), while in A 58 the disk is estimated to expand at a velocity of 90 km s^{-1} and its bipolar outflow at 280 km s^{-1} (Tafoya et al. 2022).

In this chapter we start a series of works to study the morpho-kinematics of the H-deficient ejecta of a sample of born-again PNe using the unrivaled capabilities of high-dispersion IFS observations obtained with the Multi-Espectrógrafo en GTC de Alta resolución para Astronomía (MEGARA; Pascual et al. 2019) at the 10.4 m GTC. Here we present results for A 58 that in conjunction with the available molecular emission detected by ALMA provide an unprecedented

Table 5.1: Details of the GTC MEGARA observations of A 58 analyzed in this work.

Dispersion Element	R	Spectral Range (Å)	Exposure Time (s)	Moon	Sky	Airmass	Seeing (arcsec)
VPH665HR-R	20050	6405.6–6798.0	3 × 300	Dark	Clear	1.49	0.9
VPH481MR-B	13200	4585.7–5025.1	3 × 600	Dark	Clear	1.43	0.9
VPH443MR-UB	13050	4226.4–4625.8	6 × 900	Dark	Clear	1.57	0.9

view of this born-again PN.

This chapter is organized as follows. In Section 5.2 we describe our observations and their reduction. The analysis procedure of the data is presented in Section 5.3. The discussion of our results in presented in Section 5.4. Finally, our conclusions are presented in Section 5.5.

5.2 Observations and data Reduction

5.2.1 Integral Field Spectroscopy

IFS observations of A 58 were obtained on 2022 June 21 (Program ID 24-GTC29/22A) using MEGARA at the GTC of the Observatorio de El Roque de los Muchachos (ORM, La Palma, Spain). IFU mode, also called LCB, was used. The volume phase holographics VPH443-MR (MR-UB), VPH481-MR (MR-B), and VPH665-HR (HR-R) were used as dispersion elements. The details of the observations, including spectral properties, exposure times, and observing conditions, are presented in Table 6.1.

The raw MEGARA data were reduced following the Data Reduction Cookbook (Pascual et al. 2019) using the *megaradrp* v0.10.1 pipeline released on 2019 June 29. This pipeline applies sky and bias subtraction, flat-field correction using halogen internal lamps, wavelength calibration, and spectra tracing and extraction. The final output is a FITS file that contains the science-calibrated RSS for each fiber, with metadata of the relative fiber positions to the IFU center. This RSS FITS file is converted into a 52 × 58 map of 0.2 arcsec pix^{-1} on the spatial dimension and 4300 spaxel along the spectral axis using the regularization grid task *megararss2cube*. The flux calibrations were performed using observations obtained immediately after those of A 58 of the spectrophotometric standard stars HR 7950, HR 7596, and HR 4963 for the VPH665-HR, VPH481-MR, and VPH443-MR, respectively.

5.2.2 Long-slit Echelle Spectroscopy

High-dispersion spectroscopic observations of A 58 were obtained on 2002 June 23 using the echelle spectrograph on the Cerro Tololo Interamerican Observatory (CTIO) 4 m Víctor Blanco (a.k.a. Blanco) telescope. The spectrograph was used in its long-slit mode with the 6563/75 narrow-band filter, whose ≈75 Å in FWHM bandwidth isolates the echelle order including the Hα and [N ii] $\lambda\lambda$6548,6584 emission lines. The 79 line mm^{-1} echelle grating and the long-focus red camera were used, resulting in a reciprocal dispersion of 3.4 Å mm^{-1}. The data were recorded with the SITe 2K CCD #6, whose pixel size of 24 μm provides a spatial scale of 0.26 arcsec and a spectral sampling of 0.081 Å pixel^{-1} (i.e., 3.7 km s^{-1} pixel^{-1}) along the dispersion direction. The slit has an unvignetted length of 3 arcmin and its width was set to 1.4 arcsec, resulting in an instrumental resolution of 9.1 km s^{-1}. Two individual 750 s exposures were obtained with the slit oriented along a position angle (PA) of 50°, i.e., along the central ejecta. The angular resolution, determined by the seeing measured at the DIMM, was ≈1.0 arcsec.

The spectra were reduced using standard IRAF (Tody 1993) routines for two-dimensional spectra. The wavelength scale and geometrical distortion were corrected using a two-dimensional fit to an arc exposure obtained using Th-Ar calibration lamps immediately after the science exposure. The deviation of the residuals of the two-dimensional fit to the Th-Ar arc is found to be better than ≈0.004 Å (0.2 km s^{-1}). The telluric emission lines, which includes mostly OH emission lines, but also the geocoronal Hα line, were removed by fitting and subtracting the background using low-order polynoms. Before this procedure, the telluric lines were used to confirm the accuracy of the wavelength calibration to be better than 0.3 km s^{-1} using their theoretical wavelengths (Osterbrock et al. 1996).

5.2.3 Milimeter/submillimeter Interferometric Observations

We retrieve high angular resolution (0.07×0.1 arcsec^2) observations obtained with the ALMA used to detect the continuum and molecular emission from A 58. These observations correspond to project 2019.1.01408.S (PI: D. Tafoya) and their details can be found in Tafoya et al. (2022).

5.3 Data analysis

5.3.1 Spectral Line Profiles

The GTC MEGARA observations detected emission from the [O III]$\lambda\lambda4363, 4959, 5007$, [N II]$\lambda\lambda6548, 6584$, [S II]$\lambda\lambda6716, 6731$, He I $\lambda6678$, He II $\lambda4686$, Hβ and Hα emission lines. We note that the C II 4267 Å emission line is not detected in the VPH433-MR observations at a 3-σ upper limit of 3.6×10^{-16} erg cm^{-2} s^{-1}.

Spectral profiles of key emission lines of A 58 are presented in Fig. 5.1. The profiles of the H-poor ejecta (red dashed histograms in Fig. 5.1) have been extracted from a circular region 1.8 arcsec in radius around the brightest region. These spectra include significant contamination from the surrounding old, H-rich nebula. This emission is estimated by averaging four apertures located in each quadrant of MEGARA's FoV with the same size as that used for the central ejecta. The emission line profiles from the surrounding nebula (gray solid histograms in Fig. 5.1) present a well-marked double-peak structure in the [N II] and H I Balmer lines, as well as in the fainter and noisier [S II] emission lines. The [O III] emission line seems to be consistent with a double-peak profile, but the components are broader and blended. Although this could be attributed to the lower spectral resolution of the blue MR-B VPH ($R \simeq 13200$) that registered this line compared to the red HR-R VPH ($R \simeq 20050$), the similarity of the Hβ (not shown here) and Hα nebular profiles implies that the components of the nebular [O III] emission line are truly broader. Finally the [O III] $\lambda4363$ and He lines do not present emission from the surrounding old nebula.

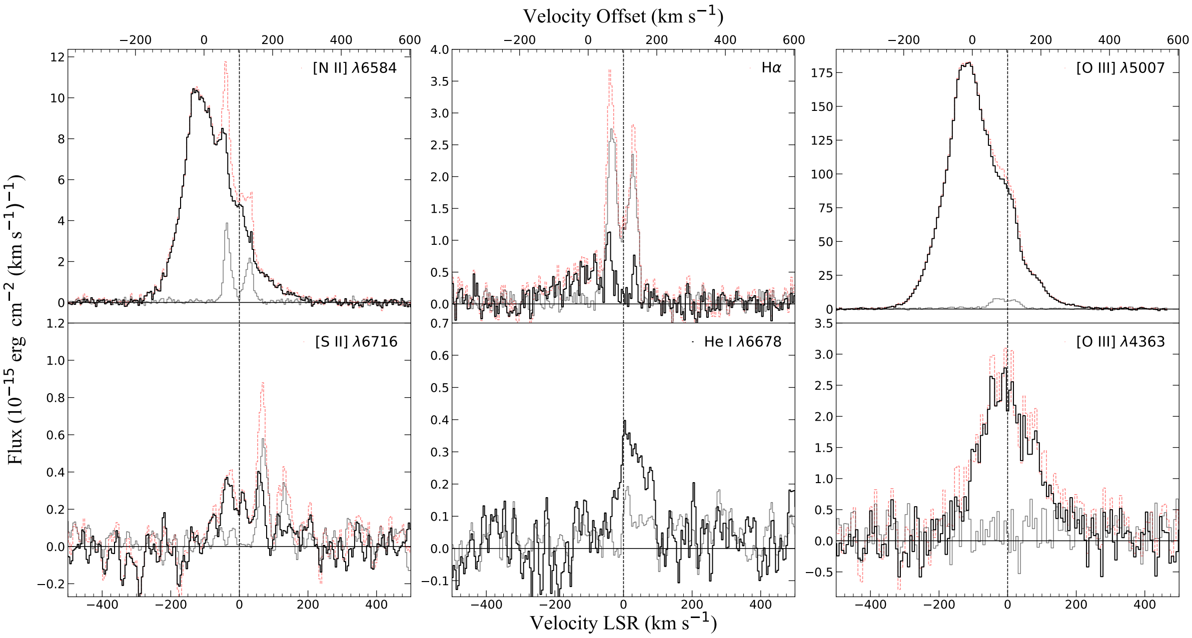

Figure 5.1: GTC MEGARA emission line profiles of the central ejecta of A 58 (red dashed line) extracted from a 1.8 arcsec in radius circular region, and surrounding nebula (grey solid line) averaged from four regions of the same size located at the corners of the MEGARA FoV. The [N II] λ6584, Hα, [O III] λ5007, and [S II] λ6716 emission line profiles of the central ejecta include notable contribution from the surrounding nebula. The surrounding nebula emission profiles of these lines have been subsequently subtracted to obtain the net emission line profiles of the central ejecta (black solid line), whereas for the He I λ6678 and [O III] λ4363 emission line profiles only a constant level representative of the continuum emission has been subtracted. As described in the text the subtraction of the emission from the surrounding nebula is not perfect most likely given its non uniform surface brightness. The horizontal line marks the continuum level, while the vertical line marks the systemic velocity of +103 km s^{-1} of the surrounding nebula.

The blue component of the different emission lines from the outer nebula is consistently narrower and more intense than its red counterpart. If the expansion velocity of the nebula, $V_{\rm exp}$, is assumed to be half the separation between the red and blue components, we derive velocities of 30 and 35 km s^{-1} for Hα and [N II], respectively, which are consistent with the expansion velocities of these emission lines derived from the CTIO long-slit echelle data.

Once the contribution of the old surrounding nebula is subtracted from the spectrum of the aperture encompassing the central ejecta, the remaining emission shall be attributed to net emission from that central ejecta (solid black lines in Fig 5.1). We note, however, that some residual emission subsists, as, for instance, the blue-shifted peak at $V_{\rm LSR} \approx 60$ km s^{-1} in the [N II] emission line and the narrow components at $V_{\rm LSR} \approx 60$ km s^{-1} and ≈ 130 km s^{-1} in Hα. These residuals most likely result from spatial variations of the emission of the surrounding old nebula (see, e.g., figure 2 in Guerrero & Manchado 1996).

The spectral profile from the central ejecta is asymmetric in all emission lines shown in Fig. 5.1. The emission peaks bluewards, very notably in the [N II] and [O III] emission lines at $V_{\rm LSR} \approx -20$ km s^{-1}. In these emission lines, the line profiles show wings that extends in the range -200 km s^{-1} $\lesssim V_{\rm LSR} \lesssim +300$ km s^{-1}. The overall properties of these emission lines

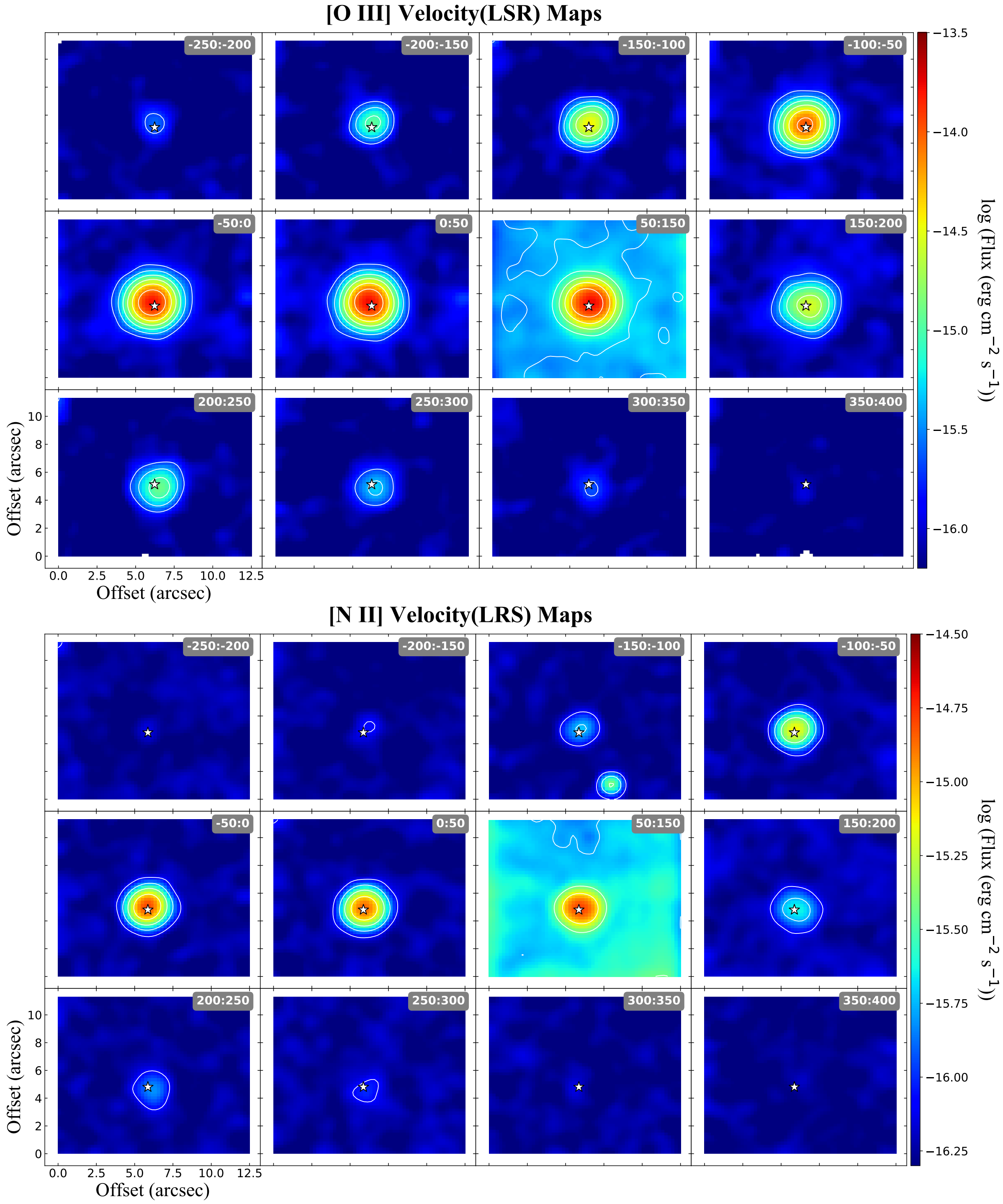

Figure 5.2: GTC MEGARA VPH481-MR [O III] λ5007 (top) and VPH665-HR [N II] λ6584 (bottom) channel maps of A 58. Each map shows the integrated emission in the channles within the LSR velocity range labeled on the upper right corner of each map. Contours corresponding to 2.4%, 5%, 11%, 23%, and 48% of the emission peak (1.71×10^{-14} and 1.61×10^{-15} for [O III] and [N II], respectively) are overlaid in all maps (solid white lines). The approximate location of the central star is marked by a white star.

are very similar to those presented by Pollacco et al. (1992), although the data presented here have higher signal-to-noise ratio and reveal more clearly the line wings. Otherwise only the blue component is detected in the Hα, [S ii], and He i emission lines. We emphasize that the non-detection of the He ii λ4686 emission line discards the possible contribution of He ii λ6560 to the emission bluewards of Hα, which is thus confidently attributed to the ejecta. This is the first time that the Hα emission of the born-again ejecta is unambiguously detected, although a revision of figure 2 in Pollacco et al. (1992) reveals arguable evidence for its detection.

5.3.1.1 Systemic velocities of A 58 and its central ejecta

Considering the average of the nebular red and blue components to be the systemic velocity, $V_{\rm sys}$, we derive velocities in the Local Standard of Rest (LSR) from the CTIO echelle data of 101.8 km s^{-1} and 104.4 km s^{-1} for the Hα and [N ii] lines, respectively. An average of 103 km s^{-1} can thus be adopted for the systemic velocity of the old surrounding nebula, which is marked by a vertical dashed line in the different panels of Fig. 5.1. These values are found to be consistent to the observed dips in the GTC MEGARA Hα and [N ii] λ6584 spectral profiles of the outer nebular shell shown in Fig. 5.1.

The only previous high-dispersion spectra of A 58, obtained with the Anglo-Australian Telescope Coudé échelle spectrograph (UCLES), implied a systemic velocity in the LSR of its outer nebula of 86 km s^{-1} (corresponding to a heliocentric velocity of 70 km s^{-1}, Pollacco et al. 1992). This value is not associated to a specific emission line by the authors, neither there is a description of the slit position, besides the information on the 2″-wide slit. Due to the broad slit width, the nebular emission in the Hα and [N ii] emission lines is more prominent than the profile shown in Fig. 5.1, making the double-peak quite noticeable. Later on, Clayton et al. (2013) analyzed the spectra presented by Pollacco et al. (1992) and derived a systemic velocity in the LSR of 96 km s^{-1} (or a heliocentric velocity of 80 km s^{-1}).

The differences between the systemic velocity derived here and those reported by Pollacco et al. (1992) and Clayton et al. (2013) are 17 km s^{-1} and 7 km s^{-1}, respectively. It is important to note that the original spectra presented by Pollacco et al. (1992) were not available to Clayton et al. (2013), who used a digitized version of the figures of the spectra and therefore adopted the same wavelength calibration. If we compare the dispersion of the UCLES and CTIO spectra, the spectral dispersion of the latter is approximately ten times higher than that of the UCLES spectra. The calibration and analysis of the CTIO data seems very reliable, as described in Section 2.2. Therefore the value of 103 km s^{-1} presented here is preferred for the systemic velocity of the outer shell of A 58.

Regarding the central ejecta of A 58, it is not possible to derive a systemic velocity from the optical emission lines as their profiles are highly asymmetric, most likely due to the strong extinction of this region (Montoro-Molina et al. 2022b) absorbing preferentially the red component. On the other hand the radio emission of molecular material, which is mostly unaffected by the extinction, allows a more reliable determination of the systemic velocity of the recent ejecta. The spectral profile of the CO ($J = 3 \rightarrow 2$) emission from the central region of A 58 detected by the 12 m Atacama Pathfinder Experiment (APEX) implied an average velocity in the LSR of 96±11 km s^{-1}, which was interpreted as the systemic velocity of the molecular gas around V605 Aql (Tafoya et al. 2017) in agreement with the value proposed by Clayton et al. (2013). We note, however, that the quality of the APEX spectral profile of the CO ($J = 3 \rightarrow 2$) emission line is limited. The subsequent ALMA spectral profiles of the CO ($J = 3 \rightarrow 2$), HCN ($J = 4 \rightarrow 3$), and HCO^+ ($J = 4 \rightarrow 3$) emission line profiles presented by Tafoya et al. (2022) are of higher quality, but these were not used to derive new values of the systemic velocity. Instead, the authors conclude that the systemic velocity derived from APEX were consistent with the double-peak symmetric spectral profiles detected in the ALMA observations.

There is thus a difference of 7 km s^{-1} between the systemic velocity of the H-rich outer nebula derived from the CTIO optical data and that of the H-poor born-again ejecta derived from the APEX radio data, but these can be considered consistent given the uncertainties.

Indeed the dips between the blue and red components of the CO ($J = 3 \rightarrow 2$) and HCO^+ ($J = 4 \rightarrow 3$) emission lines detected by ALMA are suggestive of a value of the systemic velocity slightly larger than that derived from APEX data. We will hereafter consider the systemic velocity of A 58 and the H-poor ejecta around V605 Aql to be 103 km s^{-1}. For this systemic velocity, the peaks of the H-poor ejecta [N II] and [O III] emission line profiles are shifted by ≈ -120 km s^{-1} with respect to the systemic velocity, and their wings extend ≈ -300 km s^{-1} and $\approx +200$ km s^{-1}.

5.3.2 Channel Maps

The GTC MEGARA data cube also allows obtaining spatial information for each spectral channel. The channel maps of the bright [O III] λ5007 and [N II] λ6584 emission lines in the central ejecta of A 58 are shown in Fig. 5.2. Each map is obtained by combining channels within a velocity range of 50 km s^{-1}, except those around the systemic velocity including the nebular emission that have been computed for a velocity range of 100 km s^{-1}.

Fig. 5.2 reveals a trend in the spatial location of the emission from the born-again ejecta of A 58. The bluest velocity channels, in the range from −250 to −50 km s^{-1}, show emission Northeast of the CSPN, whereas the emission of the reddest velocity channels in the range from +50 to +350 km s^{-1} departs notably towards the Southwest.

5.3.2.1 Relative location of V605 Aql and the optical outflow

The CSPN of A58, V605 Aql, has not been visible since 1923, when it underwent a brightening to fade away immediately afterwards (Seitter 1985; Harrison 1996). Ninety years later, Clayton et al. (2013) estimated its position at R.A.=$19^h18^m20^s.538$, DEC.=$+1°46'58.74''$ under the reasonable assumption that the *HST* F547M image was dominated by the C IV Wolf–Rayet emission feature in the spectrum of V605 Aql, therefore its peak emission revealing its position. The accuracy of these coordinates, however, is affected by the intrinsic limitations of *HST* to assign absolute positions. Indeed the comparison of the *HST* coordinates of V605 Aql with the position of the CO molecular emission derived from ALMA observations, which have higher absolute precision in establishing coordinates, revealed a notorious displacement between them.

At any rate there is no information on the absolute positioning of the MEGARA data cubes, which compromises a comparison of the spatial properties of the optical outflow with the *HST* and ALMA observations. To compensate this lack of information and to allow the spatial comparison of the *HST*, ALMA and MEGARA observations, the stellar continuum in the MEGARA observations can be used to determine the position of V605 Aql. Continuum images were thus built from the VPH481-MR and VPH665-HR data cubes collapsing spectrally all channels with no line emission contribution, avoiding the noisiest ones as well. The position of V605 Aql was then determined by adjusting a two-dimensional Gaussian to the stellar emission located near the center of the image. This procedure revealed an offset between the position of the star in the VPH481-MR and VPH665-HR data cubes of 1.3 pixels, i.e., 0.26 arcsec, which is most likely due to irregularities in the surface and/or exact positioning of these two VPHs.

It is worth noting that we also explored the possibility of assigning the position of the centroid of the emission at the systemic velocity to V605 Aql. However, this method revealed a quite noticeable shift with the position of the stellar continuum. Apparently the emission at the systemic velocity does not correspond to the location of the CSPN, which reveals a far from simple 3D physical structure of the ejecta.

5.3.3 Boosting the Tomography Spatial Resolution

The spatial resolution of the GTC MEGARA data is limited by the ≈0.9 arcsec seeing during the observations and the coarse 0.62 arcsec in diameter spaxel sampling, which results in a spatial resolution ≈1.1 arcsec. Otherwise the spectral resolution allows investigating the spatial location of the born-again ejecta at different velocities. The high S/N achieved in the MEGARA data actually allows increasing the accuracy of the spatial location of the emission at each velocity channel by a factor ≈10 by the determining the position of the centroid of the optical emission through a two-dimensional Gaussian fit (Condon 1997).

In the top panel of Fig. 5.3 we present both the centroids and the FWHMs (represented as ellipses) of the Gaussian resulting from the fittings for the [O III] (left) and [N II] (right) emission lines, with the position of V605 Aql marked using a ⋆ symbol. These fittings were conducted for channels within the LSR velocity range from −250 to +350 km s^{-1}. Channels with associated centroids located more than 1″ away from the position of V605 Aql or with Gaussian FWHM exceeding 1.5 arcsec in any of its axes were excluded. The centroids and FWHMs are represented with a color code indicating their velocity with respect to the adopted systemic velocity of +103 km s^{-1}.

The spatial distribution of the centroids provides a clearer representation of the trend hinted in Fig. 5.2. The red-shifted emission shifts notably towards the southeast (SE) direction, while the blue-shifted emission moves towards the northeast (NE) direction, which is more pronounced for [O III] than for [N II]. Furthermore, the [O III] emission exhibits a much more neat structure than that of [N II], with centroids of velocity channels ranging from −200 to +80 km s^{-1} with respect to the systemic velocity consistently oriented along a specific direction, whereas the centroids of the [N II] emission are more widely scattered, covering a slightly broader region around the central star. This dispersion cannot be completely attributed

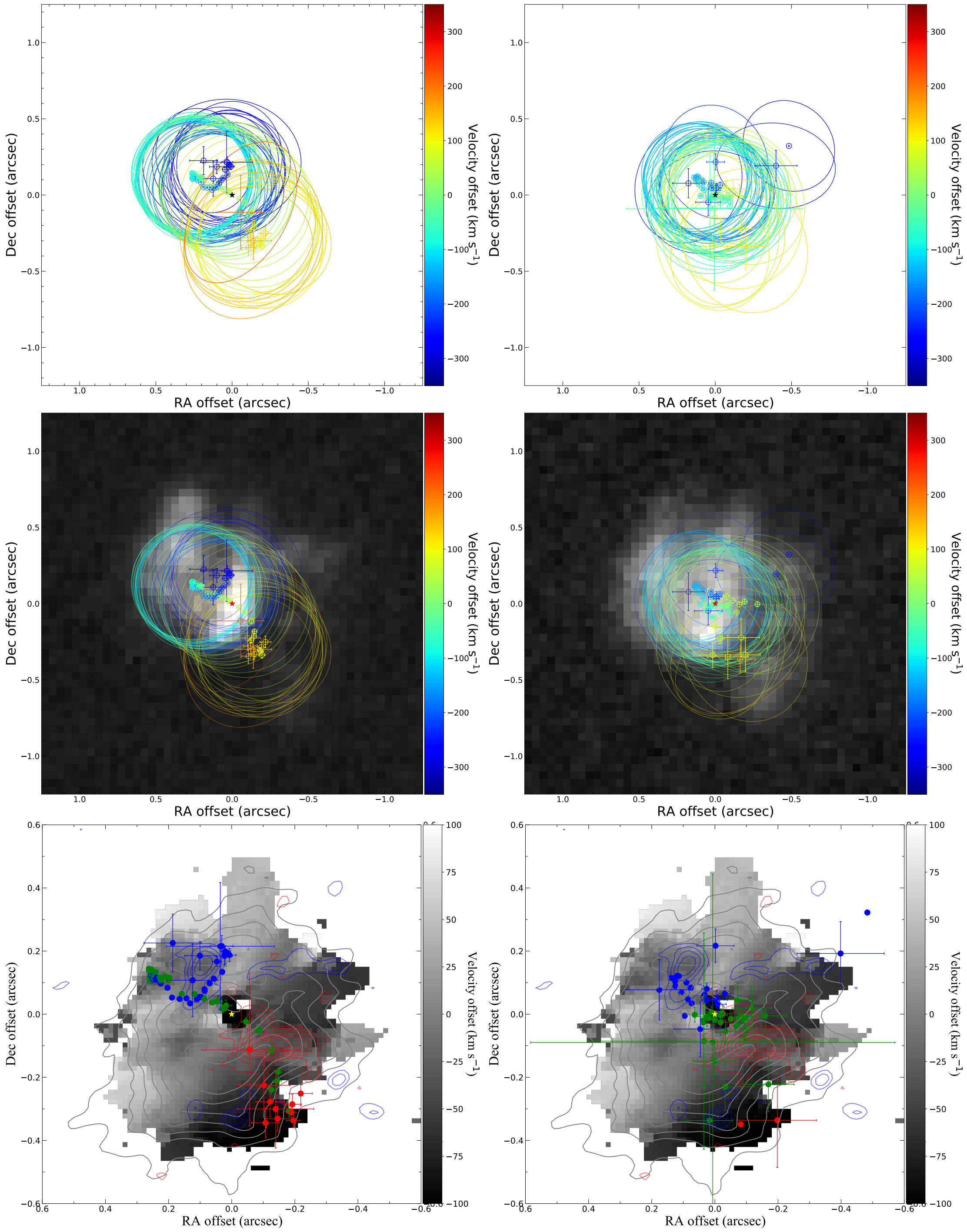

Figure 5.3: Top panels shows the positions of the centroids and the FWHM (ellipses contours) of 2-dimensional Gaussian fits to the emission of [O III] λ5007 (left panels) and [N II] λ6584 (right panels) at each spectral channel of the outflow of A 58 with a color-coded according to their velocity with respect to the $V_{\rm sys}$ (see text for details). The middle panel show the top panels superimposed over the *HST* [O III] λ5007 (left) and [N II] λ6584 (right) images of A 58 obtained in 2009 (PI: G. Clayton; Program ID: 11985). The bottom panel present the spatio-kinematic distribution of CO ($J = 3 \rightarrow 2$) obtained with ALMA (see figure 5 in Tafoya et al. 2022). In these panels the centroids in the velocity range -100 km s^{-1} $\simeq$ V$_{\rm offset}$ $\simeq$+100 km s^{-1} are plotted in green whereas centroids with velocities < -100 km s^{-1} and $> +100$ km s^{-1} are represented by blue and red filled dots, respectively. The approximate location of the central star is marked by a black, red and yellow stars in the top, middle and bottom panels, respectively.

to the lower S/N ratio of this line, but more likely to a broader spatial distribution of the [N II] emission, may be located outside that of [O III].

The spatial behavior of the [O III] emission of the highest velocity channels is noteworthy. The centroids trace a peculiar loop, moving back towards the position of the CSPN first, shifting then to the northwest (NW) direction, and finally receding back to a lesser extent to the northeast (NE) direction. Similar trend is not observed for the red-shift emission, which seems to simply move away with increasing velocity. This is further discussed in Section 5.4.

The middle panels of Fig. 5.3 show the *HST* [O III] and [N II] images with the MEGARA centroids and FWHMs of the corresponding top panel superimposed for comparison. The location of the CSPN was set at the peak of the [O III] image as settled by Clayton et al. (2013) based on the *HST* F547M continuum image. The emission observed from the ejecta by MEGARA is consistent with the emission from the *HST* images, although the emission in the MEGARA maps appears to cover a slightly smaller region than in *HST*. This is somehow unexpected because the expansion of the ejecta $\simeq$10 mas yr^{-1} (Clayton et al. 2013) implies an even larger size of the emission from the time lapse $\approx$13.3 years between the *HST* images (March 2009) and the MEGARA observations (June 2022).

Finally the lower panels of Fig. 5.3 show the CO ($J = 3 \rightarrow 2$) first momentum image presented by Tafoya et al. (2022) overplotted by the MEGARA [O III] and [N II] centroids presented in the upper panels. To establish a morpho-kinematic parallelism between the centroids obtained and the disk-jet scenario described by this author, the color code was modified. Centroids with system velocities from -100 to $+100$ km s^{-1}, in the range of the molecular material at the disk, are represented as filled green points, while centroids below -100 and above $+100$ km s^{-1} are shown in blue and red, respectively. The color code reveals that those centroids of the [O III] emission line presumed to belong to the disk are actually aligned along a distinct direction, PA=60°, while those at higher velocities deviate from this orientation.

This pattern is more evident in Fig. 5.4, where the position-velocity diagrams of the centroids are displayed along two distinct directions: PA=60° (parallel to the disk) and PA=150° (perpendicular to it). A dashed horizontal line has been added at the position of the CSPN and a vertical line for $V_{\rm sys} = +103$ km s^{-1}. In the direction of PA=60° (upper panel), it can be observed that, within the velocity range of -100 to $+140$ km s^{-1} in the LSR system, the centroids remain relatively flat around zero. For velocities below -140 and above $+160$ km s^{-1}, there is only a minimal displacement of 0.2 arcsec relative to the position of the CSPN.

5.4 Discussion

5.4.1 Physical Structure of the H-poor Ejecta of A 58

The physical structure of the H-poor ejecta of A 58 has been subject of different studies in the framework of the born-again phenomenon. Pollacco et al. (1992), Guerrero & Manchado (1996), and Clayton et al. (2013) investigated it from its optical emission, but these studies are hampered by the high and spatially inhomogeneous extinction. Otherwise the radio and sub-mm emission is much less prone to absorption (Tafoya et al. 2017, 2022).

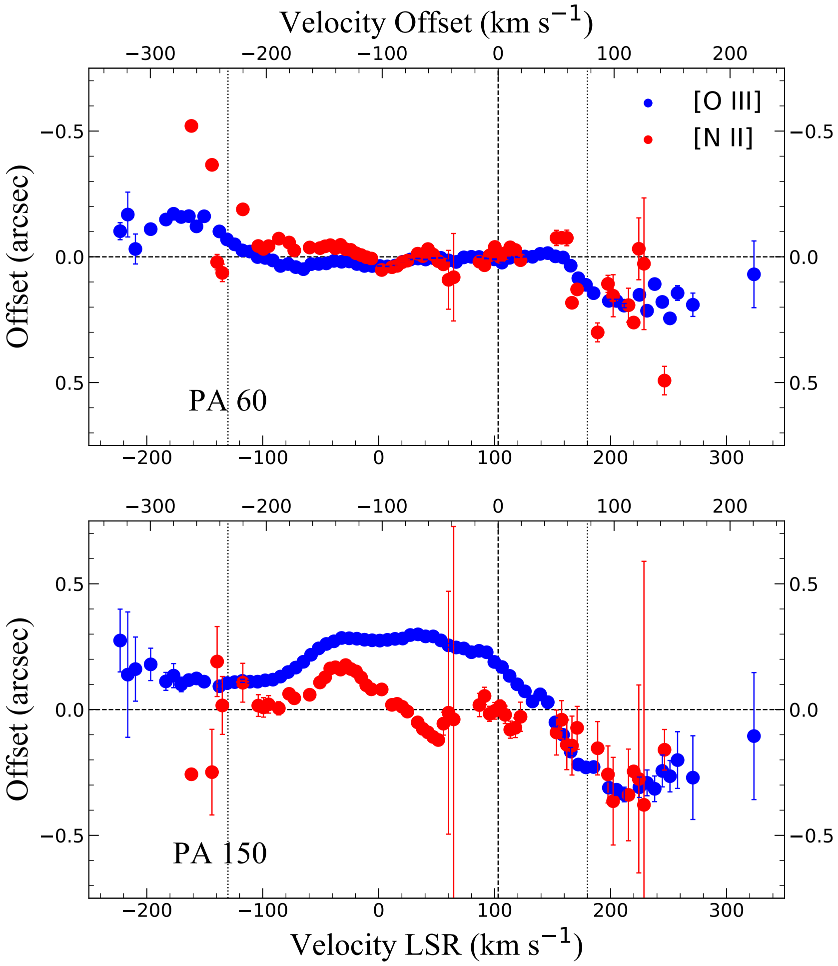

Figure 5.4: Position-velocity (PV) plots in the [O III] λ5007 (red dots) and [N II] λ6584 (blue dots) of the CSPN of A 58 along the PA=60° and PA=150°. Positions have been obtained using a 2-dimensional Gaussian fit of the emission at each spectral channel (see text for details). The x-axis are showed in LSR system (bot) and respect to the systemic velocity (top) for both panels. The systemic velocity of the ejecta and the location of the CSPN are marked by vertical and horizontal dashed lines, respectively.

Tafoya et al. (2022) proposed a model for the physical structure of the molecular gas based on the high-resolution CO (J=3→2) emission detected with ALMA. The model consisted of a radially expanding disk-like or toroidal structure tilted along a PA of 63° with an inclination angle $i \approx 60°$ with the plane of the sky and an expansion velocity up to 80 km s^{-1}, and two high-velocity components (HVCs) orthogonal to the disk with velocities $-140 \lesssim V_{\rm offset} \lesssim -100$ and $+100 \gtrsim V_{\rm offset} \gtrsim +140$.

According to this model based on the CO (J=3→2) spatio-kinematic information, the redshifted emission from the disk is found towards the NE of the CSPN, while the blueshifted emission is found towards the SW. This is exactly the opposite to the spatial distribution of the [O III] and [N II] emission (Fig. 5.3), thus indicating that the molecular disk is not emitting in the optical range, or at least, it is not the dominant structure. The spatial orientation of the CO HVCs is otherwise consistent with that of the [O III] and [N II] emission lines, but the CO HVCs exhibit noticeably lower velocities, in the range from −140 to +140 km s^{-1}, to

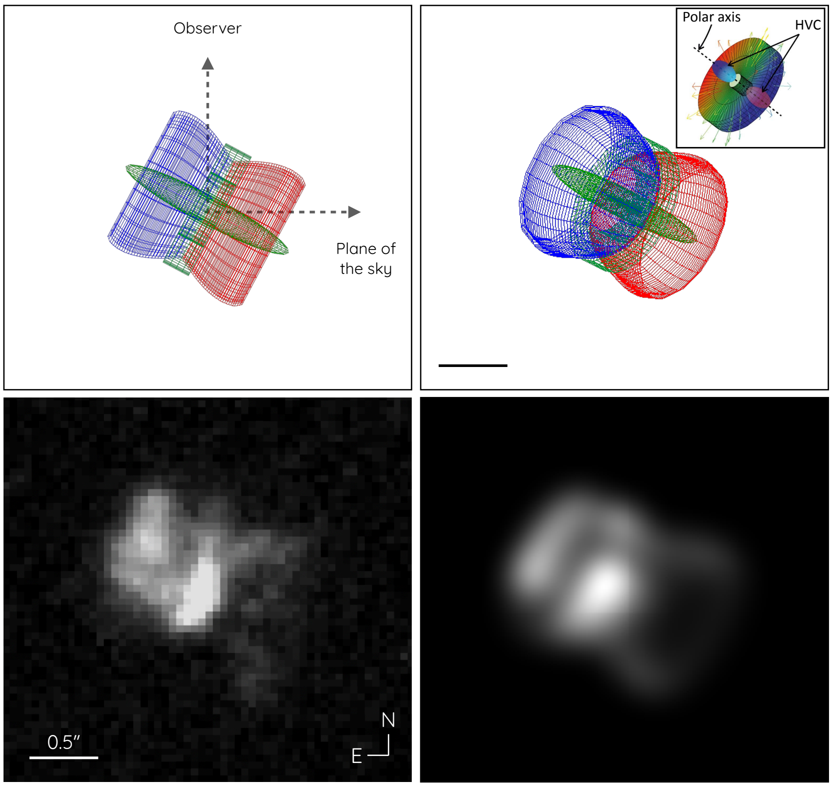

Figure 5.5: SHAPE mesh model of V605 Aql and comparison with its *HST* F502N image of the [O III] λ5007 Å emission line. (top-left) Edge-on view of the SHAPE mesh model consisting of a molecular disk (green) and collimated outflows and ionized bipolar outflows (blue and red). The inclination angle of the disk with the plane of the sky is 63°, as derived from the best-fit model. (top-right) Projection onto the plane of the sky of the SHAPE mesh model. For comparison the right panel of Fig. 5 in Tafoya et al. (2022) is shown in the upper right corner of this panel. (bottom) *HST* [O III] image (left) and synthetic image (right). The [O III] synthetic image is computed from the ionized bipolar outflows. The molecular disk does not contribute to the emission, but it rather absorbs the optical emission behind it, which is accounted for adopting an ad hoc emission law for the ionized material See Section 5.4.1 for details.

those revealed by the optical emission lines (see Fig. 5.1), in the velocity range from -300 up to $+200$ km s^{-1}. The detailed spatial distributions of the CO HVCs and optical emission lines neither agree, with the redshifted optical emission being at the edge of the disk, further away from the CSPN than the corresponding CO HVC, whereas the blueshifted optical emission is generally located closer to the central star than the HVC. The velocity and spatial differences between the molecular and ionized components of the ejecta of A 58 suggest that they do not share the same physical structure.

Elaborating on the high-dispersion spatially-unresolved spectra presented by Pollacco et al. (1992) and using high-resolution multi-epoch *HST* WFPC2 images, Clayton et al. (2013) proposed a sketch for the physical structure of the optical ejecta of A 58. This model consisted of a central disk-like or torus and material moving away from the CSPN perpendicular to the disk, very alike the model proposed for the molecular component by Tafoya et al. (2022). This structure was further geometrically simplified, assuming that the ejecta behaved as an expanding sphere and adopting an extinction that depended on the azimuthal coordinate within it with respect to the line of sight. Although the model reasonably reproduces the emission profile of the spectra, it does not provide information on the actual morphology of the ejecta. The variations in the MEGARA centroids of [O III] and [N II] (Fig. 5.3) do not follow that expected from a simple spherical model, although Clayton et al. (2013) noted variations in the profiles of these emission lines that attributed to small-scale dust inhomogeneities or material clumps. These indentations in the emission line profiles are otherwise not present in our higher-quality spectra (Fig. 5.1). Finally, the symmetric high-velocity ejecta arising from the innermost regions of A 58 sketched by Clayton et al. (2013) requires the spatial location of blue- and red-shifted velocity channels with similar offset velocity to be distributed symmetrically at both sides of the CSPN, with the systemic velocity at its position, which is not the case (Fig. 5.3).

The discrepancies of the predictions of the model presented by Clayton et al. (2013) with the MEGARA observations and the lack of correspondence between the molecular and ionized gas indicate that the physical structure of the latter is rather complex. We here propose a model, whose schematic representation is shown in Figure 5.5, that includes the different molecular and ionized gas components of the H-poor ejecta of A 58. The upper-left panel of this figure shows a spatio-kinematic model created with the software SHAPE (Steffen et al. 2011) consisting of a bipolar structure and a radially expanding disk inclined at an angle of $i = 63° \pm 4°$ with respect to the line of sight. These structures, oriented along a PA of 63° (as proposed by Tafoya et al. 2022), produce the image shown in the upper-right panel of the figure. The mesh model shows the combination of the optical (blue and red) and molecular (green) emissions of A 58, where the geometrical model of the innermost molecular component presented by Tafoya et al. (2022) is shown for comparison. In this new approach, the optical outflows exhibit an hourglass-like morphology, instead of the high-velocity clumps used for the molecular gas. The bipolar lobes have a noticeable thickness, similar to the structure recently proposed for the young molecular ejecta of the SO by Tafoya et al. (2023). The high-velocity components observed in the CO ($J = 3 \rightarrow 2$) emission line are located within the cavities formed by the ionized gas, which is escaping around it, most likely transferring momentum to the molecular material and dragging it outwards.

The molecular disk is not expected to emit in the optical emission line, but it rather extincts the emission behind it. In this sense it should be noted that SHAPE does not account for radiative transfer physics, thus the effects of the spatially-varying extinction caused by the disk cannot be modeled. Instead an arbitrary emission law has been included in the model to simulate both the effects of extinction (emission decreasing with the optical depth along the line of sight and very particularly behind the molecular disk) and distance to the CSPN (emission decreasing with radial distance to the CSPN). The bottom panels show the *HST* [O III] image (left) and a synthetic image rendered from the SHAPE model (right). We remark that the bright "equatorial" band observed in the *HST* images does not arise from the molecular disk, but it originates from the region of the hourglass structures closest to the disk, where they overlap.

Considering this physical structure for the ionized material and assuming a radial velocity vector with homologous expansion at each point, it is possible to interpret the behavior of the

[O III] emission centroids shown in Fig. 5.3. The emission from the outflow, whose kinematics is best seen in the view from the plane of the sky shown in the left panel of Fig. 5.5, can be split into two components: one expanding close to the plane of the sky (1) and another one expanding mostly perpendicularly to it (2). The first component would correspond to those centroids of the emission in the low-velocity range from -100 to $+100$ km s^{-1}. The spatial distribution of the emission at velocities within this range would be reasonably aligned with the direction of the outflow (PA of 63°) and would be more intense in the central regions for the blue emission, where material thickness is maximal, and beyond the molecular disk for the red emission, where extinction is minimal. These emissions would delineate the maximum spatial extent of the outflow. On the other hand, the emission expanding away on near- and far-side within the second, mostly along the line of sight component, will have the highest projected velocities. It would be located closer to the CSPN star in the plane of the sky compared to the emission from the first component. This behavior is reflected in the centroids of gas with velocities $> +120$ and < -120 km s^{-1}. We note that the traces of the centroids form a kind of loop, more evident in the less extincted emission heading towards us. This may suggest either density inhomogeneities within the structure or emission from the edge of the hourglass structure.

The proposed morphology for the H-deficient ionized and molecular components reveals an evolving physical structure, where the acceleration of material close to the CSPN by its sudden ionization and by the emerging stellar wind generates dynamical effects on the molecular material which has prevailed until now, eroding the molecular disk and accelerating the bipolar molecular outflows. In addition to a high adf value in A 58, in the range $\sim$90 (Wesson et al. 2018)[1], these characteristics support previous suggestions of the presence of a companion in born-again PNe (Soker 1997). A companion is definitely required to explain the formation of an equatorial disk and bipolar outflows, but the details of the (stellar or sub-stellar) companion and its orbital parameters are yet unknown.

It is interesting to note that the abundances of the H-deficient material in A 58 obtained from optical spectroscopy agree with predictions from nova events and, thus, a nova-like event has been proposed to have taken place here (Lau et al. 2011). In such models the companion is of stellar origin, but we note that the velocity of the bipolar ejection in A 58 might actually suggest differently. The velocity of the molecular jet must be similar to the escape velocity ($v_{\rm esc}$) of the companion and, thus, the ≈ 280 km s^{-1} velocity of the molecular emission (Tafoya et al. 2022) seems to suggest the presence of a substellar object more massive than a Jupiter-like planet ($v_{\rm esc} \approx 60$ km s^{-1}) or a main-sequence stellar companion with spectral type later than M9 ($v_{\rm esc} \approx 600$ km s^{-1}; Kaltenegger & Traub 2009).

An alternative channel for the formation of disk/jet structures in born-again PNe has recently been proposed by Rodríguez-González et al. (2022). It is suggested that a WD in a binary system, after experiencing a VLTP, inflates its outer layers and enters a common envelope with its companion (that, in the case of A 58, would be a substellar companion). Even though the duration of the VLTP is short ($\lesssim$200 yr; Miller Bertolami et al. 2006), these

---

[1] See `https://nebulousresearch.org/adfs/`

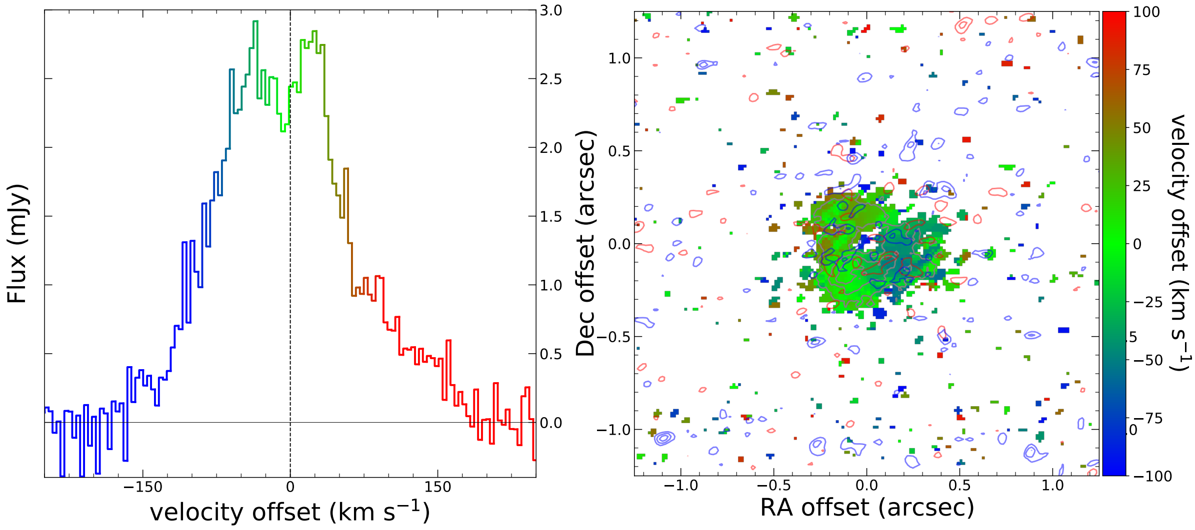

Figure 5.6: Spatio-kinematical distribution of the HCN($J = 4 \rightarrow 3$) emission around V605 Aql. Left: ALMA HCN ($J = 4 \rightarrow 3$) emission line profile from V605 Aql. Right: velocity field (first moment) of the HCN ($J = 4 \rightarrow 3$) emission around V605 Aql in the velocity range $-100 < V_{\rm offset}$ (km s^{-1}) <100. is shown as a color map, according to the color code of the emission line profile in the left panel. The pixels with emission below 3 times the rms noise level of 0.2 mJy beam^{-1} were masked. The gray contours show the velocity-integrated emission (zeroth moment) of the HCN ($J = 4 \rightarrow 3$) in the velocity range $-100 < V_{\rm offset}$ (km s^{-1}) < 100. The gray contours are drawn from 3σ on steps of 3σ (where σ = 6.5 mJy beam^{-1} km s^{-1} is the rms noise level of the zeroth moment image). The blue and red contours show the zeroth moment emission of the HCN ($J = 4 \rightarrow 3$) in the velocity range $-165 < V_{\rm offset}$ (km s^{-1}) < -100 and $+100 > V_{\rm offset}$ (km s^{-1}) $> +180$, respectively. The red contours are drawn for 9, 12 and 15 mJy whereas blue contours are drawn for 7, 9 and 11 mJy.

authors argue that it is sufficient to allow the companion to shape the H-deficient ejecta into a disk plus a bipolar structure. We note that such claims will have to be put to test with future numerical simulations following the specific evolution of a star experiencing a VLTP in a binary system.

5.4.2 Spatial distribution of the HCN and CO high-velocity components

The ALMA CO molecular emission of A 58 has been attributed to a radially expanding disk-like structure and orthogonal compact high-velocity components (Tafoya et al. 2022). This spatio-kinematical structure differs notably from that derived here from optical emission lines of ionized material. Interestingly the spectral profiles of emission lines of other molecules arising from the born-again ejecta, most notably the HCN (J=4 → 3) shown in the left panel of Figure 5.6, also present high-velocity components whose spatial distribution can be compared to those of CO (J=3 → 2), [O III] and [N II].

The ALMA observations have then been used to obtain the first moment image of the HCN (J=4 → 3) emission line shown in the right panel of Figure 5.6. Contrary to the CO molecule, the spatial distribution of the high-velocity component of HCN is not compact, but it is rather diffuse and more extended. While CO is well known for being an excellent tracer of molecular outflows, which could include a wide range of physical conditions, HCN and HCO$^+$

molecules are typically excited within high-density gas. The optical emission lines from ionized material and the HCN molecule would then trace highly excited gas, expelled from regions closer to the central source, whereas the CO molecule would probe denser material from the expanding equatorial disk and molecular outflow.

5.5 Conclusions

We presented the analysis of IFS observations of the born-again PN A 58 obtained with GTC MEGARA. These observations helped us disclose the true kinematics of the optical emission from the born-again ejecta in this PNe. MEGARA's high spectral resolution has allowed us to directly detect the H-alpha emission from the H-poor ejecta without any contamination, which, until now, had only been estimable through various methods, for instance, Wesson et al. (2008) and Montoro-Molina et al. (2022a). Only the blue component is detected, whereas the red component is deemed to be completely absorbed behind a high-density molecular and dusty disk.

We used observations from CTIO to estimate an average systemic velocity of +103 km s^{-1} consistent with the MEGARA data. Previous measurements, both 96 km s^{-1} obtained by Clayton et al. (2013) and Tafoya et al. (2017) for the inner ejecta, are also consistent within the errors values. Nevertheless, the brightening of one side of A 58 and the blue components of the nebular emission lines being broader than the red ones seem to suggest the interaction of the PN with the ISM, which may result in different radial velocities of the old nebula and recent VLTP ejecta.

We have also performed a channel-by-channel Gaussian adjusting of the ejecta emission, improving the modest spatial resolution of our data. This has allowed us to refine the description of the morphology of the optical emission of the ejecta, which initially was assumed to be practically identical to the molecular emission. The high-velocity components now result in a hourglass structure, within which the high-velocity molecular components are located. The SHAPE model presented reasonably reflects the emission detected in the [O III] λ5007 line obtained with the *HST*. It is worth mentioning that the sketches presented by Montoro-Molina et al. (2022b) are in good agreement both with the spectral variability observed in the ejecta and with the proposed spatio-kinematic structure.

Prior knowledge of the spatial distribution of the molecular content of the H-poor ejecta of A 58 has allowed us to interpret the results obtained in the optical range, which would have otherwise been nearly impossible. This insight reveals that molecular material may be playing a significant role in the rest of known born-again PNe, namely A 30, A 78, HuBi 1, and the SO.

Chapter 6

Spatially-resolved spectroscopic investigation of the born-again planetary nebula A 78

Chapter based on the article published in Monthly Notices of the Royal Astronomical Society Astrophysics by Montoro-Molina B., Guerrero M. A., Toalá J. A. in 2023, volume 526, 4359. doi:10.1093/mnras/stad2803.

Abstract

We present the analysis of spatially-resolved spectroscopic observations of the born-again PN A 78 that are used to investigate the chemistry and physical properties of its three main morphological components, namely the inner knots, its eye-like structure, and the low surface-brightness outer nebula. The H-poor chemical abundances of the inner knots confirm the born-again nature of A 78, with a N/O abundances ratio consistent with the predictions of VLTP. On the other hand, the high Ne/O is not expected in VLTP events, which prompts a possible different evolutionary path may be involving a binary system. The low N/O ratio and He/H abundances of the outer shell are indicative of a low-mass progenitor, whereas the chemical abundances of the eye-like structure, which results from the interaction between the H-poor born-again material and the outer nebula, evidence their mixture. Unlike previous works, the extinction is found to be inhomogeneous, being much higher towards the H-poor inner knots, where the presence of large amounts of C-rich dust has been previously reported. Dust-rich material seems to diffuse into outer nebular regions, resulting in zones of enhanced extinction.

6.1 Introduction

The planetary nebula (PN) A 78 consists of an old, elliptical nebula of low surface brightness surrounding a collection of clumps and filaments ordered in an eye-like structure and a series of central cometary knots distributed along a disk-like structure surrounding the CSPN. These unusual structures inside the old PN of A 78 were first imaged by Jacoby (1979), although the limited spatial resolution of these images did not allow resolving in detail the structures close to the CSPN. Spectroscopic observations revealed the innermost knots to be extremely H-deficient (Jacoby & Ford 1983), leading to the speculation that they originated from a recent ejection of material inside the old PN by an unknown mechanism. Iben et al. (1983) described a scenario where such ejections occurred in some PNe during the post-AGB phase of their CSPNe (see also Schoenberner 1979). This event is rare and only a handful of objects have been experienced it including A 30, A 58, A 78, HuBi 1 and SO.

Clegg et al. (1993) were the first to resolve the innermost structures of A 78, but the unprecedented capabilities of the *HST* disclosed in much great detail them (Borkowski et al. 1993), revealing that the inner clumps and filaments appear to be distributed in a disrupted disk plus a pair of jet-like ejections. Meaburn et al. (1998) used high-resolution echelle spectra to show that the clumps in the disrupted disk expand with velocities of $\approx$25 km s^{-1}, but the rest of the H-deficient structures in the eye-like structure reach velocities as high as $\sim$400 km s^{-1}, in particular towards the Southwest of the CSPN.

Multi-epoch *HST* observations corroborated that structures closer to the CSPN expand slower than those located farther away (Fang et al. 2014). In addition, radiation-hydrodynamic simulations presented by those authors showed that the interaction of the current fast wind with the ejecta of a single, instantaneous VLTP event is able to reproduce the complex kinematics of born-again PNe such as A 30 and A 78. Fang et al. (2014) concluded that A 78 experienced a born-again event approximately 1000 years ago.

Since then, the CSPN of A78, which is now classified as a [WC] star, has increased its effective temperature up to 120 kK whilst developing a monstrous stellar wind with terminal velocity $\gtrsim$3200 km s^{-1} (Heap 1979; Herald & Bianchi 2004; Kaler & Feibelman 1984; Toalá et al. 2015).

The born-again nature of A 78 relies on the H-deficient chemical abundances of the recent ejecta, but very few spectroscopic analyses have been obtained up to now. Jacoby & Ford (1983) presented the first intermediate-dispersion spectrum of A 78 and determined chemical abundances on an aperture $\simeq5''$ Northeast of the CSPN. The authors highlighted the multiple-shell nature of this nebula and the scarcity of H and extremely enhanced He abundances, whereas the relative abundances of N, O and Ne were found to be typical of normal PNe. Accordingly it was concluded that the material is not chemically enriched, but rather the result of nuclear processing in a H-burning shell, with conversion to He approaching to 100% completion. Later on Manchado et al. (1988) presented the first spatially-resolved optical spectroscopic study of A 78, including information on the eye-like and inner disk-like structures. The latter exhibits greatly enhanced chemical abundances not only of He, but also N, O and Ne, thus confirming the H-poor nature and chemical enrichment of the recent ejecta. The eye-like

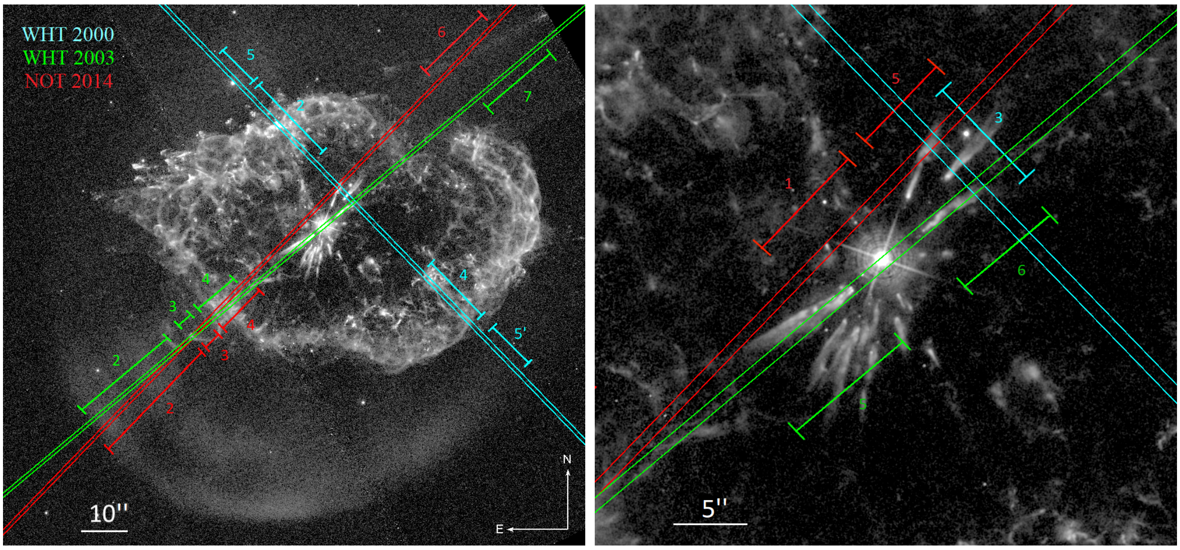

Figure 6.1: *HST* WFC3 F502N image of A 78 (left), zooming into its innermost region (right). The slit positions covered at each epoch are marked with cyan (WHT 2000.50, PA=44°), green (WHT 2003.58, PA=130°) and red (NOT 2014.55, PA=136°) rectangles, respectively. The spatial extent of the apertures used for spectra extraction are also marked with numbered segments of the same colours.

structure has also enhanced O and Ne abundances, but typical He and N abundances of PNe. The revision of the spectroscopic data of Jacoby & Ford (1983) performed by Manchado et al. (1988) seems to imply that they probe a region mixing information from the eye-like and inner disk-like structures, with intermediate abundances. Finally, Phillips et al. (2005) presented spectroscopic information of the eye-like of A 78, but did not carry an extensive analysis.

The previous works were mostly hampered by the limited quality of the pre- *HST* optical images available at their time, which made not possible to reliably assign the spectra to specific morphological features (e.g., a central cometary knot), thus making difficult their interpretation. On the other hand, the spectra mostly probed the bright eye-like structure, but no the outer nebula.

In this work we present an analysis of optical long-slit intermediate-dispersion spectra of A 78 including the outer nebula, the eye-like structure, and a number of central cometary knots, computing physical properties and abundances for them. Archival mid-infrared Spitzer data is also used. The paper is organized as follows. The spectral observations and data reduction are described in Section 6.2. Estimated parameters such as extinctions, temperatures, densities and subsequent ionic and total abundances are presented in Section 6.3. We discuss the results in Section 6.4 and finally present a summary in Section 6.5.

6.2 Observations and data preparation

6.2.1 Long-slit Optical Spectroscopy

We have gathered optical long-slit intermediate-dispersion spectroscopic observations of A 78 from three different epochs spanning from 2000 to 2014. These include two unpublished data

Table 6.1: Journal of high-dispersion spectroscopic observations of A 78.

Telescope	Instrument	Detector	Grating/Grism	λ_c (Å)	Resolution	$\Delta\lambda$ (Å pix^{-1})	PA (°)	Date	Exp. Time (s)
WHT 4.2m	ISIS	EEV12	R600B	4272	2520	0.49	44	2000 July 4	2x2400
		TEK4	R316R	6599	2430	1.47	44	2000 July 4	2x2400
		EEV12	R600B	4272	2540	0.49	130	2003 August 3	9x1800
		MARCONI2	R316R	6599	2460	0.82	130	2003 August 3	9x1800
NOT 2.5m	ALFOSC	E2V CCD	#7	5260	930	1.49	136	2014 July 20	2x1200
		E2V CCD	#14	4630	860	1.40	136	2014 July 20	2x1200

sets available at the Isaac Newton Group (ING) archive[1] obtained with the double-arm ISIS mounted on the 4.2m WHT at the ORM on 2000 July 3 (2000.50) and 2003 August 1 (2003.58) and a long-slit intermediate-dispersion spectroscopic observation obtained on 2014 July 20 (2014.55) with ALFOSC mounted on the 2.5m NOT of the ORM.

The total exposure times of the WHT ISIS observations were 4800 s (2×2400 s) in 2000.50 and 16200 s (9×1800 s) in 2003.58. The R600B grating and EEV12 detector were used for the blue-arm in both epochs, providing a spatial scale of 0.19 arcsec pix^{-1} and a resolution $\sim$ 2530 at 4272 Å.

As for the red-arm, the R316R grating was used in both epochs, but the TEK4 and MARCONI2 detectors on 2000.50 and 2003.58, respectively. The TEK4 detector provided in 2000.50 a spatial scale of 0.33 arcsec pix^{-1} and a resolution of 2430 at 6599 Å

whereas the smaller pixel of the MARCONI2 detector provided in 2003.58 a spatial scale of 0.2 arcsec pix^{-1} and a resolution of 2460 at 6599 Å.

The slit position during the 2003.58 observation was aligned along PA of 130° such that the CSPN, a high-velocity component towards the Southeast of the eye-like structure, and the central knots were registered by the slit (see Fig. 6.1). The slit used in 2000.50 has a PA of 44°, but it did not go through the CSPN. The lack of a clear fiducial reference made unclear the exact location of the slit, that we have otherwise determined comparing the emission profile in the [O III] λ5007 emission line with the profile extracted from the *HST* WFC3 F502N image taken on 2012 November 22. The approximate slit positions are shown in Figure 6.1. The slit widths were 0.88 arcsec on 2000 and 0.76 arcsec on 2003 (see Table 6.1).

The NOT ALFOSC observations used the E2V CCD detector, providing a spatial scale of 0.21 arcsec pix^{-1}. The slit position has an alignment quite similar to that of the 2003.58 observation, with a PA of 136°, just slightly displaced from the CSPN to observe knots located along the polar direction of the inner disk (see Fig. 6.1). The slit width was set to 0.75 arcsec. Two 1200 s exposures were taken with the grisms #7 and #14, which have a resolution of 930 at 5260 Å and 860 at 4630 Å, respectively.

The spectral range 3189.0 to 6875.2 Å was covered by these observations (see Table 6.1).

All data were processed following standard IRAF routines (Tody 1993), which include bias

---

[1] http://casu.ast.cam.ac.uk/casuadc/ingarch/query

subtraction and flat-field correction.

The wavelength calibration was carried out using ThAr and Ne arc lamps. The sky background was subsequently subtracted. The flux calibration was obtained using observations of spectro-photometric standard stars obtained in the same night as the object. We note that the slope of the continuum of the flux-calibrated spectrum of the standard star Hz 44 extracted from the 2000.50 observations using the R316R grating is steeper than the available calibrations, most likely implying a calibration inconsistency. In this case, we applied an additional λ dependent polynomial correction to make the flux-calibrated spectrum of the standard star consistent with the available calibrations.

6.2.1.1 Comparing Multi-epoch Spectroscopic Observations

In this work we will analyse multi-epoch long-slit spectroscopic observations of A 78 obtained on 2000.50, 2003.58 and 2014.55, i.e., up to 14 years apart in time. Recent works on born-again PNe have revealed spectroscopic variations that are noticeable on short-time scales: the H-deficient ejecta of A 58 has experienced a considerable brightening in the time from 1996 to 2021, with notable changes in many emission line ratios (Montoro-Molina et al. 2022b); the old outer nebula of HuBi 1 is recombining as the result of the brightness decline of its central star in the last ≈50 years (Guerrero et al. 2018); the H-rich old outer PN around Sakurai's Star (V4334 Sgr) is also recombining, with line strength variations up to 3% per year in the period 2007 to 2022 (Reichel et al. 2022).

We note that the central stars of these born-again PNe have luminosities and effective temperatures still varying in short-time scales, whereas those of A 78 and its twin A 30 have already entered a phase of stable luminosity and effective temperature. We will therefore assume that no noticeable spectral variations, neither in the inner VLTP ejecta nor in the outer nebular regions, have occurred in the time period from 2000 to 2014 considered here.

The comparison of multi-epoch spectroscopic data requires an accurate knowledge of the observation conditions (seeing, sky transparency, airmass, ...) and instrumental configuration (slit location and position angle, width, grating and its spectral dispersion, spatial scale, ...) at each epoch. In order verify that the calibrations applied to the spectra obtained at the different epochs used here, we have compared surface brightness profiles of the [O III] emission line, the brightest in A 78, extracted from each spectrum to similar profiles extracted from the HST WFC3 F502N image. These are shown in Figure B.1 in Appendix B.1. The comparison of the profiles shape and surface brightness indicates that the flux calibrations of the spectroscopic data are consistent within 10 per cent.

6.2.1.2 One-dimension Spectra Extraction

The born-again PN A 78 is composed of three main parts: a hydrogen-rich old outer nebula with an elliptical shape, a set of H-poor ≈1,000 yr old bright inner knots, and an intermediate eye-like structure. One-dimensional spectra have been extracted for these different structural components. The eye-like structure results from complex hydrodynamic interactions between the current fast wind from the CSPN, the previously ejected VLTP material, and the old outer nebula. This interaction produces high-speed flows as the result of the mass-load of the current stellar wind (Meaburn et al. 1998), but the projection of these features onto bright emission makes difficult its study. Interestingly, Fang et al. (2014) reported a high-velocity filament (their "Q" and "S" features) towards the Southwest of the old outer nebula with a large tangential velocity in the plane of the sky of ≈600 km s^{-1} that is registered by the WHT 2003.58 and NOT 2014.55 observations. We have thus extracted 1D spectra for this component that will be hereafter referred as high-velocity filament (HVF).

The apertures used to extract 1D spectra are shown in Figure 6.1 as numbered segments, using different colours according to the slit from which they have been extracted. In the following the apertures will be labelled according to the instrument used and observation year (W00, W03, and N14 refer to the WHT 2000, WHT 2003, and NOT 2014 data, respectively), adding the aperture number 'X' as 'AX' to the label. Thus, for instance, aperture #2 of the data obtained at the WHT in 2003 will be labelled as W03A2. We note that the spectra of apertures W00A5 and W00A5′ on the outer nebula were added to increase the signal to noise ratio. This aperture will be denoted as W0055′.

The 1D spectra correspond to five apertures on the old nebula, four on the eye-like structure, two registering the HVF, four on central knots and its tails, and one on a central knot Northeast of the CSPN that presumably does not belong to the equatorial disk and has been claimed to be a polar knot. All the 1D spectra are shown in Appendix B.2.

Lines in the spectra were identified and measured by fitting Gaussian profiles with the usual IRAF task *splot*. A list of all the lines observed from the different extraction regions is given in Table 6.2. Line fluxes are conventionally normalized to $F(\mathrm{H}\beta) = 100$ in nebular studies, but because Hβ is so weak in the innermost regions of A 78, fluxes were instead normalized to $F([\mathrm{O\ III}]) = 100$ to avoid large numbers. We emphasize the high nebular excitation, with large [O III] and He II to Hβ line ratios. The correspondence between the nebular excitation and the high effective temperature of its central star (>110 kK; Herald & Bianchi 2004; Toalá et al. 2015) implies that the nebula is in equilibrium with the stellar ionizing flux, reassuring our assumption on the similar properties of spectra obtained 14 years apart.

6.2.2 Archival IR *Spitzer* observations

After the analysis of the IR observations of the born-again PNe A 30 and A 78 presented by Toalá et al. (2021a), we realised that the [O IV] emission line at 25.9 Å is one of the brightest emission lines present in the *Spitzer* Infrared Spectrograph (IRS) spectra. Thus, an appropriate O abundance determination should include this line in the calculations. For this, we retrieved from the NASA/IPAC Infrared Science Archive[2] the *Spitzer* IRS dataset AOKey 10839808 obtained as part of the Program ID 3362 (PI: A. Evans) on 2004 November 14. The map mode was used during the observations. The *Spitzer* IRS observations of A 78 used here cover its central regions as displayed in Figure 4-left of Toalá et al. (2021a).

The *Spitzer* IRS spectra from the LL modules, which cover the 14–38.0 μm wavelength range including the [O IV] 25.9 μm emission line, were processed making use of the CUbe

---

[2] `https://irsa.ipac.caltech.edu/frontpage/`

Table 6.2: De-reddened emission line intensities of A 78. Intensities are normalised to a value of 100 for the [O III] λ5007 Å emission line.

	Old nebula				
	W03A2	N14A2	W00A55′	W03A7	N14A6
$c(\mathrm{H}\beta)$	0.40±0.07	0.37±0.03	0.03±0.00	0.15±0.02	0.14±0.06
[O II] 3726	2.90±1.97	...	...	...	...
[O II] 3729	4.27±1.98	...	...	...	...
[Ne III] 3868	11.82±1.47	7.01±0.89	7.89±0.92	13.82±3.47	...
Hζ 3889	...	...	4.19±1.09	...	...
[Ne III] 3967	4.02±1.38	...	...	5.23±3.19	...
Hϵ 3970	...	...	5.64±0.99	5.17±3.29	...
Hδ 4101	3.41±0.99	...	11.75±1.06	9.26±3.29	...
Hγ 4340	5.49±0.80	4.41±1.18	22.58±0.79	15.03±2.33	...
[O III] 4363	...	...	2.41±0.67	3.73±2.33	...
He II 4686	12.32±0.73	11.85±0.45	67.80±1.03	38.23±3.13	39.32±1.89
Hβ 4861	11.87±0.68	10.48±0.43	49.80±0.93	29.22±2.70	31.96±1.55
[O III] 4959	30.08±0.64	30.12±0.41	31.82±0.83	30.20±2.74	31.06±1.32
[O III] 5007	100.00±0.88	100.00±0.38	100.00±1.30	100.00±3.00	100.00±1.95
Hα 6563	32.79±0.35	28.95±0.24	137.61±1.28	80.75±3.37	88.29±1.46
[N II] 6584	1.40±0.27	...	...	...	...
[S II] 6717	1.38±0.30	...	...	...	...
[S II] 6731	1.18±0.37	...	...	...	...
[Ar III] 7135	1.63±0.54	...	...	...	...
[O IV] 25.9μm	3.07±0.31	3.49±0.34	...	...	...
log F([O III]) (erg cm^{-2} s^{-1})	−14.026±0.003	−14.010±0.001	−14.733±0.003	−14.358±0.009	−14.497±0.006
T_{e}([O III]) (K)	...	...	16700^{+1100}_{-200}	21200^{+200}_{-700}	...
n_{e}([O II]) (cm^{-3})	< 100	...	...	...	...
n_{e}([S II]) (cm^{-3})	370^{+100}_{-80}	...	...	...	...

Builder for IRS Spectra Maps (CUBISM; Smith et al. 2007). One-dimensional spectra were extracted from the two-dimensional data cube for extraction regions identical to the W00A2, W00A4, W03A2, W03A3, W03A4, N14A2, N14A2, N14A3, and N14A4 apertures defined for the optical spectroscopic observations illustrated in Fig. 6.1.

6.3 Results

6.3.1 Extinction

We have measured the extinction values for each aperture described in the previous section using the typical Balmer decrement method based on the Hα/Hβ ratio. It shall be noticed, however, that our spectra do not resolve the He II Pickering series lines at 4860 Å and 6560 Å from Hβ and Hα, respectively. Given the significant brightness of the He II λ4686 line, the Hα and Hβ lines can be expected to be notably contaminated from the He II Pickering lines. In the most extreme cases of the H-poor internal knots, most of the emission initially attributed to Hα and Hβ will actually correspond to emission from the adjacent He II Pickering lines. An

Table 6.2: *continued.* ⋆: The NOT ALFOSC spectral resolution does not allow resolving the components of the [O II] $\lambda\lambda$3726,3729 doublet and thus only the flux of the doublet is provided.

	Eye-like structure				High-velocity filament	
	W00A2	W00A4	W03A4	N14A4	W03A3	N14A3
c(Hβ)	0.17±0.03	0.10±0.03	0.24±0.07	0.13±0.04	0.52±0.1	0.26±0.09
[O II] 3726	0.92±0.47	4.30±0.24	6.59±0.93	...	5.18±2.24	...
[O II] 3729	0.96±0.54	3.61±0.25	6.98±0.80	9.59±0.44	9.89±2.63	17.26±11.34⋆
[Ne III] 3868	14.00±0.26	16.54±0.16	14.71±0.54	16.11±1.60	15.98±1.65	12.86±10.85
He I 3887 + + Hζ 3889	0.42±0.2	0.70±0.23	...	...	...	...
[Ne III] 3967	4.24±0.27	5.14±0.13	4.60±0.55	3.86±1.61	8.98±2.54	5.64±0.56
Hϵ 3970	0.56±0.24	0.59±0.13	...	...	...	...
Hδ 4101	1.60±0.22	1.00±0.17	1.60±0.60	...	3.57±1.86	...
Hγ 4340	3.27±0.22	2.04±0.14	2.02±0.32	2.24±0.24	4.36±0.88	5.83±0.73
[O III] 4363	2.95±0.21	2.91±0.14	2.94±0.37	2.47±0.20	3.46±1.04	...
He II 4686	9.96±0.20	6.95±0.11	5.13±0.31	4.46±0.15	10.94±0.78	8.59±0.49
[Ar IV] 4711	1.03±0.16	1.20±0.12	...	...	...	...
He I 4713 + + [Ne IV] 4715	0.71±0.20	0.66±0.11	...	...	...	...
[Ne IV] 4724	0.99±0.21	1.22±0.13	...	...	...	...
[Ar IV] 4740	0.93±0.16	0.74±0.10	...	...	...	...
Hβ 4861	6.80±0.16	4.27±0.09	4.79±0.27	4.14±0.15	9.07±0.69	8.22±0.54
[O III] 4959	30.44±0.20	32.19±0.08	29.87±0.36	31.82±0.15	30.14±0.89	31.28±0.50
[O III] 5007	100.00±0.04	100.00±0.11	100.00±0.47	100.00±0.20	100.00±1.18	100.00±0.68
[O I] 6300	...	0.60±0.04	...	...	...	...
[N II] 6548	0.22±0.07	0.73±0.03	0.88±0.09	1.08±0.10	1.74±0.31	1.58±0.20
Hα 6563	18.70±0.04	11.78±0.03	13.20±0.09	11.43±0.09	24.85±0.36	22.70±0.26
[N II] 6584	0.63±0.06	2.08±0.03	2.73±0.09	3.31±0.09	4.69±0.30	4.97±0.23
He I 6678	0.12±0.05	0.10±0.02	0.17±0.10	...	...	...
[S II] 6717	0.14±0.04	0.08±0.02	0.51±0.08	...	1.06±0.39	...
[S II] 6731	0.08±0.02	0.10±0.02	0.39±0.08	...	1.31±0.39	...
[Ar V] 7005	0.23±0.03	0.23±0.02	...	...	...	...
[Ar III] 7135	0.36±0.03	0.32±0.02	0.95±0.06	...	1.21±0.31	...
[O IV] 25.9μm	14.97±1.39	6.20±0.61	5.55±0.55	7.07±0.70	18.16±1.91	26.80±2.60
log F([O III]) (erg cm^{-2} s^{-1})	−13.785 ±0.001	−13.556 ±0.003	−13.823 ±0.001	−13.811 ±0.001	−14.673 ±0.003	−14.573 ±0.002
T_e([O III]) (K)	18480^{+780}_{-800}	18480^{+530}_{-930}	17890^{+1300}_{-170}	...	18370^{+1300}_{-600}	...
n_e([O II]) (cm^{-3})	590^{+90}_{-210}	1110^{+210}_{-240}	500^{+140}_{-140}	...	...	...
n_e([S II]) (cm^{-3})	...	1910^{+480}_{-440}	140^{+140}_{-130}	...	1940^{+400}_{-520}	...
n_e([Ar IV]) (cm^{-3})	2300±900	...	...	...	4500^{+1760}_{-1720}	...

accurate estimate of this contribution is crucial because a reliable measurement of the Hα and Hβ fluxes are needed for deriving the extinction, but also for the subsequent determination of abundances.

Since the theoretical Hα/Hβ, He II λ4860/He II λ4686, and He II λ6560/He II λ4686 line ratios depend on the electronic density n_e and temperature T_e, a prior knowledge of the physical conditions is required to correct the contamination of the He II Pickering to the H I Balmer lines. As for the density, the extinction correction has little effect, even for high extinction values, because the wavelength proximity of the density-sensitive diagnostic doublets. As for the temperature, however, the effects of these corrections acquire notable relevance. To solve this problem we have carried out an iterative process which consists of: 1) computing initial values of T_e and n_e (the details of these calculations are given in next section), 2) using those to derive the theoretical Hα/Hβ, He II λ4860/He II λ4686, and He II λ6560/He II λ4686 line ratios, 3) using these values to solve the equations system described in Appendix B.3 to provide us with a first approximation of the Hα and Hβ fluxes free from the contamination of He II lines, 4) using the Hα and Hβ fluxes to compute the extinction coefficient c(Hβ), and 5) using this to de-redden the corresponding density and temperature sensitive emission lines to compute T_e and n_e and start a new iteration. This loop ends up when the difference between the new and previous values of c(Hβ) differs by less than 0.01.

The values of c(Hβ) derived for the different apertures are listed in Table 6.2. After correcting from the contribution of the He II Pickering lines to Hα and Hβ, their fluxes in the apertures registering the H-poor knots W00A3, W03A5, and W03A6 are significantly reduced to 2.3×10^{-16}, 8.2×10^{-17}, and 2.3×10^{-16} erg cm^{-2} s^{-1}, respectively, for Hα, and 8.3×10^{-17}, 3.0×10^{-17}, and 8.5×10^{-17} erg cm^{-2} s^{-1}, respectively, for Hβ. The values of c(Hβ) for these apertures are 1.8±1.1, 1.3±0.6, and 1.6±1.0, where the large error-bars result from the significant uncertainties affecting the detection of the H I Balmer lines in these apertures. Lower limits of extinction $\geq$0.6 and $\geq$0.5 were set for apertures N14A5 and N14A1, where Hβ is not detected.

6.3.2 Physical conditions of the nebula

We used PyNeb (Luridiana et al. 2015) to obtain the physical conditions for each nebular aperture of A 78. The electronic density was derived from the line ratios of the [O II] λ3726/λ3728, [S II] λ6716/λ6730, and [Ar IV] λ4711/λ4740 density-sensitive doublets, and the electronic temperature from the [O III] λ4363/$\lambda\lambda$4959+5007 auroral-to-nebular line ratio. We note that PyNeb computes simultaneously T_e and n_e, including the cross-dependences of both parameters. The results are presented at the bottom lines of Table 6.2. When available, the [O II] doublet and [O III] emission lines were adopted for the calculation of density and temperature, respectively. In apertures where it was not possible to measure the components of the [O II] doublet, the fainter [S II] and [Ar IV] lines were used instead. The densities derived from these are deemed less reliable given the uncertainties in their fluxes.

The values listed in Table 6.2 show that the average temperature in the eye-like structure and HVF can be estimated to be around 18400 K, which matches the temperatures derived by Manchado et al. (1988), but it is higher than the value of 13000 K derived by Jacoby & Ford (1983). The central knots present slightly higher T_e, reaching up to 23000 K, whereas the temperature estimates for the outer nebula range from 16700 to 21200 K.

As for the density derived from the [O ii] doublet, its value ranges from 500 to 1000 cm^{-3} for the eye-like structure, and from 110 (i.e., the lower limit) to 580 cm^{-3} for the inner knots. The density of the outer nebula, as derived from the [S ii] doublet, is 370 cm^{-3}. These figures of density are generally higher than the low-density regime ≈100 cm^{-3} previously reported (Manchado et al. 1988). For apertures where temperature or density could not be calculated, fixed values of 18000 K and 300 cm^{-3} were adopted for the extinction and abundances calculations.

6.3.3 Chemical abundances

In born-again PNe, the abundances of the outer old nebula are expected to be typical of PNe, but the VLTP ejecta is formed by H-poor material. Therefore, the calculation of abundances in born-again PNe, as is the case of A 78, is far from simple because the H-deficient material of the inner ejecta is seen through the outer H-rich nebula. A precise determination of the fluxes of the Hα and Hβ lines in the innermost regions of born-again PNe is cumbersome, but crucial to derive their proper chemical abundances (e.g., Montoro-Molina et al. 2022a).

Abundances relative to H for ionic species of O, N, Ne and S were derived from CELs. The spectra are not deep enough to detect ORLs for those elements, thus it was not possible to estimate the ADF. This is expected to be high in the central knots, as it is the case for the inner knots of A 30, which present the highest ADF values among PNe (Wesson et al. 2003; Simpson et al. 2022). The temperatures and densities adopted for abundances calculations were the same as for the extinction determination.

The transitions probabilities and collision strengths were taken from the references listed in Table 6.3. The resultant ionic abundances are shown in Tables 6.4 and 6.5.

6.3.3.1 Total abundances

The total He abundances were obtained by adding the ionic abundances of He^{++} derived from the He ii λ4686 line and the average of the abundances of He^{+} derived from all available He i lines. We note that the non-detection of He i emission lines in a number of apertures did not make possible to derive He^{+} abundances for those.

As for the other elements, namely O, N, Ne and S, the contributions of ions inaccessible from optical spectra to the total abundances rely on ionization corrections factors (ICFs). Here we use those presented by Delgado-Inglada et al. (2014) and Kingsburgh & Barlow (1994) (hereinafter DM14 and KP94, respectively), which are specifically computed for PNe.

Both are based on similar criteria to assess the likely ionization fractions using parameters derived from He i, He ii, [O ii] and [O iii] emission line ratios. We note that the applicability of the ICFs of DM14 is more restrictive than that of KB94, depending on the number of available lines. However, their effects on the final abundance estimates remain consistent with each other.

Table 6.2: *continued*

	Disk knots and tails				Polar knot
	W00A3	W03A5	W03A6	N14A5	N14A1
c(Hβ)	1.8±1.1	1.3±0.6	1.6±1.0	≥ 0.6	≥ 0.5
[Ne V] 3345	...	...	...	202.57±17.15	248.10±27.64
[Ne V] 3426	313.80±10.58	182.88±12.63	430.91±49.70	432.82±15.82	706.69±22.61
[O II] 3726	10.10±4.95	5.60±1.04	8.65±1.96	...	...
[O II] 3729	7.47±0.47	4.91±1.03	8.34±2.17	8.06±1.44	...
[Ne III] 3868	41.65±0.36	26.15±0.71	35.93±1.44	42.19±1.43	33.95±1.87
He I 3887	1.22±0.27	...	...	...	...
[Ne III] 3967	11.22±0.25	8.10±0.65	9.50±1.24	12.22±1.44	...
? 4358	...	...	1.83±0.78	...	...
[O III] 4363	3.38±0.16	3.03±0.35	4.22±0.79	3.79±1.21	6.45±1.21
He I 4471	0.91±0.13	0.68±0.28	...	...	...
He II 4543	...	0.78±0.20	...	...	...
[Fe III] 4658	...	1.61±0.35	...	...	...
He II 4686	10.79±0.10	11.89±0.25	13.09±0.55	8.76±0.34	14.56±0.97
[Ne IV] 4715	4.64±0.12	4.36±0.29	5.79±0.69	4.93±0.34	11.41±0.97
[Ne IV] 4724	7.57±0.13	7.25±0.30	8.92±0.70	7.07±0.37	14.85±0.96
[Ar IV] 4740	...	0.77±0.32	0.87±0.57	...	...
Hβ 4861	0.0003:	0.001:	0.006:	...	...
[O III] 4959	33.79±0.07	31.91±0.29	32.62±0.43	33.57±0.24	32.84±0.45
[O III] 5007	100.00±0.09	100.00±0.38	100.00±0.56	100.00±0.32	100.00±0.58
He I 5876	1.77±0.03	1.29±0.04	1.26±0.69	1.20±0.09	...
[O I] 6300	0.34±0.02	0.73±0.05	0.61±0.07	...	...
[O I] 6363	0.06±0.02	...	...	...	...
[Ar V] 6435	0.11±0.02	...	...	...	...
? 6500	...	...	...	1.22±0.05	1.79±0.09
[N II] 6548	0.34±0.01	0.78±0.03	0.35±0.04	...	...
Hα 6563	0.04:	0.01:	0.06:	1.40±0.05	1.28±0.09
[N II] 6584	1.00±0.01	2.14±0.03	0.98±0.04	0.52±0.05	...
He I 6678	0.22±0.01	...	0.23±0.04	...	...
[S II] 6717	...	0.07±0.05	...	...	...
[S II] 6731	...	0.04±0.02	...	...	...
[Ar V] 7005	0.09±0.03	0.28±0.04	0.26±0.07	...	...
He I 7065	0.05±0.03	0.19±0.04	0.12±0.07	...	...
[Ar III] 7135	0.05±0.03	0.19±0.03	0.09±0.06	...	...
log F([O III]) (erg cm^{-2} s^{-1})	−13.935±0.001	−13.438±0.001	−13.951±0.002	−14.126±0.001	−14.256±0.002
T_e([O III]) (K)	19870^{+1680}_{-850}	18750^{+730}_{-730}	23140^{+1270}_{-1070}	...	...
n_e([O II]) (cm^{-3})	110^{+240}_{-110}	370^{+240}_{-360}	580^{+190}_{-160}	...	...

Table 6.3: List of references of the transition probabilities and collision strengths adopted to calculate ionic abundances.

Ions	Transition probabilities	Collision strengths
[O II]	Zeippen (1982)	Kisielius et al. (2009)
[O III]	Fischer & Rubin (2004)	Storey et al. (2014)
[N II]	Fischer & Rubin (2004)	Tayal (2011)
[Ne II]	Galavis et al. (1997)	McLaughlin & Bell (2000)
[Ne III]	Godefroid & Fischer (1984)	Giles (1981)
[Ne IV]	Galavis et al. (1997)	Dance et al. (2013)
[Ar IV]	Rynkun et al. (2019)	Ramsbottom et al. (1997)
[S II]	Rynkun et al. (2019)	Tayal & Zatsarinny (2010)

Table 6.4: Ionic abundances by number ($12 + \log \frac{N(X^{+i})}{N(H)}$) obtained from CELs.

		Old nebula					Eye-like structure				High-velocity filament		Disk knots and tails		
		W03A2	N14A2	W00A55′	W03A7	N14A6	W00A2	W00A4	W03A4	N14A4	W03A3	N14A3	W00A3	W03A5	W03A6
O^+/H^+	λλ 3726, 3729	6.48	…	…	…	…	6.17	6.96	7.12	7.29	6.93	7.25	9.69	10.03	9.36
O^{2+}/H^+	λλ 4959, 5007	7.73	7.78	7.20	7.21	7.30	8.00	8.21	8.13	8.22	7.87	7.92	10.62	11.14	10.28
O^{3+}/H^+	λ 25.9μm	6.52	6.60	…	…	…	7.46	7.32	7.18	7.91	7.53	7.59	…	…	…
N^+/H^+	λ 6584	5.82	…	…	…	…	5.74	6.46	6.51	6.68	6.48	6.55	8.57	9.41	8.25
Ne^{2+}/H^+	λλ 3868, 3967	7.19	7.00	6.49	6.74	…	7.43	7.70	7.68	7.78	7.53	7.44	10.58	10.93	10.16
Ne^{3+}/H^+	λλ 4715, 4726	…	…	…	…	…	8.68	8.84	…	…	…	…	12.02	12.59	11.58
Ne^{4+}/H^+	λ 3426	…	…	…	…	…	…	…	…	…	…	…	11.40	11.71	11.16
Ar^{3+}/H^+	λλ 4711, 4740	…	…	…	…	…	5.91	6.22	…	…	…	…	…	9.00	8.18
S^+/H^+	λλ 6716, 6730	5.24	…	…	…	…	4.43	4.53	5.14	…	5.32	…	…	7.23	…

Table 6.5: Ionic abundances by number ($12 + \log \frac{N(X^{+i})}{N(H)}$) obtained from ORLs.

		Old nebula						Eye-like structure				High-velocity filament		Disk knots and tails	
		W03A2	N14A2	W00A55′	W03A7	N14A6	W00A2	W00A4	W03A4	N14A4	W03A3	N14A3	W00A3	W03A5	W03A6
He^+/H^+	λ 4471	…	…	…	…	…	…	…	…	…	…	…	14.16	14.47	…
He^+/H^+	λ 5876	…	…	…	…	…	…	…	…	…	…	…	14.01	14.28	13.54
He^+/H^+	λ 6678	≤9.43	…	…	…	…	10.61	10.80	11.01	…	…	…	13.66	…	13.34
He^{2+}/H^+	λ 4686	10.97	11.01	11.08	11.07	11.04	11.11	11.16	10.98	10.98	11.03	10.97	13.86	14.37	13.75

In particular, DM14 define the ionic fractions ν and ω,

$$\omega = \frac{[\text{O III}]}{[\text{O II}] + [\text{O III}]}, \qquad \nu = \frac{\text{He II}}{\text{He II} + \text{He I}} \tag{6.3.1}$$

that are used to validate the ICF selection (see table 3 in DM14).

We present in Table 6.6 the total abundances derived for all apertures where Hβ is detected. The bottom rows of this table also present the values of ω and ν obtained from the different extraction regions. We note that ν depends on He I, which is not detected in all apertures, particularly in none of the apertures probing the outer nebula. The aperture W03A2 (Southwest of the outer nebula), with the highest signal-to-noise ratio, has been used to estimate an upper limit of the He I emission lines intensities and corresponding He$^+$ ionic abundances (Table 6.5) to assess the effects on the ICFs for the outer nebula. The O, N, Ne, and S then computed are marked by a "⋆" sign in Table 6.6.

The *Spitzer* IR spectrum provided us with measurements of the O^{+3} λ27.6 μm emission line in the eye-like, HVF, and old nebula, which have been used to determine the total abundance of oxygen by direct addition. We notice that the abundances obtained this way are ≈0.6–1 dex lower than those obtained by ICFs, likely due to the fact that He I is not detected in the outer regions, resulting in $\nu = 1$, which leads to overestimating the contribution of high-excitation species. Therefore, in the subsequent total abundances calculation for N, Ne, and S using ICFs, direct addition oxygen abundances were adopted. The Ne abundances can also be determined by direct addition because there are emission lines of the main ions in the optical spectra. As for the innermost region, the *Spitzer* spectrum was unfortunately saturated and it was not possible to measure the intensity of the O^{+3} λ27.6 μm line there. Since the parameters ω and ν in this region are in the confidence range for the calculation of abundances from the ICFs, the total oxygen abundances can be considered reliable.

Table 6.6 includes many caveats regarding the total abundances of the different apertures, but we note that the abundances derived for apertures probing the same structural component using either the direct addition or the same ICF prescription are fairly consistent among them. This has allowed us to set the representative abundances for each structure presented in Table 6.7 that will be used to clarify the final results and to make a fair comparison with those of similar objects. In particular we show in this table the abundances of the knots J1, J3 (Wesson et al. 2003) and J4 (Simpson et al. 2022) of A30 (see Jacoby 1979, for notation) and the knot of A 58 (Wesson et al. 2008), as well as the Sun abundances (Asplund et al. 2009).

6.4 Discussion

6.4.1 Spatially varying extinction and dust distribution in A 78

The logarithmic extinction coefficient $c(\mathrm{H}\beta)$ has been found to vary across the different regions of A 78, with values ≈1.5 for the inner VLTP ejecta, ≃0.15 for the eye-like structure and Northwest region of the old nebula, ≃0.38 for the HVF and Southeast region of the old nebula, and 0.03 for the East and West regions of the old nebula.

Cohen et al. (1977) presented the first extinction measurements towards A 78, with $E(B-V) = 0.13$ (or $c(\mathrm{H}\beta) = 0.18$), from an optical spectrum of its CSPN extracted from a $4'' \times 2.7''$ aperture.

Kaler (1981) obtained a similar value for $c(\mathrm{H}\beta)$ of 0.15 using photometric measurements, although the errors were so large that the measurement was deemed not reliable. Kaler & Feibelman (1984) derived more precise values for $c(\mathrm{H}\beta)$ of 0.164 from the UV bump at 2200 Å and 0.177 from optical data. These authors noted for the first time the position of the internal disk in A 78 by comparing the extinctions obtained with that previously calculated for A 30. Meanwhile, Manchado et al. (1988) obtained spatially-resolved optical spectra of A 78, including the outermost regions. Although the Hα to Hβ ratio among different regions provided by these authors certainly implied extinction variations, they only reported an average value $E(B-V)$=0.153, i.e., $c(\mathrm{H}\beta)$ of 0.22. All these values are consistent with the extinction derived here for the eye-like structure, which is reasonable given that it is the brightest extended nebular structure and presumably most easily probed by early observations.

The extinction of the inner VLTP ejecta derived in this work is significantly larger than

Table 6.6: Total abundances computed using the ICFs listed in Delgado-Inglada et al. (2014) (DM14) and Kingsburgh & Barlow (1994) (KB94), and direct addition from ionic abundances, when possible. The values of the parameters ν and ω (see Eq. 6.3.1) defined by Delgado-Inglada et al. (2014) are presented in the bottom. Abundances in units such that $\log N(\mathrm{H}) = 12.0$.
Notes:
[a]: Since no He I emission lines are detected, the oxygen ICF in Equation A10 of KB94 is unity.
[b]: It is not recommended using the ICF of equation 10 in DM14 to compute the O abundance if ν is higher than 0.95.
[c]: It is not recommended using the ICF of equation 14 in DM14 to compute the N abundance if ω is higher than 0.95.
[d]: The ICF in equation 20 of DM14 was used instead of equation 17 in DM14, because the former takes Ne^{4+} in addition to Ne^{2+} to compute the Ne abundance.
*Abundances were computed adopting an upper limit of the He^{+} ionic abundance.

		Old nebula					Eye-like structure				High-velocity filament		Disk knots and tails		
	ICFs	W03A2	N14A2	W00A55′	W03A7	N14A6	W00A2	W00A4	W03A4	N14A4	W03A3	N14A3	W00A3	W03A5	W03A6
He/H	Direct addition	≥10.97	≥11.01	≥11.08	≥11.07	≥11.04	11.16	11.22	11.11	≥10.98	≥11.03	≥10.97	14.23	14.6	13.87
O/H	KB94	$9.09^{\star}$	7.78^{a}	7.21^{a}	7.22^{a}	7.33^{a}	8.69	8.83	8.56	8.27^{a}	7.92^{a}	8.0^{a}	10.83	11.43	10.73
	DM14	$8.92^{b\star}$	9.01^{b}	8.44^{b}	8.45^{b}	8.56^{b}	8.82	8.94	8.61	9.5^{b}	9.15^{b}	9.23^{b}	10.82	11.44	10.79
	Direct addition	7.78	7.81	...	...	...	8.12	8.28	8.21	8.43	8.07	8.15	...	...	...
N/H	KB94	$7.11^{\star}$	...	...	...	...	7.68	7.78	7.60	7.80^{a}	7.61^{a}	7.45^{a}	9.7	10.81	9.62
	DM14	$6.96^{c\star}$	...	...	...	...	7.53^{c}	7.64^{c}	7.48	7.66	7.47	7.31	9.61	10.71	9.56
Ne/H	KB94	$7.23^{\star}$	7.03^{a}	6.49	6.74	...	7.54	7.77	7.76	7.98^{a}	7.72^{a}	7.67^{a}	10.79	11.22	10.61
	DM14	$7.59^{\star}$	7.29	7.98	8.22	...	7.70	7.92	7.78	8.43	8.18	8.21	11.58^{d}	11.95^{d}	11.44^{d}
	Direct addition	7.19	7.0	6.49	6.74	...	8.71	8.87	7.68	7.78	7.53	7.44	12.12	12.65	11.73
S/H	KB94	$6.75^{\star}$	...	...	...	...	6.39	6.05	6.49	...	6.66	...	...	8.70	...
	DM14	$6.32^{\star}$	...	...	...	...	6.21	5.71	6.16	...	7.32	...	...	8.64	...
ω		0.95	1.0	1.0	1.0	1.0	0.99	0.95	0.91	0.89	0.9	0.82	0.89	0.93	0.89
ν		0.99	1.0	1.0	1.0	1.0	0.91	0.87	0.74	1.0	1.0	1.0	0.42	0.59	0.75

Table 6.7: Total abundances and abundances ratios in different components of A 78. For comparison, the abundances of clumps J1 and J3 (Wesson et al. 2003) and J4 (Simpson et al. 2022) of A 30, those of the central knot of A 58 (Wesson et al. 2008), the theoretical predictions of the abundances at the surface of the star after a VLTP event (Miller Bertolami et al. 2006), and the Solar abundances (Asplund et al. 2009) are included. Abundances are provided in units such that log N(H) = 12.0, whereas abundances ratios are by number.

	A78				A30			A58	VLTP Event	Solar
	Old nebula (SW)	Eye-like structure	High-velocity filament	Disk knots and tails	J1	J3	J4	Central knot	Star Surface	
He/H	11.03	11.16	11.00	14.23	13.03	13.07	12.62	12.51	14.21	10.93
O/H	7.80	8.26	8.11	10.82	9.26	9.32	9.72	10.03	13.24	8.69
N/H	7.03	7.62	7.46	9.85	8.88	8.90	9.18	9.21	12.67	7.83
Ne/H	7.41	7.74	7.94	12.16	9.70	9.78	9.25	9.92	12.46	7.93
S/H	6.53	6.16	...	8.09	...	...	6.96	...	...	7.12
N/O	0.17	0.23	0.22	0.10	0.41	0.38	0.28	0.15	0.26	0.13
Ne/O	0.41	0.3	0.67	21.87	2.75	2.88	0.33	0.77	0.16	0.17
S/Ne	0.13	0.026	...	0.0003	...	...	0.005	...	...	0.15

any value reported previously. A seemingly high extinction of $c(\mathrm{H}\beta)$=1.23 has recently been estimated from the Balmer decrement for the J4 knot (see Jacoby 1979, for notation) of A 30 (Simpson et al. 2022), while that of the J1 and J3 knots have been derived to be 1.02 and 0.64, respectively, adopting temperatures from He line ratios (Wesson et al. 2003). The higher extinction of the inner ejecta of these born-again PNe can be expected given the significant presence of dust in their central region (e.g., Cohen & Barlow 1974; Cohen et al. 1977), with the dust spatially correlated with the disk knots as recently described by Toalá et al. (2021a). The infrared emission of the dust in A 30 has been attributed to hot ($\lesssim$160 K) and small carbon-rich dust spatially correlated with the inner disrupted disk, and larger and cooler (<80 K) dust located farther away up to the swept-up clumps and filaments (Toalá et al. 2021a). The similar properties of the dust emission of A 30 and A 78 makes reasonable assuming they also have similar dust spatial distributions. Interestingly the dust coexists with X-ray-emitting material (Toalá et al. 2015).

Finally, the old outer nebula in A 78 shows remarkable extinction variations in correspondence with morphological and excitation variations. The lowest extinction values, $c(\mathrm{H}\beta)$=0.03, are found towards the Northeast and Southwest regions registered by the W00A55′ aperture. Then the extinction increases towards the Northwest region to $c(\mathrm{H}\beta)$=0.15 in the W03A7 and N14A6 apertures and very notably towards the Southeast region and at the HVF with $c(\mathrm{H}\beta)$=0.38. There is a notable correlation between extinction and intensity of the [O III] emission lines. If the lowest extinction value were assumed to correspond to the interstellar extinction towards A 78, then the higher extinction at other regions of the outer nebula would require the presence of dust there. It must be noted, however, that there is no near-IR nor mid-IR dust emission beyond the spatial extent of the eye-like structure (Toalá et al. 2021a), although the broken morphology of the eye-like feature along the Southeast-Northwest direction suggests that material from the innermost region may leak up to the outer shell. We noted above that the dust model of A 30, which implies that large dust grains with emission peaking at longer wavelengths are located further away from the CSPN (Toalá et al. 2021a), may also apply to A 78. This hypothesis will be assess by future photoinization modeling of A 78 including both gas and dust (Rodríguez-González et al., in preparation).

6.4.2 Spatially varying physical properties and chemical abundances in A 78

An inspection of the physical properties and chemical abundances listed in Tables 6.2, 6.4, 6.5 and 6.7 immediately reveals notable variations in the excitation, physical properties and chemical abundances among the different structural components of A 78. These are described below for the old H-rich nebula, the innermost and most recent VLTP ejecta, and the eye-like structure and other features indicative of mixing processes between H-poor and H-rich material.

6.4.2.1 Old H-rich nebula

The line intensities derived from the spectra of the old hydrogen-rich nebula, presented in Table 6.2, do not show significant variations in the ≈14 years elapsed between the different observations. The prevalence of [O iii] over [O ii], which is only detected in the W03A2 aperture, He ii over He i, and the He ii/Hβ ratio of ~1 evidence a high-excitation nebula. Thus, if the nebula experienced a period of recombination after the born-again event, as is currently the case of the outer nebulae of Sakurai's Object and HuBi 1 (Guerrero et al. 2018; Reichel et al. 2022), it has by now recovered due to the action of its CSPN strong ionizing flux ($T_{\rm eff}$ ≈113 kK).

The average He/H abundances (≃0.11) are similar throughout the old nebula. As for the other elements, the abundances derived from spectra of apertures that allow their calculation are mostly consistent. Accordingly the abundances of the Southwest W03A2 aperture, with the highest signal to noise ratio, were chosen to be representative of the outer nebula in Table. 6.7.

The N/O ratio ∼0.17 is the average value for a type II PN (Peimbert 1978). The S/Ne ratio also reveals a lack of S, which is otherwise typical among PNe (Henry et al. 2004). The chemical enrichment models presented by Karakas & Lugaro (2016) indicate that the progenitor star initial mass can be fairly restricted to be $\leq$2.5 M$_\odot$ by the He/H abundance, with the N/O ratio suggesting even a lower mass ($\lesssim$1 M$_\odot$) progenitor.

6.4.2.2 The VLTP ejecta

The cometary knots of A 78 distributed along the innermost disrupted disk and polar ejecta have been attributed to a VLTP event experienced by its CSPN. These features have experienced complex dynamical processes (Rodríguez-González et al. 2022) with proper motions inconsistent with homologous expansion (Fang et al. 2014). As a result, the age derived from their angular expansion, which is distance independent, varies for different knots and filaments. Only a crude estimate ≈1000 yr can be obtained for the age of the VLTP event.

The most prominent property of the cometary knots of A 78 is their extremely low H content, which is confirmed by the weak Hα and Hβ emission lines (Table 6.2) once that the overwhelmingly large contribution (≃90%) of the He II Pickering lines has been taken into account. We emphasise that the correction of the contribution of the He II Pickering lines to the H I Balmer lines was accomplished here through an iterative process that accounted consistently for the dependence of the H I Balmer and He II Pickering theoretical ratios on the temperature and density, which are coupled with the extinction.

The chemical abundances of the disk knots confirm their hydrogen deficiency, with abundances ratios by number of He/H∼170, O/H∼0.067 and N/H∼0.007, i.e., around 1000 times larger than the abundances of the old H-rich nebula. We also note an excess of the Ne/H abundance, ∼1.4, and Ne to O abundance ratio by number of ∼22, which is otherwise seen in other born-again PNe, although to a lower extent.

This high Ne/O ratio is in stark contrast with the predictions of the surface of the star after undergoing a VLTP in a born-again event (Ne/O∼0.16, Miller Bertolami et al. 2006).

On the other hand, nova explosions result in Ne/O ratios of 1 or higher, which historically has led to a debate between the VLTP or nova event as the origin of born-again PNe. Particularly for A58, Lau et al. (2011) proposed two binary scenarios, both with an oxygen-neon-magnesium (ONeMg) star as primary. In the first one, a nova event occurred shortly after a VLTP, while in the second a double common-envelope process is suggested. None of them fit perfectly with the observations, however, as they can only explain to some extent the O, C, and Ne rich ejecta. More recently, Rodríguez-González et al. (2022) proposed that A 30, a twin of A 78, would have acquired its peculiar internal morphology after a common envelope process following the VLTP event. The single or double common-envelope scenario would be a potential explanation for the morphology of A 78 and to some extent for its chemical composition, but its extremely high Ne/O ratio indicates that there must be some additional process besides the nova, VLTP or common-envolope scenarios, implying either depletion of oxygen or an additional process for neon enrichment.

The abundances obtained for the H-poor knots of A 78 are significantly higher, 1–2 dex, than those of the H-poor knots J1 and J3 (Wesson et al. 2003) and J4 (Simpson et al. 2022) of A 30, and the central knot of A 58 (Wesson et al. 2008). This difference may be ascribed to the careful removal of the He II contamination to the Balmer lines, whose fluxes has to be reckoned are subject to large uncertainties.

Hydrogen determination aside, the trend followed by the abundances in A 78 is N<O<Ne, alike the polar knots J1 and J3 of A 30, but different from the trend N<Ne<O presented by its equatorial J4 knot. Such difference in the abundances of A 30, if true, would suggest inhomogeneities in the eyected material in the VLTP. This may be the case in A 78 as well, but it has only been possible to calculate abundances of the knots located in the equatorial disk. The N/O ratio, ≈0.1, similar to those obtained in the knots of A 30 and A 58, is expected in VLTP episodes (Miller Bertolami et al. 2006). It is very notorious the extremely low S/Ne

ratio ≈0.0003. This can be attributed to the Ne enrichment in this region, but also to the underestimation of the S abundances caused by the available ICFs in highly ionized nebular regions (Henry et al. 2012).

We note that the temperature and density structure of the knots of A 78 can be expected to be complex given the similarity with those in A 30. These have been proposed to have dense, cold and chemically inhomogeneous cores in order to explain the temperature differences obtained from the ORL and CEL carbon lines (Harrington & Feibelman 1984). The knots, with large CNO and He abundances, would be heated by the input photoionization but would immediately radiate away the energy excess through infrared fine-structure lines. This would produce a stratification where the knot outermost regions are highly ionized, whereas its innermost regions are denser and colder. These regions with different physical conditions cannot be isolated by the spatial resolution of ground-based observations, but we note that low ionization species find in the innermost core of the knots a shelter from the harsh CSPN ionizing flux. The detection of He I emission lines in the innermost knots of A 78 thus support the stratification of chemical abundances and physical conditions within the knots, as He would be otherwise doubly ionized by the strong ionizing flux of the CSPN as in the eye-like structure and outer nebula.

6.4.2.3 Mixing regions

All of the H-deficient structures inside the old H-rich nebula in A 78 can be considered to be remnants of the VLTP event experienced by its CSPN about 1000 years ago (Fang et al. 2014), either directly from the VLTP event, such as the cometary knots, or as the result of the interaction between the H-poor ejecta and the H-rich old nebula, giving rise to the eye-like structure very alike the petal-like structure seen in A 30.

The expected gradual transition between the material of the VLTP and the material of the old nebula, hinted by Manchado et al. (1988), is clearly confirmed here, with chemical abundances of O, N and Ne in the eye-like structure, 2–4 times larger than those in the old nebula.

The notorious high-velocity filament HVF, with a velocity clearly different from that of the eye-like structure (Fang et al. 2014), could be a fragment of pristine ejecta that has reached the outermost nebular regions. Although that might be the case, its physical and chemical properties do not reveal any appreciable difference with the eye-like structure. Spectroscopic observations at higher spatial and/or spectral resolution would be required to avoid the emission of this interesting feature to be diluted by the background nebular emission that is also registered by the spectral aperture used here.

6.5 Summary

We present here the analysis of long-slit optical and Spitzer mid-infrared spectra of the born-again PN A78. The spectra from 3 different epochs have allowed us to determine the ionic and total abundances from the CELs for the main structures in this PN, namely, the old H-rich nebula, the eye-like structure and the central cometary knots formed as a result of a born-again event. Our main findings can be sumarized as follows:

1. The temperature of the nebula derived from [O III] lines remains relatively uniform, around T_e =18,000 K, with a possible increase towards the central regions (T_e ≈23,000 K). The densities derived from the [O II] $\lambda\lambda$3726,3729 doublet range from 100 (low density limit) to 1000 cm^{-3}. The temperature and density structure of these knots is complex, as those in A 30, with presumably high density and cold cores at their heads as revealed by emission in low-ionization lines (e.g., He I).

2. We have found an inhomogeneous extinction over the nebula unnoticed in previous spectroscopic investigations. In the eye-like structure and Northwest corner of the old H-rich nebula, the extinctions are similar and agree with previous estimates, while in the Southeast regions of the old nebula the extinction is higher. This increase may be due to the diffusion of dust leaking from the eye-like structure to the outer regions. The extinction in the central knots, even subject to large uncertainties, is undoubtedly higher than in the rest of the nebula, consistent with the large infrared dust emission.

3. The chemical abundances of the old nebula set A 78 as a type II nebula following Peimbert's classification. A comparison of these chemical abundances with models of chemical enrichment indicates that the mass of the progenitor star is lower than 2.5 M$_\odot$, probably even $\lesssim$1 M$_\odot$.

4. The chemical abundances in the central knots are extremely H deficiency, with a low N/O ratio, ≈0.10, and greatly enhanced Ne abundances and Ne/O ratio typical of other born-again PNe. These abundances are neither consistent with a VLTP event nor a nova explosion, and have been suggested to result from post-VLTP strong binary interactions (Lau et al. 2011; Rodríguez-González et al. 2022).

5. The eye-like structure and the high-velocity filament towards the Southeast show evidence of mixed material between the H-poor ejecta and the H-rich surrounded nebula.

Chapter 7

Summary and Conclusion

The research carried out here tried to broaden our understanding of the born-again PNe phenomenon. We used a diverse range of methodologies to interpret our IFU and long-slit spectra observations. Our aim in this work was to determine physical conditions, chemical abundances and morpho-kinematic features. The capabilities of the IFU observations have once again proven to be able to spatially and spectroscopically resolve the ejecta produced during the VLTP in the CSPN with exquisite precision. In this chapter, I summarize the main results reached, followed by suggestions on how to extend this work, which might solve the long-standing problems in the study of this kind of PNe.

7.0.1 Summary

- In Chapter 3, we have separated the emission originating from the recent, uncontaminated ejecta from the outer shell of HuBi 1. This has enabled the creation of extinction maps and the precise calculation of both T_e (electron temperature) and n_e (electron density) for the different layers. Thanks to this and by using the MAPPINGS software, given the presence of shocks, the abundances in the ejecta were determined. The lack of H obtained was the missing piece to **confirm the occurrence of a born-again event in HuBi 1** about 250 years ago. This has increased the number of reliably confirmed born-again cases up to five.

- In Chapter 4, **we have detected variability in the emission lines of long-slit spectra of A 58 over 27 years** (1994-2021), approximately 80 years after the VLTP. The variability indicated the **existence of shocks**, as opposed to the previously suggested photoionization excitation of the gas, and a complex morpho-kinematic structure similar to that reported for Sakurai's object.

- The previous results inspired us to investigate the detailed kinematics of ionized and molecular gas of A 58 using IFS GTC-MEGARA data and ALMA data, as detailed in 5. We have obtained a tomographic view of the central ejecta using spatial resolution enhancement techniques. We thus have proposed a **model of the morphology of the ionized material in A 58**. Surprisingly, the ionized emission exhibited a complex structure indicative of an hourglass-like morphology, contrary to the disk-jet morphology seen in molecular emission. The **bipolar structure could be explained through a VLTP and a subsequent phase of common envelope with a binary companion**, as recently proposed for other born-again PNe. In this case, the companion would be sub-stellar. The use of ALMA data was crucial, providing key information to interpret correctly the optical emission. This work, along with similar studies conducted on Sakurai's object, highlights the significant role played by molecular gas in the evolution of born-again PNe.

- Finally, in Chapter 6 we have demonstrated that **there are inhomogeneities in extinction** (which was previously assumed to be homogeneous), **physical conditions, and chemical abundances in A 78**. Treating the latter with special care, we confirm the deficiency in H in the central region and that the N/O ratio is consistent with a born-again scenario. Additionally, **abundances in the structure known as the eye-like reveal a mixture between the recent H-poor ejecta and the old H-rich nebula**. It can be concluded that the hashes of the VLTP event reach the outer nebula and diffuse into it in timescales as short as 1,000 yr after the eruptive event took place.

In addition to all the results presented, I would also like to discuss some implicit conclusions on born-again PNe reached throughout this thesis.

- Born-again PNe have shown to exhibit very rapid time evolution, comparable to human timescales, at least in the initial phases after the VLTP. This is more evident in the case of Sakurai's object, which in just 20 years since the born-again event has undergone drastic changes in brightness, fading, creation, and destruction of dust, with molecular material still being expelled from the CSPN. To a lesser extent, but equally notable are the cases of A 58 and HuBi 1. In A 58, after the brightening and fading that occurred shortly after the VLTP, it has been reported that emission from the CSPN has gradually (in less than 100 years) reappeared, still with significant amounts of dust around it. The results of this thesis demonstrate how a brightening in the central ejecta and a change in its ionization state (likely due to the existence of a shock) is occurring in less than 30 years. In HuBi,1, the changes have been rather the opposite. The apparent magnitude of its CSPN has decreased in the last 50 years due to the dust shell that has formed around it. It is unclear whether HuBi 1 provides a forecast of the next evolutionary stages of A 58, or whether these two sources are different. On the other hand, in A 78, and very likely also in A 30, the changes are less drastic, as seen in Chapter 6.

  We can therefore infer that the evolution is very rapid in the initial phases after the VLTP and then settles down. This reinforces the importance not only of increasing efforts to search for (it is estimated that 20% of low and intermediate mass stars undergo a VLTP) and confirm new born-again PNe, but also of conducting thorough monitoring to fully understand the born-again process and refine stellar evolution models.

- A key aspect is the presence of shocks in the ejecta of the most recent born-again PNe, in ascending age Sakurai's Object, A 58, and HuBi 1. When calculating chemical abundances or modeling newly formed dust around CSPN, it is necessary to use models that account for shocks, such as MAPPINGS. After some time, when the CPSN returns to a high temperature and photoionization dominates again, we can use photo-ionization codes such as CLOUDY. The physics and chemical processes involved in these sources are very rich.

- This leads us to the following reasoning. Without intending to disparage any scientific work, it is mandatory to advise that the excessive simplification of such complex sources as born-again PNe can lead to erroneous conclusions. In HuBi 1, parallel to the work described here, Peña et al. (2021) presented a study using part of the same data, specifically the OSIRIS long-slit spectra. The authors similarly inferred the presence of shocks in the innermost regions of HuBi 1, however their results were completely different. The abundances they obtained implied that HuBi 1 has not got poor ejecta, but that its abundances were similar to those of the outer nebula. The devil is in the details. The authors assumed that the contribution from the outer shell was minor compared to the inner one. Whereas this is a fact normally true in multiple shell PNe, it is not in this case, where the emission from the outer shell dilutes the H abundances of the inner shell enormously unless it is correctly accounted for. Furthermore, they derived the abundances assuming photoionization, although previously had confirmed the importance of shocks. Another example is found between the works of Toalá et al. (2021b) and Rodríguez-González et al. (2023). Both perform hydrodynamic simulations but in 3D and 1D respectively. Without detracting from the latter work, the results of the first are more robust and revealing, calling for the avoidance of excessive simplification of the sources.

  One might think that it is a matter of obtaining latest generation data data but not so. Guerrero et al. (2018), with medium resolution long-slit OSIRIS data (in fact the same used here and by Peña et al. (2021)), does an exquisite and detailed job, once again bringing to the table the born-again origin of HuBi 1 which was later confirmed. It is worth mentioning that the data suffered from DCR, a fact that we only noticed thanks to the later acquisition of IFS data.

- These types of objects greatly benefit from IFS data. IFS provides a more accurate view of born-again by giving spectral and spatial information at the same time. Nonetheless, even IFS data are challenged in certain cases. In the chapter 5, it was described how spatial resolution limited us when imaging the central ejecta. These objects force us to squeeze the data to the extreme by resorting to advanced and delicate techniques. Finally, it is worth to mention that it is necessary to have information from various spectral ranges, as we have seen for A 58, to have the overall picture of what is happening in the central regions. Thus, we encourage the acquisition of molecular and infrared data of the highest quality, for example with instruments like ALMA or the James Webb Space Telescope.

7.0.2 Future works

The potential lines of future work are numerous. Here, those intended for progress in the short and medium term, along with the projects that are currently underway, will be mentioned.

- **Real 3D Visualization of the Ejecta**: A line of work that unfortunately is not yet ready for this thesis but is already underway is the study of the morpho-kinematic structure of A 30 and A 78 using available GTC MEGARA high-dispersion IFS data. The IFU observations map the central region of both nebulae, primarily dominated by cometary structures, as seen in the right-hand panels of 1.15. Previous studies of the kinematics of the knots in the innermost regions of both nebulae used long-slit spectra in conjunction with optical images (Meaburn & Lopez 1996; Meaburn et al. 1998). The investigation which is carried out includes for the first time the velocities along the line of sight of all these knots, as provided by high spectral resolution MEGARA observations, as well as those on the plane of the sky derived from multi-epoch images (Fang et al. 2014). The use of both datasets provides the unique opportunity to investigate the expansion of the knots in the central regions of A 30 and A 78 in 3D, without the need for any geometrical assumption. Additionally, by applying a backtracking technique, we can estimate the position of the clumps at least to the point when the common envelope event supposedly occurred. Before this event, the velocities of disk and jet clumps were different, and we cannot know them directly.

- **Enlarging the sample of born-again PNe**: Although the predicted percentage of CSPNe undergoing a VLTP event ranges between 15-25%, currently only five out of more than 4000 PNe have been confirmed as such. To clarify the aspects that remain open, it is necessary to search for more candidates to join this reduced group. In section 1.4.3 we described two very promising candidates to born-again PNe, namely PM 1-89 and WR 72. We have been awarded VLT MUSE Integral Field Spectroscopic observations for these two sources, pending its execution. The main goal of these observations would be assessing whether the abundances in their central regions are deficient in H. Otherwise the spectra of the surrounding nebulae will be used to obtain the fluxes of key emission lines to derive temperatures, densities, and chemical abundances using the software PyNeb (in this region, we can assume photoionization a priori). Then, in the inner region, we will consider whether a shock is occurring, in which case we will use MAPPINGS to derive temperatures, densities, and abundances as in chapter 3. Simultaneously, we aim to map the spatio-kinematics of the ejecta to determine whether they follow the "canonical" disk+jet structure or not, although this goal is limited by the limited spectral resolution of the VLT MUSE observations and may require follow-up high-dispersion spectroscopic observations. Successful results in both sources would result in a 40% increase in the current sample of known born-again PNe.

- **Assesing the role of binarity in born-again PNe**: In Chapter 5, the physical structure described for A 58, featuring a molecular disk and bipolar jets and an ionized hourglass structure, most likely requires a binary system to form. Similarly, in Sakurai's Object, A 30, and A 78, it has been observed that their morphologies are only possible with the existence of a binary (Tafoya et al. 2023; Meaburn & Lopez 1996; Meaburn et al. 1998; Fang et al. 2014). Indeed, a binary companion has been confirmed for the CSPN of A 30 (Jacoby et al. 2020), although its possible effects on the nebular shaping are still to be explored. Moreover the ADFs reported for A 58 and A 30 are among the highest ever recorded in any PN and, in the absence of calculations for the other born-again PNe, it is reasonable to expect that they will also be elevated. Wesson et al. (2018) present solid evidence that there is a link between high ADF values and the presence of a binary, which can arguably be extended to born-again PNe. Last, but not least important, the high Ne abundances seen in most born-again PNe (see Wesson et al. 2003, 2008, and chapter 6) are unexpected in theoretical models of VLTP. This initially cast doubts on the occurrence of a VLTP in favor of a nova event, although Lau et al. (2011) later proposed several binary scenarios that involved a VLTP (not exclusively) to achieve the observed high Ne abundances. On the other hand, the abundances of other elements, such as H, C, O, and N, are rather consistent with single stellar evolution models after undergoing a VLTP (see for instance Miller Bertolami et al. 2006). In particular the C/O ratio has been found to be consistent once that the C trapped in dust is accounted for, so far only for A 30, A 78, and HuBi 1 (Toalá et al. 2021a, Rodriguez-Gonzalez et al. 2024, Rodriguez-Gonzalez et al. in prep.).

Questions naturally arise on wehther all born-again PNe have a binary as their CSPN. It is also unclear what is the role played by a binary in both the morphology and chemical composition of the ejecta. Or even if it affects only one of these aspects, but not the other. As for the morphology, as described earlier, it is more than clear that it does play a role, but it is still unclear to what extent. Rodríguez-González et al. (2022) presented a CE scenario that could qualitatively explain the morphology in A 30. However, this still needs to be confirmed by conducting 3D hydrodynamic simulations. As for the chemical abundances, Lau et al. (2011) proposed scenarios on the effects of a binary involving a CE episode on those. Unfortunately, the scenarios proposed have notorious shortcomings, especially in the occurrence ratio. It is therefore necessary to explore other scenarios involving binaries that, being more probable, would explain the observed abundances. Finally there is the question on whether all born-again PNe require a binary, whose answer seems to be negative, as supported by the case of HuBi 1. The abundances obtained in chapter 3 are consistent with single star evolution models (except for the C/O ratio), and 3D hydrodynamic simulations for a single star reproduce its morphology (Toalá et al. 2021b). Nevertheless, it cannot be ruled out that its CSPN would be binary, with little or negligeable effctes on both its morphology and abundances.

- **Shocks and the role of molecular gas**: As highlighted in the previous section, the presence of shocks in the ejecta of born-again PNe is clear and must be taken into account when determining chemical abundances or modeling dust. One short-to-medium term goal is to delve deeper into the use of MAPPINGS for calculating abundances and to apply it to cases like A 58, as mentioned in Chapter 5, and in Sakurai's Object, which exhibits a similar morpho-kinematic structure and where a shock likely exists. Simultaneously, I plan to obtain new observations in the submillimeter and millimeter range with APEX and ALMA, to which I will have access in the coming year, in order to have a complete view of the structure of the central regions. Indeed, molecular gas, we have seen, plays a key role in born-again PNe.

Bibliography

Abell, G. O. 1966, ApJ, 144, 259

Abell, G. O. & Goldreich, P. 1966, PASP, 78, 232

Ali, A., Sabin, L., Snaid, S., & Basurah, H. M. 2012, A&A, 541, A98

Allen, M. G., Groves, B. A., Dopita, M. A., Sutherland, R. S., & Kewley, L. J. 2008, ApJS, 178, 20

Althaus, L. G., García-Berro, E., Isern, J., & Córsico, A. H. 2005, A&A, 441, 689

Arkhipova, V. P. 1994, Astronomy Letters, 20, 804

Arkhipova, V. P., Esipov, V. F., Noskova, R. I., et al. 1998, Astronomy Letters, 24, 248

Asplund, M., Grevesse, N., Sauval, A. J., & Scott, P. 2009, ARA&A, 47, 481

Asplund, M., Gustafsson, B., Lambert, D. L., & Kameswara Rao, N. 1997, A&A, 321, L17

Asplund, M., Lambert, D. L., Kipper, T., Pollacco, D., & Shetrone, M. D. 1999, A&A, 343, 507

Baldwin, J. A., Phillips, M. M., & Terlevich, R. 1981, PASP, 93, 5

Balick, B., Guerrero, M. A., & Ramos-Larios, G. 2021, ApJ, 907, 104

Ballik, E. A. & Ramsay, D. A. 1963, ApJ, 137, 84

Barlow, M. J. & Hummer, D. G. 1982, in Wolf-Rayet Stars: Observations, Physics, Evolution, ed. C. W. H. De Loore & A. J. Willis, Vol. 99, 387–392

Becker, S. A. & Iben, I., J. 1979, ApJ, 232, 831

Bédard, A. 2024, Ap&SS, 369, 43

Bédard, A., Bergeron, P., & Brassard, P. 2023, ApJ, 946, 24

Bianchi, L. & Grewing, M. 1987, A&A, 181, 85

Bidelman, W. P. 1971, ApJ, 165, L7

Bidelman, W. P. 1973, in Bulletin of the American Astronomical Society, Vol. 5, 442

Binette, L., Dopita, M. A., & Tuohy, I. R. 1985, ApJ, 297, 476

Blöcker, T. 2001, Ap&SS, 275, 1

Bloecker, T. & Schoenberner, D. 1997, A&A, 324, 991

Bond, H. E., Meakes, M. G., Liebert, J. W., & Renzini, A. 1993, in Planetary Nebulae, ed. R. Weinberger & A. Acker, Vol. 155, 499

Borkowski, K. J. & Harrington, J. P. 1991, ApJ, 379, 168

Borkowski, K. J., Harrington, J. P., Blair, W. P., & Bregman, J. D. 1994, ApJ, 435, 722

Borkowski, K. J., Harrington, J. P., Tsvetanov, Z., & Clegg, R. E. S. 1993, ApJ, 415, L47

Borkowski, K. J., Harrington, J. P., & Tsvetanov, Z. I. 1995, ApJ, 449, L143

Borkowski, K. J., Sarazin, C. L., & Soker, N. 1990, ApJ, 360, 173

Chesneau, O., Clayton, G. C., Lykou, F., et al. 2009, A&A, 493, L17

Christy-Sackmann, I. J. & Despain, K. H. 1974, ApJ, 189, 523

Chu, Y.-H., Chang, T. H., & Conway, G. M. 1997, ApJ, 482, 891

Chu, Y.-H. & Ho, C.-H. 1995, ApJ, 448, L127

Clayton, G. C., Bond, H. E., Long, L. A., et al. 2013, ApJ, 771, 130

Clayton, G. C. & De Marco, O. 1997, AJ, 114, 2679

Clayton, G. C., Kerber, F., Pirzkal, N., et al. 2006, ApJ, 646, L69

Clayton, G. C., Sugerman, B. E. K., Stanford, S. A., et al. 2011, ApJ, 743, 44

Clegg, R. E. S., Devaney, M. N., Doel, A. P., et al. 1993, in Planetary Nebulae, ed. R. Weinberger & A. Acker, Vol. 155, 388

Cohen, J. G. & Gillett, F. C. 1989, ApJ, 346, 803

Cohen, J. G. & Phillips, A. C. 1980, ApJ, 237, 99

Cohen, M. & Barlow, M. J. 1974, ApJ, 193, 401

Cohen, M., Hudson, H. S., O'Dell, S. L., & Stein, W. A. 1977, MNRAS, 181, 233

Condon, J. J. 1997, PASP, 109, 166

Corradi, R. L. M., García-Rojas, J., Jones, D., & Rodríguez-Gil, P. 2015, ApJ, 803, 99

Corradi, R. L. M., Sánchez-Blázquez, P., Mellema, G., Gianmanco, C., & Schwarz, H. E. 2004, A&A, 417, 637

Cox, D. P. 2005, ARA&A, 43, 337

Crowther, P. A., De Marco, O., & Barlow, M. J. 1998, MNRAS, 296, 367

Dance, M., Palay, E., Nahar, S. N., & Pradhan, A. K. 2013, MNRAS, 435, 1576

Danehkar, A. 2014, PhD thesis, Macquarie University, Australia

Delgado-Inglada, G., Morisset, C., & Stasińska, G. 2014, MNRAS, 440, 536

Dinerstein, H. L. & Lester, D. F. 1984, ApJ, 281, 702

Dopita, M. A. 1976, ApJ, 209, 395

Dopita, M. A. 1977, ApJS, 33, 437

Dopita, M. A. 1978, ApJS, 37, 117

Dopita, M. A., Vogt, F. P. A., Sutherland, R. S., et al. 2018, ApJS, 237, 10

Dreizler, S. & Heber, U. 1998, A&A, 334, 618

Duerbeck, H. W. 1996, IAU Circ., 6328, 1

Duerbeck, H. W. 2002, Ap&SS, 279, 5

Duerbeck, H. W. & Benetti, S. 1996, ApJ, 468, L111

Duerbeck, H. W., Benetti, S., Gautschy, A., et al. 1997, AJ, 114, 1657

Duerbeck, H. W., Liller, W., Sterken, C., et al. 2000, AJ, 119, 2360

Ercolano, B., Barlow, M. J., Storey, P. J., et al. 2003, MNRAS, 344, 1145

Evans, A., Geballe, T. R., Tyne, V. H., et al. 2004, MNRAS, 353, L41

Evans, A., Gehrz, R. D., Woodward, C. E., et al. 2020, MNRAS, 493, 1277

Evans, A., Tyne, V. H., van Loon, J. T., et al. 2006, MNRAS, 373, L75

Eyres, S. P. S. 2002, Ap&SS, 279, 69

Eyres, S. P. S., Evans, A., Geballe, T. R., Salama, A., & Smalley, B. 1998a, MNRAS, 298, L37

Eyres, S. P. S., Geballe, T. R., Tyne, V. H., et al. 2004, MNRAS, 350, L9

Eyres, S. P. S., Richards, A. M. S., Evans, A., & Bode, M. F. 1998b, MNRAS, 297, 905

Eyres, S. P. S., Smalley, B., Geballe, T. R., et al. 1999, MNRAS, 307, L11

Fang, X., Guerrero, M. A., Marquez-Lugo, R. A., et al. 2014, ApJ, 797, 100

Faundez-Abans, M. & Maciel, W. J. 1986, A&A, 158, 228

Feibelman, W. A. 1996, ApJ, 464, 910

Ferland, G. J., Chatzikos, M., Guzmán, F., et al. 2017, Rev. Mexicana Astron. Astrofis., 53, 385

Ferrario, L., de Martino, D., & Gänsicke, B. T. 2015, Space Sci. Rev., 191, 111

Filippenko, A. V. 1982, PASP, 94, 715

Fischer, C. F. & Rubin, R. H. 2004, MNRAS, 355, 461

Ford, H. C. 1971, ApJ, 170, 547

Fragkou, V., Parker, Q. A., Zijlstra, A. A., et al. 2022, ApJ, 935, L35

Frew, D. J., Bojičić, I. S., Parker, Q. A., et al. 2014, MNRAS, 440, 1345

Frogel, J. A., Cohen, J. G., & Persson, S. E. 1983, ApJ, 275, 773

Galavis, M. E., Mendoza, C., & Zeippen, C. J. 1997, A&AS, 123, 159

García-Rojas, J., Morisset, C., Jones, D., et al. 2022, MNRAS, 510, 5444

García-Rojas, J., Peña, M., Morisset, C., et al. 2013, A&A, 558, A122

García-Rojas, J., Peña, M., Morisset, C., & Ruiz, M.-T. 2012, in Planetary Nebulae: An Eye to the Future, Vol. 283, 364–365

García-Segura, G., Villaver, E., Langer, N., Yoon, S. C., & Manchado, A. 2014, ApJ, 783, 74

Gehrz, R. D. 1999, Phys. Rep., 311, 405

Gentile Fusillo, N. P., Tremblay, P.-E., Gänsicke, B. T., et al. 2019, MNRAS, 482, 4570

Gesicki, K., Zijlstra, A. A., Hajduk, M., & Szyszka, C. 2014, A&A, 566, A48

Giles, K. 1981, MNRAS, 195, 63P

Gillett, F. C., Jacoby, G. H., Joyce, R. R., et al. 1989, ApJ, 338, 862

Godefroid, M. & Fischer, C. F. 1984, Journal of Physics B Atomic Molecular Physics, 17, 681

Gonzalez, G., Lambert, D. L., Wallerstein, G., et al. 1998, ApJS, 114, 133

Górny, S. K. & Tylenda, R. 2000, A&A, 362, 1008

Green, G. M., Schlafly, E. F., Finkbeiner, D., et al. 2018, MNRAS, 478, 651

Greenstein, J. L. & Minkowski, R. 1964, ApJ, 140, 1601

Griffith, R. L., Wright, J. T., Maldonado, J., et al. 2015, ApJS, 217, 25

Guerrero, M. A., Chu, Y.-H., Hamann, W.-R., et al. 2012, in Planetary Nebulae: An Eye to the Future, Vol. 283, 378–379

Guerrero, M. A., Fang, X., Miller Bertolami, M. M., et al. 2018, Nature Astronomy, 2, 784

Guerrero, M. A. & Manchado, A. 1996, ApJ, 472, 711

Guinan, E. F., McCook, G. P., & Thrash, T. A. 1992, IAU Circ., 5632, 1

Gvaramadze, V. V., Kniazev, A. Y., Gräfener, G., & Langer, N. 2020, MNRAS, 492, 3316

Hackwell, J. A., Gehrz, R. D., & Grasdalen, G. L. 1979, ApJ, 234, 133

Hajduk, M., Zijlstra, A. A., Herwig, F., et al. 2005, Science, 308, 231

Hamann, W. R. & Gräfener, G. 2004, A&A, 427, 697

Harman, R. F. & Seaton, M. J. 1966, MNRAS, 132, 15

Harrington, J. P. 1996, in Astronomical Society of the Pacific Conference Series, Vol. 96, Hydrogen Deficient Stars, ed. C. S. Jeffery & U. Heber, 193

Harrington, J. P., Borkowski, K. J., & Tsvetanov, Z. 1995, ApJ, 439, 264

Harrington, J. P. & Feibelman, W. A. 1984, ApJ, 277, 716

Harrington, J. P. & Marionni, P. A. 1976, ApJ, 206, 458

Harrington, J. P. & Paltoglou, G. 1993, ApJ, 411, L103

Harrison, T. E. 1996, PASP, 108, 1112

Hartwick, F. D. A., Cowley, A. P., & Grindlay, J. E. 1982, ApJ, 254, L11

Hawley, S. A. & Miller, J. S. 1978, ApJ, 221, 851

Hazard, C., Terlevich, R., Morton, D. C., Sargent, W. L. W., & Ferland, G. 1980, Nature, 285, 463

Heap, S. R. 1979, in Mass Loss and Evolution of O-Type Stars, ed. P. S. Conti & C. W. H. De Loore, Vol. 83, 99–102

Henry, R. B. C., Kwitter, K. B., & Balick, B. 2004, AJ, 127, 2284

Henry, R. B. C., Speck, A., Karakas, A. I., Ferland, G. J., & Maguire, M. 2012, ApJ, 749, 61

Herald, J. E. & Bianchi, L. 2004, ApJ, 609, 378

Herbig, G. H. 1958, PASP, 70, 605

Herbig, G. H. & Boyarchuk, A. A. 1968, ApJ, 153, 397

Herwig, F. 2001a, Ap&SS, 275, 15

Herwig, F. 2001b, ApJ, 554, L71

Herwig, F. 2005, ARA&A, 43, 435

Herwig, F., Blöcker, T., Langer, N., & Driebe, T. 1999, A&A, 349, L5

Hinkle, K. & Joyce, R. 2002, Ap&SS, 279, 51

Hinkle, K. H. & Joyce, R. R. 2014, ApJ, 785, 146

Hinkle, K. H., Joyce, R. R., & Hedden, A. 2001, A&A, 367, 250

Hinkle, K. H., Joyce, R. R., Matheson, T., Lacy, J. H., & Richter, M. J. 2020, ApJ, 904, 34

Hinkle, K. H., Joyce, R. R., & Smith, V. 1995, AJ, 109, 808

Hinkle, K. H., Lebzelter, T., Joyce, R. R., et al. 2008, A&A, 479, 817

Howarth, I. D. 1983, MNRAS, 203, 301

Hu, J. Y. & Bibo, E. A. 1990, A&A, 234, 435

Hummer, D. G. & Storey, P. J. 1987, MNRAS, 224, 801

Höfner, S. & Olofsson, H. 2018, The Astronomy and Astrophysics Review, 26, 1

Iben, I., J. 1975, ApJ, 196, 525

Iben, I., J. 1984, ApJ, 277, 333

Iben, I., J. 1991, in Evolution of Stars: the Photospheric Abundance Connection, ed. G. Michaud & A. V. Tutukov, Vol. 145, 257

Iben, I., J. 1995, Phys. Rep., 250, 2

Iben, I., J., Kaler, J. B., Truran, J. W., & Renzini, A. 1983, ApJ, 264, 605

Iben, I., J. & MacDonald, J. 1995, in White Dwarfs, ed. D. Koester & K. Werner, Vol. 443, 48

Iben, I., J. & Renzini, A. 1983, ARA&A, 21, 271

Jacob, R., Schönberner, D., & Steffen, M. 2013, A&A, 558, A78

Jacoby, G., De Marco, O., Willmarth, D., et al. 1998, IAU Circ., 7065, 2

Jacoby, G. H. 1979, PASP, 91, 754

Jacoby, G. H. & Ford, H. C. 1983, ApJ, 266, 298

Jacoby, G. H., Hillwig, T. C., & Jones, D. 2020, MNRAS, 498, L114

Jacoby, G. H., Morse, J. A., Fullton, L. K., Kwitter, K. B., & Henry, R. B. C. 1997, AJ, 114, 2611

Jeffery, C. S. & Schönberner, D. 2006, A&A, 459, 885

Jones, D., Wesson, R., García-Rojas, J., Corradi, R. L. M., & Boffin, H. M. J. 2016, MNRAS, 455, 3263

Jurcsik, J. 1992, Information Bulletin on Variable Stars, 3775, 1

Kaler, J. B. 1981, ApJ, 250, L31

Kaler, J. B. & Feibelman, W. A. 1984, ApJ, 282, 719

Kaler, J. B., Feibelman, W. A., & Henrichs, H. F. 1988, ApJ, 324, 528

Kaltenegger, L. & Traub, W. A. 2009, ApJ, 698, 519

Kamath, U. S. & Ashok, N. M. 1999, MNRAS, 302, 512

Kameswara Rao, N., Venugopal, V. R., & Patnaik, A. R. 1987, Journal of Astrophysics and Astronomy, 8, 227

Karakas, A. I. & Lugaro, M. 2010, PASA, 27, 227

Karakas, A. I. & Lugaro, M. 2016, ApJ, 825, 26

Karakas, A. I., van Raai, M. A., Lugaro, M., Sterling, N. C., & Dinerstein, H. L. 2009, ApJ, 690, 1130

Kauffmann, G., Heckman, T. M., Tremonti, C., et al. 2003, MNRAS, 346, 1055

Keller, G. R., Bianchi, L., & Maciel, W. J. 2014, MNRAS, 442, 1379

Kerber, F., Köppen, J., Roth, M., & Trager, S. C. 1999, A&A, 344, L79

Kerber, F., Pirzkal, N., De Marco, O., et al. 2002, ApJ, 581, L39

Kewley, L. J., Dopita, M. A., Sutherland, R. S., Heisler, C. A., & Trevena, J. 2001, ApJ, 556, 121

Kewley, L. J., Groves, B., Kauffmann, G., & Heckman, T. 2006, MNRAS, 372, 961

Kimeswenger, S., Gratl, H., Kerber, F., et al. 1997, IAU Circ., 6608, 1

Kimeswenger, S., Kerber, F., & Weinberger, R. 1998, MNRAS, 296, 614

Kimeswenger, S., Koller, J., & Schmeja, S. 2000, A&A, 360, 699

Kingsburgh, R. L. & Barlow, M. J. 1994, MNRAS, 271, 257

Kisielius, R., Storey, P. J., Ferland, G. J., & Keenan, F. P. 2009, MNRAS, 397, 903

Kleinman, S. J., Kepler, S. O., Koester, D., et al. 2013, ApJS, 204, 5

Koesterke, L. & Werner, K. 1998, ApJ, 500, L55

Koller, J. & Kimeswenger, S. 2001, ApJ, 559, 419

Kwok, S., Purton, C. R., & Fitzgerald, P. M. 1978, ApJ, 219, L125

Langer, G. E., Kraft, R. P., & Anderson, K. S. 1974, ApJ, 189, 509

Lau, H. H. B., De Marco, O., & Liu, X. W. 2011, MNRAS, 410, 1870

Lawlor, T. M. 2021, MNRAS, 504, 667

Lawlor, T. M. & MacDonald, J. 2003, ApJ, 583, 913

Lederle, C., Kimeswenger, S., & Whitelock, P. 2001, IAU Circ., 7592, 3

Lee, M. G., Freedman, W. L., & Madore, B. F. 1993, ApJ, 417, 553

Leuenhagen, U. & Hamann, W. R. 1998, A&A, 330, 265

Leuenhagen, U., Hamann, W. R., & Jeffery, C. S. 1996, A&A, 312, 167

Liller, W., Duerbeck, H. W., van der Meer, A., & van Genderen, A. 1998a, IAU Circ., 7049, 2

Liller, W., Janson, M., Duerbeck, H. W., & van Genderen, A. 1998b, IAU Circ., 6825, 2

Liu, X. W., Barlow, M. J., Zhang, Y., Bastin, R. J., & Storey, P. J. 2006, MNRAS, 368, 1959

Liu, X. W., Luo, S. G., Barlow, M. J., Danziger, I. J., & Storey, P. J. 2001, MNRAS, 327, 141

Liu, X. W., Storey, P. J., Barlow, M. J., et al. 2000, MNRAS, 312, 585

Ludendorff, H. 1922, Astronomische Nachrichten, 217, 161

Lundmark, K. 1921, PASP, 33, 314

Luridiana, V., Morisset, C., & Shaw, R. A. 2015, A&A, 573, A42

Lynch, D. K., Rudy, R. J., Russell, R. W., et al. 2002, Ap&SS, 279, 57

Manchado, A., Garcia-Lario, P., & Pottasch, S. R. 1989, A&A, 218, 267

Manchado, A., Pottasch, S. R., & Mampaso, A. 1988, A&A, 191, 128

Manick, R., Miszalski, B., & McBride, V. 2015, MNRAS, 448, 1789

Marcolino, W. L. F., Hillier, D. J., de Araujo, F. X., & Pereira, C. B. 2007, ApJ, 654, 1068

Marigo, P., Girardi, L., Groenewegen, M. A. T., & Weiss, A. 2001, A&A, 378, 958

Marigo, P., Girardi, L., Weiss, A., Groenewegen, M. A. T., & Chiosi, C. 2004, A&A, 423, 995

Marston, A. P., Chu, Y. H., & Garcia-Segura, G. 1994, ApJS, 93, 229

Marten, H. & Schoenberner, D. 1991, A&A, 248, 590

McCarthy, J. K., Mould, J. R., Mendez, R. H., et al. 1990, ApJ, 351, 230

McCook, G. P. & Sion, E. M. 1999, ApJS, 121, 1

McLaughlin, B. M. & Bell, K. L. 2000, Journal of Physics B Atomic Molecular Physics, 33, 597

Meaburn, J. & Lopez, J. A. 1996, ApJ, 472, L45

Meaburn, J., Lopez, J. A., Bryce, M., & Redman, M. P. 1998, A&A, 334, 670

Medina, S. & Peña, M. 2000, Rev. Mexicana Astron. Astrofis., 36, 121

Mellema, G. 1993, PhD thesis, University of Leiden, Netherlands

Méndez-Delgado, J. E., Esteban, C., García-Rojas, J., Kreckel, K., & Peimbert, M. 2023, Nature, 618, 249

Miller Bertolami, M. M. 2016, A&A, 588, A25

Miller Bertolami, M. M. & Althaus, L. G. 2007, MNRAS, 380, 763

Miller Bertolami, M. M., Althaus, L. G., Serenelli, A. M., & Panei, J. A. 2006, A&A, 449, 313

Monteiro, H. & Falceta-Gonçalves, D. 2011, ApJ, 738, 174

Montoro-Molina, B., Guerrero, M. A., Pérez-Díaz, B., et al. 2022a, MNRAS, 512, 4003

Montoro-Molina, B., Guerrero, M. A., & Toalá, J. A. 2023, MNRAS, 526, 4359

Montoro-Molina, B., Guerrero, M. A., Toalá, J. A., & Rodríguez-González, J. B. 2022b, ApJ, 934, 18

Morisset, C. 2018, in Walking the Line 2018, 2

Moseley, H. 1980, ApJ, 238, 892

Nakano, S., Sakurai, Y., Hazen, M., et al. 1996, IAU Circ., 6322, 1

Ohnaka, K. & Jara Bravo, B. A. 2022, A&A, 668, A119

Osterbrock, D. E. & Ferland, G. J. 2006, Astrophysics of gaseous nebulae and active galactic nuclei

Osterbrock, D. E., Fulbright, J. P., Martel, A. R., et al. 1996, PASP, 108, 277

Paczyński, B. 1970, Acta Astron., 20, 47

Paczyński, B. 1971, Acta Astron., 21, 417

Pascual, S., Cardiel, N., Gil de Paz, A., et al. 2019, in Highlights on Spanish Astrophysics X, ed. B. Montesinos, A. Asensio Ramos, F. Buitrago, R. Schödel, E. Villaver, S. Pérez-Hoyos, & I. Ordóñez-Etxeberria, 227–227

Pavlenko, Y. V., Geballe, T. R., Evans, A., et al. 2004, A&A, 417, L39

Peña, M. 2005, Rev. Mexicana Astron. Astrofis., 41, 423

Peña, M., Hernández-Martínez, L., & Ruiz-Escobedo, F. 2021, MNRAS, 503, 972

Peña, M., Stasińska, G., & Medina, S. 2001, A&A, 367, 983

Peimbert, M. 1978, in Planetary Nebulae, ed. Y. Terzian, Vol. 76, 215–224

Perea-Calderón, J. V., García-Hernández, D. A., García-Lario, P., Szczerba, R., & Bobrowsky, M. 2009, A&A, 495, L5

Perinotto, M. 1991, ApJS, 76, 687

Phillips, J. P., Cuesta, L., & Kemp, S. N. 2005, MNRAS, 357, 548

Pismis, P. 1989, MNRAS, 237, 611

Plait, P. & Soker, N. 1990, AJ, 99, 1883

Pollacco. 1996, IAU Circ., 6328, 1

Pollacco, D. L. & Hill, P. W. 1994, MNRAS, 267, 692

Pollacco, D. L., Lawson, W. A., Clegg, R. E. S., & Hill, P. W. 1992, MNRAS, 257, 33P

Pottasch, S. R. 1980, A&A, 89, 336

Pottasch, S. R., Bernard-Salas, J., Beintema, D. A., & Feibelman, W. A. 2003, A&A, 409, 599

Pottasch, S. R., Mampaso, A., Manchado, A., & Menzies, J. 1986, in IAU Colloq. 87: Hydrogen Deficient Stars and Related Objects, ed. K. Hunger, D. Schoenberner, & N. Kameswara Rao, 359

Raga, A. C., Riera, A., Mellema, G., Esquivel, A., & Velázquez, P. F. 2008, A&A, 489, 1141

Ramos-Larios, G., Phillips, J. P., & Cuesta, L. C. 2011, MNRAS, 411, 1245

Ramsbottom, C. A., Bell, K. L., & Keenan, F. P. 1997, MNRAS, 284, 754

Rauch, T., Furlan, E., Kerber, F., & Roth, M. 2000, in Astronomical Society of the Pacific Conference Series, Vol. 199, Asymmetrical Planetary Nebulae II: From Origins to Microstructures, ed. J. H. Kastner, N. Soker, & S. Rappaport, 341

Reay, N. K., Atherton, P. D., & Taylor, K. 1983, MNRAS, 203, 1079

Rechy-García, J. S., Guerrero, M. A., Santamaría, E., et al. 2020, ApJ, 903, L4

Rechy-García, J. S., Toalá, J. A., Cazzoli, S., et al. 2021, MNRAS, 508, 2254

Reichel, M., Kimeswenger, S., van Hoof, P. A. M., et al. 2022, ApJ, 939, 103

Reindl, N., Rauch, T., Miller Bertolami, M. M., Todt, H., & Werner, K. 2017, MNRAS, 464, L51

Reindl, N., Rauch, T., Parthasarathy, M., et al. 2014, A&A, 565, A40

Renzini, A. 1989, in Planetary Nebulae, ed. S. Torres-Peimbert, Vol. 131, 391–400

Rodríguez, L. F., Carrasco-González, C., Cantó, J., et al. 2017, Rev. Mexicana Astron. Astrofis., 53, 45

Rodríguez-González, A., Peña, M., Hernández-Martínez, L., et al. 2023, ApJ, 955, 151

Rodríguez-González, J. B., Santamaría, E., Toalá, J. A., et al. 2022, MNRAS, 514, 4794

Rynkun, P., Gaigalas, G., & Jönsson, P. 2019, A&A, 623, A155

Santamaría, E., Guerrero, M. A., Ramos-Larios, G., et al. 2020, ApJ, 892, 60

Schlafly, E. F., Green, G. M., Lang, D., et al. 2018, ApJS, 234, 39

Schmidt-Voigt, M. & Koeppen, J. 1987, A&A, 174, 211

Schoenberner, D. 1979, A&A, 79, 108

Schoenberner, D. 1990, in From Miras to Planetary Nebulae: Which Path for Stellar Evolution?, ed. M. O. Mennessier & A. Omont, 355

Schwarzschild, M. & Härm, R. 1965, ApJ, 142, 855

Seitter, W. C. 1985, in European Southern Observatory Conference and Workshop Proceedings, Vol. 21, European Southern Observatory Conference and Workshop Proceedings, 253–258

Seitter, W. C. 1987, The Messenger, 50, 14

Shklovsky, I. S. 1957, in Non-stable stars, ed. G. H. Herbig, Vol. 3, 83

Simpson, J., Jones, D., Wesson, R., & García-Rojas, J. 2022, Research Notes of the American Astronomical Society, 6, 4

Sippel, A. C. & Hurley, J. R. 2013, MNRAS, 430, L30

Smith, J. D. T., Armus, L., Dale, D. A., et al. 2007, PASP, 119, 1133

Smith, L. F. & Aller, L. H. 1969, ApJ, 157, 1245

Soker, N. 1994, MNRAS, 270, 774

Soker, N. 1997, ApJS, 112, 487

Soker, N. & Zucker, D. B. 1997, MNRAS, 289, 665

Steffen, W., Koning, N., Wenger, S., Morisset, C., & Magnor, M. 2011, IEEE Transactions on Visualization and Computer Graphics, 17, 454

Storey, P. J., Sochi, T., & Badnell, N. R. 2014, MNRAS, 441, 3028

Suárez, O., García-Lario, P., Manchado, A., et al. 2006, A&A, 458, 173

Sutherland, R., Dopita, M., Binette, L., & Groves, B. 2018, MAPPINGS V: Astrophysical plasma modeling code, Astrophysics Source Code Library, record ascl:1807.005

Sutherland, R. S. & Dopita, M. A. 2017, ApJS, 229, 34

Tafoya, D., Toalá, J. A., Unnikrishnan, R., et al. 2022, ApJ, 925, L4

Tafoya, D., Toalá, J. A., Vlemmings, W. H. T., et al. 2017, A&A, 600, A23

Tafoya, D., van Hoof, P. A. M., Toalá, J. A., et al. 2023, A&A, 677, L8

Tatarnikov, A. M., Shenavrin, V. I., Yudin, B. F., Whitelock, P. A., & Feast, M. W. 2000, Astronomy Letters, 26, 506

Tayal, S. S. 2011, ApJS, 195, 12

Tayal, S. S. & Zatsarinny, O. 2010, ApJS, 188, 32

Toalá, J. A., Guerrero, M. A., Todt, H., et al. 2015, ApJ, 799, 67

Toalá, J. A., Jiménez-Hernández, P., Rodríguez-González, J. B., et al. 2021a, MNRAS, 503, 1543

Toalá, J. A., Lora, V., Montoro-Molina, B., Guerrero, M. A., & Esquivel, A. 2021b, MNRAS, 505, 3883

Toalá, J. A., Ramos-Larios, G., Guerrero, M. A., & Todt, H. 2019, MNRAS, 485, 3360

Todt, H. & Hamann, W. R. 2015, in Wolf-Rayet Stars, ed. W.-R. Hamann, A. Sander, & H. Todt, 253–258

Tody, D. 1986, in Society of Photo-Optical Instrumentation Engineers (SPIE) Conference Series, Vol. 627, Instrumentation in astronomy VI, ed. D. L. Crawford, 733

Tody, D. 1993, in Astronomical Society of the Pacific Conference Series, Vol. 52, Astronomical Data Analysis Software and Systems II, ed. R. J. Hanisch, R. J. V. Brissenden, & J. Barnes, 173

Tresse, L., Maddox, S., Loveday, J., & Singleton, C. 1999, MNRAS, 310, 262

Tsamis, Y. G. & Péquignot, D. 2005, MNRAS, 364, 687

Tweedy, R. W. & Kwitter, K. B. 1996, ApJS, 107, 255

Tyne, V. H., Evans, A., Geballe, T. R., et al. 2002, MNRAS, 334, 875

Tyne, V. H., Eyres, S. P. S., Geballe, T. R., et al. 2000, MNRAS, 315, 595

Ueta, T. & Otsuka, M. 2021, PASP, 133, 093002

van den Bergh, S. 1971, PASP, 83, 819

van der Hucht, K. A., Jurriens, T. A., Olnon, F. M., et al. 1985, A&A, 145, L13

van der Veen, W. E. C. J., Habing, H. J., & Geballe, T. R. 1989, A&A, 226, 108 van Genderen, A. M. & Gautschy, A. 1995, A&A, 294, 453

van Hoof, P. A. M., Bryce, M., Evans, A., et al. 2006, in Planetary Nebulae in our Galaxy and Beyond, ed. M. J. Barlow & R. H. Méndez, Vol. 234, 75–78

van Hoof, P. A. M., Hajduk, M., Zijlstra, A. A., et al. 2007, A&A, 471, L9

van Hoof, P. A. M., Hajduk, M., Zijlstra, A. A., et al. 2008, in Astronomical Society of the Pacific Conference Series, Vol. 391, Hydrogen-Deficient Stars, ed. A. Werner & T. Rauch, 155

van Hoof, P. A. M., Kimeswenger, S., Van de Steene, G. C., et al. 2018, Galaxies, 6, 79

van Hoof, P. A. M., Kimeswenger, S., Van de Steene, G. C., et al. 2015, in Astronomical Society of the Pacific Conference Series, Vol. 493, 19th European Workshop on White Dwarfs, ed. P. Dufour, P. Bergeron, & G. Fontaine, 95

Vassiliadis, E. & Wood, P. R. 1994, ApJS, 92, 125

Veilleux, S. & Osterbrock, D. E. 1987, ApJS, 63, 295

Wareing, C. J., Zijlstra, A. A., & O'Brien, T. J. 2007, MNRAS, 382, 1233

Weidmann, W. A., Mari, M. B., Schmidt, E. O., et al. 2020, A&A, 640, A10

Weiss, A. & Ferguson, J. W. 2009, A&A, 508, 1343

Werner, K. 2001, Ap&SS, 275, 27

Werner, K. & Herwig, F. 2006, PASP, 118, 183

Wesson, R., Barlow, M. J., Liu, X. W., et al. 2008, MNRAS, 383, 1639

Wesson, R., Jones, D., García-Rojas, J., Boffin, H. M. J., & Corradi, R. L. M. 2018, MNRAS, 480, 4589

Wesson, R., Liu, X. W., & Barlow, M. J. 2003, MNRAS, 340, 253

Wolf, M. 1920, Astronomische Nachrichten, 211, 119

Wood, P. R., Olivier, E. A., & Kawaler, S. D. 2004, ApJ, 604, 800

Woodward, C. E., Lawrence, G. F., Gehrz, R. D., et al. 1993, ApJ, 408, L37

Worters, H. L., Rushton, M. T., Eyres, S. P. S., Geballe, T. R., & Evans, A. 2009, MNRAS, 393, 108

Yuan, H. B., Liu, X. W., Péquignot, D., et al. 2011, MNRAS, 411, 1035

Zeippen, C. J. 1982, MNRAS, 198, 111

Appendix A

Chapter 1

A.1 Selection and correction of emission lines in OSIRIS data

The emission of the inner shell of HuBi 1 is contaminated by that of the surrounding outer shell. This is a typical situation in multiple shell PNe where the contribution of the emission from the outer shell to the inner shell is normally ignored because the emission from the inner shell is much brighter than that of the outer shell. This is not the case for the emission from the inner shell of HuBi 1, for which the emission from some lines (e.g., the H Balmer lines) is much fainter than that from the outer shell. Therefore the contribution of the emission from the outer shell to the inner shell cannot be ignored and the measurement of the emission line fluxes for the inner and outer shells of HuBi 1 require a tailored approach.

The OSIRIS data provide information on the spatial location of the emission and cannot be used to disentangle the fraction of the emission at the location of the inner shell that corresponds to the inner and outer shells. Fortunately, the kinematic information provided by the MEGARA data can be used to separate the emission of the inner shell from that of the outer shell given their different expansion velocities (Rechy-García et al. 2020). Accordingly, we have defined four different types of emission lines: purely internal, purely external, external with some inner emission, and internal with some external emission. The classification for each emission line detected in HuBi 1 is presented in Table A.1.1.

- Purely internal (PI) or external (PE) emission lines.
  Lines whose emission arises mostly from the inner or outer shell, such as the [O III] or He II and the He I lines, respectively. The fluxes are measured directly from the spectra extracted from the corresponding apertures overlaid on Figure 3.1, i.e, the top and bottom spectra in Figure 3.5, but for the emission lines with available GTC MEGARA images (e.g., the [O III], He II and He I emission lines), whose total integrated fluxes are computed from these images.

- Lines mostly from the external shell with internal emission (EwI).
  The emission of the outer shell is dominated by H Balmer and He I recombination lines, implying strong contamination to the emission of the inner shell in these lines. The different expansion velocity of the inner and outer shells and the tomographic capability

of the GTC MEGARA data have allowed us to disentangle the emission in the Hα and Hβ lines as described in Sections 3.3.2.1 and 3.3.2.2. The flux of these emission lines from both shell is thus measured directly on the GTC MEGARA images of each shell. In the case of He I lines, with only GTC OSIRIS data, only 5875 He I line had enough S/N to obtain the emission of the inner shell by using lines profile. As well as in Hβ and Hα lines profiles has slight bumps at the location of inner shell corresponding with the emission of this shell, He I should has this bumps and we use Hβ to extract the inner emission of the He I line. First, the dereddened Hβ profile of inner shell (see, section 3.3.2.1) was subtracted from the total profile in order to obtain non-contaminated emission of the outer shell. Then the peaks of total emission He I profile and Hβ pure outer emission profile were equated to estimated the pure emission of He I line. Finally we subtract the Hβ profile from He I to obtain the emission purely internal of the later. Although this method is subject to a worse S/N, it provide an estimation of He I 5875 line. A similar method was also applied to other He I lines however the S/N was too large to obtain emission of the inner shell. Therefore these lines were assumed to be PE.

- Lines mostly from the internal shell with external emission (IwE).
  A number of important emission lines are notably bright in the inner shell, but the outer shell still presents significant emission. In the case of the emission lines of [N I] and [O II], with only GTC OSIRIS data, the surface brightness of the outer shell (top panel Figure 3.5) in these lines was measured and an average value adopted on the assumption that it is an homogeneous shell. Then, that emission was subtracted from the emission of the inner shell (bottom panel Figure 3.5) considering an equivalent aperture for the inner shell to obtain its net flux. The flux for outer shell was computed scaling its average surface brightness to the yellow and red apertures in Figure 3.1 to consider the flux of the outer shell projected onto the inner shell. In the case of the emission lines of [N II] and [S II], which have GTC MEGARA data, a similar procedure to that used for the Hα and Hβ lines could have been applied. However, the emissions from the inner and outer shells of [N II] and [S II] could not be perfectly separated in the velocity space, as was done for Hα and Hβ, because the emission from the inner shell is present in all velocity channels, not only in high-velocity components, whereas that of the outer shell has emission from an intermediate region occupying velocity channels with relatively high expansion velocities (Toalá et al. 2021b). In this case, we first determined the emission of these lines from the inner shell that could be isolated in high-velocity components as for Hα and Hβ. Then at lower velocities, where intermediate/outer and inner shells are present, a mask of 2.5 arcsec in radius was applied and the flux measured on this aperture. The flux of the inner shell was the sum of both terms, whereas for the outer shell, the flux adopted was that of the emission beyond 2.5 arcsec.

We note that the Hβ emission line is used to compute the different line ratios listed in Table 3.1. For the inner shell, these are computed using the total Hβ and line fluxes derived from the GTC MEGARA image if there is available GTC MEGARA image of the inner shell for that line. If there were no available GTC MEGARA image of that line, the Hβ flux is computed

Line	DCR shift (arcsec)	Line Classification
[O II] 3727	+1.22	IwE
[Ne III] 3869	+1.08	PI
Hζ+He I 3889	+1.06	PE
Hϵ+[Ne III] 3969	+0.99	...
He I 4026	...	PE
[S II] 4069	+0.91	PI
Hδ 4101	+0.88	PE
Hγ 4340	+0.71	PE
[O III] 4363	+0.70	PI
He I 4471	+0.63	PE
C I:O II:N II:4562+4570	+0.58	PI
He II 4686	+0.51	PI
Hβ 4861	+0.43	EwI
[O III] 4959	+0.38	PI
[O III] 5007	+0.36	PI
He I 5016	+0.36	PE
[N I] 5199	+0.29	IwE
[N II] 5755	+0.11	PI
He I 5876	+0.08	EwI
[O I] 6300	+0.01	PI
[S III] 6312	−0.01	PI
[O I] 6363	−0.02	PI
[N II] 6548	−0.05	IwE
Hα 6563	−0.05	EwI
[N II] 6584	−0.06	IwE
He I 6678	−0.07	PE
[S II] 6717	−0.08	IwE
[S II] 6731	−0.08	IwE
He I 7065	−0.13	PE
[Ar III] 7135	−0.14	PI
C II 7236	−0.16	PI
C I, O II? 7289	−0.16	PI
[O II] 7320	−0.17	PI
[O II] 7330	−0.17	PI
N I:O II 7379	−0.18	PI

Table A.1.1: Atmospheric differential chromatic refraction (DCR) shift for the emission lines detected in the GTC OSIRIS spectrum of HuBi 1 and line classification according to the fraction of emission from the inner and outer shells.

from a pseudo-slit onto the GTC MEGARA image at the location of the GTC OSIRIS slit (see next Appendix).

A.2 Correcting the Atmospheric Differential Chromatic Refraction in the OSIRIS Data

The OSIRIS observations of HuBi 1 were obtained at the time around its culmination, but still at large airmass values at the ORM, in the range from 1.49 to 1.41, when notable differential chromatic refraction (DCR) effects can be expected. DCR effects are usually minimised selecting the position angle (PA) of the slit along the parallactic angle, which is close to the North-South direction near culmination. The PA of the slit during the observations was however set almost orthogonally, at PA 90° along the East-West direction, to avoid background stars and to register nebular areas of the highest surface brightness, thus optimising the scientific return of the observations. As a result, DCR effects cannot be ignored and need to be accounted for in the analysis of this data set.

According to Filippenko (1982), the positional shift along the parallactic angle caused by the DCR can be expressed in terms of λ and zenith distance z (or airmass m), which is a function of the observing time t. This shift is computed for a wavelength reference at 5000 Å adopting typical conditions of the ORM. We have computed the spatial shifts for the wavelength of each emission line of interest according to Filippenko's expressions, but referred them to the central wavelength of the Sloan r' filter at 6204 Å that was used for the acquisition of HuBi 1.

$$\mathrm{DCR}(\lambda) = R(\lambda) - R(\lambda_0) \approx 206265[n(\lambda) - n(\lambda_0)]\tan(z) \tag{A.2.1}$$

$$n(\lambda)_{15,760} - 1 = \left[64.328 + \frac{29498.1}{146 - (1/\lambda)^2} + \frac{255.4}{41 - (1/\lambda)^2}\right] \tag{A.2.2}$$

$$n(\lambda)_{T,P} - 1 = (n(\lambda)15,760 - 1) \times \frac{P[1 + (1.049 - 0.0157T)10^{-6}P]}{720.883(1 + 0.003661T)} \tag{A.2.3}$$

The positional shift between emission lines at the blue and red extremes of the spectral range (for instance, the [O II] λ3727 and [O II] $\lambda\lambda$7320,7330 emission lines) was found to be larger than the slit width.

Since the parallactic angle is a function of time $pa(t)$ that varies quite rapidly near culmination, the shift of the slit along the orthogonal direction caused by DCR effects $s(t)$ needs to be corrected accordingly:

$$s(t) = DCR(\lambda, t) \times \cos pa(t) \tag{A.2.4}$$

The variations of the shifts with respect to [N II] for different emission lines of interest such as [O II] λ3727, He II λ4686, Hβ, [O III] λ5007, [S II] $\lambda\lambda$6716,6731, and [O II] $\lambda\lambda$7320,7330 are shown in Figure A.1. This figure reveals that the variations of the shifts during the observations are not dramatic for the wavelength of each emission lines of interest.

We can thus define slit positions for each emission line using median values of their shifts in Figure A.1 to characterise the spatial regions of HuBi 1 registered by these emission lines. A number of these equivalent slit positions are overlaid on an image of HuBi 1 in the [N II] λ6584 emission line in Figure A.2. The figure immediately reveals that different emission lines register different nebular regions. This is particularly significant for the small-sized inner shell of HuBi 1, implying that the comparison of spatial profiles and fluxes for different emission

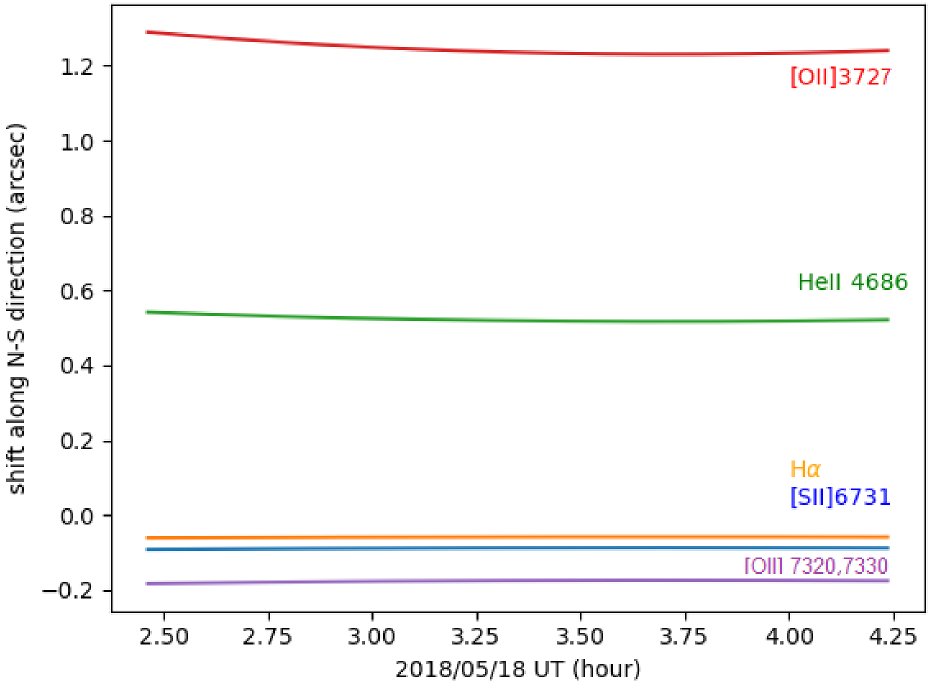

Figure A.1: Variations of the shifts with respect to [N II] for different emission lines during the observations. DCR becomes noticeable in the blue zone of spectrum rising up 1.2 arcsec for [O II]λ3727. Due to the negligible variation, an average value of the shifted for each line can be adopted for the whole observation.

lines of this shell extracted from the OSIRIS 2D spectra has to consider these shifts (unlike the analysis presented by Peña et al. 2021).

In order to correct from these effects the intensity line ratio of a particular emission line to Hβ, we have adopted different strategies. For the inner shell, the intensity line ratio to Hβ of emission lines covered in the spectral range of the MEGARA data is derived from the whole emission of the inner shell, whereas that of emission lines only covered in the OSIRIS data are compared to the Hβ flux derived from the corresponding pseudo-slit of this line in the MEGARA data. For the outer shell, the MEGARA data do not cover the whole outer shell, thus the intensity line ratio to Hβ has been solely derived using the latter approach, i.e., the flux of the emission line is compared to the Hβ flux derived from the corresponding pseudo-slit of this line in the MEGARA data. This procedure warranties that the intensity line ratio to Hβ of a particular emission line is derived using line fluxes measured in the same nebular apertures for both emission lines.

A.3 MAPPINGS V shock models of the inner shell of HuBi 1

MAPPINGS V (see Sutherland & Dopita 2017) is able to produce line and continuum emissivity from shocked plasmas from non-equilibrium ionisation objects, for example, radiative shocks in supernova remnants or shock structures surrounding Herbig-Haro objects. MAPPINGS V solves the coupled ionisation and cooling equations in a time-dependent scheme. The first version of MAPPINGS (see Binette et al. 1985) was developed as a result of a series of works

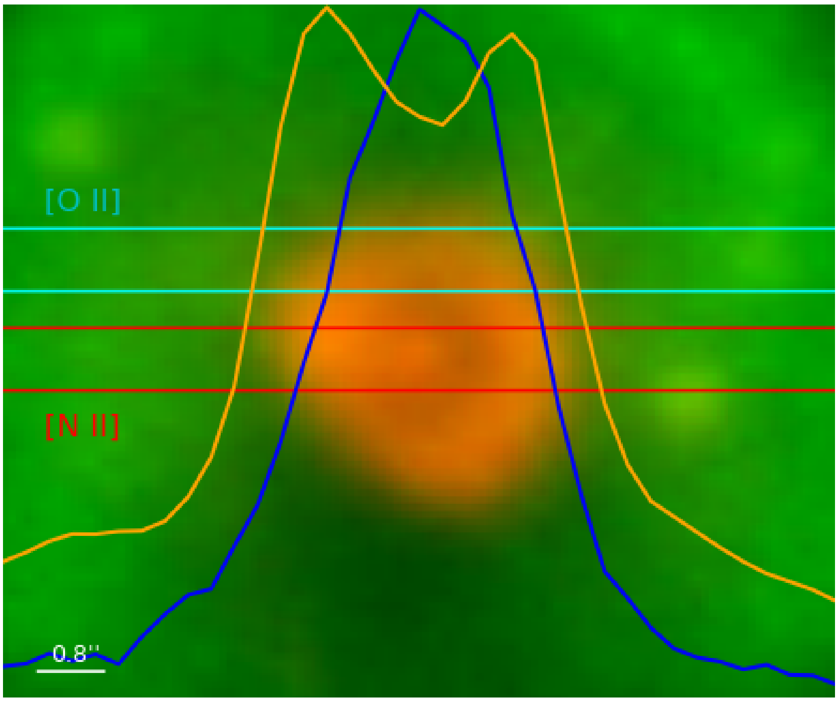

Figure A.2: NOT ALFOSC [N II] λ6584 (red) and Hαλ6563 (green) colour composite picture of HuBi 1. Relative positions of OSIRIS slit for [O II] (cyan) and [N II] (red) are superimposed and also its corresponding lines profiles (blue) and (orange), respectively. The relative position of [O II] line falls just on the edge of the inner region, providing and single-peak profile, and not two as would be expected looking at figure 3.2, showing the DCR suffered by OSIRIS data set.

presented by Dopita (1976, 1977, 1978). The code has been greatly improved since then and it now includes a detailed treatment of temperature-dependent collision strengths, new cooling functions, computations for optically thin plasmas and up to 80,000 cooling and recombination lines (see the historical improvement of the code presented in Sutherland & Dopita 2017).

Here we present in Tables A.3.1 to A.3.4 the predicted line intensities of some of the models computed with MAPPINGS V following the methodology explained in Sec. 3.4.5 to estimate the chemical abundances of the inner shell of HuBi 1. All models are computed with a spectral resolution $R \approx 3000$, i.e. the line intensity ratios presented in Tables A.3.1 to A.3.4 include the contribution of all emission lines computed in the model around the nominal wavelength that would be unresolved at this spectral resolution. We note that the expected contribution of contaminant emission lines is mostly negligible.

Tables A.3.1 and A.3.2 present emission line ratios referred to $I(\mathrm{H}\beta)$=100 as they constrain the chemical abundances of helium, oxygen, and nitrogen with respect to hydrogen. The first five models in Table A.3.1 were computed at fixed values of He/H and N/H to explore the variations of the emission line ratios with the O abundances. Then the O/H abundances ratio was fixed at its best value and the N/H abundances ratio varied in the next five columns. This table shows that high oxygen and nitrogen abundances are necessary to reproduce the emission lines of [O III] and [N II]. Once the best-fit values of the O/H and N/H abundances ratios were determined, the He/H abundances ratio was varied in Table A.3.2. Although the

He I λ5876 emission line is not well reproduced by the adopted value of He/H, we note that different values of He/H lead to notable differences in the estimate of most emission lines (being clearly overestimated for 12+log(He/H) $>$ 13.0).

Tables A.3.3 and A.3.4 explore the variations of the intensity line ratios of He, N, O, Ne, S, and Ar induced by changes of the physical conditions of the shock, namely the shock velocity v_s and the pre-shock density n_pre. We therefore preferred to refer the emission line ratios to I([O III] 5007)=100 to assess the relative changes in the line ratios from ions of those elements. It should be noted in Table A.3.3 that the [O II] to [O III] line ratio peak at v_s of 100 km s^{-1}, then drops gradually at higher velocities. Indeed, the notable increase of the [O III] line intensities at velocities 140 km s^{-1} and above produces a sharp decline in most line ratios, particularly in the H I , He I, and He II recombination lines. Meanwhile the effects of the variations of the pre-shock density n_pre explored in Table A.3.4 reveal notable changes in the intensity ratios of lines from low ionization species, such as He I, [O I], [O II], [N I], [N II], and [S II], with respect to [O III], whereas other higher ionization species show less dramatic variations.

Table A.3.1: MAPPINGS V models assessing the variation of the oxygen and nitrogen abundances for the inner shell of HuBi 1. The values of $v_{\rm s} = 80$ km s^{-1}, $n_{\rm pre} = 1$ cm^{-3}, $B = 1\,\mu$G, 12+log$_{10}$(He/H)=13.0, and H/H$^+$=He/He$^+$=1 have been fixed in all models. O/H stands for 12+log$_{10}$(O/H), N/H for 12+log$_{10}$(N/H), and RO3 denotes the ratio [O III] λ4363/[O III] λ5007.

Line	Obs.	N/H=7.9					O/H=9.8				
		O/H=8.0	O/H=9.0	O/H=9.8	O/H=10.0	O/H=10.2	N/H=7.9	N/H=8.9	N/H=9.9	N/H=10.9	N/H=11.9
[O II] 3727	8360	166.6	723.2	1049.7	978.6	985.3	1049.7	968.8	571.2	66.5	398.1
[Ne III] 3869	622	1.7	15.6	54.6	97.0	88.4	54.6	74.9	54.9	13.0	63.8
[S II] 4069	111	5.2	20.4	21.1	24.0	21.7	21.1	23.7	14.2	2.1	37.4
[O III] 4363	30.6	0.7	6.1	22.8	44.2	43.7	22.8	31.1	25.0	6.3	28.3
He II 4685	134	43.8	48.2	49.2	75.3	60.6	49.2	70.6	66.8	49.7	69.0
[O III] 4959	101	3.2	26.8	109.9	229.0	252.6	109.9	149.1	129.2	45.1	143.3
[O III] 5007	324	9.2	77.7	317.8	662.1	730.1	317.8	431.0	373.4	130.4	414.5
[N I] 5199	75.6	58.4	18.7	2.1	1.1	0.7	2.1	22.1	119.3	266.9	111.3
[N II] 5755	60.2	9.2	4.4	1.1	0.7	0.5	1.1	10.4	66.3	85.7	88.4
He I 5876	< 20.5	286.0	361.8	468.9	399.5	322.6	468.9	422.7	336.7	165.6	388.1
[O I] 6300	95.5	27.2	88.9	51.1	37.7	33.9	51.1	56.6	30.4	5.3	76.5
[S III] 6312	4.5	0.6	3.4	7.1	9.2	9.4	7.1	7.6	5.3	1.1	5.7
[O I] 6363	28.3	8.7	28.4	16.3	12.1	10.8	16.3	18.1	9.7	1.7	24.5
[N II] 6548	330	126.6	45.2	8.1	5.6	3.4	8.1	86.9	552.2	871.3	754.3
Hα	274.0	323.5	325.2	397.3	410.0	436.3	397.3	392.4	407.4	472.3	361.9
[N II] 6584	1390	372.6	132.9	24.0	16.4	10.0	24.0	255.6	1624.6	2563.6	2219.4
[S II] 6716	135	62.3	181.2	160.4	144.5	133.7	160.4	172.2	104.0	18.1	75.7
[S II] 6731	112	50.3	168.1	163.7	159.5	128.7	163.7	190.4	115.0	17.4	117.4
[Ar III] 7135	11.1	0.5	3.7	8.3	13.8	12.9	8.3	11.0	7.8	1.7	9.2
[O II] 7319	31.6	7.4	42.9	70.7	73.9	62.5	70.7	73.8	43.1	3.7	88.8
[O II] 7329	26.2	6.0	34.7	57.1	59.7	50.5	57.1	59.6	34.8	3.0	72.0
RO3	0.094	0.076	0.078	0.072	0.067	0.060	0.072	0.072	0.067	0.048	0.068

Line	Obs.	He/H 12.2	12.9	13.0	13.1	13.2
[O ii] 3727	8360.0	185.7	493.7	571.2	652.6	721.9
[Ne iii] 3869	622.0	38.7	58.8	54.9	50.2	49.9
[S ii] 4069	111	6.4	12.0	14.2	16.9	21.1
[O iii] 4363	30.6	20.6	27.9	25.0	21.8	20.5
He ii 4685	134.0	19.1	66.0	66.8	66.7	73.0
[O iii] 4959	101.0	129.4	149.8	129.2	108.6	98.5
[O iii] 5007	324.0	374.2	433.0	373.4	314.1	284.9
[N i] 5199	75.6	221.4	90.6	119.3	152.1	190.1
[N ii] 5755	60.2	17.2	58.8	66.3	74.3	83.3
He i 5876	$<$ 20.5	60.8	299.7	336.7	395.9	474.7
[O i] 6300	95.5	44.6	20.4	30.4	42.2	57.9
[S iii] 6312	4.4	3.0	5.4	5.3	5.4	5.6
[O i] 6363	28.3	14.2	6.5	9.7	13.5	18.5
[N ii] 6548	330	285.6	485.5	552.2	622.0	718.5
Hα	274.0	487.2	406.6	407.4	408.0	404.5
[N ii] 6584	1390	840.3	1428.5	1624.6	1830.1	2114.2
[S ii] 6716	135	101.7	87.0	104.0	119.7	137.3
[S ii] 6731	112	72.8	92.8	115.0	136.3	164.4
[Ar iii] 7135	11.1	5.3	8.2	7.8	7.3	7.4
[O ii] 7319	31.6	6.3	35.0	43.1	51.7	62.5
[O ii] 7329	26.2	5.1	28.3	34.8	41.8	50.4
RO3	0.094	0.055	0.065	0.067	0.070	0.072

Table A.3.2: MAPPINGS V models assessing the variation of the helium abundances in the inner shell of HuBi 1. The values of v_s = 80 km s^{-1}, n_pre = 1 cm^{-3}, $B = 1\,\mu$G, 12+log$_{10}$(O/H)=9.8, 12+log$_{10}$(N/H)=9.9, and H/H$^+$=He/He$^+$=1 have been fixed in all models. He/H stands for 12+log$_{10}$(He/H) and RO3 denotes the ratio [O iii] λ4363/[O iii] λ5007.

Line	Obs.	v_s (km s^{-1}) 80	100	120	140	160	180	200
[O ii] 3727	2580.2	153.0	495.2	219.4	50.5	22.6	13.6	9.0
[Ne iii] 3869	192.0	14.7	10.1	13.5	6.5	7.0	6.8	6.5
[S ii] 4069	34.3	3.8	6.0	3.6	0.8	0.4	0.4	0.3
[O iii] 4363	9.4	6.7	6.5	7.8	2.6	3.5	4.0	4.1
He ii 4685	41.4	17.9	13.2	17.7	1.2	1.5	2.5	3.4
Hβ	30.9	26.8	54.8	43.5	0.3	0.4	1.0	0.6
[O iii] 4959	31.2	34.6	34.6	34.6	34.6	34.6	34.6	34.6
[O iii] 5007	100.0	100.0	100.0	100.0	100.0	100.0	100.0	100.0
[N i] 5199	23.3	31.9	64.3	24.9	3.2	2.2	2.3	1.5
[N ii] 5755	18.6	17.7	50.8	23.9	5.4	2.8	1.8	1.3
He i 5876	$<$ 6.3	90.2	131.7	63.9	2.4	1.7	2.4	1.4
[O i] 6300	29.5	8.1	13.8	7.8	0.7	0.5	0.8	0.4
[S iii] 6312	1.4	1.4	3.2	1.8	0.7	0.8	0.8	0.8
[O i] 6363	8.7	2.6	4.4	2.5	0.2	0.2	0.2	0.1
[N ii] 6548	101.9	147.9	296.6	183.8	36.0	15.4	13.6	6.9
Hα	84.5	109.1	245.5	175.6	1.0	1.7	3.8	2.2
[N ii] 6584	429.0	435.0	872.7	540.9	106.0	45.4	40.1	20.2
[S ii] 6716	41.7	27.9	48.9	26.4	6.7	3.2	2.8	1.7
[S ii] 6731	34.6	30.8	41.9	29.5	4.8	2.3	2.7	1.3
[Ar iii] 7135	3.4	2.1	2.0	1.7	0.9	0.6	0.5	0.4
[O ii] 7319	9.8	11.5	28.6	16.0	2.2	1.1	0.8	0.5
[O ii] 7329	8.1	9.3	23.2	13.0	1.8	0.9	0.6	0.4

Table A.3.3: MAPPINGS V models assessing the variation of the shock velocity v_s. The values of n_pre = 1 cm^{-3}, $B = 1\,\mu$G, 12+log$_{10}$(O/H)=9.8, 12+log$_{10}$(N/H)=9.9, 12+log$_{10}$(He/H)=13.0, and H/H$^+$=He/He$^+$=1 have been fixed in all models.

Table A.3.4: MAPPINGS V models assessing the variation of the pre-shock density $n_{\rm pre}$. The values of $v_{\rm s} = 80$ km s^{-1}, $B = 1\,\mu$G, 12+log(O/H)=9.8, 12+log(N/H)=9.9, 12+log(He/H)=13.0, and H/H$^+$=He/He$^+$=1 have been fixed in all models.

		$n_{\rm pre}$ (cm^{-3})			
Line	Obs.	0.1	1.0	10	100
[O II] 3727	2580.2	1104.2	153.0	693.9	98.7
[Ne III] 3869	192.0	11.5	14.7	12.6	17.0
[S II] 4069	34.3	9.8	3.8	13.6	21.7
[O III] 4363	9.4	6.3	6.7	6.3	7.7
He II 4685	41.4	13.2	17.9	11.6	15.9
Hβ	30.9	16.6	26.8	93.3	25.8
[O III] 4959	31.2	34.6	34.6	34.6	34.5
[O III] 5007	100.0	100.0	100.0	100.0	100.0
[N I] 5199	23.3	45.4	31.9	124.1	20.6
[N II] 5755	18.6	100.2	17.7	72.7	40.7
He I 5876	< 6.3	47.0	90.2	444.8	107.6
[O I] 6300	29.5	10.0	8.1	32.0	44.6
[S III] 6312	1.4	6.1	1.4	3.9	1.8
[O I] 6363	8.7	3.2	2.6	10.2	14.3
[N II] 6548	101.9	611.1	147.9	461.8	199.4
Hα	84.5	68.7	109.1	371.2	84.8
[N II] 6584	429.0	1797.9	435.0	1358.7	586.6
[S II] 6716	41.7	87.4	27.9	79.7	13.7
[S II] 6731	34.6	62.1	30.8	68.2	18.0
[Ar III] 7135	3.4	2.2	2.1	2.4	2.6
[O II] 7319	9.8	54.8	11.5	46.2	37.1
[O II] 7329	8.1	44.4	9.3	37.4	30.1

Appendix B

Chapter 3

B.1 Surface brightness profiles

Continuum-subtracted surface brightness profiles of [O III] λ5007 extracted from the 2000.50 and 2003.58 WHT and 2014.55 NOT spectra (solid black lines in Figure B.1). The continuum-subtraction, effectively removing the contribution of stars in the slit, was estimated from both sides of the emission line. In the case of 2000.50 WHT profile, the aperture did not pass through the CSPN and its location in A 78 relies on nebular features such as the central knots or the eye-like structure.

These surface brightness profiles are compared with those extracted from the HST WFC3 F502N image along pseudo-slits with the same widths and position angles of the spectroscopic observations (orange dashed-dotted lines in Fig. B.1) to assess possible time variation and to determine the exact location of each slit onto the nebula. The HST profiles have been smoothed to make a fair comparison, however, the emissions from both the central star and the background stars is not subtracted.

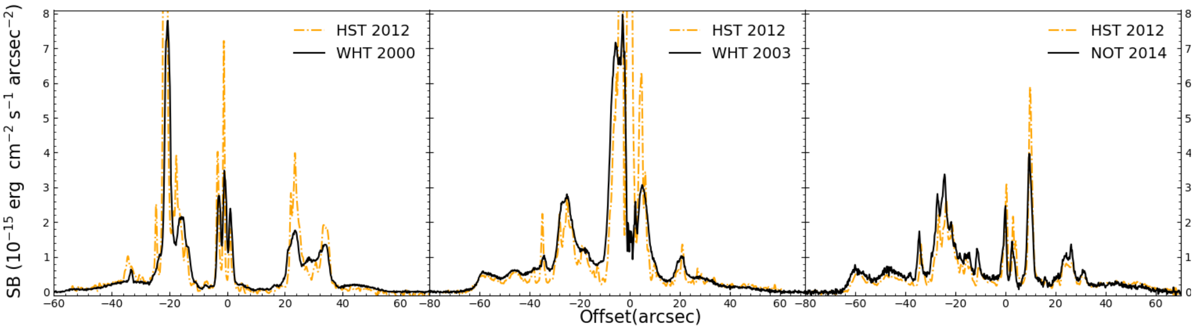

Figure B.1: Comparison of surface brightness profiles of the [O III] λ5007 Å emission line extracted from the spectroscopic WHT ISIS 2000.50 and 2003.58, and NOT ALFOSC 2014.55 observations (solid black lines) and HST WFC3 F502N (2012.89.44) image (dash-dotted orange lines).

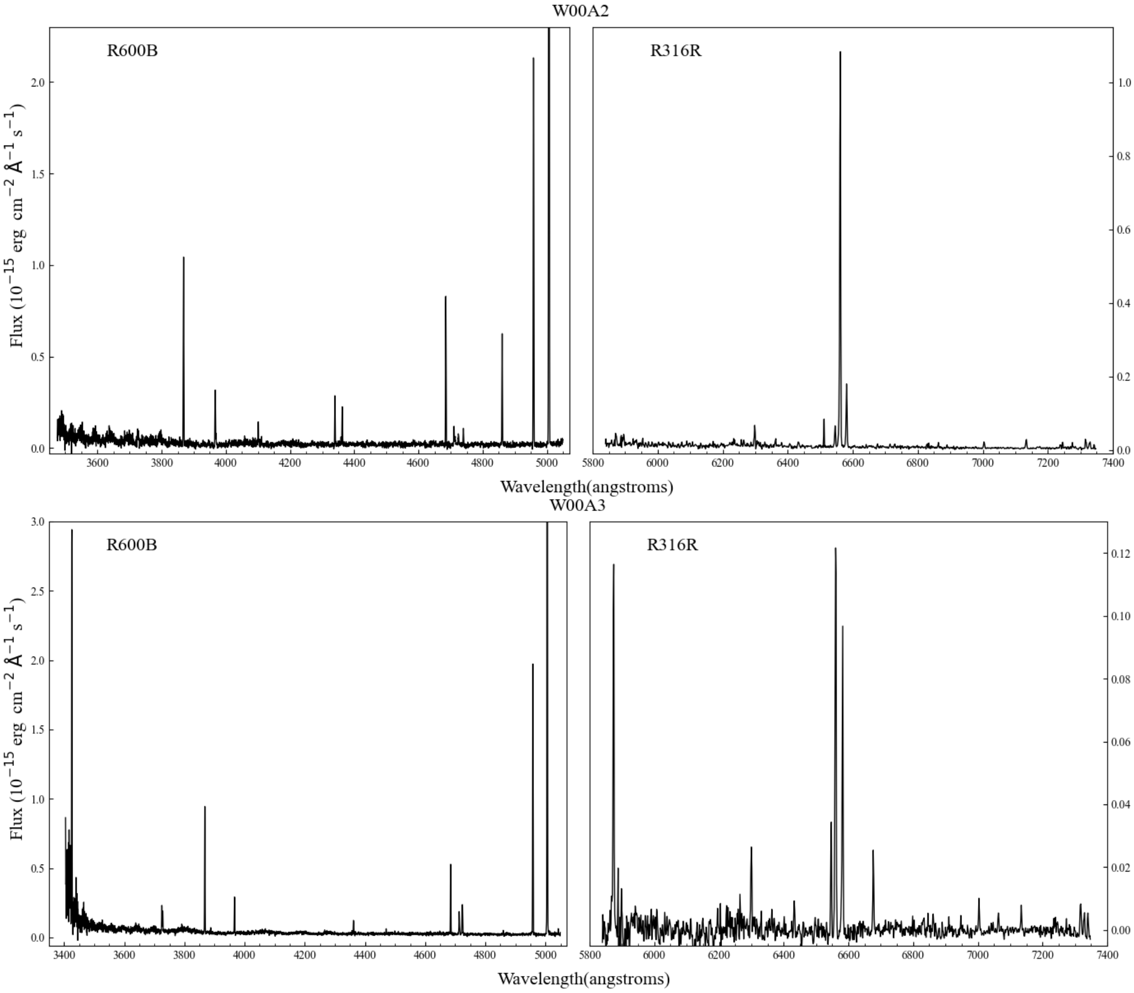

Figure B.2: Spectra of the apertures extracted from the 2000.50 observations at WHT.

B.2 One-dimensional Spectra

The spectra extracted from the apertures shown in Figure 6.1 are presented in Figures B.2, B.3, and B.4, corresponding to the WHT 2000.50 and 2003.58, and NOT 2014.55 observations, respectively. Sky lines are marked by red ticks in those spectra with an imperfect sky background subtraction. The two-dimensional spectra obtained in the WHT present a diffraction pattern that was not possible to avoid and the subsequent one-dimensional spectra present this effect as a sinusoidal continuum. This is specially noticeable in spectra of the faintest regions. Despite the fact that the apertures selected for the extraction of the spectra of the knots are separated from the CSPN (Fig. 6.1), both the seeing and the spatial resolution of the observations caused the emission of the star to smear within the nebular spectra. The stellar features in those spectra have not been used during the data analysis.

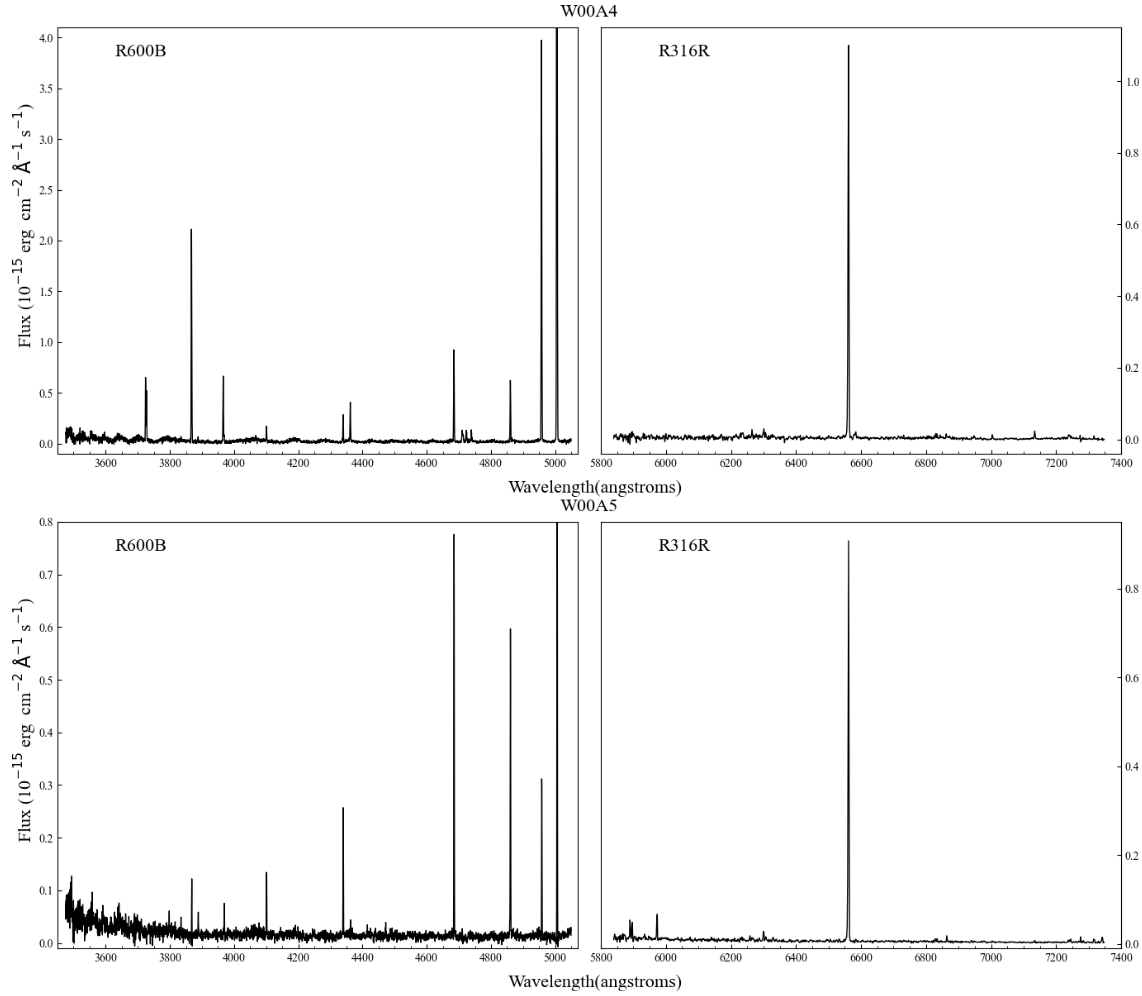

Figure B.2: Continued.

B.3 Equations system for the iterative removal of the He II contribution to Balmer lines

$$\begin{cases} F(\mathrm{H}\alpha_c) & = F(\mathrm{H}\alpha) - F(\mathrm{He}, 6560) \\ F(\mathrm{H}\beta_c) & = F(\mathrm{H}\beta) - F(\mathrm{He}, 4860) \\ \mathrm{c}(\mathrm{H}\beta) & = \frac{1}{\frac{f6562}{f4861} - 1} \cdot \log_{10}\left(\frac{R_{\mathrm{t}}(F(\mathrm{H}\alpha)/F(\mathrm{H}\beta))}{R_{\mathrm{o}}(F(\mathrm{H}\alpha)/F(\mathrm{H}\beta))}\right) \end{cases} \tag{B.3.1}$$

$$\begin{aligned} F(\mathrm{He\,II}, 6560) = & F(\mathrm{He\,II}, 4686) \cdot 10^{c(\mathrm{H}\beta)\cdot\frac{f(4686)}{f(4861)}} \\ & \cdot R_{\mathrm{t}}\left(\frac{F(\mathrm{He\,II}, 6560}{F(\mathrm{He\,II}, 4686}\right) \cdot 10^{-c(\mathrm{H}\beta)\cdot\frac{f(6560)}{f(4861)}} \\ F(\mathrm{He\,II}, 4860) = & F(\mathrm{He\,II}, 4686) \cdot 10^{c(\mathrm{H}\beta)\cdot\frac{f(4686)}{f(4861)}} \\ & \cdot R_{\mathrm{t}}\left(\frac{F(\mathrm{He\,II}, 4860}{F(\mathrm{He\,II}, 4686}\right) \cdot 10^{-c(\mathrm{H}\beta)\cdot\frac{f(4860)}{f(4861)}} \end{aligned}$$

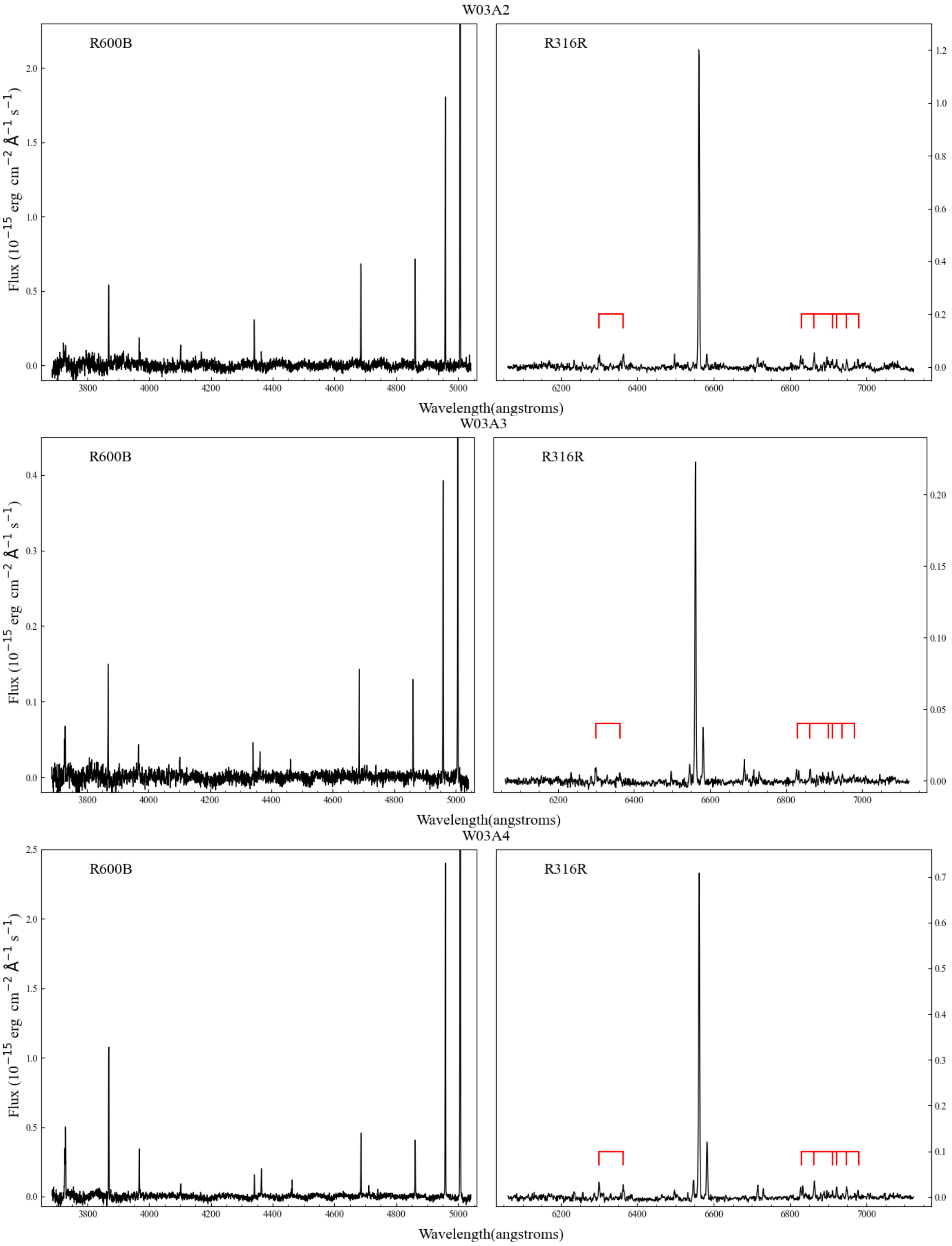

Figure B.3: Spectra of the apertures extracted from the 2003.58 observations at WHT. The sky emission lines are marked by red ticks to avoid confusing them with nebular emission lines.

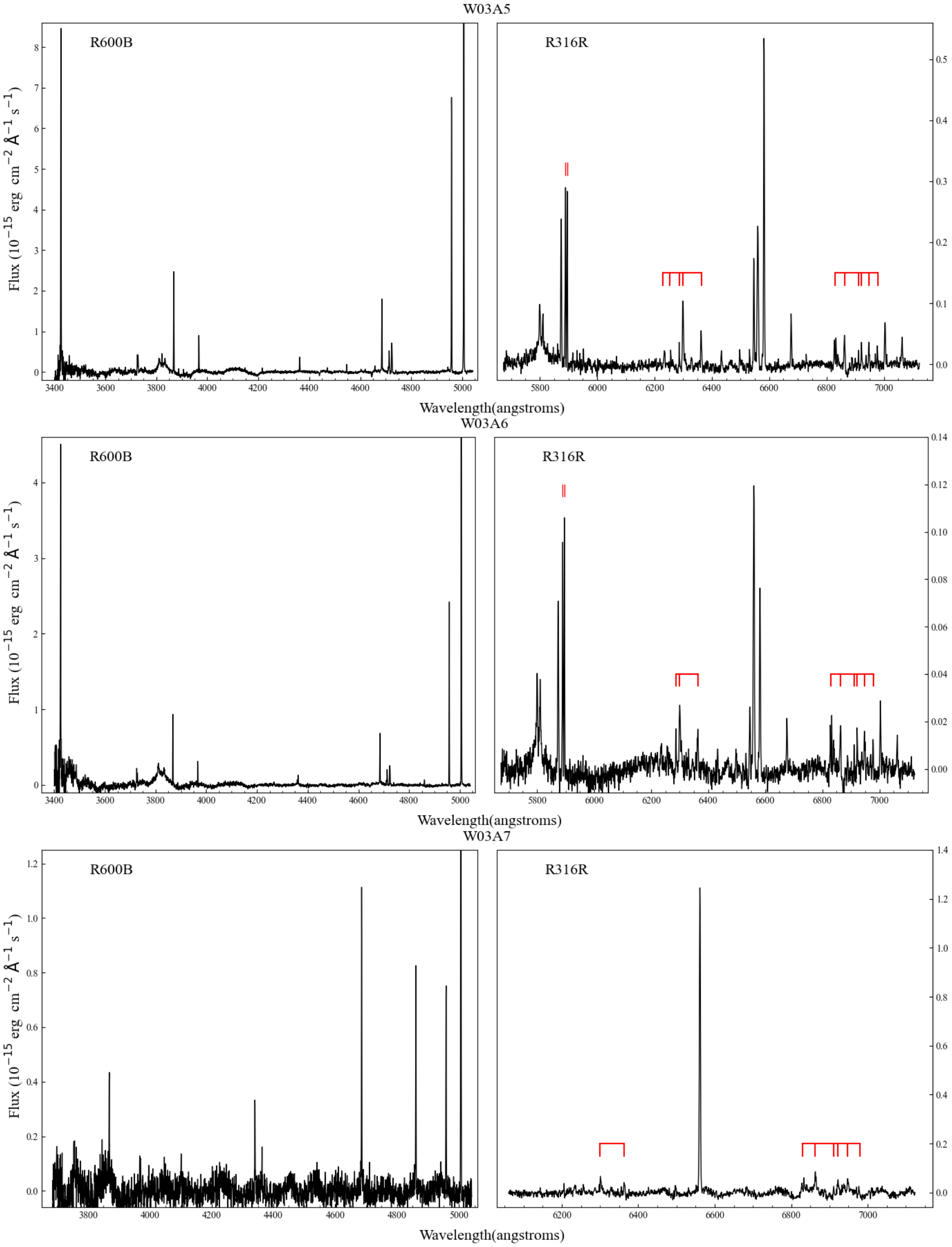

Figure B.3: Continued.

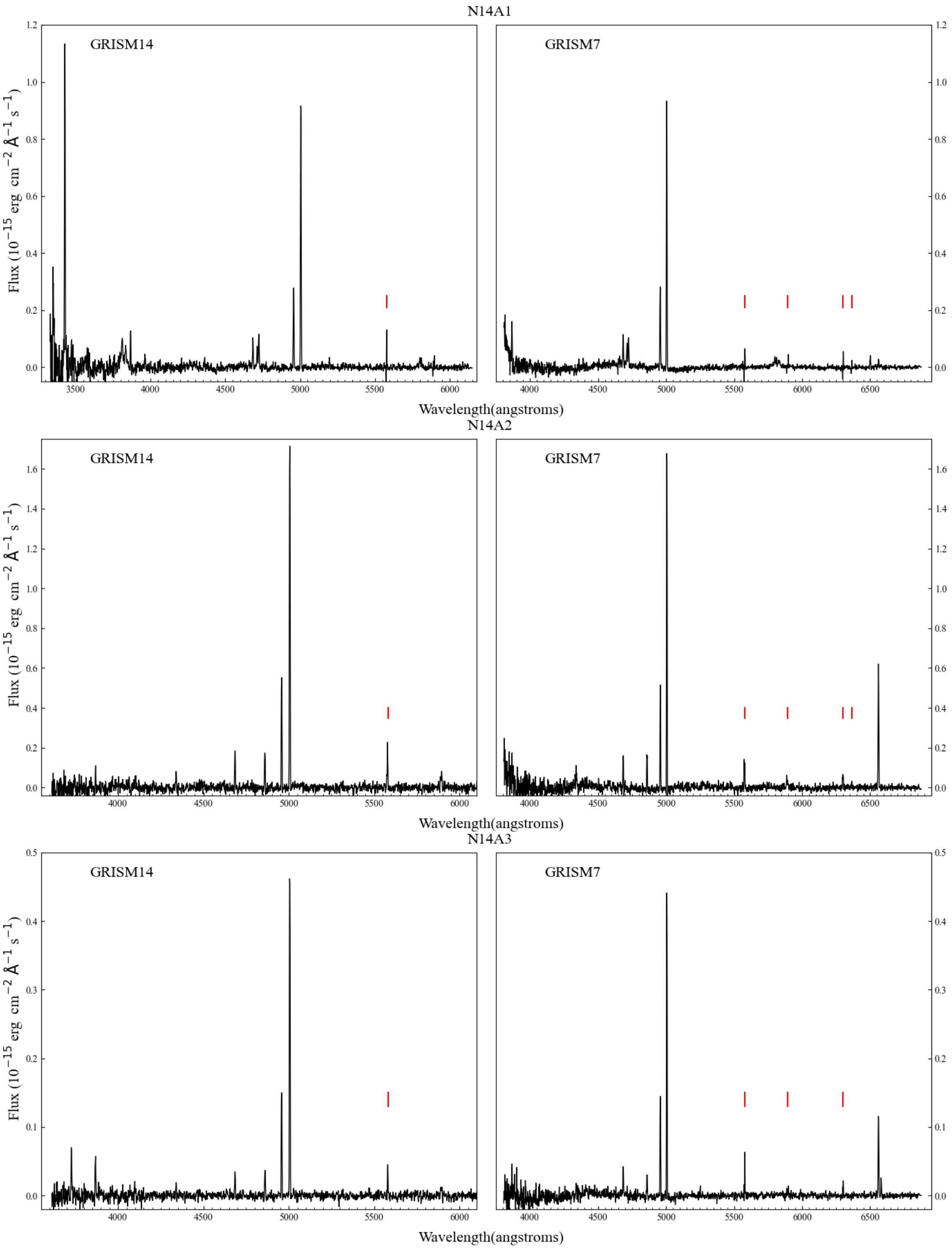

Figure B.4: Spectra of the apertures extracted from the 2014.55 observations at NOT. The sky emission lines are marked by red ticks to avoid confusing them with nebular emission lines.

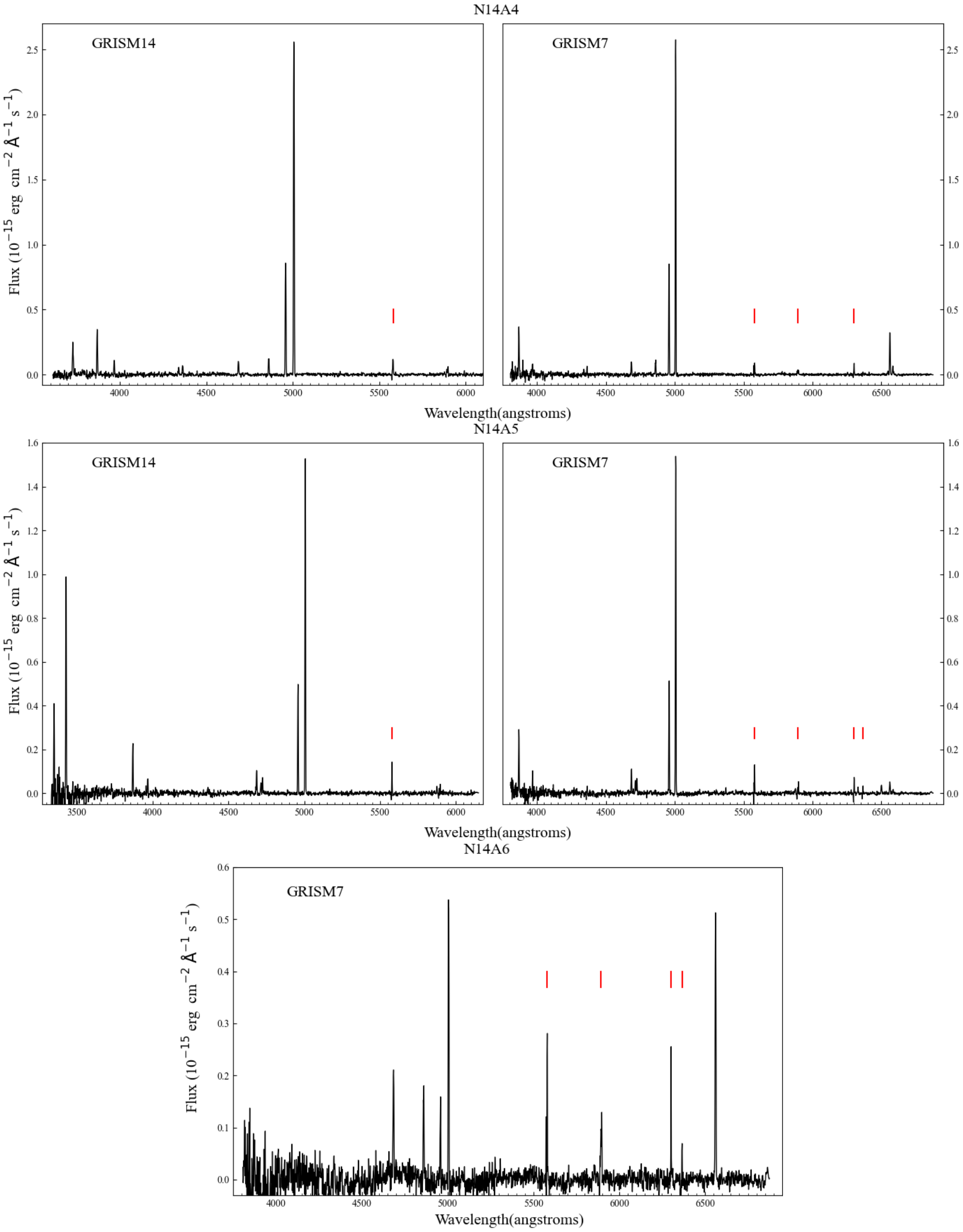

Figure B.4: Continued.

Appendix C

Glossary

AFTP	AGB final thermal pulse
AGB	Asymptotic Giant Branch
ALMA	Atacama Large Milimeter/submillimeter Array
ADF	Abundances discrepancy factor
APEX	Atacama Pathfinder Experiment
ALFOSC	ALhambra Faint Object Spectrograph and Camera
CAHA	Calar Alto Astronomical Observatory
CEL	Collisionally excited lines
CS	Central Star
CSE	Circumstellar envelope
CSPN	Central Star of Planetary Nebula
CTIO	Cerro Tololo Interamerican Observatory
DCR	Differential chromatic refraction
E-AGB	Early-AGB
FOC	Faint Object Camera
FoV	Field of view
FWHM	Full-width half-maximum
GTC	Gran telescopio Canarias
HB	Horizontal Branch
HR	Hertzprung-Russell
HR	High-resolution[1]
HST	Hubble Space Telescope
HVC	High-Velocity Component
HVF	High-Velocity Filament
ICF	Ionization corrections factors
IFS	Integral field spectroscopic
IFU	Integral-field unit
ING	Isaac Newton Group
IR	Infrared
IRAF	Image Reduction and Analysis Facility

IRS	Infrared Spectrograph
ISIS	Intermediate-dispersion Spectrograph and Imaging System
ISM	Interstellar Medium
LCB	Large compact bundle
LSR	Local Standard of Rest
LTP	Late thermal pulse
MEGARA	Multi-Espectrógrafo en GTC de Alta Resolución para Astronomía
MLT	Mixing-Length Theory
MR	Medium-resolution
MS	Main sequence
N	North
NE	Northeast
NOT	Nordic Optical Telescope
NW	Northwest
ORL	Optical recombination lines
ORM	Observatorio de El Roque de los Muchachos
OSIRIS	Optical System for Imaging and low-Intermediate-Resolution Integrated Spectroscop
PA	Position angle
PBCZ	Proton-Burning Convection Zone
PN	Planetary Nebulae
pPN	Protoplanetary Nebula
RGB	Red Giant Branch
S	South
SALT	Southern African Large Telescope
SB	Surface brightness
SDU	Second Dredge-Up
SE	Southeast
SNR	Signal-to-noise ratio
SO	Sakurai's Object
SW	Southwest
TCS	Twin Cassegrain Spectrograph
TRGB	Tip of the RGB
TP	Thermal Pulse
TP-AGB	Thermal-Pulsing AGB
UV	Ultraviolet
VLTP	Very late thermal pulse
VPH	Volume phase holographic
WC	Wolf-Rayet Carbon type
WD	White Dwarfs
WFPC	Wide Field Planetary Camera
WHT	William Herschel Telescope
WISE	Wide-field Infrared Survey
WR	Wolf-Rayet
ZAMS	Zero-Age Main Sequence